Title

Performance Tuning of Ultrafiltration and Reverse Osmosis Membranes Surface Nano-structured with Tethered Poly(acrylic acid) Chains

Author

Chen, Yian

Publication Date

2022

Peer reviewed|Thesis/dissertation

UNIVERSITY OF CALIFORNIA

Los Angeles

Performance Tuning of Ultrafiltration and Reverse Osmosis Membranes Surface Nano-structured with Tethered Poly(acrylic acid) Chains

A dissertation submitted in partial satisfaction of the

requirements for the degree Doctor of Philosophy

in Chemical Engineering

by

Yian Chen

2022

ABSTRACT OF THE DISSERTATION

Performance Tuning of Ultrafiltration and Reverse Osmosis Membranes Surface Nano-structured with Tethered Poly(acrylic acid) Chains

by

Yian Chen

Doctor of Philosophy in Chemical Engineering

University of California, Los Angeles, 2022

Professor Yoram Cohen, Chair

Surface tethering of hydrophilic polymer brush layers is a popular approach for membrane surface modification with the target of overcoming and mitigating various challenges such as perm-selectivity tradeoff, removal of specific contaminants, and membrane fouling and mineral scaling. In the present study, a systematic investigation of membrane surface structuring with tethered polyacrylic acid (PAA) layers was conducted to tune both reverse osmosis (RO) and ultrafiltration (UF) membranes performance in terms of water permeability, solute rejection, molecular weight cutoff (*MWCO*), fouling resistance, scaling propensity and cleaning efficacy.

Surface nano-structured (SNS) PAA brush layers were synthesized onto the base polysulfone (PSf) UF and polyamide (PA) thin-film composite (TFC) RO membranes via membrane surface activation with different atmospheric pressure plasma (APP) types (i.e., Air, He/O_2, and He), followed by graft polymerization (GP) of acrylic acid (AA). Effective tuning of SNS-PAA-PSf UF membrane performance in terms of hydraulic permeability and molecular weight cutoff (*MWCO*) was feasible by adjustments of the APP and graft polymerization conditions. It was shown, for the first time, that SNS-PAA-PSf membranes can be synthesized with a range of hydraulic permeability (spanning a factor of 1.1-2.6 in magnitude) for a given *MWCO*, or a range of *MWCO* (spanning a factor of 1.5-2.3 in magnitude) for a given hydraulic permeability, thereby overcoming the hydraulic permeability-*MWCO* tradeoff. The SNS-PAA-PSf membrane characteristics (surface hydrophilicity, intrinsic membrane resistance, and PEG *MWCO*) were responsive to pH and ionic strength due to the conformational change (i.e., swelling/collapse) of the surface tethered PAA chains. Within the tested range of pH (3-11) and ionic strength (0-547 mM), the SNS-PAA-PSf membrane demonstrated self-regulated membrane performance (i.e., R_m 0.74 - 2.29×10^{13} m^{-1}, and *MWCO* 1.8 - 15.0 kDa) and surface hydrophilicity (i.e., surface energy -114.5 to -139.2 mJ/m^2). UF fouling stress tests with bovine serum album (BSA) and alginic acid in high salinity water and post-cleaning with D.I. water demonstrated reduced flux decline (by ~11.3%) and improved permeability recovery (by ~34%) for the SNS-PAA-PSf membrane relative to the native PSf membrane.

The surface tethered PAA chains also improved polyamide (PA) RO membrane removal of nitrate, boron, As (III), and As (V), with rejection of 98.0%, 90.7%, 96%, and 99.6%, respectively, relative to 76.8-84.9%, 87.3-92.1%, and 94.5-97.2% for the tested commercial RO membranes. The increased membrane removal of the specific contaminants is attributed to the surface tethered

PAA layer sealing of microscopic defects in the polyamide membrane active layer. The SNS-PAA-PA membrane also exhibited lower flux decline for both gypsum and calcium carbonate scaling tests compared to the tested commercial RO membranes and 100% and 94% permeability recovery post D.I. water flushing, respectively.

Scale up of the membrane surface nano-structuring approach, atmospheric pressure plasma-induced graft polymerization (APPIGP), was developed for SNS-PAA-PA membrane sheets of size sufficient for fabrication of 2.5 inch × 21 inch spiral-wound RO elements. Laboratory testing of 18 membrane coupons (~2" x 4") extracted from different locations of the SNS-PAA-PA membrane sheet, in terms of water and salt permeability coefficients and intrinsic membrane rejection, demonstrated the similar or higher performance uniformity level compared to Base-PA. SNS-PAA-PA spiral wound elements, fabricated with the above SNS-PAA-PA membrane sheets, outperformed the commercial Dow SW30 element exhibiting lower flux decline and 100% permeability recovery in fouling tests of both BSA and sodium alginate model foulant solutions. Results of the present study suggest that the APPIGP approach can be scaled up to fabricate commercial scale spiral-wound RO elements of superior antifouling properties.

The dissertation of Yian Chen is approved.

Panagiotis D. Christofides

Samanvaya Srivastava

Ximin He

Yoram Cohen, Committee Chair

University of California, Los Angeles

2022

To my parents.

TABLE OF CONTENTS

ABSTRACT OF THE DISSERTATION ii

LIST OF FIGURES xiv

LIST OF TABLES xxii

ACKNOWLEDGEMENTS xxv

VITA xxvi

PUBLICATIONS xxvii

CONFERENCE PRESENTATIONS xxvi

Chapter 1 Introduction and Objectives 1

1.1 Introduction 1

1.2 Problem Statement 10

1.3 Objectives of the Dissertation 11

1.4 Research Approach 12

Chapter 2 Background and Literature Review 17

2.1 Membrane processes fundamentals and challenges 17

2.1.1 Membrane Types 17

2.1.2 Fundamental concepts and equations 21

2.1.3 Major challenges in membrane processes 25

2.1.4 Major approaches to improve membrane performance 41

2.2 Polymer brush layer for membrane surface modification 42

2.3.1 Plasma-induced Graft Polymerization 48

2.3.2 Surface modification of spiral wound elements 54

2.4 Polymer brush layer structures 57

2.5 Impact of brush layer on membrane properties 61

2.6 Responsive brushes 79

2.7 Summary 92

Chapter 3 Modification of PSf membranes via AA Surface Graft Polymerization induced by Surface Activation with atmospheric pressure Air, He/O_2 and He plasmas 94

3.1 Overview 94

3.2 Experimental 95

3.2.1 Materials 95

3.2.2 Preparation of PSf surrogate membrane surfaces 96

3.2.3 Atmospheric pressure plasma-induced graft polymerization (APPIGP) 97

3.2.4 Surface characterization 99

3.3 Results and Discussion 103

3.3.1 PSf surface functionalization 103

3.3.2 PSf surface topography 106

3.3.3 PSf Surface contact angle 111

3.3.4 PSf Surface Charge 114

3.4 Conclusions 116

Chapter 4 Tuning the Performance of Surface Nano-structured UF Membranes Surface Activated by He/O_2 APP 118

4.1 Overview 118

4.2 Experimental 119

4.2.1 Materials 119

4.2.2 Preparation of PSf surrogate membrane surfaces 120

4.2.3 Atmospheric pressure-induced graft polymerization (APPIGP) 121

4.2.4 Surface Characterization 123

4.2.5 Performance Characterization 124

4.3 Results and Discussion 126

4.3.1 AFM characterization of tethered PAA layer on surrogate PSf membrane substrate 126

4.3.2 SNS-PAA-PSf membranes 130

4.3.3 Tailored membrane performance summary 142

4.4 Conclusions 147

Chapter 5 PSf UF Membrane Performance Tuning via APPIGP surface activated by Air and He plasmas 149

5.1 Overview 149

5.2 Experimental 150

5.2.1 Materials 150

5.2.2 Atmospheric pressure plasma-induced graft polymerization (APPIGP) 151

5.2.3 UF Performance characterization 151

5.3 Results and Discussion 153

5.3.1 Influence of surface plasma treatment on SNS-PAA-PSf membrane performance 153

5.3.2 Cost analysis and future scale-up expectations 156

5.4 Conclusions 157

Chapter 6 Stimuli-Responsive PSf UF Membrane with Self-Adaptive Membrane Performance and Surface Wettability 159

6.1 Overview 159

6.2 Experimental 163

6.2.1 Materials 163

6.2.2 Atmospheric pressure-induced graft polymerization (APPIGP) 164

6.2.3 Membrane Surface Hydrophilicity 165

6.2.4 Membrane Performance Characterization 166

6.3 Results and Discussion 167

6.3.1 Salinity-responsive membrane performance 171

6.3.2 pH-responsive performance 174

6.3.3 Self-regulated membrane performance and surface wettability 177

6.4 Conclusions 180

Chapter 7 Reduced PSf UF Fouling Propensity with A Surface Tethered PAA Brush Layer 182

7.1 Overview 182

7.2 Experimental 183

7.2.1 Materials 183

7.2.2 Atmospheric pressure plasma-induced graft polymerization (APPIGP) 184

7.2.3 Surface hydrophilicity 185

7.2.4 Fouling resistance 187

7.3 Results and Discussion 189

7.4 Conclusions 195

Chapter 8 Selective RO membrane with a surface tethered polymer brush layer for enhanced rejection of nitrate, boron, and arsenic 197

8.1 Overview 197

8.2 Experimental 202

8.2.1 Materials 202

8.2.2 Atmospheric pressure-induced graft polymerization (APPIGP) 203

8.2.3 Membrane selective removal 204

8.3 Results and Discussion 206

8.4 Conclusions 209

Chapter 9 Impact of PAA Brush Layer on RO Membrane Scaling Propensity 211

9.1 Overview 211

9.2 Experimental 213

9.2.1 Materials 213

9.2.2 Atmospheric pressure-induced graft polymerization (APPIGP) 214

9.2.3 Surface scanning images 215

9.2.4 Performance Characterization 215

9.3 Results and Discussion 218

9.4 Conclusions 226

Chapter 10 Scaleup of APPIGP for the Fabrication of Spiral Wound RO Elements 228

10.1 Overview 228

10.2 Experimental 230

10.2.1 Materials 230

10.2.2 Scaled-up plasma surface activation 230

10.2.3 Scaled-up graft polymerization 231

10.2.4 Spiral-wound element fabrication 234

10.2.5 Membrane surface characterization 237

10.2.6 Membrane performance evaluation 237

10.3 Results and Discussion 244

10.3.1 SNS-PAA-PA membrane sheet performance uniformity 244

10.3.2 SNS-PAA-PA coupon membrane anti-fouling properties 246

10.3.3 SNS-PAA-PA element fouling resistance and cleaning efficacy 249

10.3.4 SNS-PAA-PA element separation performance 251

10.4 Conclusions 253

Appendix 255

A. Supplementary Materials 255

A.1. Surface characterization of PSf surfaces 255

A.2. Surface characterization of PA RO membranes 259

A.3. PSf UF membrane performance characterization 261

A.4. PA RO membrane performance characterization 263

B. Zeta Potential Characterization Protocol 267

C. Membrane Surface Nano-structuring Procedures for PSf Membrane Coupons 274

C.1. Preparation of the base membrane 274

C.2. He or He/O_2 plasmas 276

C.3. Air plasma 279

C.4. Graft polymerization 280

D. Dead-end stirred-cell UF system 282

References 284

LIST OF FIGURES

Figure 1-1. Osmosis (left) and reverse osmosis (right) processes. 2

Figure 1-2. A summary diagram of the membrane desalination process and its major challenges. 3

Figure 1-3. Membrane flux decline and recovery during the fouling and D.I. cleaning cycles. Depending on whether membrane fouling can be recovered by the simple D.I. water cleaning, it is then divided into reversible fouling and irreversible fouling. 5

Figure 1-4. Overall objectives and workflow of the dissertation study. 12

Figure 1-5. Research flowchart outlining for PSf UF membrane performance tuning via surface tethered PAA brush layers (**Chapters 3-7**). 13

Figure 1-6. Research flowchart outlining PA RO membrane performance tuning via surface tethered PAA brush layer (**Chapters 8-10**). 15

Figure 2-1. An illustration of membrane classifications (i.e., microfiltration, ultrafiltration, nanofiltration, and reverse osmosis) and their process characteristics. 17

Figure 2-2. Process diagram for dead-end filtration (mostly for MF and UF membranes; left) and cross flow filtration (mostly for NF and RO membranes; right). 19

Figure 2-3. Schematic diagram of concentration polarization phenomenon developed in a crossflow membrane channel. 23

Figure 2-4. Upper-bound tradeoff relations between membrane permeability and selectivity for polymeric membranes: (a) bovine serum album (BSA)/water separation and hydraulic permeability in porous UF membranes [9]; (b) water/NaCl selectivity (A/B) and water permeance in nonporous thin-film composite (TFC) polyamide (PA) membranes [73]. 27

Figure 2-5. Flux decline performance in gypsum scaling tests (feed solution of $SI_g = 2.0$) comparing the different SNS-PA-TFC and LFC-1 membranes (adapted from [108]). 35

Figure 2-6. Illustration of different UF membrane fouling mechanisms. 38

Figure 2-7. Configuration of UF membrane backwash. 39

Figure 2-8. Illustration of reversible and irreversible fouling. 40

Figure 2-9. Surface tethered polymer brush layer synthesized via physical adsorption and chemical attachment (grafting to and grafting from). 45

Figure 2-10. Surface graft polymerization with surface initiation sites formed using chemical initiators, and surface exposure to gamma or UV irradiation, plasma, and ozone..... 47

Figure 2-11. Tethered polymer brush layer structure regimes defined by grafting density: (a) "mushroom" regime at low grafting density and (b) "brush" regime at high grafting density (adapted from [119]). 58

Figure 2-12. Illustration of the gradient responsive conformational change of the surface tethered poly(vinyl pyrrolidone) (PVP) chains on zirconia-based ceramic UF membrane at the range of ionic strength and pH (adapted from [46])..... 81

Figure 2-13. Schematic representation of the conformational change of polymer chains tethered in proximity or inside a membrane pore leading to narrowing ("close") or enlarging ("open") of the membrane pore. 82

Figure 2-14. Schematic illustration of different locations of tethered polymer chains with respect to membrane pores: (a) complete tethered polymer chains coverage of the entire membrane surface (including pore), preferred for MF membranes with relatively large barrier pores (>50 nm; [218]), and (b) tethered polymer chains coverage of the external membrane surface, preferred for UF membranes with small pores (< 10 nm; [218]). 85

Figure 3-1. Schematics of the APPIGP process mechanisms where Path A designates surface treatment with Air APP and Path B is for surface treatment with either He or He/O_2 plasma. 97

Figure 3-2. Manually scratched stripes of SNS-PAA-PSf-Si (top), and AFM 3-D topography cross-sectional height profile of the scratched area (bottom). 102

Figure 3-3. AFM 3-D topography for plasma treated PSf-PEI-Si surfaces (in D.I. water): (left), PAA-PSf-PEI-Si surfaces activated with plasma treatment followed by AA graft polymerization (middle), and the respective FH distributions (right) for (a) Air, (b) He/O_2, and (c) He APP. 108

Figure 3-4. Cross-sectional AFM FH profiles obtained in D.I. water for PSf-PEI-Si surface after surface treatment with (a) Air APP, (b) He/O_2 APP, and (c) He APP, and corresponding AA graft polymerized PSf surfaces (d), (e) and (f)..... 109

Figure 3-5. Sessile drop water contact angle of PSf surfaces (PSf-PEI-Si) treated with He, He/O_2, and Air plasmas at PSS of 10 mm and 1-5 sequential plasma scans (equivalent exposure time of 0.4-2 s)..... 112

Figure 3-6. Stability of plasma treatments as indicated by hydrophobic recovery (i.e., ratio of sessile drop water contact angle measurements of the plasma treated Base-PSf membrane surface to the one of the original Base-PSf membrane surface) upon increased time of exposure to air after plasma treatment.... 113

Figure 3-7. Free energy of hydration (**Section 3.2.4.3**) for native PSf and PAA-PSf-PEI surfaces formed on smooth silicon wafer substrates (calculated based on water contact angles; **Table 3-5**; Also, exposure to ambient air was for a period of 30 hrs). 114

Figure 3-8. Comparison of zeta potential variation with pH for the SNS-PAA-PSf membranes, synthesized via AA graft polymerization post-surface activation (with different plasmas) of the base PSf membrane (Toray MUF-20K), compared with a tight commercial UF membrane (Toray MUF-10K)..... 116

Figure 4-1. AFM derived topography images (under D.I. water) of (a) native PSf-PEI-Si surface and PAA-PSf-PEI-Si surfaces synthesized via APPIGP: surface activation with He/O_2 plasma treatment (PSS=10 mm, N=1), followed by AA graft polymerization at initial monomer concentration ($[M]_o$) of (b) 15 vol%, (c) 17 vol%, (d) 20 vol%, (e) 23 vol%, and (f) 25 vol% at 70°C for 1 h..... 127

Figure 4-2. AFM derived surface FH distributions (under D.I. water) of native PSf-PEI-Si surface and PAA-PSf-PEI-Si surfaces synthesized via APPIGP: surface activation with He/O_2 plasma treatment (PSS=10 mm, N=1), followed by AA graft polymerization at initial monomer concentration ($[M]_o$) in the range of 15-25 vol% at 70°C for 1 h. 128

Figure 4-3. Cross-sectional AFM FH profiles (in water) with respect to the average FH of PAA-PSf-PEI-Si surfaces activated with He/O_2 plasma treatment (PSS=10 mm, N=1), followed by AA graft

polymerization (70°C for 1 h) at $[M]_o$ of (a) 15 vol%, (b) 17 vol%, (c) 20 vol%, (d) 23 vol%, and (e) 25 vol%. 129

Figure 4-4. SEM top surface images of (a) PSf base membrane MUF-20K, and (b) SNS-PAA-PSf membrane, also cross section images of (c) PSf base membrane MUF-20K, and (d) SNS-PAA-PSf membrane..... 131

Figure 4-5. Dependence of SNS-PAA-PSf membranes (utilizing MUF-20K base membrane) hydraulic permeability (L_p) and MWCO on surface activation conditions (i.e., plasma source-surface (PSS) distance and number of sequential He/O_2 APP scans (N)..... 134

Figure 4-6. Effect of graft polymerization (GP) temperature on membrane hydraulic permeability (L_p) and MWCO for SNS-PAA-PSf membranes (utilizing MUF-20K base membrane). 136

Figure 4-7. Dependence of SNS-PAA-PSf membranes (based on MUF-20K membrane) hydraulic permeability (L_p) and MWCO on graft polymerization time..... 137

Figure 4-8. Effct of initial monomer concentration on membrane hydraulic permeability (L_p) and MWCO for SNS-PAA-PSf membranes (utilizing MUF-20K base membrane). 138

Figure 4-9. The effect of initial monomer solution pH on (a) membrane hydraulic permeability (L_p) and (b) MWCO for SNS-PAA-PSf membranes (prepared using base membrane MUF-20K). 140

Figure 4-10. Dependence of membrane performance (MWCO and hydraulic permeability) tunability range of SNS-PAA-PSf membranes derived based on two different UF base membranes: (a) MUF-10K and (b) MUF-20K. SNS-PAA-PSf membrane performance was tuned by adjustment of various plasma and graft polymerization conditions..... 140

Figure 4-11. Mapping of MWCO and hydraulic permeability of SNS-PAA-PSf membranes (synthesized utilizing base membrane MUF-20K) at various plasma and graft polymerization conditions that achieve (a) a range of hydraulic permeability at a target MWCO, and (b) a range of MWCO at essentially the same hydraulic permeability. 146

Figure 4-12. Comparison of SNS-PAA-PSf membranes performance, at various plasma and graft polymerization conditions, and for other modified and the present commercial base UF membranes (Toray-MUF: 10K and 20K), demonstrating (a) tradeoff relationship between membrane MWCO and hydraulic permeability, and (b) L_p/MWCO ratio vs the water permeability..... 147

Figure 5-1. Permeability coefficient and MWCO for the SNS-PAA-PSf membranes synthesized via surface activation Air APP over a range of different operating conditions. Also shown are data from [156] for SNS-PAA-PSf UF membranes synthesized via AA graft polymerization post-surface activation with He/O_2 plasma. (Membrane synthesis conditions and performance data are provided in **Table 5-1**). 154

Figure 6-1. Schematics of (a) "through-pore" mechanism and (b) "through-polymer" mechanism of responsive membrane tethered with polyelectrolyte chains..... 161

Figure 6-2. Dependence of the surface captive bubble contact angle for the Native-PSf and SNS-PAA-PSf membranes on solution ionic strength (0 - 547 mM) at pH of 7..... 173

Figure 6-3. Normalized intrinsic membrane resistance of Native-PSf and SNS-PAA-PSf membranes over solution ionic strength in the range of 0 - 547 mM at constant pH of 7. 173

Figure 6-4. Normalized PEG MWCO of Native-PSf and SNS-PAA-PSf membranes over solution ionic strength range of 0 - 547 mM at pH of 7. 174

Figure 6-5. Illustration of tethered chains in the proximity of a membrane pore under collapsed (left), swollen (right) and "normal" (middle) conditions. 174

Figure 6-6. Dependence of Native-PSf and SNS-PAA-PSf membranes surface captive bubble contact angle on solution pH (3 - 11). 176

Figure 6-7. Normalized intrinsic membrane resistance for Native-PSf and SNS-PAA-PSf membranes over solution pH range of 3-11. 176

Figure 6-8. Normalized PEG MWCO of Native-PSf and SNS-PAA-PSf membranes over solution pH range of 3-11. 177

Figure 6-9. Mapping of PEG MWCO and intrinsic membrane resistance of the SNS-PAA-PSf and Native-PSf membranes by adjusting solution ionic strength and pH. (Raw data: **Table 6-1**)..... 179

Figure 6-10. Membrane surface hydrophilicity (i.e., surface energy) of both Native-PSf (MUF-10K) and SNS-PAA-PSf membranes variation with solution ionic strength and pH. (Raw data: **Table 6-2**)..... 180

Figure 7-1. Configuration of the UF filtration system. 188

Figure 7-2. (A) Membrane surface free energy of cohesion and its components, and (B) free energy of adhesion between membrane surface and the foulants (contact angle measured on the BSA fouled membranes)..... 191

Figure 7-3. Normalized overall UF membrane resistance for fouling stress tests comparing the SNS-PAA-PSf and a commercial UF membranes for (a) BSA filtration of 1 g/L BSA in PBS aqueous solution at pH 7.4 for 2 h, and (b) filtration of 1 g/L sodium alginate saline solution (with 32 g/L NaCl) at pH 7 for 2 h. All fouling tests were at the same initial flux (9 $L \cdot m^{-2} \cdot h^{-1}$). The SNS-PAA-PSf synthesis conditions: Air APP treatment at PSS =10 mm and N = 1; AA graft polymerization at $[M]_o$ = 20 vol% and 70 °C for 1 h. 195

Figure 8-1. Configuration of the laboratory plate-and-frame RO (PFRO) membrane test unit (adapted from [49]). 206

Figure 8-2. Rejection of nitrate, boron, As (III), and As (V) for SNS-PAA-PA membrane as compared to the commercial Dow SW30, Toray SWRO, and Base-PA membranes. (Feed solutions: 60 ppm NO_3 prepared using KNO_3, 3 ppm boron prepared using H_3BO_3, 750 ppb As (III) prepared using $AsNaO_2$, and 750 ppb As (V) prepared using $HAsNaO_4 \cdot 7H_2O$). Characterization conditions: crossflow velocity: 49 cm/s, permeate flux: 25.5 $L \cdot m^{-2} \cdot h^{-1}$, transmembrane pressure: 55.2 bar (~800 psi), and temperature: 20°C).. 209

Figure 9-1. Flux decline for the SNS-PAA-PA membrane after 24 h gypsum scaling (left) and calcium carbonate scaling (right) tests, also showing the corresponding flux decline curves for the commercial membranes of Dow SW30, Toray SWRO, and Base-PA membranes. (Gypsum feed solution pH of 5.7,

membrane surface saturation index of gypsum SI_g=1.3; Calcium carbonate feed solution pH of 7.9, membrane surface saturation index of calcite SI_c=6.9)..... 219

Figure 9-2. SEM top-view images of the gypsum (left) and calcium carbonate (right) scaled SNS-PAA-PA membrane surfaces, at the end of the 24 hr scaling tests. (Membrane surface saturation index of gypsum SI_g=1.3; membrane surface saturation index of calcite SI_c=6.9). 219

Figure 9-3. SEM top-view images of the two different structures of gypsum crystals, i.e., rosette arrangements consisting of gypsum needles growing from a core region (left) and needle-shaped structure (right), scaled on Dow SW30 and Toray SWRO membranes, respectively, at the end of the 24 hr scaling tests. 220

Figure 9-4. SEM top-view images of SNS-PAA-PA membrane after 24 h calcium carbonate scaling test, followed by 30 min D.I. water flushing, compared to selected commercial membranes (Dow SW30, Toray SWRO, and Base-PA). The shown level of membrane surface calcium carbonate scale coverage is 40.5%, 59.9%, 57.8%, and 4.3% for Dow SW30, Toray SWRO, Base-PA, and SNS-PAA-PA membranes, respectively. 223

Figure 10-1. (Top) Graft polymerization reactor system schematic, and (Bottom) arrangement of membrane placement in the reactor. 233

Figure 10-2. (a) Assembly of a spiral wound element using the SNS-PAA-PA membrane sheets, and (b) SNS-PAA-PA spiral wound membrane elements (**Section 10.2.4**)..... 235

Figure 10-3. Illustration of the locations of individual membrane coupons, each measuring 11 cm × 5.6 cm (4.4" × 2.2") extracted from a large membrane sheet 76 cm × 61 cm (30" × 24") for performance uniformity testing. (Note that a portion of the edge area of the membrane sheet was trimmed when combining sheets for the production of the spiral-wound element). 240

Figure 10-4. Configuration of the RO system for testing spiral-wound elements. (Sensors: P – pressure transducer, C – conductivity meter, T – thermometer, and F – flow meter.)..... 242

Figure 10-5. Water permeability coefficient (L_p) and salt permeability coefficient (B) for membrane coupon samples from different locations of the Base-PA (Toray 73AC) and SNS-PAA-PA 30" × 24" membrane sheets (**Fig. 10-3**). (Experimental conditions and characterization protocol are provided in **Section 10.2.6.1**). 245

Figure 10-6. Comparison of SNS-PAA-PAA and commercial membranes (Dow SW30, Toray SWRO (82V) and Base-PA(73AC)) with respect to the contributions of membrane resistances (R_m, R_{rev}, and R_{irr}) to total membrane resistance (R_T) after 24 h fouli filtration test, followed by 30 min D.I. water flushing, for (a) aqueous saline solution (32 g/L NaCl) of 0.1 g/L BSA in and (b) aqueous saline (32 g/L NaCl) solution of 0.1 g/L sodium alginate..... 247

Figure 10-7. Comparison of SNS-PAA-PA and Dow SW30 spiral-wound elements in terms of flux decline (left) and relative contributions of resistances (**Table 10-5**), R_m, R_{irrev}, and R_{cake} to the total membrane permeation resistance, R_T (right) for fouling filtration tests of aqueous saline solution (32 g/L NaCl) of (a) 0.1 g/L BSA, and (b) 0.1 g/L sodium alginate. (Filtration tests at initial permeate flux of 25.5 $L \cdot m^{-2} \cdot h^{-1}$ and constant cross flow velocity of 11.4 cm/s.; Filtration period: 24 hours. Note: Intrinsic membrane resistances of the Dow SW30 #1, #2 and SNS-PAA-PA #1, #2 elements were 8.1×10^{13}, 7.8×10^{13}, 7.8×10^{13}, and 1.0×10^{14} m^{-1}, respectively.)..... 250

LIST OF TABLES

Table 2-1. Summary table of commercial RO membrane nitrate rejection. 32

Table 2-2. Summary table of commercial RO membrane boron rejection. 32

Table 2-3. Summary table of commercial RO membrane As (III) and As (V) rejection. 34

Table 2-4. Literature review of air plasma induced graft polymerization in membrane surface modification[a] 50

Table 2-5. Summary of studies that conducted membrane surface modification in spiral wound RO elements. 55

Table 2-6. Literature review (2018-2022) of surface tethered brush layer affecting UF and RO membrane surface characteristics[a,b] 74

Table 2-7. Literature review (past 5 years) of surface tethered brush layer affecting UF and RO membrane performance[a,b] 76

Table 2-8. Summary of literature reported pH and ionic strength-responsive UF and RO membranes with surface tethered polymer brush layer. 88

Table 2-9. Summary of literature reported explanations of pH and ionic strength-responsive membrane performance. 90

Table 3-1. Summary of plasmas properties information 98

Table 3-2. XPS spectra of C 1s and O 1s scan peak area (%) for the native PSf-PEI-Si surface, and PSf surfaces treated with Air, He/O_2, and He plasmas [(a)]. 105

Table 3-3. The surface elemental atomic composition of PSf surfaces after plasma treatment with Air, He/O_2, and He plasmas and post-AA graft polymerization [(a)]. 105

Table 3-4. Surface roughness and average FH for the native PSf-PEI-Si and PAA-PSf-PEI-Si surfaces activated with Air, He/O_2 and He plasmas. 107

Table 3-5. Sessile drop water contact angle and free energy of hydration(a) for the PSf and PAA tethered surfaces formed on silicon wafer substrates. 112

Table 4-1. Surface roughness, average FH and average major peak separation distance for the native PSf-PEI-Si and PAA-PSf-PEI-Si surfaces. 128

Table 4-2. Performance of SNS-PAA-PSf membranes synthesized at various plasma and graft polymerization conditions, based on the MUF-20K membrane. 132

Table 4-3. Performance of SNS-PAA-PSf membranes synthesized at various plasma and graft polymerization conditions, based on the MUF-10K membrane [(1)] 133

Table 4-4. PSf and SNS-PAA-PSf surface hydrophilicity measured via sessile drop (SD) water contact angle. 144

Table 4-5. Summary of the trend of SNS-PAA-PSf membranes L_p and MWCO with respect to surface nano-structuring (APP and GP) conditions. 145

Table 5-1. Summary of performance for the SNS-PAA-PSf[a] and commercial PSf membranes. 155

Table 5-2. Cost analysis of the research grade SNS-PAA-PSf membrane coupon synthesis. The use of Air plasma can lead to significant cost reduction relative to He/O_2 plasma. 155

Table 6-1. Membrane hydraulic permeability coefficient and PEG MWCO for Native-PSf and SNS-PAA-PSf membranes in response to NaCl concentration and pH. 169

Table 6-2. Membrane surface captive bubble (CB) water contact angle for Native-PSf and SNS-PAA-PSf membranes at different pH and salt concentrations 170

Table 7-1. Surface tension of liquids used in contact angle measurements[a]. 186

Table 7-2. Sessile drop water contact angle and free energy of hydration for the Native-PSf, plasma treated and SNS-PAA-PSf membranes. 189

Table 7-3. Contact angle and surface energy parameters of Native PSf membrane (MUF-10K) and SNS-PAA-PSf membrane. 191

Table 7-4. Membrane hydraulic resistance, MWCO, and rejection of BSA and sodium alginate for the Base-PSf (MUF-20K), Native-PSf (MUF-10K), and SNS-PAA-PSf membranes. 192

Table 7-5. Intrinsic membrane resistance (R_m), reversible fouling resistance (R_{rev}) and irreversible fouling resistance (R_{irrev}) for Commercial PSf (Toray MUF-10K) membrane and SNS-PAA-PSf[(a)] membrane post 2 hr filtration with BSA[(b)] (in PBS solution) and sodium alginate[(b)] in a high salinity aqueous solution. 194

Table 8-1. Summary of membrane rejections for nitrate, boron, As (III), and As (V) for commercial PA BWRO and SWRO membranes (both flat sheet and spiral-wound elements) selected removal for (detailed literature review summary table[*] in **Section 2.1.3.2**)..... 198

Table 8-2. Summary of the proposed key factors affecting solute rejection performance imparted by tethered hydrophilic polymers 201

Table 8-3. Commercial membrane performance reported by the manufacturers. 203

Table 8-4. Membrane water and salt permeability coefficients, and observed and intrinsic salt rejections [(a)]. 208

Table 8-5. Membrane rejection of Nitrate, Boron, Arsenite, and Arsenate. 208

Table 9-1. Summary of gypsum and calcium carbonate scaling and cleaning test results for membrane coupons [(a)] 223

Table 9-2. Predicted membrane surface TDS concentration, permeate TDS concentration, and nominal membrane TDS rejection for all four tested membranes at the end of 24 hr filtration of gypsum and calcium carbonate model solutions [a]. 225

Table 10-1. RO spiral wound elements [a] used in the study 236

Table 10-2. Comparison of performance of SNS-PAA-PA membrane with commercial membranes[(a)] . 236

Table 10-3. Data summary table of membrane BSA and Sodium Alginate fouling [a]. 247

Table 10-4. Summary of membrane surface hydrophilicity 248

Table 10-5. Intrinsic membrane resistance (R_m), reversible fouling resistance (R_{rev}), and irreversible fouling resistance (R_{irrev}) for SNS-PAA-PA and Dow SW30 spiral wound elements filtration of BSA and sodium alginate [(a)]. 251

ACKNOWLEDGEMENTS

I would like to express my gratitude to my advisor Professor Yoram Cohen for his guidance, support, and instruction throughout my study and research at UCLA. He taught me by example about the most crucial characteristics to succeed in conducting scientific research and pursuing a career in academia, which are curiosity, patience, persistency, creativity, criticism, logic, and rigorousness. Without his caring and patient mentorship, my journey to advanced education and scientific research would not have been possible. I would also like to acknowledge all of my colleagues in Professor Cohen's research group, Dr. Soomin Kim, Dr. Jin Yong Choi, Dr. Anditya Rahardianto, Dr. Tae Lee, Dr. John Thompson, Dr. Gu Han, Dr. Jie Zhang, Dr. Shangwen Zha, and Yeunha Kim for their generous help and critical feedback. I truly appreciate the support and understanding from my family, Zhiping Chen, and Haihong Xu. I am also thankful to all of my friends for their inspiration and optimism, as well as for the joy that they bring to my life. Lastly, I would like to thank my cat, Bacon, for his love and companionship.

The present work was supported, in part, by the U.S. Army (Grant W56HZV-16-0117) and the California Department of Water Resources (Agreement Number 4600011630). I would also like to acknowledge the support from Surfx Technologies, Toray Membrane USA Inc., US Bureau of Reclamation, Orange County Water District, and Panoche Drainage District.

VITA

2017	B.S., Chemical and Biomolecular Engineering University of California, Los Angeles
2017-2022	Graduate Student Researcher Teaching Assistant Department of Chemical and Biomolecular Engineering University of California, Los Angeles

CONFERENCE PRESENTATIONS

Y. Cohen and **Y. Chen**, *Dual stimuli-responsive polysulfone UF and polyamide RO membranes due to the "through-polymer" mechanism*, 2022 North American Membrane Society (NAMS) Annual Meeting, May 14-18, 2022, Tempe, AZ.

Y. Chen, and Y. Cohen, High Performance Surface Nano-Structured Reverse Osmosis Membranes for Seawater and Brackish Water Desalination, 2021 AIChE Annual Meeting, Nov. 7-11, Boston, MA.

Y. Chen, S. Kim, Y. Kim, and Y. Cohen, Surface Nano-Structured Spiral-Wound Polyamide TFC RO Membranes, 2021 North American Membrane Society (NAMS) Annual Meeting, Aug. 29-Spet. 2, Denver, CO.

Y. Chen, S. Kim, and Y. Cohen, Tuning Ultrafiltration Membrane Performance via Surface Graft Polymerization of Acrylic Acid Enabled by Air Plasma Activation, 2020 North American Membrane Society (NAMS) Annual Meeting, May 18-21, 2020, Virtual.

Y. Chen, S. Kim, A. Rahardianto, and Y. Cohen, Surface Nano-structuring with Tethered Poly(acrylic acid) Chains for Tuning Ultrafiltration Membrane Performance, 2020 North American Membrane Society (NAMS) Annual Meeting, May 18-21, 2020, Virtual.

Y. Chen, S. Kim, A. Rahardianto, and Y. Cohen, Surface Nano-structuring with Hydrophilic Polymer Brush Layers for Membrane Performance Tailoring and Optimization, 2019 North American Membrane Society (NAMS) Annual Meeting, May 11-15, 2019, Pittsburgh, PA.

PUBLICATIONS

Y. Chen, S. Kim, Y. Kim, J. Walker, T. Wolfe, K. Coleman, Y. Cohen*, Scale Up of Polyamide Reverse Osmosis Membranes Surface Modification with Tethered Poly(Acrylic Acid) for Fabrication of Low-Fouling Spiral-Wound Elements, *Desalination* 536 (2022): 115762

Y. Chen, J. Zhang, Y. Cohen*, Fouling resistant and performance tunable ultrafiltration membranes via surface graft polymerization induced by atmospheric pressure air plasma, *Separation and Purification Technology* (2022): 120490.

Y. Chen, S. Kim, Y. Cohen*, Tuning the hydraulic permeability and molecular weight cutoff (MWCO) of surface nano-structured ultrafiltration membranes, *Journal of Membrane Science* 629 (2021) 119180.

Y. Chen, M. Rovira-Bru, F. Giralt, Y. Cohen*, Hydraulic Resistance and Protein Fouling Resistance of a Zirconia Membrane with a Tethered PVP Layer, *Water* 13(7) (2021) 951.

J.Y. Choi, T. Lee, A.B. Aleidan, A. Rahardianto, M. Glickfeld, M.E. Kennedy, **Y. Chen**, P. Haase, C. Chen, Y. Cohen*, On the feasibility of small communities wellhead RO treatment for nitrate removal and salinity reduction, *Journal of Environmental Management* 250 (2019) 109487.

Y. Cohen, **Y. Chen**, S. Kim, Surface Restructuring of RO membranes, *Water Desalination: Current Status and New Developments*, Yoram Cohen (Ed.), World scientific Publishing Company, 2022, ***In Press*** (Book Chapter)

Y. Chen, Y. Cohen*, Dual stimuli-responsive surface nano-structured polysulfone UF and polyamide RO membranes due to the "through-polymer" mechanism, *Journal of Membrane Science*, ***In Progress***

Y. Chen, J.Y. Choi, T. Lee, A. Aleidan, Y. Cohen, Novel flexible RO system (FLERO) integrated with portable online monitoring system for nitrate and salinity reduction in remote communities, ***In Progress***

Y. Chen, Y. Cohen*, High Selective Surface Nano-structured Polyamide Reverse Osmosis Membrane with Improved Selected Removal for Nitrate, Boron, and Arsenic, ***In Preparation***

Y. Chen, Y. Cohen*, Gypsum and Calcium Carbonate Scaling Resistant Polyamide Reverse Osmosis Membrane with Surface Tethered Poly(acrylic acid) Brush Layer, ***In Preparation***

Chapter 1 Introduction and Objectives

1.1 Introduction

In the last few decades, membrane-based separation—based on the differences in component mass transport through a semi-permeable barrier, which allows passage of some while retaining the others [1]—has become increasingly popular. Compared to traditional thermal distillation, membrane separation is more efficient, flexible, cost-effective, and environmentally friendly [2]. It has thus become entrenched in numerous industries, such as chemical and pharmaceutical, food and beverage, gas and oil, wastewater treatment, water purification and desalination.

Membranes are classified into microfiltration (MF), ultrafiltration (UF), nanofiltration (NF), and reverse osmosis (RO) according to membrane pore size and thus the degree of selectivity [1]. RO is a nonporous membrane with an average pore size of less than 1 nm. RO membrane is used to selectively permeate solute lean product water (permeate) through the membrane from saline feedwater via solution diffusion. RO desalination is achieved by applying a high external pressure that is greater than the feed osmotic pressure [2], thus forcing water to flow in the opposite direction of natural osmosis (**Fig. 1-1**). Unlike RO membrane, UF is a porous membrane, with average pore size range of 0.1−0.001 μm [3], used to separate small particles, dissolved macromolecules, bacteria, and viruses based on size exclusion [4]. UF separation is applied in numerous industries such as chemical and pharmaceutical manufacturing, and food and beverage processing [3, 5, 6]. Due to its effective removal of suspended particles, UF is widely used for pretreatment of the RO process (to ensure RO feedwater with consistent quality) for drinking water production and wastewater treatment [7, 8].

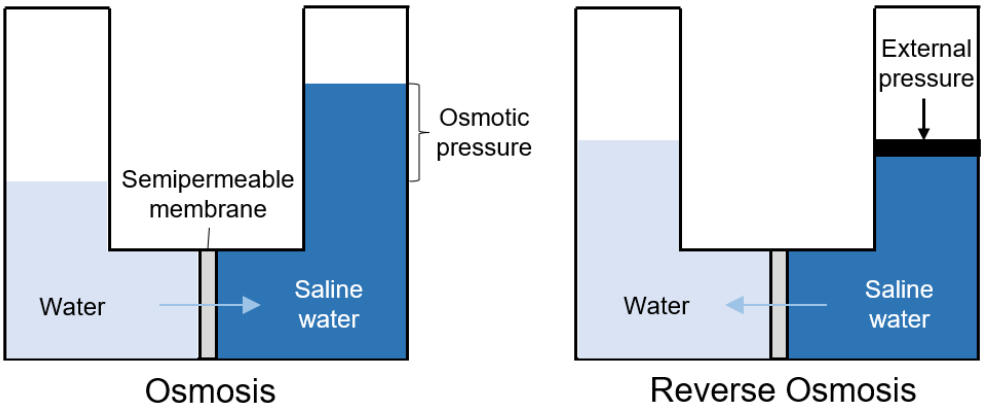

Figure 1-1. Osmosis (left) and reverse osmosis (right) processes.

Extensive research efforts have been devoted to improve the membrane desalination process in three major directions: productivity, quality, and cost (**Fig. 1-2**), which are often be interrelated. For polymeric membranes, there is a typical tradeoff between productivity and product quality, referred to as perm-selectivity tradeoff [9]. Membrane water permeance and rejection are often inversely correlated: highly permeable membranes have low selectivity and vice versa [9]. Such tradeoff is largely due to broad distributions of free-volume pores in the porous membranes and nonspecific interactions between small solutes (e.g., inorganic salts, organic molecules, proteins) and polymers that constitute the membrane active layer [9]. Therefore, breaking the tradeoff effect between permeability and selectivity by tuning membrane polymeric structures is of great significance.

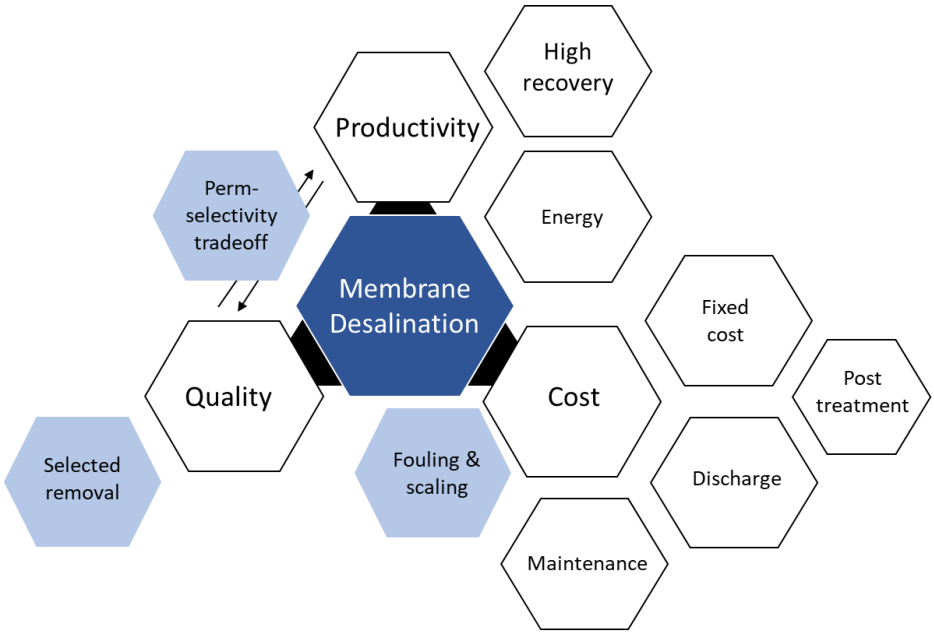

Figure 1-2. A summary diagram of the membrane desalination process and its major challenges.

In addition to the typical tradeoff between membrane permeability and selectivity, RO membrane's removal of specific contaminants, such as nitrate, boron, and arsenic, is another major challenge in RO desalination. Overexposure to the above contaminants, through drinking water with a concentration level, above the safe drinking water limit as suggested by the World Health Organization (WHO) Guidelines for Drinking Water Quality can be harmful to human health and even fatal [10-12]. Even though regular RO membranes can achieve seawater salt rejection above 99% [10, 13], their rejections for nitrate, boron, As (III), and As (V) are still limited, with the reported rejection range of 40.4-97.7%, 12-96%, 5-99%, and 68-99%, respectively (**Section 2.1.3.2**). While the maximum total boron concentration, for example, in seawater could amount up to about 15 g/L [14]. To comply with the safe drinking water standard and reduce boron concentration below 0.5 mg/L in the treated permeate stream [15], a minimum RO boron rejection of 97% is required. Thus, the current technology of commercial RO membranes is insufficient for

reducing contaminant concentrations and meeting the drinking water quality requirements under normal operational conditions [13].

Membrane fouling also limits the applications of both UF and RO membranes. Fouling generally refers to the temporary or permanent non-specific surface adsorption/deposition of rejected inorganic, organic and biological matters on the membrane surface and/or within the pores [16]. Membrane fouling is often quantified by flux decline at fixed transmembrane pressure, due to the accumulation of foulants on and/or in the membrane pores leads to increased water transport resistance through the membrane. Both surface fouling and fouling in pores (i.e., pore plugging and pore narrowing) were observed for UF membranes. However, surface fouling is the main fouling mechanism for RO membranes since they do not have distinguishable pores and are considered to be essentially non-porous [17].

A specific type of membrane fouling, inorganic fouling, or membrane mineral scaling, is of particular concern for brackish water RO (BWRO) desalination. For RO membrane BW desalination, with the feedwater total dissolved solids (TDS) within the range of 1000-15,000 mg/L, membrane mineral scaling remains a major challenge that occurs when the solubility limits of the sparingly soluble salts (i.e., $CaCO_3$, $CaSO_4$, $BaSO_4$, $SrSO_4$, and silica) present in the feed water are exceeded [18-21]. Scale formation on RO membrane surface is a combined consequence of two different mechanisms, homogeneous nucleation in the bulk solution followed by deposition of the scalant crystals onto the membrane surface (bulk deposition) and heterogeneous nucleation on the membrane surface followed by crystal growth (surface crystallization) [22], both of which can lead to membrane flux decline [23]. As membrane permeability decreases, the required energy for the production of a given volume of permeate will increase. Moreover, the presence of a foulant cake layer or mineral scale on the membrane surface can lead to impairment of membrane product

quality, loss of membrane rejection [22, 24, 25], increased frequency of chemical cleaning, shortened membrane service life, a diminished period for membrane element replacement, and up to 30% escalated operational costs [26-31].

Membrane fouling can then be divided into two categories: reversible fouling and irreversible fouling (**Fig. 1-3**). Membrane reversible fouling can be easily removed via simple D.I. water cleaning, while removing irreversible fouling would require more aggressive chemical cleaning [32]. The irreversible fraction of membrane fouling, which increases with the number of filtration cycles, is especially undesirable as chemical cleaning is typically cumbersome and requires plant shutdown or taking membrane system offline (from hours to days), leading to reduced overall water treatment plant capacity, a residual stream that is difficult to dispose of [33], or even membrane damage [34]. Membrane D.I. water cleaning, including backwash (for UF membranes) and simple flush (for RO membranes), is a convenient mechanical cleaning method that is done during the filtration cycle (**Fig. 1-3**). Periodical D.I. water cleaning can provide for partial recovery of membrane permeability (due to detached/sheared foulant cake layer from the membrane surface), reduced frequency of chemical cleaning, and extended membrane service life.

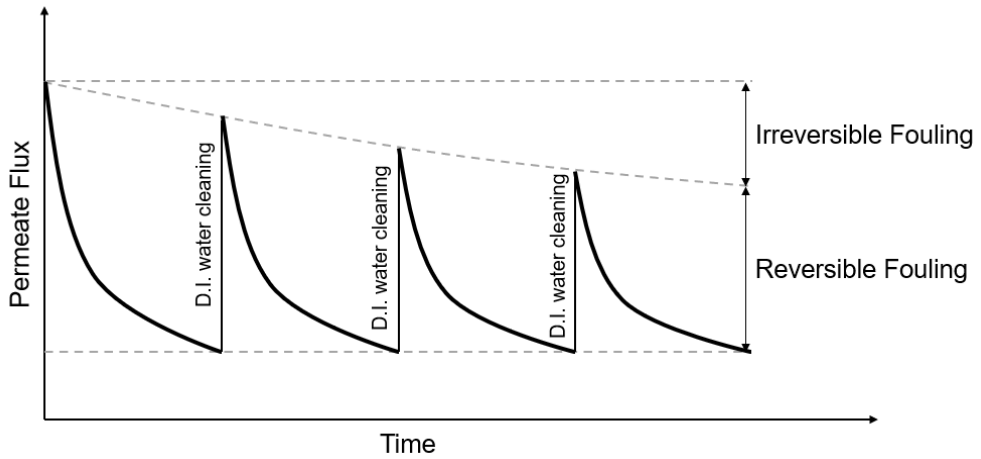

Figure 1-3. Membrane flux decline and recovery during the fouling and D.I. cleaning cycles. Depending on whether membrane fouling can be recovered by the simple D.I. water cleaning, it is then divided into reversible fouling and irreversible fouling.

In industrial applications, membrane fouling is mitigated by pretreatment (i.e., coagulation, biological treatment), adjusting operating conditions (i.e., permeate flux, transmembrane pressure, crossflow velocity), and proper cleaning (i.e., cleaning frequency, backwash/forward flush, chemical cleaning, air scouring) [35]. As a specific type of membrane fouling, membrane mineral scaling can be inhibited by the use of antiscalant and adjustment of feedwater pH [36]. These approaches, even though effective, require additional chemicals and thus can lead to a concentrate stream that is difficult to be disposed of, and/or increase desalination process operational complexity [36].

As an alternative to the above fouling mitigation strategies that focus on operational conditions, surface engineering that can tune membrane performance and mitigate membrane fouling and scaling has generated significant interest. Previous studies [18, 36-42] reported that membrane surface characteristics (i.e., surface chemistry, topography, hydrophilicity, and charge) can affect membrane separation properties, as well as membrane fouling, scaling, and cleaning performance. Tuning of membrane separation properties, reduced fouling and scaling propensities, and increased cleaning efficacy were achieved via physical coatings and grafting with various chemical species including polymers [39, 43], surface treatment with acids and oxidation [22, 24, 25], dispersion of modifiers in the membrane active layer [43, 44], and graft polymerization [45].

Among the various membrane surface modification approaches, membrane surface tethering of polymer brush layer has shown to be a long-lasting, cost-efficient, and a convenient approach to tailor membrane surface characteristics, tuning membrane performance, and reducing membrane fouling and scaling propensity [45]. It was previously demonstrated that surface tethered polymer brush layers can reduce membrane propensities for gypsum scaling and biofouling via increasing surface hydrophilicity, effective screening of the underlying membrane

surface including the pores, and partial mobility (due to Brownian motion) of the segments of the anchored polymer chains [46 , 47, 48]. The surface tethered polymer brush layer can also serve to tune PA-TFC RO membrane water and salt (i.e., NaCl) permeability coefficients and overcoming the typical perm-selectivity tradeoff [49]. However, the effects of surface tethered polymer brush layer on RO membrane removal of specific contaminants including nitrate, boron, and arsenic have not been previously investigated. The impact of various surface tethered polymer brush layer synthesis conditions on the porous membrane separations behavior, and thus the interaction between specific solutes and membrane pores, also remain unexplored.

The modification of membrane surfaces with tethered polyelectrolyte chains [50] can change the physicochemical properties (i.e., surface charge, functionality, and wettability) of the base membrane in response to adjustment (reversibly) of external stimuli such as pH, and solution ionic strength [51, 52]. Such external stimuli can impact the membrane water permeability and selectivity, primarily due to conformational changes of the tethered polymer brush layer (e.g., extension/collapse of the tethered chains) [51, 52]. The stimuli-responsive conformational changes of the tethered polymer brush layer may also influence membrane-solute affinity, and thus the feasibility of reducing membrane fouling propensity and improving membrane cleaning efficacy [52, 53]. However, previous studies on responsive membranes mainly focused on the "through-pore" mechanism (**Section 2.6**) where short polyelectrolyte chains were tethered inside the membrane pores, leading to the tuning of membrane separation behaviors consistent with the typical perm-selectivity tradeoff. In contrast, it is possible that different responsive membrane mechanism such as "through-polymer" mechanism (**Section 2.6**) could overcome the typical tradeoff with sufficiently long polyelectrolyte chains tethered mainly on the membrane external surface.

Tethering of polymer chains of the desired length and surface number density (to ensure that the chains are both in the brush-like regime [119] and tethered mainly onto the membrane external surface) can be synthesized via the atmospheric pressure plasma-induced graft polymerization (APPIGP) [54]. Atmospheric pressure plasma (APP) shown to be effective for activating membrane surfaces, over a short duration (order of seconds), to generate a high surface density of active sites, followed by surface-initiated free radical graft polymerization of vinyl monomers [49, 55]. Unlike low-pressure plasma (LPP) sources that require vacuum chambers, APP can be operated in ambient air and thus has the potential for scalability to treat large membrane surfaces [54, 56-59]. It is noted that surface activation process scale-up to handle sufficiently large membrane surface area for fabrication of spiral-wound elements has not been previously demonstrated.

In order to assess the utility of tethered polymer chains to tune the performance of UF and RO membranes, a systematic study was undertaken focusing on the tethering of polyacrylic acid (PAA) brush layer onto surfaces of base UF and RO membranes. The impact of tethered PAA layer was assessed with respect to membrane water permeability, salt rejection, molecular weight cutoff (*MWCO*), removal of specific contaminants, stimuli-responsiveness, fouling and scaling propensity, and cleaning efficacy. The impacts of the surface tethered PAA brush layer on polysulfone (PSf) UF membrane were investigated for: (a) tuning of membrane water permeability and *MWCO* and overcoming the typical perm-selectivity tradeoff by carefully adjusting the various plasma treatment and graft polymerization conditions; (b) pH and ionic strength-responsive membrane surface hydrophilicity and separation properties via “through-polymer” mechanism; and (c) membrane fouling propensity and cleaning efficacy. Similarly, the applications of PAA brush layer were also assessed on PA TFC RO membrane with the target of: (a) increased

membrane removal for nitrate, boron, and arsenic; (b) reduced membrane mineral scaling and organic fouling propensity and increased cleaning efficacy; and (c) scale-up of the APPIGP process to fabricate commercial-scale spiral wound SWRO elements with superior anti-fouling properties.

1.2 Problem Statement

To overcome the typical membrane perm-selectivity tradeoff and decrease membrane fouling and mineral scaling propensities, it is critical to develop an approach to optimize the surface tethering of hydrophilic PAA brush layer. To better understand the impact of surface tethered brush layer on the surface nano-structured (SNS) membrane properties, various characteristics of the resulting membrane surfaces were investigated in terms of surface topography, chemical composition, zeta potential, and water contact angle. Systematic tuning of the surface tethered PAA chains synthesis (i.e., plasma surface activation and graft polymerization) conditions was then required to tailor SNS-PAA-PSf UF membrane hydraulic permeability and *MWCO*. It is important to find the optimal PAA brush layer synthesis conditions to develop UF membranes that will both overcome the traditional perm-selectivity tradeoff, and demonstrate lower fouling propensity. Another approach to tune UF membrane separation performance is that of stimuli-responsive membranes. Accordingly, it is necessary to explore the stimuli-responsiveness of PSf UF membranes with surface tethered PAA chains, to both tune SNS-PAA-PSf UF membrane separation properties, and assess the feasibility to overcome the typical perm-selectivity tradeoff.

To increase RO membrane rejection of specific contaminants (i.e., nitrate, boron, and arsenic), reduce membrane fouling and scaling propensities, and increase the ease of membrane cleaning, optimal PAA brush layer synthesis conditions need to be determined for PA-TFC RO membrane. Here, it is noted that APPIGP effectiveness was only investigated for small laboratory-scale flat sheet membrane coupons. Scale-up of the approach for fabrication of spiral-wound elements has not been previously demonstrated. For the APPIGP approach to be commercially viable, it must scale to uniformly activated base membrane sheets of area sufficiently large for the fabrication of spiral-wound elements.

1.3 Objectives of the Dissertation

Considering various issues in membrane-based separation processes, the present dissertation research aimed to develop and demonstrate the utility of surface tethered hydrophilic brush layers for tuning permeability and selectivity of both UF and RO membranes. The major objectives of this dissertation research were to:

1. Develop the approach to optimize the surface tethering of hydrophilic PAA brush layer.
2. Identify the optimal PAA brush layer synthesis conditions that would allow the development of UF membranes that can overcome the traditional perm-selectivity tradeoff, and demonstrate lower fouling propensity.
3. Correlate the UF membrane separation performance, reduced membrane fouling propensity, and the ease of membrane cleaning with the unique properties of the hydrophilic PAA brush layer and surface characteristics of the modified membrane surfaces (i.e., surface charge, surface chemistry, surface hydrophilicity, surface topography, and responsive swelling and collapse triggered by environmental stimuli such as pH and ionic strength).

For RO membranes, the present dissertation study aimed to:

4. Demonstrate and quantify the effectiveness of membranes with surface modified brush layer to lower fouling and mineral scaling propensity, enable increased rejection of selective solutes (i.e., nitrate, boron, and arsenic), as well as overcome the perm-selectivity tradeoff.
5. Correlate the RO membrane increased selectivity for the removal of specific contaminants, reduced membrane fouling and scaling propensity, and increased ease of membrane cleaning with the unique properties of the surface tethered PAA brush layer.

1.4 Research Approach

Surface tethered PAA brush layers, synthesized via the APPIGP approach, were investigated with respect to their impact on tuning UF and RO membrane performance, including separation properties, removal of selected contaminants, fouling and scaling propensity, and cleaning efficacy. The overview of this dissertation research workflow is outlined in **Fig. 1-4**, and the dissertation flowchart in **Figs. 1-5** and **1-6**.

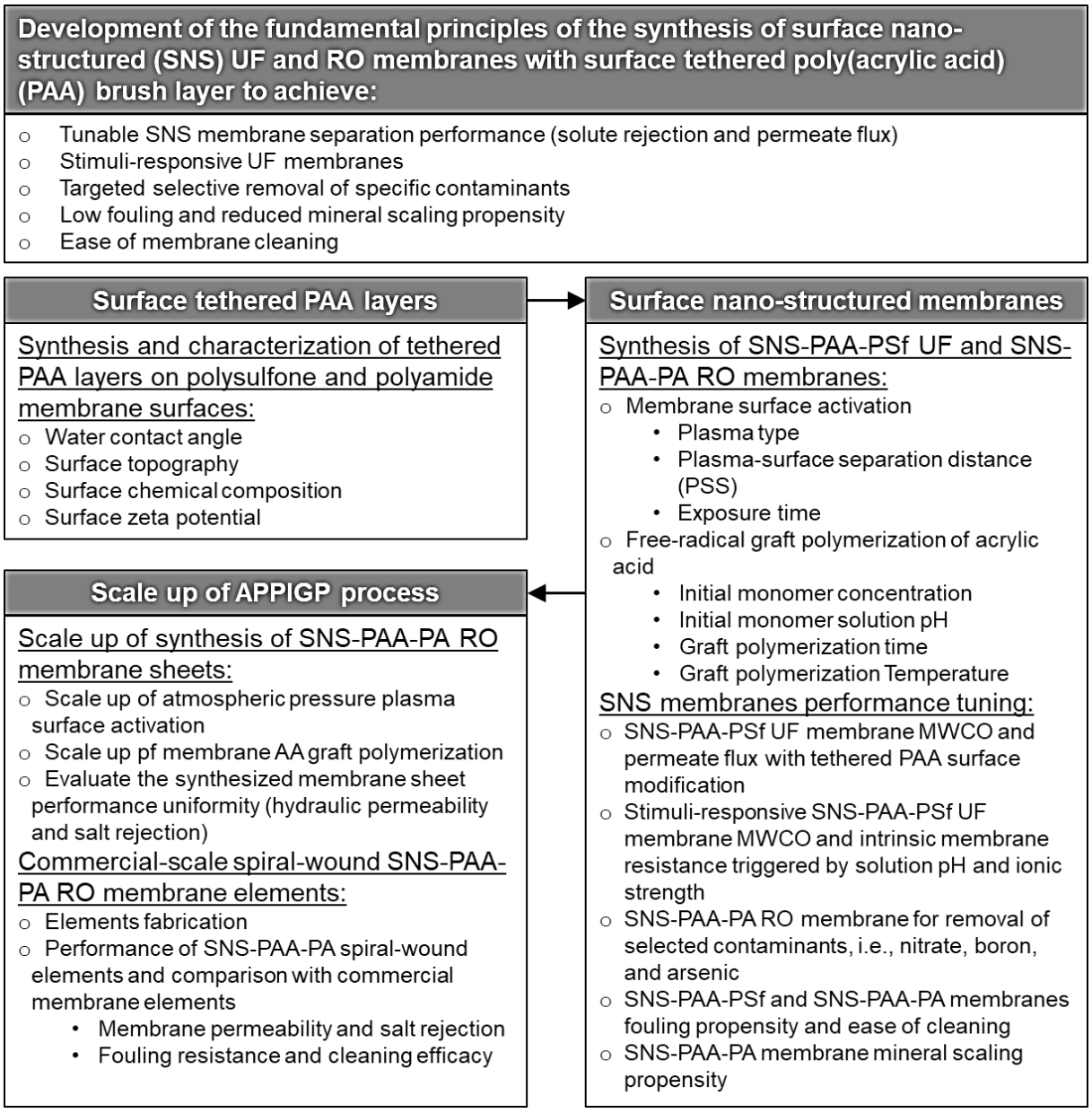

Figure 1-4. Overall objectives and workflow of the dissertation study.

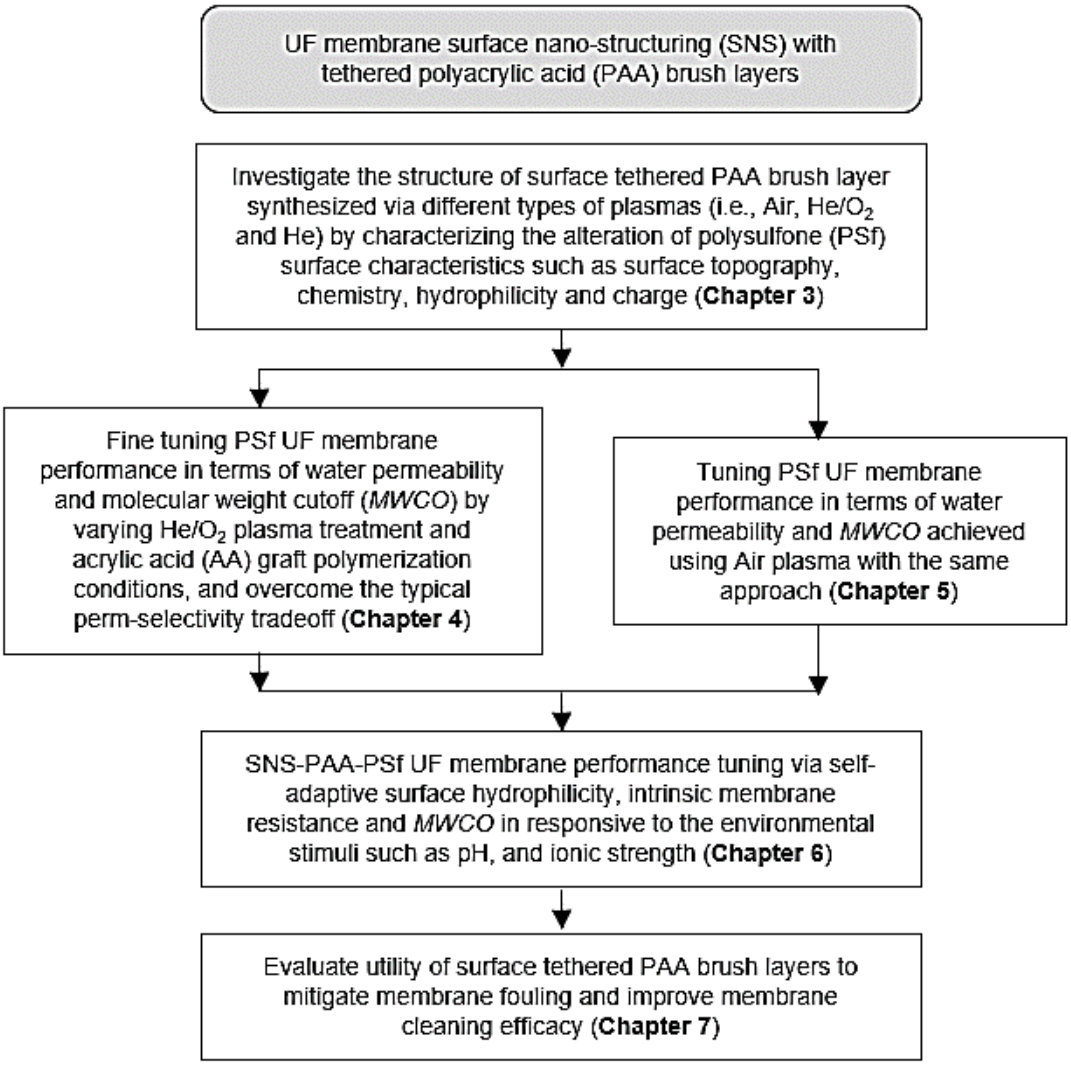

Figure 1-5. Research flowchart outlining for PSf UF membrane performance tuning via surface tethered PAA brush layers (**Chapters 3-7**).

The feasibility and effectiveness of polymeric membrane surface activation by Air, He, and He/O_2 APP, followed by AA graft polymerization was assessed and compared with the resulting surface nano-structured polymeric surface characteristics (**Chapter 3**). Comparison of the impact of surface treatment with the three plasmas focused on characterizing the increase in surface oxygen composition, change in surface topography, and increase in surface hydrophilicity (a) prior to AA graft polymerization, and (b) post AA graft polymerization of the plasma activated membrane surface. The surface charge of SNS-PAA-PSf membranes post surface activation by

three types of plasmas followed by AA graft polymerization was characterized with respect to zeta potential, as compared to the Native-PSf UF membrane.

Tuning of PSf UF membrane water permeability and *MWCO* via membrane surface nano-structuring with tethered PAA layers, synthesized with a range of plasma surface activation and AA graft polymerization conditions, is detailed in **Chapter 4**. The impact of plasma treatment (plasma-surface separation (*PSS*) distance, and number of sequential plasma scan(s) (*N*)) and graft polymerization conditions (initial monomer solution concentration and pH, and graft polymerization time and temperature) was evaluated with respect to the path for tuning the SNS-PAA-PSf performance (in terms of hydraulic permeability and *MWCO*) and also overcoming the typical perm-selectivity tradeoff.

It was shown that Air plasma, as with the He/O_2 plasma, can also serve to tune SNS-PAA-PSf UF membrane hydraulic permeability and *MWCO* as shown in **Chapter 5**. Tuning of SNS-PAA-PSf UF membrane water permeability and *MWCO* was achieved by varying Air plasma treatment conditions such as plasma source-surface separation distance (*PSS*) and number of sequential plasma scans (*N*), prior to AA graft polymerization. Performance tailoring of the SNS-PAA-PSf UF membranes via the route of Air plasma activation was then compared with He/O_2 plasma as demonstrated in **Chapter 4**.

Tuning of the stimuli-responsive SNS-PAA-PSf UF membrane intrinsic membrane resistance and *MWCO* is detailed in **Chapter 6**. The change of water contact angle, intrinsic membrane resistance, and *MWCO* were characterized for the SNS-PAA-PSf membrane and compared to the commercial PSf UF membrane as triggered by solution pH and ionic strength. The SNS-PAA-PSf UF membrane responsive tuning of intrinsic membrane resistance and *MWCO* was also evaluated with respect to the perm-selectivity tradeoff.

In **Chapter 7**, the fouling propensity and cleaning efficacy of the PSf UF membrane with surface tethered PAA chains were assessed and quantified based on the fouling tests of flux decline and permeability recovery, respectively. Fouling resistance of the SNS-PAA-PSf membrane was evaluated in filtration tests of bovine serum album (BSA) and sodium alginate model solutions, as compared to the Native-PSf membrane. The fouled membranes were subsequently backwashed with pure water to quantify membrane cleaning efficacy, and thus reduction and/or elimination of membrane irreversible fouling resistance, facilitated by the surface tethered PAA brush layer. Membrane fouling and cleaning performance was then correlated with the surface characteristics of the SNS membranes as described in **Chapter 3**.

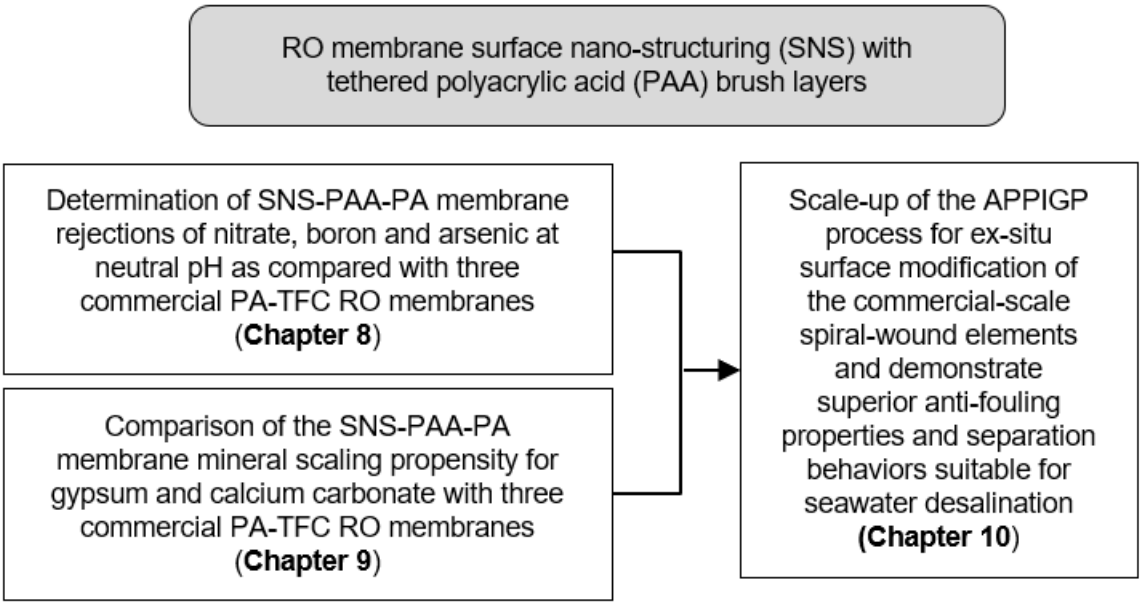

Figure 1-6. Research flowchart outlining PA RO membrane performance tuning via surface tethered PAA brush layer (**Chapters 8-10**).

As demonstrated in an earlier study [49], the surface tethering of PAA brush layer onto the commercial PA-TFC BWRO membrane led to increased membrane NaCl rejection. It was thus also expected that SNS-PAA-PA membrane should have increased membrane rejection of nitrate,

boron, and arsenic, the removal of which remains a challenge in RO desalination (**Section 2.1.3.2**). Accordingly, the SNS-PAA-PA membrane rejections of nitrate, boron, As (III), and As (V) were characterized at neutral pH (within the range of commercial RO processes) and compared to three commercial PA-TFC RO membranes (i.e., Dow SW30, Toray SWRO, and Base-PA) as illustrated in **Chapter 8**.

In **Chapter 9**, gypsum and calcium carbonate scaling propensities are preserved for the PA TFC RO membrane with surface tethered PAA brush layer and compared with commercial Dow SW30, Toray SWRO, and Base-PA membranes. During membrane gypsum and calcium carbonate desalting, permeate flux, feed, and permeate conductivities were recorded over the entire period of filtration to determine the decline of membrane flux and loss of solute rejection. The scaled membranes were also flushed with D.I. water to determine the effectiveness of membrane cleaning as quantified by membrane permeability recovery. Membrane surface SEM images were taken both after the scaling test and after D.I. water cleaning.

In **Chapter 10**, an approach to scale-up of the APPIGP process was developed to enable surface nano-structuring of large RO PA-TFC flat membrane sheets (dimensions of 30” × 24”) for the fabrication of small commercial-scale spiral-wound elements. The performance uniformity of the resulting SNS-PAA-PA RO membrane sheets was examined for both water and salt permeability coefficient and compared with the Base-PA RO membrane sheet. Four SNS-PAA-PA RO membrane sheets were used to fabricate a commercial-scale spiral wound element (2.5” in diameter and 21” in length). The performance of the fabricated membrane elements was then characterized in terms of water permeability, salt rejection, fouling resistance, and cleaning efficacy as compared to one of the most widely used commercial SWRO membrane elements (Filmtec Dow SW30).

Chapter 2 Background and Literature Review

2.1 Membrane processes fundamentals and challenges

2.1.1 Membrane Types

In the last few decades, membrane processes have become an increasingly popular separation method due to their numerous attractive advantages including low energy consumption, competitive operating cost, mild operating condition, unique separation principles, transport selectivity, and high separation efficiency [1, 2]. There is a wide range of applications for the membrane-based separation processes including wastewater treatment, water purification and desalination, medical applications, pharmaceuticals and biotechnology, food and beverage, oil and gas, and chemical industries. Currently, the majority of membranes are made of polymers (~59% of the membrane market share relative to 25% for ceramics [46]) due to their ease of manufacture, relatively low cost, and flexibility in structural design [60]. According to the range of membrane pore size, operational pressure, and degree of selectivity (**Fig. 2-1**), membranes are classified as being suitable for microfiltration (MF), ultrafiltration (UF), nanofiltration (NF), and reverse osmosis (RO).

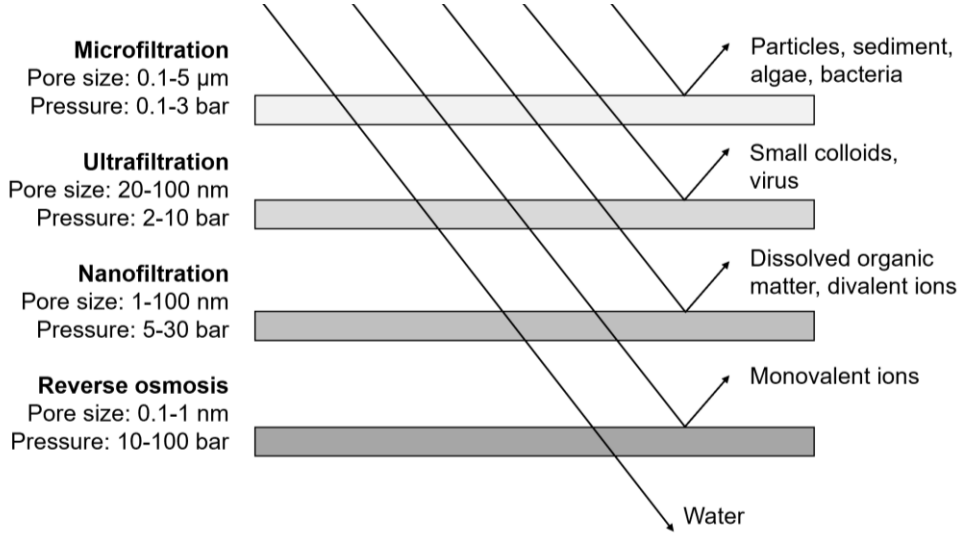

Figure 2-1. An illustration of membrane classifications (i.e., microfiltration, ultrafiltration, nanofiltration, and reverse osmosis) and their process characteristics.

Among the four membrane types, UF and RO membranes are of particular interest in the present dissertation study. UF is a porous membrane filtration process with pore size range 0.1−0.001 μm [3] used to separate small particles, dissolved macromolecules, bacteria, and viruses based on size exclusion [4]. UF membranes are mostly operated in a dead-end filtration mode (**Fig. 2-2**) where the fluid flows vertically toward the membrane surface, and thus in theory leading to complete system recovery (i.e., the feed stream is 100% converted to the permeate). UF membranes have gained an important place and made great progress in numerous industries such as chemical and pharmaceutical manufacturing, food and beverage processing, and wastewater treatment due to their unique ability to purify, concentrate, and fractionate a large range of macromolecules and proteins via a physical membrane barrier [3, 5, 6]. Specifically, UF membranes are used in a wide range of applications including purification/fractionation of high-value biomolecules from complex mixtures including proteins, peptides, and polysaccharides [61]. Fractionation using UF is effective in a wide range of applications including preparation of protein-free filtrates, purification of polymer chains, and separation of unbound or unincorporated labels from DNA and protein samples. However, sharp separation is still difficult to achieve. UF membrane separation is usually based on molecular sieving effect and size exclusion. Molecules larger than the membrane pores will be retained at the surface of the membrane and concentrated during the ultrafiltration process. *MWCO* refers to the approximate molecular weight (*Mw*) of solute which is 90% retained by the membrane. UF membrane with the target *MWCO* should be selected according to the molecular weight of the solute to be retained. However, as the properties of available materials for UF membranes do not cover the whole range of industrial needs, improvement of the membrane selectivity and throughput remains an intense field of research. In addition, due to the effective UF removal of suspended particles, the UF process is also a preferred

pretreatment of RO feedwater for drinking water production and wastewater treatment [7, 8]. However, membrane fouling remains a major challenge for UF membranes that can lead to a decreased membrane flux, degradation of membrane structure, and increased energy and maintenance costs [40, 42, 62].

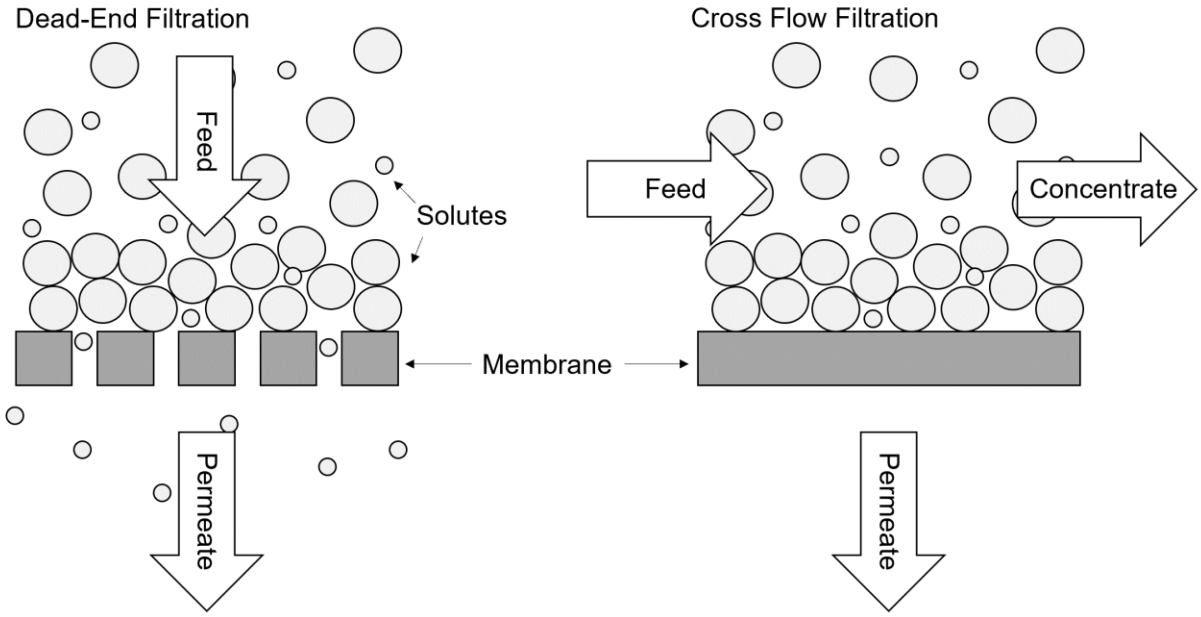

Figure 2-2. Process diagram for dead-end filtration (mostly for MF and UF membranes; left) and cross flow filtration (mostly for NF and RO membranes; right).

Unlike UF membrane, RO is a nonporous membrane with pore size less than 1 nm used to selectively permeate solute lean product water (permeate) through the membrane from saline feedwater via solution diffusion. As a result, RO is the most widely used in water treatment and desalination industries to generate clean water suitable for household, agricultural, and industrial applications [29, 39, 63]. RO desalination is achieved by applying a high hydraulic pressure to the RO feed-side that is greater than the osmotic pressure and to force water to flow in the opposite direction of natural osmosis. RO membranes are operated in the mode of cross flow filtration (**Fig. 2-2**) where the feed solution passes tangentially along the membrane surface. As a result, a solute-rich brine stream (concentrate) is generated as a byproduct which may require post-treatment and

disposal, especially for brackish water (BW) desalination. Depending on the feed source, RO desalination can be categorized into seawater (SW) and BW desalination, and thus RO membranes are also classified as SWRO and BWRO. For SW desalination, the RO feed concentration of total dissolved solids (TDS) is usually within the range of 32,000-40,000 mg/L, whereas for BW desalination, typical salinity is in the range of 1000-15,000 mg/L [18]. SWRO membranes are operated at a higher pressure range of 800-1,200 psi relative to 150-600 psi for BWRO. Moreover, SWRO membranes have higher salt rejection (at least 99.7% in high salinity of 32,000 mg/L NaCl) but lower water permeability relative to BWRO membranes (3-5 $L \cdot m^{-2} \cdot h^{-1} \cdot bar^{-1}$ with 99.0-99.8% NaCl rejection in low salinity range of 500-2,000 mg/L NaCl) according to their different process requirements [16]. In RO membrane desalting, the increase in solutes concentration near or at the feed-side of the RO membrane surface is a widely recognized phenomenon, termed concentration polarization. Membrane surface concentration polarization can lead to increased feed-side osmotic pressure and thus decreased net driving force. Concentration polarization also leads to higher concentration driving force for salt transport through the membrane, and thus lower membrane selectivity. It is also noted that RO membranes suffer from perm-selectivity tradeoff, limited efficiency of specific contaminants removal, membrane fouling, and mineral scaling.

2.1.2 Fundamental concepts and equations

2.1.2.1 UF membranes

The UF membrane productivity per unit area is quantified by permeate water flux defined as:

$$J_v = \frac{Q_p}{A} \tag{2-1}$$

where J_v is the volumetric permeate flux, Q_p is the volumetric permeate flow rate, and A is the membrane active area. UF membrane permeate flux depends on the applied transmembrane pressure (ΔP), whose correlation is described as:

$$J_v = L_p \cdot \Delta P \tag{2-2}$$

where L_p is water permeability coefficient. Membrane hydraulic resistance (R_m) is another important intrinsic membrane characteristic determined based on Darcy's law:

$$J_v = \Delta P / \mu R_m \tag{2-3}$$

where μ is the permeate viscosity.

Membrane product quality depends not only on membrane characteristics but also on feedwater quality, which is affected by the membrane solute passage (*SP*):

$$SP = \frac{C_p}{C_f} \tag{2-4}$$

where C_p and C_f are the permeate and feed solute concentrations, respectively. Unlike *SP* which describes the percentage of solute passage through the membrane into the permeate stream, membrane rejection quantifies the percentage of solute that is removed by the membrane. Consequently, the nominal/observed membrane solute rejection (R_o) can be determined using solute passage:

$$R_o = 1 - SP = 1 - \frac{C_p}{C_f} \tag{2-5}$$

For porous membranes such as UF, transport of both solvent and solute is based on convective flow, and thus properties and characteristics of membrane pores can be significant. The separation of UF membranes is typically based on size exclusion. The separation performance is quantified in terms of molecular weight cut-off (*MWCO*) [64, 65], defined as the approximate molecular weight (*Mw*) of solute which is rejected by the membrane to a level of 90%.

As described in Hagen–Poiseuille equation, membrane permeate flow rate is a function of both membrane pore size and pore length:

$$q_p = \frac{\pi d_p^4}{128 \mu \delta_m} \tag{2-6}$$

where q_p is the volumetric permeate flow rate per membrane pore, and δ_m is the membrane thickness. The Hagen–Poiseuille equation is after simplified by assuming that the pore length (δ_p) is the same as the membrane thickness, while for actual membranes, the membrane tortuosity (τ, the ratio of average pore length and membrane thickness) is typically between 1.5 and 2.5:

$$\tau = \frac{\delta_p}{\delta_m} \tag{2-7}$$

Another important indicator of membrane pore characteristics is the membrane porosity (ε), which is defined as the ratio of the volume of membrane pores to the volume of the membrane:

$$\varepsilon = \frac{n_p A_p \delta_p}{A_m \delta_m} \tag{2-8}$$

where n_p is the number of membrane pores, A_p is the average area of the pore, and A_m is membrane surface area.

2.1.2.2 RO membranes

For RO membranes, the driving force of the permeate flux is the difference between applied external pressure and the osmotic pressure ($\Delta\pi$) across the membrane. The membrane volumetric permeate flux is expressed as:

$$J_v = L_p(\Delta P - \sigma \cdot \Delta\pi) \tag{2-9}$$

where σ is the reflection coefficient indicating membrane selectivity (i.e., the ratio of water passage to salt passage across the membrane). It is noted that the reflection coefficient is typically unity ($\sigma \approx 1$) for RO membranes of high solute rejection.

In addition to solute passage (**Eqn. 2-4**) and nominal/observed membrane solute rejection (**Eqn. 2-5**), the separation performance of RO membranes can also be described using the solute permeability coefficient (*B*) as per the solution diffusion model:

$$J_v \cdot C_p = B \cdot (C_m - C_p) \tag{2-10}$$

where C_m is the solute concentration at the membrane surface. Due to concentration polarization (*CP*) (**Fig. 2-3**), the local solute concentration near and at the RO membrane surface is higher than the bulk concentration (C_b).

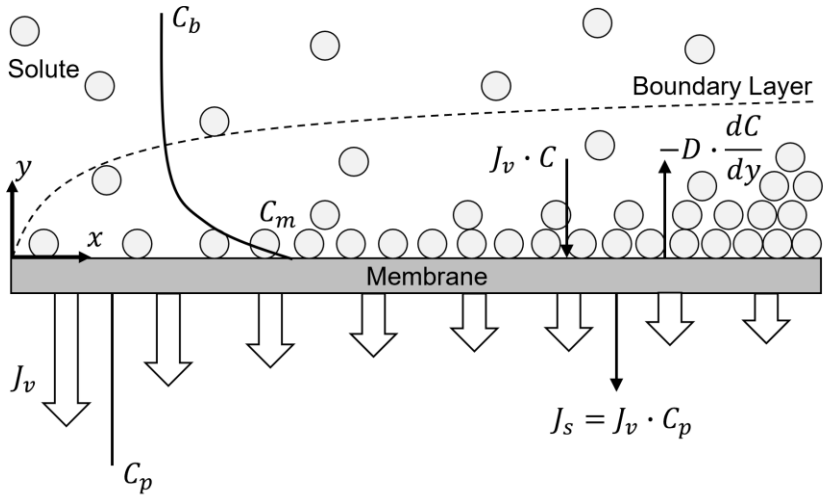

Figure 2-3. Schematic diagram of concentration polarization phenomenon developed in a crossflow membrane channel.

Concentration polarization can be assessed following a solute mass balance across the membrane assuming fully developed concentration and velocity profiles:

$$J_v \cdot C = J_v \cdot C_p - D\frac{dC}{dy} \tag{2-11}$$

where C is the solute concentration at distance y from the membrane surface and D is the solute diffusion coefficient in water. Solving **Eqn. 2-11** leads to the classical simple film model:

$$\overline{CP} = \frac{\overline{C_m} - \overline{C_p}}{\overline{C_b} - \overline{C_p}} = \exp\left(\frac{J_v}{k}\right) \tag{2-12}$$

where $\overline{CP}$ is the average concentration polarization module, $\overline{C_m}$, $\overline{C_b}$, and $\overline{C_p}$ are the average solute concentrations on the membrane surface, in the bulk and permeate streams, respectively, and k is the mass transfer coefficient defined as:

$$k = \frac{\delta}{D} \tag{2-13}$$

where δ is the concentration boundary layer thickness. By combining **Eqns. 2-5**, **2-10**, and **2-12**, the correlation between membrane nominal rejection (R_o) and permeate flux (J_v) can be determined:

$$\ln\left(\frac{J_v \cdot (1 - R_o)}{R_o}\right) = \frac{J_v}{k} + \ln(B) \tag{2-14}$$

The values of k and B can be obtained by varying the flux at a constant crossflow velocity, and plotting $\ln\left(\frac{J_v \cdot (1 - R_o)}{R_o}\right)$ vs J_v, where $\frac{1}{k}$ is the slope and $\ln(B)$ is the y-intercept. Knowing the value of k, C_m can thus be determined, as well as the membrane intrinsic rejection (R_i), which is calculated via:

$$R_i = 1 - \frac{C_p}{C_m} \tag{2-15}$$

For commercial applications of RO technology, spiral-wound RO element modules are commonly used due to their high productivity and packing density (i.e., membrane area to volume ratio) [27, 66, 67], robustness during high-pressure applications [68], reasonably lower pressure drop and low cost [69]. For spiral-wound RO elements, the average $\overline{CP}$ can be estimated from element specific correlations such as these provided in the Filmtec™ and CSM Reverse Osmosis Membranes Technical Manuals [70]:

$$\overline{CP} = \frac{\overline{C_m} - \overline{C_p}}{\overline{C_b} - \overline{C_p}} = \exp\left(0.7Y\right) \tag{2-16}$$

where Y is the system recovery defined as:

$$Y = \frac{Q_p}{Q_f} \tag{2-17}$$

and Q_p and Q_f are the permeate and feed volumetric flow rates, respectively.

2.1.3 Major challenges in membrane processes

2.1.3.1 Permeability-Selectivity Tradeoff

Despite the rapid growth of membrane-based desalination technology, there are major challenges to overcome in order to further improve process efficiency and lower the cost of water desalination/purification. For a membrane-based seawater desalination plant, energy consumption is still the greatest operational cost, varying from 1/3 to more than 1/2 the total cost of produced water [71]. The thermodynamic minimum energy required for seawater desalination can be ~18 times higher than for brackish water (1.1 kWh/m^3 and 0.06 kWh/m^3, respectively, at 50% recovery) due to the higher osmotic pressure of seawater [16]. Due to the typical permeability-selectivity tradeoff, increasing membrane permeability often comes at the cost of reducing selectivity. Such permeability-selectivity tradeoff (**Fig. 2-4**) is typical for both dense and porous membranes in spite

of their different mechanisms of small-molecule transport mode (i.e., solution and diffusion, and pore flow, respectively); thus, the challenges for optimizing the membrane performance. For UF membranes, separation performance is often quantified via *MWCO*, solute rejection, and separation factor. However, for RO membrane, selectivity is described using the ratio of water and solute permeability coefficients (A and B, respectively) [72].

$$R_o = \frac{(A/B)(\Delta P - \Delta\pi)}{1+(A/B)(\Delta P - \Delta\pi)} \tag{2-18}$$

From **Eqn. 2-18**, one can conclude that membrane salt rejection is not an intrinsic membrane property. It depends on both membrane intrinsic water and salt transport properties and the process operating conditions. According to the solution-diffusion model, the membrane water permeability as expressed as

$$L_p = K_w D_w \tag{2-19}$$

where K_w is the water partition/solubility coefficient, and D_w is the average water diffusion coefficient. The salt permeability coefficient can be expressed as

$$B = K_s D_s \tag{2-20}$$

where K_s is the salt partition coefficient (or salt solubility in the membrane) and D_s is the average salt diffusion coefficient in the membrane. Membrane water/salt selectivity is defined as the ratio of water and salt permeability coefficients [72]:

$$A/B = \frac{K_w}{K_s} \times \frac{D_w}{D_s} \tag{2-21}$$

where K_w / K_s is the water/salt solubility selectivity, and D_w / D_s is the water/salt diffusivity selectivity. Such tradeoff correlation was then used as the upper bound relation for membrane desalting properties. One example of the empirical upper bound relation [72] is

$$A/B = \frac{1.4\times10^{-7}}{A^2} \text{ (bar}^{-1}\text{)} \quad (2\text{-}22)$$

It is claimed that the tradeoff trend for polymeric membranes is mainly attributed to the structural properties of the polymer active layer (e.g., thickness, porosity) and interactions between small solutes and the polymeric membrane materials [9].

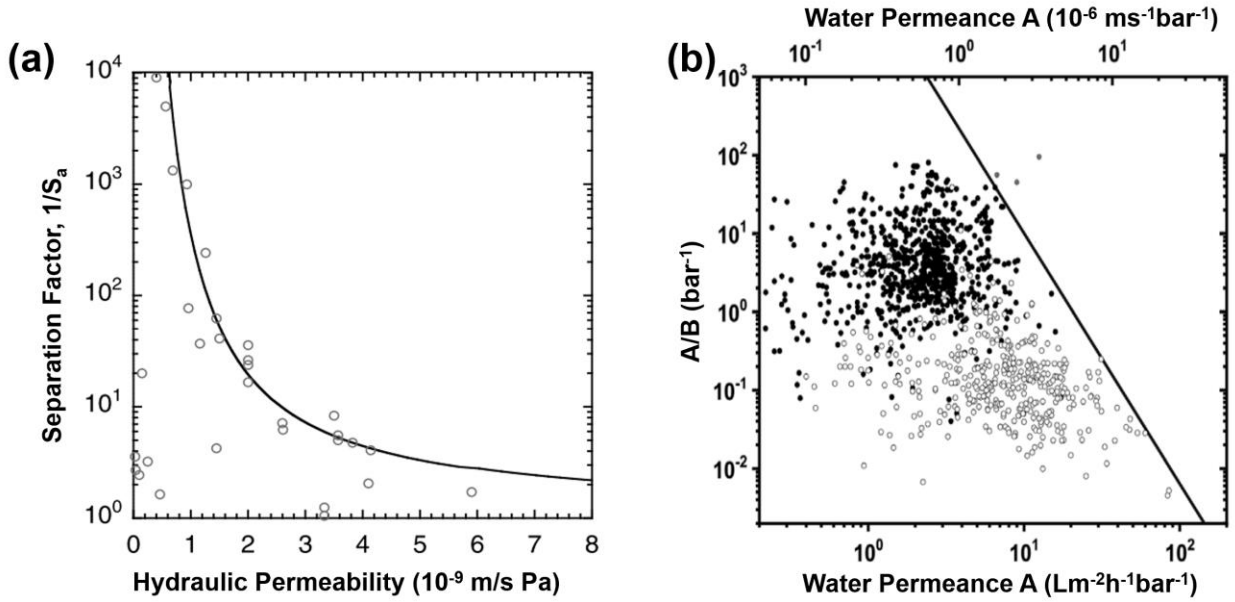

Figure 2-4. Upper-bound tradeoff relations between membrane permeability and selectivity for polymeric membranes: (a) bovine serum album (BSA)/water separation and hydraulic permeability in porous UF membranes [9]; (b) water/NaCl selectivity (*A/B*) and water permeance in nonporous thin-film composite (TFC) polyamide (PA) membranes [73].

Increased membrane overall thickness can lead to reduced water permeability but increased membrane selectivity, due to the increased resistance of mass transfer for both water and solutes through the membrane. Similarly, UF membrane polymetric matrix structural parameters, such as pore size, porosity, and tortuosity, and RO membrane structural properties, including active layer thickness, free volume, size, spatial distributions, and total number of cavity sites present in membrane active layer, all strongly influence both water and salt transport through the membranes. However, it is difficult to simultaneously increase membrane water permeability and solute

selectivity. Hence, there have been many attempts to fine-tune membrane performance in order to overcome the typical tradeoff between membrane permeability and selectivity.

2.1.3.2 Selective removal

Efforts for optimizing RO membrane separation performance are required not only for salt rejection but also for the removal of specific contaminants such as nitrate, boron, and arsenic. The current technology of commercial RO membranes is still insufficient for reducing contaminant concentrations to meet drinking water quality requirements under normal operational conditions [13].

Nitrate Removal

The presence of nitrate in groundwater is the result of excessive use of fertilizers, uncontrolled discharges of wastewater, and other land use activities including septic tanks, livestock operations, orchards, and trucks [74-76]. Overexposure to nitrate has potential adverse health effects, including birth defects, cancer, nervous system impairments, and methemoglobinemia [74]. As a result, the World Health Organization (WHO) Guidelines for Drinking Water Quality suggests the safe drinking water limit of 10 mg/L Nitrate-N [77]. RO technology has been used for nitrate removal and to produce safe drinking water. However, although high seawater salt rejection (above 99%) achieved by regular RO membranes, their nitrate rejection is significantly lower (e.g., 40.4-97.7% as determined for flat sheet coupons and 65-98% for spiral wound elements; **Table 2-1**).

Boron Removal

Boron is present in various water bodies, primarily in the form of boric acid, $B(OH)_3$. In seawater boron concentration ranges from 0.5 to 15 mg/L [78]. The presence of boron in water

bodies is mainly due to both natural weathering processes and anthropogenic sources, especially from various manufacturing industries such as additives for fiberglass, enamels, cosmetics, leather, textile, paint wood-processing, detergents, insecticides, disinfectants, and drugs [15, 78]. Boron is reported to cause adverse reproductive and developmental effects, as well as plant and crop damage [17]. Intake of boron may lead to acute boron toxicity which causes nausea, headache, diarrhea, kidney damage, and death from circulatory collapse [15]. Long-term consumption of boron-contaminated water and food may lead to syndromes and diseases in cardiac-vascular, nervous, and alimentary systems [78]. Given the toxicity of boron, the maximum concentration in drinking water is recommended to be below 0.5 mg/L [15]. RO membranes are capable of complete boron removal under alkaline conditions (pH>9.24), where boron exists mostly in the form of $B(OH)_4^-$ [78]. The tetrahydroxyborate ion is formed by the dissociation of the boric acid by accepting a hydroxyl ion:

$$B(OH)_3 + 2H_2O \leftrightarrow \left[B(OH)_4\right]^- + H_3O^+ \quad (\text{pKa} = 9.24) \qquad (2\text{-}23)$$

The excellent RO boron rejection at high pH is attributed to the fully hydrated dissociation form of tetrahydroxyborate ion has a negative charge and a larger radius, and thus is more easily rejected by RO membranes both by size exclusion and charge repulsion [79]. However, the rejection of boron by RO membranes is low under neutral or acidic conditions where the undissociated boron molecules are dominant. Due to the absence of ionic charges, boric acid molecules are poorly hydrated, resulting in smaller molecular size (0.244-0.261 nm [78, 80]) and lower RO boron rejection [78, 79]. Indeed, the current commercially available RO membranes had low boron rejections at neutral pH: 12-91% for flat sheet membranes, and 70-96% for spiral wound elements (**Table 2-2**).

Arsenic Removal

Arsenic removal is another challenge in drinking water production. Arsenic is present in groundwater and surface water bodies originating from natural processes such as soil erosion, mineral leaching and weathering, and industrial activities including mining and smelting of metal ores, combustion of fossil fuels, and waste effluents from the manufacturing of paints, fungicides, herbicides, pesticides, wood preservatives, and cotton desiccants [81, 82]. Depending on the pH and redox potential, arsenic can be present in water in several forms, with total concentration ranges from 0.01 to 2 mg/L. At the typical pH range (5-8) in the natural environment, arsenic is rarely encountered as the free element and occurs in four oxidation states (-3, 0, +3, +5), but the two predominated oxidation states common in the aqueous environment are trivalent arsenite As (III) and pentavalent arsenate As (V). The trivalent arsenite As(III) dissociates at high pH, and exists as fully protonated oxyanions (H_3AsO_3) at neutral pH [81].

$$H_3AsO_3 \rightarrow H^+ + H_2AsO_3^- \text{ (pKa = 9.22)} \quad (2\text{-}24)$$

$$H_2AsO_3^- \rightarrow H^+ + HAsO_3^{2-} \text{ (pKa = 12.3)} \quad (2\text{-}25)$$

While on the other hand, pentavalent arsenate As (V) exists as an anion in the forms of $H_2AsO_4^-$ and $HAsO_4^{2-}$ at neutral pH [81].

$$H_3AsO_4 \rightarrow H^+ + H_2AsO_4^- \text{ (pKa = 2.2)} \quad (2\text{-}26)$$

$$H_2AsO_4^- \rightarrow H^+ + HAsO_4^{2-} \text{ (pKa = 7.1)} \quad (2\text{-}27)$$

$$HAsO_4^{2-} \rightarrow H^+ + AsO_4^{3-} \text{ (pKa = 11.5)} \quad (2\text{-}28)$$

The lethal range of arsenic in a human adult is estimated at a dose of 1-3 mg As/kg, and exposure to arsenic may cause gastrointestinal discomfort, vomiting, and diarrhea with even a small amount (<5 mg) [82, 83]. Intake of arsenic above the toxicity threshold may lead to bloody urine, anuria, shock, convulsions, coma, or even death (if 100-300 mg of arsenic is consumed) [82,

83]. As a result, U.S. Environmental Protection Agency (EPA) has set the maximum contaminant level (MCL) of total arsenic to be 10 μg/L [84].

RO membrane water treatment is one of the most commonly used arsenic removal technology. RO membrane rejection for As (V) is typically higher than for As (III) due to the existence of strong electrostatic exclusion of the anionic components by the negatively charged membrane surfaces [81, 85]. As summarized in **Table 2-3**, commercial RO flat sheet membranes have been reported to perform at the rejection of 61-99% and 68-98% for As (III) and As (V), respectively. In contrast, the reported spiral-wound RO elements rejections of As (III) and As (V) are 5-85% and 92-99%, respectively.

Table 2-1. Summary table of commercial RO membrane nitrate rejection.

Ref	Membrane		Feed concentration	pH	Rejection
[86]	Flat sheet	SEPA CF-SS 10	100 mg/L NO_3^-	-	76.3%
[86]	Flat sheet	SEPA CF-ST 10	100 mg/L NO_3^-	-	66.7%
[86]	Flat sheet	SEPA CF-SR 10	100 mg/L NO_3^-	-	65%
[86]	Flat sheet	SEPA CF-SF	100 mg/L NO_3^-	-	50.9%
[86]	Flat sheet	SEPA CF-SX	100 mg/L NO_3^-	-	40.4%
[87]	Flat sheet	Filmtec BW30	100 mg/L NO_3^-	3-12	60-96%
[88]	Flat sheet	Filmtec SW30 HR	15.6 mg/L NO_3-N	7.9	93.9%
[88]	Flat sheet	Hydranautics Espa2	15.6 mg/L NO_3-N	7.9	97.4%
[88]	Flat sheet	KOCH TFC ULP	15.6 mg/L NO_3-N	7.9	97.7%
[88]	Flat sheet	Sepro RO1	15.6 mg/L NO_3-N	7.9	96.0%
[89]	Flat sheet	Hydraunautics ESPA1	500-1000 mg/L NO_3^-	7	89-92%
[89]	Flat sheet	Hydraunautics LFC1	1000 mg/L NO_3^-	7	88%
[90]	Spiral wound element	4040-LHA-CPA2	42.46 mg/L NO_3-N	7.22	98%
[91]	Spiral wound element	TFCL 4821 LP	13-23 mg/L NO_3-N	-	97%
[91]	Spiral wound element	Filmtec BW30 4040	13-23 mg/L NO_3-N	-	97%
[92]	Spiral wound element	FT 30	26 mg/L NO_3-N	5.9	76.5%
[93]	Spiral wound element	Cellulose acetate	18-25 mg/L NO_3^-	-	65%
[94]	Spiral wound element	Filmtec TW30-18-12	38 mg/L NO_3-N	6.84	87-97%

Table 2-2. Summary table of commercial RO membrane boron rejection.

Ref	Membrane		Feed concentration	pH	Rejection
[95]	Flat sheet	Osmonics SG	1-4 mg/L	7-8.2	12-31%
[95]	Flat sheet	Toray UTC80	1-4 mg/L	7-8.2	67-70%
[95]	Flat sheet	Toray UTC80A	1-4 mg/L	7-8.2	57-72%
[95]	Flat sheet	Toray UTC80S	1-4 mg/L	7-8.2	48-61%
[96]	Flat sheet	Dow SW30HR	6.2-7.3 mg/L	7.9-8.1	87%
[96]	Flat sheet	GE-AD	4.5-7.8 mg/L	7.8-8.2	80%
[96]	Flat sheet	KOCH-SW	6.5-8.4 mg/L	8.1-8.4	82%
[96]	Flat sheet	Dow-SW30XLE	5.2-8.6 mg/L	8.0-8.2	85%

[96]	Flat sheet	Toray UTC-SW	5.5-7.8 mg/L	7.5-8.0	91%
[97]	Spiral wound element	Filmtec SW30-2540	1 mg/L	-	70%
[98]	Spiral wound element	Filmtec XUS SW30XHR-2540	4-6 mg/L	7-7.5	87.7%
[98]	Spiral wound element	Filmtec SW30-2540	4-6 mg/L	7-7.5	84.6%
[99]	Spiral wound element	Toray TM820A-400	5 mg/L	8	93%
[99]	Spiral wound element	Toray TM820C-400	5 mg/L	8	93%
[99]	Spiral wound element	Toray TM820E-400	5 mg/L	8	91%
[100]	Spiral wound element	Toray TM820-370	5 mg/L	8	91-93%
[100]	Spiral wound element	Toray TM820H-370	5 mg/L	8	91-93%
[78]	Spiral wound element	Toray TM820M	5 mg/L	8	95%
[78]	Spiral wound element	Toray TM820R	5 mg/L	8	95%
[78]	Spiral wound element	Toray TM800V	5 mg/L	8	92%
[78]	Spiral wound element	Toray TM800K	5 mg/L	8	96%
[100]	Spiral wound element	Toray SU-820	5 mg/L	8	91-93%
[100]	Spiral wound element	Toray SU-820BCM	5 mg/L	8	91-93%
[99]	Spiral wound element	Dow SW30XHR-400i	5 mg/L	8	93%
[99]	Spiral wound element	Dow SW30HRLE-400	5 mg/L	8	91%
[78]	Spiral wound element	Dow SW30HRLE-370/34i	5 mg/L	8	92%
[99]	Spiral wound element	Dow SW30XLE-400i	5 mg/L	8	88%
[99]	Spiral wound element	Dow SW30ULE-400i	5 mg/L	8	87%
[78]	Spiral wound element	Dow SEAMAXX	5 mg/L	8	87%
[99]	Spiral wound element	Hydranautics SWC4+	5 mg/L	6.5-7	83%
[99]	Spiral wound element	Hydranautics SWC4+ B	5 mg/L	6.5-7	95%
[78]	Spiral wound element	Hydranautics SWC4 MAX	5 mg/L	7	93%
[99]	Spiral wound element	Hydranautics SWC5	5 mg/L	6.5-7	92%
[99]	Spiral wound element	Hydranautics SWC6	5 mg/L	6.5-7	91%

Table 2-3. Summary table of commercial RO membrane As (III) and As (V) rejection.

Ref	Membrane		Feed concentration	pH	As (III) Rejection	As (V) Rejection
[80]	Flat sheet	GE Osmonics AD	100 μg/L	-	-	94-96%
[80]	Flat sheet	Woongjin Chemical BE	100 μg/L	-	-	90-98%
[80]	Flat sheet	Filmtec SW30HR	100 μg/L	-	-	90-94%
[80]	Flat sheet	Toray UTC 80 B	100 μg/L	-	-	95-97%
[101]	Flat sheet	Filmtec SW30HR	49.5 μg/L	7.6	96%	-
[101]	Flat sheet	Hydranautics SCW5	49.5 μg/L	7.6	99%	-
[101]	Flat sheet	Fimtec BW30LE	49.5 μg/L	7.6	91%	-
[101]	Flat sheet	Hydranautics ESPAB	49.5 μg/L	7.6	95%	-
[101]	Flat sheet	Hydranautics ESPA2	49.5 μg/L	7.6	86%	-
[102]	Flat sheet	Filmtec XLE	100 μg/L	7.5	97%	-
[102]	Flat sheet	Filmtec BW30	100 μg/L	7.5	99%	-
[103]	Flat sheet	Filmtec SWHR	50 μg/L	7	-	96%
[103]	Flat sheet	Filmtec BW30	50 μg/L	7	-	68%
[103]	Flat sheet	Filmtec SWHR	12 μg/L	7	77%	-
[103]	Flat sheet	Filmtec BW30	12 μg/L	7	61%	-
[104]	Spiral wound element	Nitto Electric ES-10	50 μg/L	7	75%	95%
[104]	Spiral wound element	Nitto Electric NTR-729HF	50 μg/L	7	20%	92%
[105]	Spiral wound element	TFC 4921	15-20 μg/L	-	63%	95%
[105]	Spiral wound element	TFC 4820-ULPT	15-20 μg/L	-	77%	99%
[105]	Spiral wound element	Desal AG 4040	15-20 μg/L	-	70%	99%
[105]	Spiral wound element	Hydranautics 4040 LSA-CPA2	15-20 μg/L	-	85%	99%
[12]	Spiral wound element	KOCH TFC-ULP	60 μg/L	-	Total As rejection of 99%	
[12]	Spiral wound element	Desal DK2540F	-	-	5%	96%
[12]	Spiral wound element	Toyobo HR3155			55%	95%

2.1.3.3 Mineral scaling

For RO membrane BW desalination, with the feedwater total dissolved solids (TDS) within the range of 1000-15,000 mg/L, membrane mineral scaling remains to be a major challenge that occurs when the solubility limits of the sparingly soluble salts (i.e., $CaCO_3$, $CaSO_4$, $BaSO_4$, $SrSO_4$, and silica) present in the feed water or in the RO element feed channels and at the membrane surface are exceeded [18-21]. Even though with feed salt within the solubility range, local supersaturation may occur due to permeating withdrawal and corresponding concentration increase of the remaining concentrate as well as concentration polarization at the membrane surface-liquid interface [25, 106]. Supersaturation, with respect to the mineral scalant, at any level will eventually lead to scale formation on the membrane surface that is initiated by the nucleation sites. It is noted that spontaneous homogeneous nucleation occurs when supersaturation exceeds a certain threshold value [107]. Below this threshold supersaturation, crystal nucleation occurs after a certain period time (**Fig. 2-5**), referred to as induction time [107]. However, heterogeneous nucleation can occur at the membrane surface at significantly lower supersaturation levels relative to homogeneous nucleation.

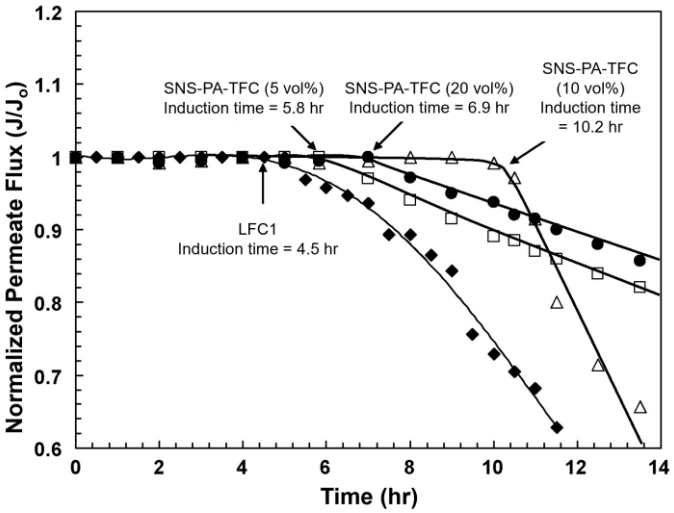

Figure 2-5. Flux decline performance in gypsum scaling tests (feed solution of $SI_g = 2.0$) comparing the different SNS-PA-TFC and LFC-1 membranes (adapted from [108]).

The most frequently encountered scalants in RO desalination are calcium sulfate dihydrate (gypsum), followed by calcium carbonate [109]. The saturation index, which is widely used to quantify the saturation level of the mineral salt, is defined as

$$SI_x = IAP / K_{sp,x} \tag{2-29}$$

where *IAP* is the ion activity product and $K_{sp,x}$ is the solubility product for the mineral salt *x* (e.g., where $x = c$ is $CaCO_3$ (as calcite) and $x = g$ is gypsum). Scale formation on RO membrane surfaces is a combined consequence of two different mechanisms, homogeneous nucleation in the bulk solution followed by deposition of the scalant crystals onto the membrane surface (bulk deposition) and heterogeneous nucleation on the membrane surface, followed by crystal growth (surface crystallization) [22]. Bulk deposition involves four stages: (i) formation of the micro-aggregates of mineral ions, which serve as nucleation centers; (ii) formation of micro-crystals from the micro-aggregates through nucleation; (iii) aggregation of the micro-crystals and growth into large microcrystals; and (iv) growth of larger micro-crystals and the eventual formation of scale layer on the membrane surface [109, 110]. Surface crystallization involves nucleation that occurs on the membrane surface rather than in the bulk solution. The dominance of either mechanism, i.e., bulk crystallization versus membrane surface crystallization, depends on the system hydrodynamics, feed solution chemistry, and membrane surface characteristics [18, 22, 111, 112].

The consequence of surface crystallization and deposition of mineral salt crystals onto the membrane is typically permeate flux decline. Permeate flux decline is due to: (i) the crystals deposition layer that forms on membrane surface which is an additional barrier layer to water transport leading to increased membrane hydraulic resistance; and (ii) the presence of scale cake layer that may elevate the osmotic pressure and thus reduce the net pressure driving force for water permeation [23]. Scaling also increases the operation and maintenance costs of the RO process,

increases energy consumption, system downtime as well as higher frequency of membrane cleaning and replacement [18, 36]. More importantly, membrane mineral scaling can limit water product recovery (i.e., the ratio of the permeate to feed volumetric flow rates). Thus, the deployment of mineral scaling impedes high water recovery desalination, or zero liquid discharge process that are critical for desalination. High recovery is critical because residual concentrate disposal options for the membrane concentrate are often limited, costly [22], and can cause damage to the environment [113-115]. Moreover, the presence of mineral scale on the membrane surface can lead to decreased solute rejection and irreversible deterioration of membrane performance [22, 24, 25].

2.1.3.4 Fouling

Membrane fouling generally refers to the temporary or permanent non-specific surface adsorption/deposition of rejected organic and biological matters on the membrane surface and/or within its pores. Membrane fouling is a major challenge because it can lead to rapid decline of permeate flux, impaired water quality, elevated energy consumption, increased frequency of chemical cleaning, shortened membrane service life, diminished period for membrane element replacement, and escalated operational cost. Membrane fouling is caused by complex foulant-foulant and foulant-membrane surface physical and chemical interactions [110]. Previous studies demonstrated that membrane fouling is affected by various factors including feed solution chemistry (chemical composition, foulant concentration, pH, ionic strength, and divalent cation concentration), membrane properties (surface topography, hydrophilicity, charge, and separation properties), and operating conditions (temperature, mode of operation, initial permeate flux, and crossflow velocity) [110].

1.2.3.4.1 UF membrane fouling

Fouling is one of the major problems in UF technology due to the hydrophobic nature of the UF polymeric materials. Mass transport of organic and biological matter through the membrane can lead to the attachment, accumulation, or adsorption of foulant molecules onto membrane surfaces and/or within membrane pores [110]. This explained the various fouling mechanisms including pore plugging, pore narrowing, and cake layer buildup (surface fouling) as depicted in **Fig. 2-6**.

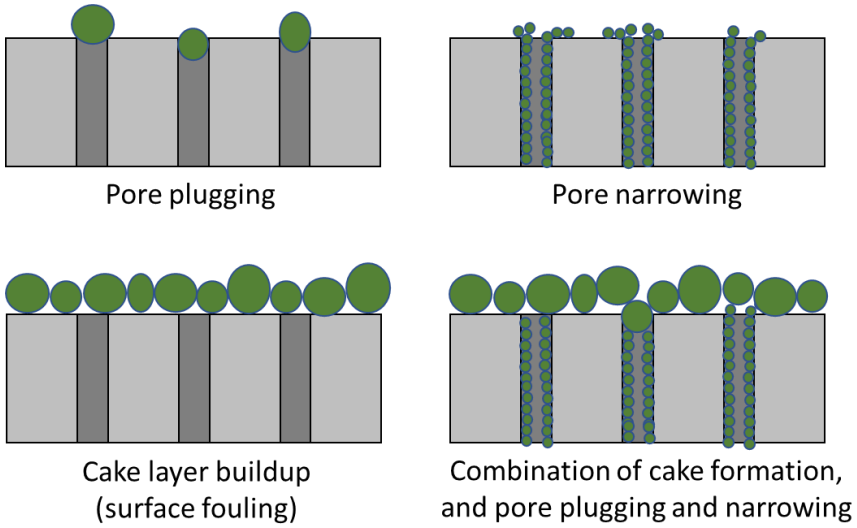

Figure 2-6. Illustration of different UF membrane fouling mechanisms.

UF membrane permeate flux can be described by a Darcy's law type equation:

$$J = \frac{\Delta P}{\mu(R_m + R_{rev} + R_{irrev})} \tag{2-30}$$

where J is the permeate flux, ΔP is the transmembrane pressure, μ is the solvent viscosity, R_m is the membrane hydraulic resistance, and R_{rev} and R_{irrev} are reversible and irreversible fouling resistance, respectively. The classification of UF membrane reversible and irreversible fouling depends on the context in which the membrane fouling tests are conducted and the fouled

membranes are cleaned. Reversible UF membrane fouling is mainly due to cake/gel layer buildup or concentration polarization at the membrane surface (i.e., accumulation of rejected colloidal and macromolecular material on the membrane surface) [110]. Irreversible membrane fouling, on the other hand, is mainly due to chemisorption and pore plugging. Reversible fouling can be restored through physical washing protocol such as backwashing (**Fig. 2-7**), which is performed by D.I. water or permeate flushing from the permeate to the feed side for ~30 s up to several minutes [110]. While for irreversible fouling, the loss in transmembrane flux cannot be recovered via simple physical cleaning, and thus more aggressive chemical cleaning will be required [32].

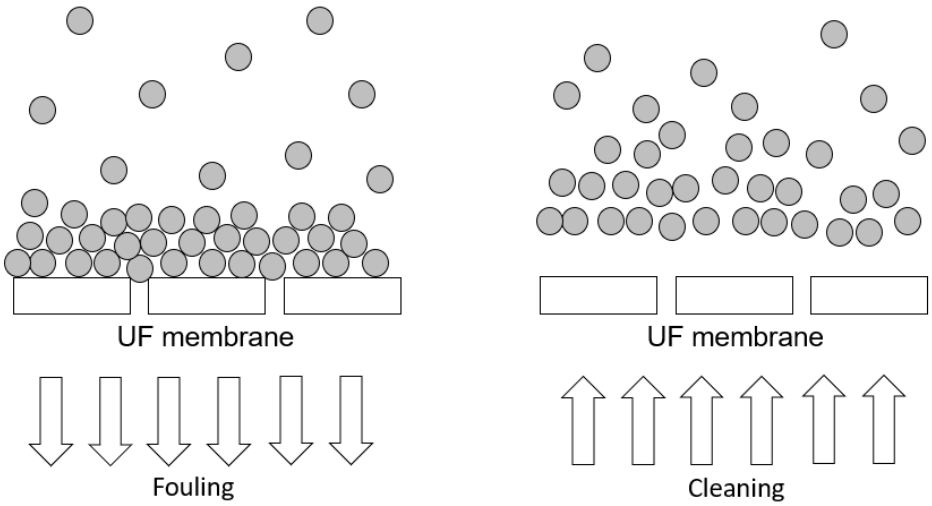

Figure 2-7. Configuration of UF membrane backwash.

1.2.3.4.2 RO fouling

Membrane fouling is also a major challenge in RO desalination. Unlike UF membranes, surface fouling is the main fouling mechanism for RO membranes, since they do not have distinguishable pores and are considered to be non-porous [17]. Compared with internal fouling (i.e., pore adsorption and clogging), surface fouling can be more easily controlled, and thus it is usually more reversible [116]. Nevertheless, surface fouling can also be irreversible depending on feed water

composition and interactions between the foulant molecules and the RO membrane surface [116]. Also, it is noted that RO membrane fouling can also be divided into reversible and irreversible fouling, depending on if it can be removed by hydrodynamic surface flushing (**Fig. 2-8**). RO membrane biofouling is affected by membrane surface characteristics (e.g., surface hydrophobicity, surface charge, surface morphology, surface chemistry), operational conditions (e.g., permeate flux, crossflow velocity, temperature, pressure, pH, salt concentration, feed spacer, presence of certain ions or molecules), microbial properties, and surface-bacteria interactions [116].

RO membrane biofouling, the process of microorganism adhesion and proliferation on the membrane surface, can lead to the surface formation of a biofilm. The formation of a biofilm on the RO membrane surface is highly undesirable as it can be difficult to remove. There are two key components of the biofilm, namely, bacteria and the extracellular polymeric substances (EPS) excreted by bacteria during the metabolism process [116]. Depending on different feedwater compositions and bacteria communities, EPS may be made up of polysaccharides, proteins, lipids, nucleic acids, humic and fulvic acids, and lipoproteins. RO membrane biofouling is affected by membrane surface characteristics (e.g., surface hydrophobicity, surface charge, surface morphology, surface chemistry), operational conditions (e.g., permeate flux, crossflow velocity, temperature, pressure, pH, salt concentration, feed spacer, presence of certain ions or molecules), microbial properties, and surface-bacteria interactions [116].

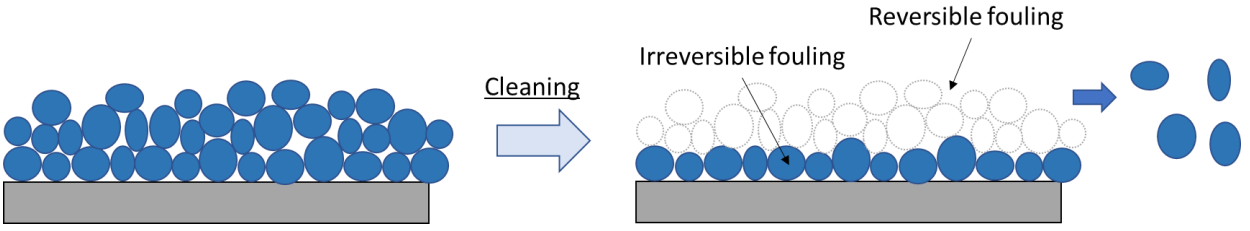

Figure 2-8. Illustration of reversible and irreversible fouling.

2.1.4 Major approaches to improve membrane performance

Many of the current strategies to overcome and mitigate membrane perm-selectivity tradeoff and fouling in water desalination focus on operational conditions and plant design configurations. For example, the traditional approaches to increasing RO membrane removal to specific contaminants such as nitrate, boron and arsenic include adjusting feedwater pH, using multi-pass RO, and implementing processes such as adsorption, ion exchange, and oxidation [10-13, 81, 117]. Current strategies to mitigate the adverse impact of membrane mineral scaling include (i) scalants removal via feedwater pretreatment, i.e., chemical softening, ion exchange, nanofiltration, and capacitive deionization; (ii) inhibition of nucleation by the use of an antiscalant; and (iii) scaling mitigation via process operational condition adjustments, such as pH adjustment (e.g., to avoid calcium carbonate scaling), increase the flow velocity, and periodic membrane cleaning [36]. Commonly used approaches for membrane fouling control focus primarily on pretreatment (i.e., coagulation, adsorption, pre-oxidation, biological treatment), operating conditions (i.e., permeate flux, transmembrane pressure, crossflow velocity), and proper cleaning (i.e., cleaning frequency, backwash/forward flush, chemical cleaning, air scouring) [35]. Even though they are effective to some extent, the above approaches require additional chemicals, equipment, and energy input, and thus increase the operational complexity and costs of membrane desalination processes [36].

As an alternative to the above various strategies, the engineering of membrane surfaces has been promoted to tune membrane performance and mitigate membrane fouling and scaling. It is reported that membrane surface characteristics (e.g., hydrophilicity, surface roughness, surface chemistry, and surface charge) can affect membrane separation properties, which in turn affect membrane fouling, scaling, and cleaning performance [18, 36-42]. Membrane performance improvement can be achieved via both physical surface modification including adsorption and dip-

coating with hydrophilic polymers [118], hydrogel, TiO_2 nanoparticles [119], and polymeric coating with embedded nanoparticles [120], and chemical surface modification including free radical graft polymerization, alkaline hydrolysis and acid treatment [121], chemical coupling, controlled oxidation [43], and blending and incorporation of organic additives [122], polymers [123] and carbon nanotubes [124] during membrane casting [3].

2.2 Polymer brush layer for membrane surface modification

Among the various membrane surface modification approaches, membrane surface tethered hydrophilic polymer brush layer has been shown to be a long-lasting, cost-efficient, and convenient approach to tailor membrane surface characteristics, tuning of membrane performance, and reducing membrane fouling and scaling propensity [45]. Broadly defined, polymer brushes refer to long polymer chains that are end-anchored to a surface with sufficiently high surface number density so that the chains are obliged to stretch away from the surface [125, 126]. A polymer brush or "tethered polymer chains" [127], are commonly synthesized by physisorption of polymers onto the surface, or graft polymerization with covalent bond attachment ("grafting-to" and "grafting-from") [55, 127, 128]. The structure of the surface tethered polymer brushes can be classified into three regimes: (1) "mushroom" or weakly interacting regime, (2) the crossover regime, (3) "brush" or highly stretched regime [127]. The polymer brush layer structure (or architecture) is commonly characterized in terms of a few important parameters, including grafting density, polymer chain length, polymer chain molecular weight, chain-chain separation distance, brush layer thickness, and chain polydispersity.

For decades, polymer brushes have been widely explored for their applications in membrane surface modification. A polymer brush layer with a thickness of just a few nanometers is sufficient

to alter membrane surface structures while keeping the bulk properties virtually unaltered. Membrane properties that can be altered upon tethering of a polymer brush layer include: (1) surface wettability; (2) surface chemistry, functionality, and charge; (3) diffusion control; (4) stimuli-responsiveness; (5) bio-compatibility; (6) steric hindrance force; and (7) surface adsorption of molecules [127, 128].

It was previously demonstrated the surface tethered polymer brush layer can reduce membrane propensities for mineral scaling and biofouling via increasing surface hydrophilicity, effective screening of the underlying membrane surface including the pores, and having partial mobility (due to Brownian motion) of the free segments of the anchored polymer chains [46 , 47, 48]. The surface tethered polymer brush layer can also tune the PA-TFC RO membrane water and salt permeability coefficients and overcome the typical perm-selectivity tradeoff [49]. Moreover, modification of membrane surfaces with tethered polyelectrolyte chains [50] can impact the physicochemical properties of the base membrane with reversible stimuli-responsiveness [51, 52]. Responsive membrane performance (e.g., water permeability and selectivity) is primarily achieved owing to conformational changes of the tethered polymer brush layer (e.g., via extension/collapse of the tethered chains) [51, 52]. Self-regulated conformational changes of the tethered polymer brush layer may also influence membrane-solute affinity, and thus the feasibility of reducing membrane fouling propensity and improving membrane cleaning efficacy [52, 53].

Consequently, surface tethered polymer brush layers are of particular interest for optimizing and improving membrane performance. However, in order to tune membrane performance by surface engineering of the polymer brush layer architecture, an extensive investigation of the correlation between brush layer structure and membrane properties/performance are required.

2.3 Synthesis approaches

Membrane surface tethered polymer brush layers can be synthesized via physical adsorption or covalent attachment [45]. In physical adsorption, the polymer chains are attached to the membrane surface through van der Waals force. Such attachment suffers from thermal and solvent instability, and thus the process can be easily reversed and the resulting modified membranes may lose surface functionalities. Covalent attachment, on the other hand, relies on chemical linker molecules and a number of wet-chemistry steps to form covalent bonds between the polymer brush chains and the membrane surface. The resulting polymer brushes were chemically-anchored to the membrane active layer and thus are robust and resistant to common chemical environmental conditions [129].

The synthesis of covalently surface tethered brush layers can be accomplished by *grafting to* or *grafting from* methods (**Fig. 2-9**). The *Grafting to* approach (i.e., polymer grafting) refers to preformed, end-functionalized polymers covalently attached to the membrane surface via a coupling reaction [129]. In the *grafting from* approach (i.e., graft polymerization), the membrane surface is modified to introduce active sites where monomers are polymerized and propagated until chain termination. The addition of monomers to surface chains can be accomplished via free-radical polymerization, anionic polymerization, atom-transfer radical-polymerization, and living polymerization techniques. Compared to *grafting from* approach, the *grafting to* method has the potential advantage that the structure of the polymer chains to be grafted for membrane surface modification can be well controlled and characterized [130], leading to narrow molecular weight distribution. However, as the tethered layer of polymer chains form, the previously bounded chains can impede the diffusion of homopolymer radicals toward the membrane surface anchoring sites due to diffusion hindrance. It is thus difficult to achieve high grafting densities or desirable overall

polymer grafting yield in the *grafting to* method [128].

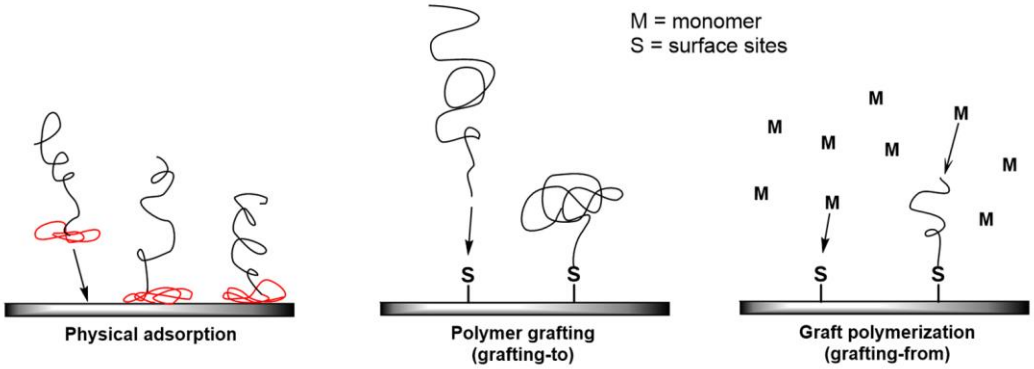

Figure 2-9. Surface tethered polymer brush layer synthesized via physical adsorption and chemical attachment (*grafting to* and *grafting from*).

Graft polymerization (i.e., *grafting from* approach) enables the synthesis of a tethered polymer layer of high grafting densities with controlled chain lengths [45]. Various approaches have been reported for surface activation to induce graft polymerization. These methods include chemical initiator grafting, gamma irradiation, ultraviolet (UV), ozone, and plasma-initiated reactions (**Fig. 2-10**). For example, it was reported that photo/UV-initiated graft polymerization of polyethylene glycol (PEG) methacrylate onto commercial polyethersulfone (PES) UF membranes can serve as a basis for fine-tuning membrane sieving properties by forming a crosslinked hydrogel layer with the aid of added crosslinker monomers (N, N-methylene bisacrylamide and pentaerythritol triallyl ether) [131]. The modified UF membranes had improved membrane myoglobin rejection (up to 89% relative to the base membrane) but with 90% water permeability reduction [131]. An alternative surface activation approach (for graft polymerization (GP) initiation) using low-pressure plasma has also been widely investigated given its effectiveness in creating surface radicals on a broad range of polymeric substrates [45, 132, 133]. However, the requirement of an ultra-high vacuum environment limits the potential scalability of the above approach. Nonetheless, low-pressure plasma surface activation has enabled the exploration of surface modification with

tethered layers over a wide range of membrane materials. For example, surface activation of polyethylene membrane (0.06 μm pore size) via low-pressure Argon plasma, followed by carboxybetaine graft polymerization (at a fixed set of reaction conditions), was reported to modify the base membrane's *MWCO* (assessed using glucose and dextran as model solutes) in the range of 5-580 kDa [132]. The *MWCO* was reported to vary with the polymer grafting density, but neither the relevant graft polymerization conditions nor the modified membranes' permeabilities were reported in the above study [132]. In another study, surface modification of polyacrylonitrile UF membranes, via low-pressure plasma-induced graft polymerization of different monomers (acrylic acid (AA), methacrylic acid, and 2-hydroxyl-ethyl methacrylate), resulted in lysozyme rejection that increased by 2-28%, while the hydraulic permeability decreased by 26-61% relative to the base UF membrane [133]. The above studies have shown that the tethered polymer graft yield (i.e., grafted polymer weight per surface area), which affected membrane hydraulic permeability and solute rejection (or *MWCO*), increased with initial monomer concentration and reaction time as expected for free-radical graft polymerization [132, 133].

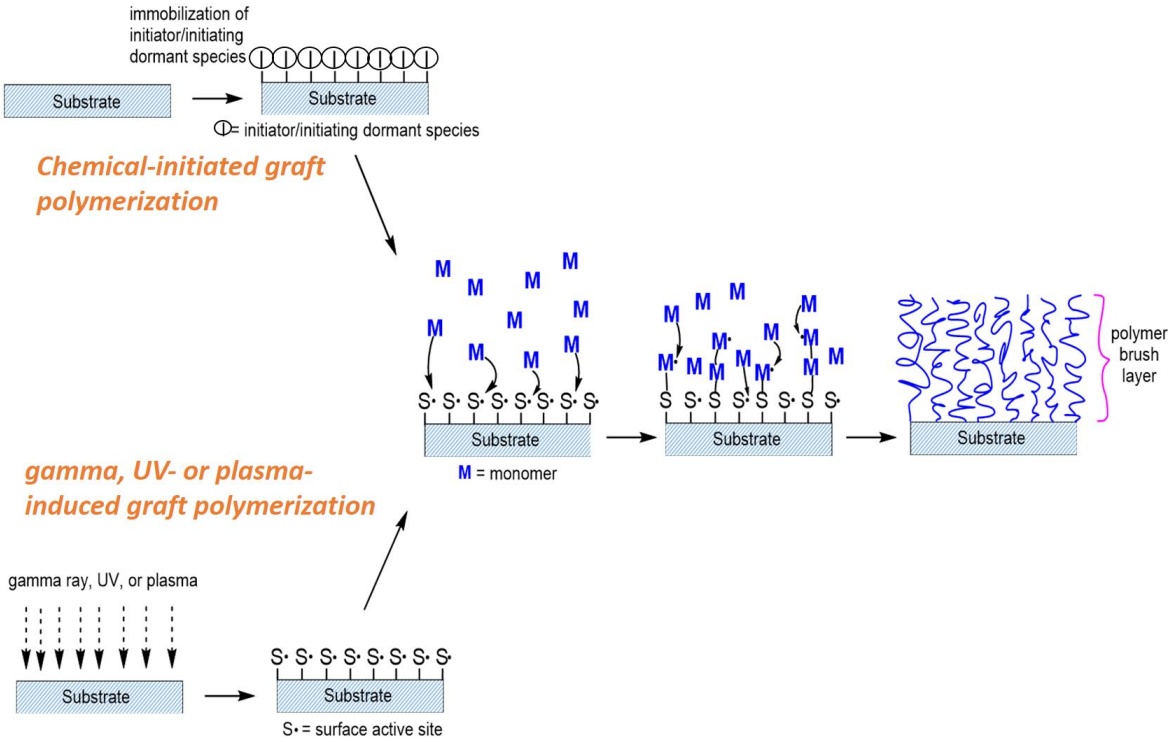

Figure 2-10. Surface graft polymerization with surface initiation sites formed using chemical initiators, and surface exposure to gamma or UV irradiation, plasma, and ozone.

However, in chemical-initiated free radical graft polymerization, the chemical initiators can initiate polymerization in the bulk solution, which may lead to homopolymerization and polymer grafting (*grafting to*), which in turn reduces the surface chain density and can decrease the average molecular weight of the tethered surface polymer chains [45]. Gamma irradiation, UV and ozone treatments can result in polymer chain scission, surface etching, alteration of the surface pore structure [45, 134], degradation of the polymer in the active layer [135, 136], and deterioration of the membrane mechanical properties [137, 138]. Moreover, gamma-induced graft polymerization is not commercially recommended because it is an expensive, time-consuming (1-24 h surface activation) process, and its safety considerations are also paramount [45, 134]. Among the various approaches of membrane surface activation to induce graft polymerization, plasma-induced graft polymerization is most commonly used.

2.3.1 Plasma-induced Graft Polymerization

In plasma-induced graft polymerization (PIGP), plasma is used to activate the substrate surface, and monomers in either a liquid or vapor phase are sequentially grafted onto the initiation sites via free radical polymerization [139]. Various gases (e.g., helium, argon, nitrogen, hydrogen, oxygen, ammonia, nitrous oxide, carbon dioxide, water, and tetrafluoromethane [140]) have been shown to be effective in inducing graft polymerization reaction and thus synthesizing the membrane surface tethered polymer brush layer. The capability of plasma to alter the physical and chemical properties of the upper molecular layer on the polymeric surfaces, thus improving wettability, adhesion, and biocompatibility [140] without affecting the bulk properties (especially mechanical properties) of the base material, is advantageous for the design and development of surface-modified polymer membranes [141].

Plasma surface activation is effective in producing a high density of surface active sites, in a relatively short plasma exposure time (<1 min), thereby enabling the formation of a high-density layer of tethered chains upon graft polymerization. Moreover, since the initiation sites are generated directly on the membrane surface without the use of chemical initiators, homopolymerization of monomers in the solution is avoided. PIGP proceeds via: (1) surface plasma treatment to generate free radicals on the substrate surface, (2) radicals' exposure to ambient air to create peroxide groups (–O-O or –O-O-H), and (3) thermal decomposition of peroxide bonds (O-O) and initiation of monomer graft polymerization. In contrast with plasma, which is based on more costly purified gases (e.g., He, Ar, O_2, CO_2), there has also been an interest in using air-based low-pressure [41, 140, 142-145] and corona discharge [40, 42, 62, 146-151]; the latter relying on ambient air at atmospheric pressure.

Surface treatment of polymeric membranes with air plasma can lead to surface etching [152], which can compromise the membrane surface active layer [153], thereby degrading membrane performance [154]. Hence, corona [40, 62, 145-150] and low-pressure air plasma [41, 142-144, 155] (**Table 2-4**) have been primarily used for surface modification of UF and microfiltration (MF) membranes where minor surface etching is less detrimental to membrane performance given that the membrane active layer is of sufficient thickness. Studies have shown that Air plasma surface treatment (via corona and low-pressure plasma sources) of various polymeric membranes reduced membrane water permeability but increased solute rejection (or smaller pore size) [40, 42, 148], or increased permeability at the cost of reduced solute rejection (or enlarged pore size) [140, 142, 146]. Improved membrane antifouling properties were reported after both low-pressure and corona air plasma surface modification of polypropylene, polyethylene, and polyethersulfone UF and microfiltration (MF) membranes used in a submerged membrane bioreactor (SMBR) [140, 144], and for filtration of oil-in-water (o/w) emulsions [40, 62, 146], and proteins (i.e., bovine serum album (BSA) and milk) [41, 42, 143, 148, 149]. Plasma treatment of the above UF and MF membranes [40-42, 140, 143, 144] also led to more effective permeability recovery, relative to the base membranes, via water cleaning.

Table 2-4. Literature review of air plasma induced graft polymerization in membrane surface modification[a]

Ref	Base membrane	Membrane surface modification method	Increase (%) in O/C ratio (XPS)[b]	Change (%) in water contact angle relative to base membrane [°]	Change (%) in water permeability[c] relative to base membrane [$L \cdot m^{-2} \cdot h^{-1} \cdot bar^{-1}$]	Change (%) solute rejection, solute permeability, or pore size, relative to base membrane	Change (%) in fouling flux decline (Operating Conditions)	Change (%) in permeability recovery (Cleaning Approach)	Comment[d]
[144]	Polypropylene hollow fiber microporous UF membrane	Low-pressure air plasma-induced N-vinyl-2-pyrrolidone graft polymerization (two-step process)	-	-44% sessile drop [129.3]	18.8% [1375]	-	-17.8% (50 h SMBR)	53% (D.I. water cleaning)	Increasing PVP immobilization degree[e] up to 6.8 wt%
[41]	Polypropylene MF membrane	Low-pressure air plasma-induced N-vinyl-2-pyrrolidone graft polymerization (two-step process)	515%	-33% sessile drop [112] -58% captive bubble [99]	109% [41.7]	-	-35% (40 min BSA filtration)	14.5% (D.I. water and 0.05N NaOH cleaning)	Increasing PVP immobilization degree[e] up to 14.18 wt%
[145]	Poly (vinylidene fluoride) MF membrane	Low-pressure air plasma-induced acrylamide and acrylic acid graft polymerization (two-step process)	-	-	-	100% (rejection of BSA and blue dextran) [Base membrane rejection: 0% and 0%]	-	-	Investigated the pH-responsiveness of the grafted membranes
[149]	Polyether sulfone MF membrane	Corona air plasma-induced acrylic acid graft polymerization (two-step process)	43%	-62% sessile drop [107]	188% [320]	-10% (pore size) [Base membrane pore size: 0.71 μm]	7% (90 min BSA filtration)	-	Investigated various plasma and graft polymerization conditions
[150]	High-density polyethylene MF membrane	Corona air plasma-induced acrylic acid graft polymerization (two-step process)	-	-100% sessile drop [106.4]	201% [220]	-	-	-	Investigated a range of AA grafting yield

[40]	Polyether sulfone UF membrane	Corona air plasma-induced hyperbranched ethylene glycol graft polymerization (two-step process)	-	-29% sessile drop [76]	-11% [92.3]	-27% (pore size) [Base membrane pore size: 30 nm] 2.8% (rejection of o/w emulsion) [Base membrane rejection: 91.8%]	-2.6% (20 h o/w filtration)	18% (pure water, 0.2% NaOH and 0.2% HNO_3 cleaning)	Investigated exposure time of up to 6 min and power up to 450W

[a] Percentage change with a positive number indicates performance value of the modified membrane is greater than the base membrane, while a negative number indicates the opposite.

[b] Change (%) represent the change of membrane performance after modification relative to the base membrane, defined as $\Delta A=[(A_{modified}-A_{Base})/A_{Base}]\cdot 100\%$ for O/C, contact angle, water permeability, pore size and solute permeability; and $\Delta A=A_{modified}-A_{Base}$ for solute rejection, fouling flux decline and permeability recovery.

[c] Water permeability coefficient L_p was evaluated with D.I. water, defined as $L_p=J_v/\Delta P$ where J_v is volumetric permeate flux and ΔP is the transmembrane pressure.

[d] Contributions of the studies other than performance alternation relative to the base membrane.

[e] Immobilization degree is calculated by the membrane weight change (%) before and after PVP immobilization (plasma-induced graft polymerization).

Surface treatment with both corona and low-pressure air plasma leads to alteration of the polymeric membrane surface chemistry, notably the introduction of oxygen-containing groups (e.g., C–O–C, C–OH, C(O)OH, C–O, and C=O) that increase surface hydrophilicity and whereby peroxide groups are active groups for subsequent initiation of radical polymerization [40, 41, 144, 149, 150]. The latter added modification step is of particular interest since it can be harnessed to tune UF membrane performance, via adjustments of plasma surface treatment and free-radical graft polymerization (with a suitable monomer) conditions [156]. Unlike low-pressure plasma, which requires the use of a vacuum chamber and thus the membrane surface area that can be treated is limited [157-159], membrane surface treatment via corona plasma can be scaled to large surface areas. However, the latter plasma type has been reported to be of lower plasma density compared to atmospheric pressure air jet plasma (Air APP) [160, 161]. The latter plasma produces a greater fraction of reactive/ionized species, while corona discharge has been reported to produce a non-uniform low ionizable plasma with ozone as its main reaction product [157, 162]. Moreover, corona plasma is reported to require higher energy consumption relative to Air APP [147].

In recent years, polymeric surface activation with atmospheric pressure plasma (APP), over a short duration (order of seconds), followed by free-radical GP has been advanced as an approach with the potential of scalability to treat large membrane surfaces, given the ability for plasma surface activation in ambient air [54, 56-59]. Moreover, APP surface activation has been reported to enable the creation of a high number density of surface-active sites, and thus a high degree of tethered polymer chain density on the membrane surface [54]. The type of plasma gas, surface exposure time, and surface-plasma source separation distance all affect the resulting surface density of active sites on the polymeric substrate [54, 163]. Graft polymerization of various vinyl

monomers on polyamide (PA) and polysulfone (PSf) surfaces also showed that the synthesized tethered chain length increased with initial monomer concentration [54].

For example, it was shown that the hydrophilic tethered polymer type is important in establishing the performance of modified UF membranes as shown in a detailed high throughput atmospheric pressure plasma-induced graft polymerization (APPIGP) study comparing the performance of PES UF membrane coupons modified via graft polymerization using 44 different vinyl monomers [57]. Membrane modification was carried out at a specific fixed set of conditions of surface activation (i.e., plasma head scan speed, RF power, and plasma-surface separation distance) and graft polymerization (2 hr reaction at 60°C and initial monomer concentration of 0.2 mol/L) [57]. Upon modification, membrane bovine serum albumin (BSA) rejection increased by 6-10% accompanied by 11-22% hydraulic permeability reduction. For certain monomers, the resulting modified membranes had greater hydraulic permeability (by up to 44%) relative to the base UF membrane but with the tradeoff of up to 37% decline of BSA rejection relative to the base PES UF membrane (hydraulic permeability and BSA rejection of 225 $L \cdot m^{-2} \cdot h^{-1} \cdot bar^{-1}$ and 50%, respectively) [57].

Commercial TFC-PA RO membranes can also be surface modified with polyacrylic acid (PAA) brush layer synthesized via atmospheric pressure plasma-induced graft polymerization [49]. By varying plasma treatment (i.e., number of sequential plasma scans and plasma-source separation distance) and graft polymerization conditions (i.e., initial monomer solution concentration and pH), the surface nano-structured (SNS) membrane performance can be tuned with respect to water and salt permeability coefficients, in the ranges of 2.3-3.4 $L \cdot m^{-2} \cdot h^{-1} \cdot bar^{-1}$ and 0.15-0.54 $L \cdot m^{-2} \cdot h^{-1}$, respectively, and overcome the typical perm-selectivity tradeoff [49]. More importantly, the SNS-PAA-PA membrane demonstrated a 17% reduced flux decline after 24 hr filtration of BSA model

solution, and 14% improved permeability recovery due to the effective surface screening effect of the surface tethered PAA chains [49].

2.3.2 Surface modification of spiral wound elements

Despite the extensive knowledge and advanced modification strategies to surface tether polymer brush layer, most of the reported studies have focused on laboratory-scale demonstrations with small flat sheet membrane coupons [66], typically of size in the range of 1-41 $inch^2$ in size [49, 164, 165]. Here it is noted that for a target membrane modification approach to be commercially viable, it must demonstrate a high degree of performance uniformity for membrane sheets of area sufficient for fabrication of spiral-wound elements (~720 $inch^2$) [27, 66, 67]. There are still challenges for membrane surface modification scalability and suitability for industrial applications, especially for producing spiral wound element. To date, however, scalability of RO membrane surface modifications has been demonstrated only for in-situ surface coating [166-168] and chemically-initiated free-radical surface graft polymerization [26, 169-172] of commercial spiral wound RO elements (**Table 2-5**). Physical adsorption/coating of RO membranes was achieved by either filling the RO element with a solution of the target solute and a subsequent equilibration period [167], or circulating the solution through the RO elements [166]. However, the physically coated layers may not be durable since such layers are not chemically affixed to the membrane surface [45]. Moreover, physical coating is difficult to control, the adsorbed layer is not permanently anchored to the membrane active layer [45], and the long-term impact of modification of other element surfaces (e.g., feed spacer, connecting tubes) has not been established.

In-situ modification of spiral-wound RO elements was also achieved via one-step or two-step chemically-initiated graft polymerization to create a tethered layer of polymer brushes [169-172].

The chemical initiators and the monomer solutions were circulated through the base RO membrane element in a single step or subsequently, followed by D.I. water rinsing. Even though in-situ graft polymerization offers the advantage of chemical attachment of graft polymerization of polymer chains onto the base RO membrane surface, the approach requires a large volume of chemicals. Also, configuration of the RO plant (or element manufacturing facility) whereby each element is essentially a chemical reactor (or a segment in a train of reactor elements) is likely to represent major technical and economic challenges.

An alternative to in-situ RO membrane element modification via graft polymerization is that of ex-situ modification, which can be easily implemented in the downstream process of TFC flat sheet membrane manufacturing prior to fabrication of spiral wound elements, and thus is more preferable for commercialization. There are various approaches to surface-graft polymerization [45] and their suitability for manufacturing spiral-wound elements depends on their scale-up potential for sufficiently large membrane surface area, but their use for ex-situ modification remains largely unexplored.

Table 2-5. Summary of studies that conducted membrane surface modification in spiral wound RO elements.

Reference	Basic spiral wound membrane element used for membrane surface modification	Membrane Surface Modification Technique
[169]	Hydranautics SWC2-2521 (SWRO)	Redox-initiated surface graft polymerization of polyethylene glycol ester of methacrylate (PEGMA) was performed by filtering a PEGMA solution containing redox initiators (potassium persulfate and potassium metabisulfite) through the base membrane element at a rate of 600 mL/min for 30 min.
[170]	Dow XLE-2540 (LPRO)	Redox-initiated surface graft polymerization of glycidyl methacrylate (GMA) was carried out by filtering GMA solutions containing redox initiators (sodium persulfate and potassium metabisulfite) through the base RO membrane element at 20-30°C at 15 bar and 100% recovery for 35 min. Subsequently, the modified membrane element was thoroughly rinsed with D.I. water for 24 h.

[171, 172]	Hydranautics ESPA1-2521 (LPRO)	Redox-initiated surface graft polymerization of glycidyl methacrylate (GMA) was carried out by filtering a feed water containing GMA and Triton X-100 (nonionic surfactant) through the base RO membrane element at a feed pressure of 20 bar for 5 min at a crossflow velocity of 1.8 cm/s and a permeate recovery of 30-40%. Subsequently, an aqueous solution containing N'N-methylenebis(acrylamide) (cross-linker) and redox-initiators (potassium sulfate and potassium metabisulfite) were added to the feed water to start the membrane surface modification, which was carried out at 24°C for 30 minutes. The modified membrane element was then rinsed with deionized water for 24 h.
[166]	Dow FilmTec TW30-1812	A dopamine solution was circulated through the base membrane element at ~1 L/min using a peristaltic pump at room temperature for 30 min. Then, the element was rinsed by circulating deionized water at the same flow rate for ~1 h. Subsequently, an aqueous Jeffamine solution was circulated through the element at 50°C for 30 min, followed by deionized water circulation through the element at room temperature for 1 h to rinse the modified element.
[167]	Hydranautics SWC3	Spiral wound membrane element was filled with a dopamine solution and gently rolled back and forth to contact the active side of the membrane with the dopamine solution for 1 h during which fresh oxygen was introduced into the element every 10 min in order to polymerize dopamine. The modified element was then flushed with deionized water.
[26]	EM-RO-1812-50	The membrane module loaded in the pressure vessel was filled with morpholinoethanesulfonic acid buffer solution containing 1-Ethyl-3-(3-dimethylaminopropyl) carbodiimide and *N*-hydroxysuccinimide for 4.0 h at 30.0 °C to surface activate the TFC PA membrane. Post thorough pure water cleaning, monomers amidosulfonic acid (ASA), diethanolamine (DEA) and piperazine (PIP) were then grafted onto the membrane surface by having the membrane module soaked with the 0.03 M grafting solution for 9.0 h at 30.0 °C.
[168]	Dow SW30-2540	Solutions of the aliphatic amine molecules (i.e, Amylamine, n-Octylamine, Decylamine, Dodecylamine) at 4 different concentrations 0.1, 0.5, 1 and 2 mM was filtered through the membrane element for amine molecules adsorption and immobilization within the PA. For each element the modifying solutions of a specific amine were applied consecutively, starting from the lowest concentration up to the highest one. After each solution treatment, the membrane was washed with pure water.

2.4 Polymer brush layer structures

The structure of the surface tethered polymer brush layer is governed by the polymer chain length *N*, distance between grafting chains or chain-chain separation distance *D*, grafting density of σ chains per unit area, brush layer thickness *h*, and the tethered density Σ (see **Eqn. 2-36**). As the chain-chain separation distance decreases to approach the size of grafted polymer chains, the grafted chains overlap, and lead to the transition of polymer brush structures from a single grafted polymer chain (mushroom) regime to a brush regime (**Fig. 2-11**). The resulting conformational regime is the consequence of the balance between the two contrary tendencies of the polymer brushes to: (1) maximize their configurational entropy by adopting random configuration (avoid contact with each other), and (2) maximize their contact with the solvent molecules, especially in a good solvent [126]. At low graft density, the graft polymer chains exist as a single chain or as clusters with a few chains, weakly interacting with each other. When the chain-chain separation distance *D* is larger than the radius of the gyration of the tethered chain, R_g, the polymer chains form a more flattened mushroom structure with the coil dimension, spreading onto the surface. As the graft density increases, graft chains overlap each other where $D < R_g$, and thus the chains stretch away from the surface to form orderly structures, minimizing interactions between polymer segments (i.e., excluded volume effect). The thickness of the interface increases as the spacing between anchor points becomes smaller due to the mutual interchain interactions.

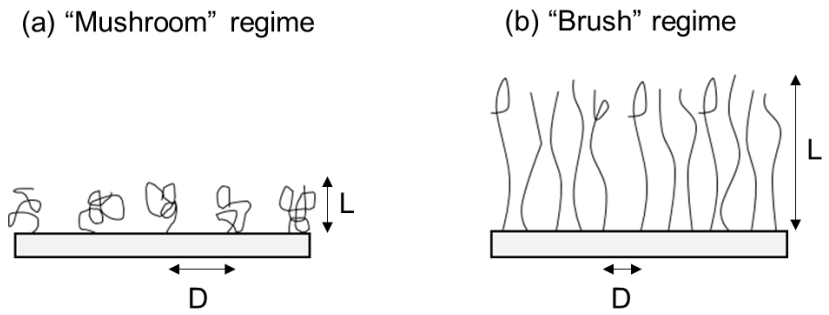

Figure 2-11. Tethered polymer brush layer structure regimes defined by grafting density: (a) “mushroom” regime at low grafting density and (b) “brush” regime at high grafting density (adapted from [119]).

A simple model to the balance achieved by the surface tethered polymer brushes is the Flory argument presented by Alexander and de Gennes [173-177], in which it is assumed that the polymer chains of length *N* are regarded as entropic “springs” with a spring constant $k_B T / R_g^2$, where k_B is the Boltzmann’s constant, *T* is the absolute temperature, and R_g is the radius of gyration of the tethered chain. The radius of the tethered chain can be calculated by

$$R_g = N^{1/2} a \tag{2-31}$$

where *a* is the Kuhn length.

The grafting density σ is defined by:

$$\sigma = \frac{h \cdot \rho \cdot N_A}{M_n} \tag{2-32}$$

where h is the brush layer thickness, ρ is the bulk density of the brush composition, and N_A is the Avogadro’s number. The grafting density σ is related to the chain-chain separation distance, *D*:

$$\sigma = \frac{1}{D^2} \tag{2-33}$$

The free-energy cost per chain (Δf) to stretch and overlap is derived from the Flory's argument as follows:

$$\Delta f \propto k_B T\left[\frac{3h^2}{2Na^2}+\omega N\left(\frac{N\sigma}{h}\right)\right] \tag{2-34}$$

where ω is the excluded volume parameter, representing the strength of the repulsion between the chain segments. From **Eqn. 2-34** it is concluded that for brushes with the same grafting density σ and increasingly large *N*, the height *h* increases linearly with *N*.

$$h \propto N\left(\omega\sigma a^2\right)^{1/3},\ f \propto k_B TN\left(\omega\sigma a^{-1}\right)^{2/3} \tag{2-35}$$

Another quantitative parameter used to characterize the conformational transition between mushroom to brush regime of the polymer brushes is the tethered density (Σ):

$$\Sigma = \sigma \cdot \pi \cdot R_g^2 \tag{2-36}$$

which represents the number of chains that occupy the area that a free nonoverlapping polymer chain would normally fill under the same experimental conditions [127]. According to the range of the absolute value of Σ, the structure of the surface tethered polymer brush layer can be classified into three regimes: (1) mushroom or weakly interacting regime (Σ<1), (2) transition regime between mushroom to brush (1< Σ<5), and (3) brush or highly stretched regime (Σ>5) [127]. It was also reported that the tethered polymer brush layer thickness is a function of chain-chain separation distance, $h \propto D^{-2/3}$ [178].

The theoretical model that the resulting tethered polymer brush layer thickness is a function of both grafting density and tethered polymer chain length, $h \propto N\sigma^{1/3}$ was indeed confirmed by various experimental studies, which investigated the polymer brush system structure using optical probes such as evanescent waves, ellipsometry, infrared spectroscopy, surface plasmon resonance measurement, X-ray reflection interferometry, neutron reflectometry, and atomic force

microscopy [129]. Moreover, attempts were made to increase the tethered brush layer thickness by increasing the tethered polymer chain length and/or grafting density. Indeed, increased grafting density is directly correlated to the greater density of surface active sites, which can be achieved by (1) increasing power and time of the plasma treatment, (2) decreasing plasma-surface separation distance, and (3) increasing the polymerization reaction time and thus increase the conversion (more initiator molecules are activated) [129, 179]. In contrast, decreasing grafting density can also be achieved by (1) diluting the initiator with an inert compound that is unable to initiate the polymerization reaction, and (2) deactivating some initiator species [49, 179]. Increased brush layer thickness can also result from increased the tethered polymer chain length or molecular weight, which can be fine-tuned by the initial monomer solution concentration and pH, graft polymerization time and temperature, the addition of transfer agents, and the addition of "free" initiator [49, 179].

In addition to solvent quality, the surface tethered polyelectrolyte bush layer is also responsive to environmental stimuli (e.g., temperature, pH, ionic strength, light, electrical/magnetic field, etc.) that lead to its conformational change (i.e., swelling/collapsing), which is often accompanied by changes in other surface properties (e.g., wetting/non-wetting, adhesive/non-adhesive, attractive/repulsive (to a target object), etc.). Polymer chains demonstrate conformational change (i.e., swell/collapse) mainly due to electrostatic interactions among the charged chain segments. For example, surface tethered polyacid chains swell at high pH as the surface tethered polymer chains deprotonate, which further leads to chain swelling owing to electrostatic repulsion between charged segments [180]. Polyelectrolytes also collapse with increasing solution ionic strength due to the charge screening effect of Na^+ and Cl^- ions also disrupted the electrostatic interactions among the charged polyelectrolyte chain segments [125, 181]. As a result, in addition to synthesis

conditions, the membrane surface tethered polymer brush layer structure can also be tuned by the aqueous environment. It is noted that the extent of polymer brush layer swelling, i.e., the swelling ratio (defined as the ratio of polymer brush layer thickness after swelling in the solvent to the dry layer thickness), strongly depends on the brush layer chemistry, composition (homogeneous, mixed, or block-copolymer brushes), degree of polymerization, graft layer thickness, graft polymer molecular weight, chain length, and grafting density [127].

2.5 Impact of brush layer on membrane properties

Surface tethered polymer brush layers affect both UF and RO membrane surface characteristics (i.e., surface chemistry, hydrophilicity, topography, and charge; **Table 2-6**) and thus membrane performance (i.e., water permeability, selectivity, fouling resistance, and cleaning efficacy; **Table 2-7**). Alteration of the above properties relative to the base membrane is affected by the polymer brush layer characteristics (i.e., grafting yield, grafting density, tethered polymer chain length, and molecular weight), and thus can be tuned by various synthesis conditions such as monomer and initiator concentrations, and grafting time.

For example, the sulfobetaine methacrylate (SBMA) grafted polyvinylidene difluoride (PVDF) UF membranes via UV polymerization demonstrated up to 27% increased surface O/C ratio, 67% lower membrane surface water contact angle, and 67% reduced negative zeta potential relative to the native membrane [182]. Membrane surface chemistry and hydrophilicity were tuned by adjusting the UV polymerization time from 30 s to 300 s, which impacts the degree of SBMA grafting. The modified membranes also exhibited a range of water permeability (76-286 $L \cdot m^{-2} \cdot h^{-1} \cdot bar^{-1}$) and BSA rejection (78.3-99.6%) relative to 176 $L \cdot m^{-2} \cdot h^{-1} \cdot bar^{-1}$ and 73.8% for the base membrane [182]. Additionally, excellent antifouling properties of the modified membranes were

claimed based on 9.5% reduced flux decline and 3% increased permeability recovery of the modified membrane relative to the base membrane for three cycles of BSA filtration and pure water cleaning [182]. However, it is noted the base PVDF and SBMA grafted membranes' fouling propensities were characterized at different initial permeate fluxes.

Another study also synthesized SBMA brush layers (100-400 nm) onto the PVDF UF membranes through dopamine-initiated atom transfer radical polymerization (ATRP) [183]. The resulting modified membranes' water permeability and areal porosity were tuned with the polymerization time. Indeed, the modified membranes' water permeability continued to increase (by 32.3%) for the increased ATRP reaction time (from 0 to 90 min) due to the greater surface hydrophilicity [183]. Further increase in the ATRP reaction time (from 90 to 120 min), however, led to a decrease in membrane permeability (by 6.7% relative to the modified membrane with an ATRP reaction time of 90 min) due to pore obstruction [183]. The effect of pore obstruction by the tethered polymer chains was also observed by SEM micrographs showing 9% and 66.7% decreased pore size and number density, respectively, as ATRP reaction time increased (from 0 to 120 min) [183]. In addition, the surface tethered zwitterionic brush layers resulted in reduced surface foulant adhesion/adsorption, with increased surface fouling resistance correlating with the increased ATRP reaction time [183]. This was confirmed by reduced flux decline during 3 cycles of 30 min BSA filtrations [183]. It was argued that PSBMA grafted membrane fouling propensity can be further reduced by interior graft polymerization (grafted both on the membrane surface and inside the pores) relative to surface graft polymerization (grafted only on the membrane surface) [183].

In a different study, [2-(Methacryloyloxy)ethyl]dimethyl-(3-sulfopropyl) ammonium hydroxide (SPE) brush layers were tethered onto the polyethersulfone (PES) UF membranes via

UV initiated ink-jet printed graft polymerization [184]. This approach was investigated by printing a layer of zwitterionic acrylate monomer on the PES UF membrane with subsequent UV irradiation. The resulting membranes demonstrated decreased C/N and C/O ratios, from 25.0 to 18.2, and 4.0 to 3.7, respectively, with increasing UV treatment time from 10 to 30 min [184]. The modified membranes also exhibited increased surface hydrophilicity, as indicated by the lower contact angles of 30-45°, compared to 75° of the pristine membrane [184]. More importantly, the modified membrane demonstrated less than 20% reduced membrane water permeability relative to the base membrane, compared to up to 87% reduction for the dip-coated membrane modification approach [184].

Tripath et al., conducted controlled surface-initiated atom transfer radical polymerization of 1-allyl-3-vinylimidazolium bromide (VAIB), 1-hexyl-3-vinylimidazolium bromide (VHIB), and 1 butyl-3-vinylimidazolium chloride (VBIC) onto the regenerated cellulose UF membrane [185]. Upon graft polymerization, the presence of -OH groups on the membrane surface decreased (qualitatively indicated by the reduced peak area in the FTIR spectra at wavelength 3300-3500 cm^{-1}) due to their utilization in initiator immobilization [185]. The modified membranes demonstrated increased surface hydrophilicity relative to the base membrane, as indicated by the reduced water contact angle from 70° to 47-64°, due to the electrostatic interaction between the brushes and the water molecules induced by the repeated unit of ionic moieties [185]. Membrane surface hydrophilicity further increased (as indicated by up to a 27% decrease in water contact angle) when denser polymer chains were tethered onto the membrane surface, achieved by the increased initiator immobilization time from 5 to 10 min [185]. The surface tethered polymer brush layer also caused membrane surface zeta potential to switch to positive at pH of 7 relative to the negative zeta potential for the base membrane, due to the presence of positively charged imidazolium

cationic moieties in the brushes. The positive membrane surface zeta potential also increased from 28-33 mV to 45-55 mV with the initiator immobilization time increased from 5 to 10 min [185]. Moreover, the modified membranes are of higher surface roughness (from 16.4 nm to 18.1-26.1 nm), and up to 62% decreased O/C ratio relative to the base membrane [185]. The grafted membranes also demonstrated electric field (0-1000 Hz) responsive performance tuning in terms of permeate water flux (165-372 L/m^2-h), BSA rejection (87-98%), and *MWCO* (171-246 kDa) [185].

Liu et al., reported that electron transfer−atom transfer radical polymerization of SBMA onto the PVDF hollow fiber UF membranes led to 90% reduced areal porosity (from 8% to 0.8%) [186]. Functionalization of zwitterionic polymers on membrane surfaces also effectively enhanced membrane surface hydrophilicity (with surface water contact angle decreasing from 96.2° to 61.0°). The increase in surface hydrophilicity was attributed to the same units of cationic and anionic groups possessed by the zwitterionic polymers that associate with water molecules, via electrostatic interactions to form a strong hydration layer [186]. The longer PSBMA polymerization time resulted in higher membrane hydrophilicity (as indicated by the membrane surface contact angle decreased from 78˚ to 62˚ as graft polymerization time increased from 1 hr to 2 hr). In addition, grafting of PSBMA polymer brushes on membrane surface led to ~14% increased membrane surface roughness. The PSBMA grafted PVDF membranes also exhibited increased water permeability from 0.25 $L \cdot m^{-1} \cdot h^{-1} \cdot kPa^{-1}$ to 0.36-1.65 $L \cdot m^{-1} \cdot h^{-1} \cdot kPa^{-1}$, with the maximum permeability reached at polymerization time of 1.5 h [186]. The existence of a maximum permeability with increasing polymerization reaction time is due to two competing factors: increased surface hydrophilicity with grafting of the hydrophilic PSBMA which should lead to increased membrane permeability, while surface coverage (blocking the pore) by the

functional layer should lead to the opposite effect. The modified membrane also demonstrated improved fouling resistance as indicated by 3.3% reduced flux decline and 57% enhanced final stable membrane flux relative to the pristine membrane post one month gravity-driven membrane fouling tests with sewage wastewater [186]. However, the fouling tests were conducted at different initial permeate flux (with controlled transmembrane pressure), of 78.8 $L \cdot m^{-1} \cdot h^{-1}$ and 113.7 $L \cdot m^{-1} \cdot h^{-1}$, respectively, for the pristine and modified membranes [186], and thus different were used or comparison of their anti-fouling properties.

Porter et al., conducted surface-initiated atom transfer radical polymerization of *tert*-butyl acrylate (*t*BA) and 2-hydroxy ethyl acrylate (HEA) onto the porous cellulosic UF membrane and achieved the modified membranes with ~10.6% reduced surface roughness [187]. The membrane surface tethered hydrophobic P*t*BA layer increased surface water contact angle from 44˚ to 80˚ compared to the base membrane, while the subsequently added PHEA layer reduced it to 60-69˚. It was also demonstrated that membrane surface characteristics and performance can be tuned with surface tethered polymer chain length, grafting density, and brush layer thickness, controlled by varying the crosslinker (adipoyl chloride) and initiator (α-bromoisobutyryl bromide) concentrations [187]. A positive trend was observed between brush density and initiator content (its composition relative to the crosslinker), with the maximum brush density of 1.70 chain/nm^2 achieved at 55 mol% initiator content [187]. The modified membranes had water permeability below that of the virgin membrane (~290 $L \cdot m^{-2} \cdot h^{-1} \cdot bar^{-1}$) and continued to diminish (by up to 99.6%) with increased polymer chain length (with M_n of the P*t*BA brush from 0 to 4 kg/mol) [187]. The P*t*BA modified membrane also led to increased membrane rejection of lysozyme to 97% relative to 18% of the pristine membrane [187]. The modified membrane solute fluxes (i.e.,

selectivity) of L-asparagine, NaCl, hydroquinone, and thymol were also tunable with the tethered polymer chain length (M_n).

Carter et al., used the activators generated electron transfer (AGET) method coupled with atom transfer radical polymerization (ATRP) to carry out the surface-initiated polymerization reaction of 2-hydroxyethyl methacrylate (HEMA) on the regenerated cellulose (RC) membranes [188]. Optimization of the AGET-ATRP method was investigated with respect to the initiator concentration, polymerization reaction time, and the reducing agent (activator) concentration. For example, a sharp drop in membrane permeate flux (from 301 to 0 $L \cdot m^{-2} \cdot h^{-1}$) was achieved when the initiator concentration increased from 100 to 1000 mM [188]. The above study also investigated control of polymer grafting only on the membrane surface versus both on the membrane surface and inside the pores, via the utilization of different pore filling solvents with a wide range of viscosity and reactivity. The results indicated that without using a pore filling solvent, the grafted membrane demonstrated reduced *MWCO* (from 120 to 72 kDa), increased dextran rejection (from 0 to 35.3%) and increased BSA rejection (from 41 to 78.4%) relative to the pristine membrane [188]. While with the use of pore filling solvents, the membrane pore size were less affected, as indicated by *MWCO* range of 74-112 kDa, dextran rejection of 5.6-33.4%, and BSA rejection of 42-76.2% [188].

Pourziad et al., modified a commercial polyvinylidene fluoride (PVDF) membranes using surface-initiated atom transfer radical polymerization (SI-ATRP) of poly(N-isopropylacrylamide) (PNIPAAm) and poly (ethylene glycol) methacrylate (PEGMA) [189]. The amount of PNIPAAm and PEGMA grafting can be tuned with polymerization reaction time and initial monomer concentration. The resulting modified membranes demonstrated a 9.8% reduced surface roughness, and improved surface hydrophilicity as indicated by the water contact angle decreased to 58-92°

from 96° for the pristine membrane [189]. The grafted membranes also exhibited lower fouling propensity (as indicated by 64% flux decline) and higher flux recovery ratio (by 5.1%) for the filtration of synthetic oily water ascribed to the hydrophilic brush layer tethered on the membrane surface decreasing the surface oil molecules attachment [189].

Sengupta et al., developed an approach to selectively graft glycidyl methacrylate (GMA) only on the external surface of regenerated cellulose (RC) ultrafiltration (UF) membranes using activator generated electron transfer (AGET) atom transfer radical polymerization (ATRP) with the appropriate pore filling solvent [190]. The modified membranes demonstrated decreased water flux, and increased BSA and dextran rejection, by 12-59% and 2-30%, respectively, relative to the pristine membrane, indicating the reduction of membrane pore size [190]. The tuning of the surface modified membrane performance in terms of permeate flux and protein rejection was achieved via a range of polymerization time (30-150 min) and different pore filing solvents (i.e., acetonitrile, ethanol, PEG 400, L 64, and glycerol) [190].

He et al., fabricated the nonionic poly(N-acryloyl morpholine)-brush-grafted-poly(vinylidene fluoride) membranes (PVDF-g-PACMO) via surface-initiated atom transfer radical polymerization (ATRP) [55]. Upon PACMO graft polymerization, the surface modified membranes demonstrated reduced membrane pore size and porosity, increased surface hydrophilicity and negative zeta potential, and improved membrane pure water flux. The degree of changes can be tuned via the polymerization time, which governs membrane surface grafting density. Indeed, it was observed that the grafting density of PACMO increased from 49 to 76 $\mu g/cm^2$ as the polymerization time increased from 30 min to 90 min [55]. The resulting membranes exhibited decreased membrane pore size and porosity, from 0.38 μm and 71.7%, respectively, to 0.34 μm and 66.9%, as the grafting time increased from 30 min to 90 min [55]. Similarly, 20.9%

increase in negative membrane surface zeta potential, 44.4% reduce in membrane surface water contact angle, and 19.9% increase in membrane pure water flux was observed with the increasing polymerization time [55]. The PVDF-g-PACMO membranes also demonstrated improved fouling resistance (i.e., 15% reduced flux decline) after five cycles of surfactant stabilized oil/water emulsions fouling tests, and 6% improved flux recovery post periodic water backflush [55].

Chen et al., investigated the influence of surface modification of zirconia (ZrO_2) membrane with silylated poly(vinyl pyrrolidone) (PVP) chains on membrane hydraulic resistance, protein rejections, and fouling resistance for the filtration of bovine serum albumin (BSA) and lysozyme (Lys) [46]. The PVP chains were graft polymerized onto the zirconia (ZrO_2)-based ceramic UF membranes after surface vinyl-silylation and hydrolysis [46]. The modified membranes demonstrated improved membrane fouling resistance (lower irreversible fouling resistance for BSA and Lys by ~11–49% and 18–74%, respectively) but at the cost of 118% increased membrane resistance tested with NaCl ionic strength from 0.001 to 0.5 M and pH from 3 to 10 [46].

In another study, thin-film composite RO membranes were modified with the zwitterionic polymer brushes (sulfobetaine methacrylate) via activators regenerated electron transfer atom transfer radical polymerization (ARGET-ATRP) [25]. The zwitterionic polymer brush layer density and thickness can be tuned by initiator immobilization and graft polymerization time. The resulting grafted membranes demonstrated surface superhydrophilicity as indicated by the membrane surface water contact angle of <20°, which increased surface roughness (from 29.8 to 61.3 nm), and increased zeta potential (from -13 mV to -8 mV) relative to the pristine membrane [25]. The zwitterionic polymer grafted membranes also exhibited 55.6% decreased water permeability and 0.1% increased NaCl rejection [25]. RO scaling experiments indicated that membranes modified with the zwitterionic brushes had delayed gypsum surface nucleation and

crystal adsorption relative to the base membrane. At the end of the RO scaling experiments with only-heterogeneous gypsum nucleation, the zwitterion-modified membranes exhibited a much lower flux decline of 23.7%, relative to 49.5% of the pristine RO membrane [25]. Membrane flux decline by surface deposition of gypsum crystals in the combined homogeneous and heterogeneous nucleation was about 1.6 times delayed for the zwitterion-modified membranes compared to the base membrane [25].

Tong et al., conducted activators regenerated by electron transfer−atom transfer radical polymerization (ARGET-ATRP) of acrylamide (AM), sulfobetaine methacrylate (SBMA), and [2-(methacryloyloxy)-ethyl] trimethylammonium chloride (MTAC), redox radical graft polymerization of acrylic acid (AA), and direct grafting of ethylenimine (EI) and 1H,1H,2H,2H-perfluorodecanethiol (FDT) onto the commercial TFC RO membranes (SW30 XLE) [191]. After modification with PAM, PSBMA, PEI, and PAA polymers, the resulting membrane surfaces a more hydrophilic, with the water contact angle < 20° relative to 30° for the pristine membrane, attributed to the introduction of polar functional groups to the membrane surface [191]. In contrast, membrane surface grafting of PFDT led to a significant increase in water contact angle (from 30° to >110°), and membrane surface modification with PMTAC, PDA, and PDA-Bibb resulted in a slight increase in surface hydrophilicity [191]. The surface tethered polymer brush layers also led to alteration of the membrane surface charge. For example, the PSBMA and PAM modified membranes surface zeta potential increased to -6 mV from -12 mV for the pristine membrane at pH of 7 [191]. In addition, most of the polymer brushes modified membranes exhibited slightly higher water permeability coefficients (2.6-3.0 $L \cdot m^{-2} \cdot h^{-1} \cdot bar^{-1}$) than 2.5 $L \cdot m^{-2} \cdot h^{-1} \cdot bar^{-1}$ for the pristine membrane [191]. Decreased permeability was also observed for the PEI modified membranes, of 2.3 $L \cdot m^{-2} \cdot h^{-1} \cdot bar^{-1}$ [191]. Compared to the 99.0% average salt rejection of the base

SW30 XLE membrane, the modified membranes demonstrated similar or slightly lower salt rejection of 98.4-99.1% [191]. The surface tethered polymer brush layer also affected membrane scaling propensity by the tuning of membrane surface charge. Compared to 15% flux decline after the 1,400 min silica scaling test of the pristine membrane, the modified membranes demonstrated 12-30% flux decline [191].

In another study, a commercial TFC-PA RO membrane was surface modified with 3-sulfopropyl methacrylate potassium (SPMK) by atom transfer radical polymerization [192]. The surface tethered PSPMK layer led to reduced membrane surface water contact angle from 58.5° to 10.6-36.3° [192]. Upon SPMK graft polymerization, membrane surface roughness also decreased from 40 μm to 33-37 μm [192]. The grafted membranes also demonstrated increased permeate flux from 57.1 $L \cdot m^{-2} \cdot h^{-1}$ to 71.2 $L \cdot m^{-2} \cdot h^{-1}$, and decreased salt rejection from 97.5% to 95.3% [192]. Increasing membrane surface hydrophilicity and permeate flux as well as decreasing salt rejection was observed with increasing graft polymerization monomer concentration.

Wang et al., modified a base PA RO membrane via UV polymerization of 2,2,3,4,4,4-Hexauorobutyl methacrylate (HFBM) and tobramycin (TOB) [193]. The resulting membranes demonstrated increased O/C ratio from 0.18 to 0.21, decreased water contact angle from 75.1° to 60.2°, increased surface zeta potential from -42 mV to -35 mV, and decreased surface roughness from 91.5 nm to 80.1 nm relative to the virgin membrane [193]. The modified membrane perm-selectivity (water flux of 54.1 $L \cdot m^{-2} \cdot h^{-1}$ and salt rejection of 99.05%) was similar to those of the virgin membrane (water flux of 53.7 $L \cdot m^{-2} \cdot h^{-1}$ and salt rejection of 98.99%) [193]. Moreover, improved membrane fouling resistance upon surface modification with the tethered polymer brush layer, as indicated by dramatically reduced flux decline (from 64.7% to 9.5%) after 3 cycles of 4 hr BSA fouling tests, and increased flux recovery (from 48.1% to 96.5%) after 1 hr D.I. water

cleaning [193]. However, such comparison of the virgin and modified membranes fouling properties were not conducted at the same initial permeate flux.

Liu et al., surface modified TFC-PA RO membranes via sequential surface treatment using acidic aqueous glutaraldehyde (GA) and monomethoxy-poly(ethylene glycol) (MPEG) solutions [194]. It was found that grafting density increased from 0.9 to 3.3 g/m^2 with increasing MPEG concentration from 0.5 to 2.5 wt% [194]. The resulting PA-GA-MPEG membranes had increased O/C ratio from 0.22 to 0.29, increased surface roughness from 69.8 nm to 76.9-102.5 nm, increased surface zeta potential from negative 48.2 mV to negative 31.6-38.5 mV, and reduced water contact angle from 59.8° to 42.3°-48.3° relative to the virgin membrane [194]. The modified membranes also demonstrated reduced water flux from 30.0 $L \cdot m^{-2} \cdot h^{-1}$ to 26.5-28.9 $L \cdot m^{-2} \cdot h^{-1}$ and increased salt rejection from 98.1% to 98.2-98.6% [194]. The above membrane surface characteristics and performances were tuned based on settings of the initial MPEG concentration. Improved membrane fouling resistance and cleaning efficacy were also observed for the modified membrane relative to the virgin membrane, as indicated by 11.9% reduced flux decline post three-cycle 20 hr filtration of secondary textile effluent, and 4.8% increased flux recovery after 5 hr pure water cleaning. However, the virgin and modified membranes fouling properties were not compared at the same initial permeate flux.

Kim et al., surface modified commercial TFC-PA RO membranes with polyacrylic acid (PAA) brush layer synthesized via atmospheric pressure plasma-induced graft polymerization [49]. By varying plasma treatment (i.e., number of sequential plasma scans and plasma-source separation distance) and graft polymerization conditions (i.e., initial monomer solution concentration and pH), the surface nano-structured (SNS) membrane performance was tuned in terms of water and salt permeability coefficients, in the ranges of 2.3-3.4 $L \cdot m^{-2} \cdot h^{-1} \cdot bar^{-1}$ and 0.15-0.54 $L \cdot m^{-2} \cdot h^{-1}$,

respectively; thus, overcoming the typical perm-selectivity tradeoff [49]. More importantly, the SNS-PAA-PA membrane demonstrated 17% reduced flux decline after 24 hr filtration of BSA model solution, and 14% improved permeability recovery due to the membrane surface tethered PAA chains effectively screening the underlying membrane surface [49].

Yang et al., used surface-initiated atom transfer radical polymerization (SI-ATRP) to uniformly modify the surface of TFC-PA RO membranes with zwitterionic polymer layers, [(2-methacryloyloxy)ethyl]dimethyl[3-sulfopropyl]ammonium hydroxide (pMEDSAH) [195]. Membrane surface modification led to the tuning of surface chemistry especially the presence (%) of C, Si, and Br, via the monomer and initiator concentrations, and graft polymerization time [195]. Membrane surface roughness increased significantly upon initiator immobilization (from 90 nm to 138 nm), and decreased with polymerization time, as the longer pMEDSAH chains better filled the ridges and valleys that existed on the pristine PA layer. It was estimated that the weight-average molecular weight of pMEDSAH chains increased from 22,054 to 60,811 kDa upon increasing the polymerization time from 30 to 120 min [195]. Membrane surface hydrophilicity also increased after initiator immobilization and ATRP treatment, and as indicated the membrane surface contact angle decreased from 44° to 17° as the polymerization time increased from 0 to 120 min [195]. The modified membrane salt rejection barely changed with monomer and initiator concentrations, but water permeability decreased from 68 $L \cdot m^{-2} \cdot h^{-1} \cdot MPa^{-1}$ for the virgin membrane to 38-57 $L \cdot m^{-2} \cdot h^{-1} \cdot MPa^{-1}$ [195].

Hirsch et al., surface modified TFC RO membranes via a combination of plasma activation, plasma bromination, and surface-initiated atom transfer radical polymerization of hydroxyethyl methacrylate (HEMA), 2-methacryloyloxyethyl phosphorylcholine (MPC) and [2-(methacryloyloxy) ethyl]-dimethyl-(3-sulfopropyl) ammonium hydroxide (SBMA) [196]. It was

found that the tethered layer mass increased (from 0.18 to 0.95 μg/cm^2 and 0.24 to 1.23 μg/cm^2 for MPC and SBMA, respectively) with increasing monomer concentration (from 10 mmol to 100 mmol). The resulting membranes demonstrated reduced surface water contact angle, from 51.9° for the pristine membrane to 25.1°, 42.2°, and 34.9° for membranes grafted with oligo-HEMA (OHEMA), oligo-MPC (OMPC), and oligo-SBMA (OSBMA), respectively [196]. The grafted membranes also had increased presence of oxygen (from 11.8% to 22.1%) with increasing reaction time from 5 min to 20 hr [196].

A commercial RO membrane was also surface modified via redox-initiated graft polymerization of N-(3- sulfopropyl)-N-methacroyloxyethyl-N,N-dimethylammonium betaine, 2-hydroxyethyl methacrylate (SPE), poly(ethylene glycol) methacrylate (PEGMA), 2-hydroxyethyl methacrylate (HEMA), [2-(methacryloyloxy)- ethyl]trimethylammonium chloride (MOETMA)), and methacrylate (MA) [197]. The surface modified membranes demonstrated up to 5% increase in O/C ratio, tuned membrane surface water contact angle from 21° to 35°, and surface zeta potential from -20 to -50 mV at pH of 7, relative to 26° and -30 mV, respectively, for the base membrane [197].

Table 2-6. Literature review (2018-2022) of surface tethered brush layer affecting UF and RO membrane surface characteristics[a,b]

Ref	Base membrane	Membrane surface modification method	Increase (%) in O/C ratio (XPS)	Change (%) in water contact angle relative to base membrane [°]	Change (%) in surface roughness relative to base membrane [nm]	Change (%) in surface zeta potential to base membrane [mV]	Other[c]
[182]	Polyvinylidene difluoride UF membrane	UV treatment polymerization of sulfobetaine methacrylate	27%	-67% sessile drop [70.93]	-	67% [-25]	Tuned with UV polymerization reaction time
[184]	Polyethersulfone UF membrane	UV-mediated graft polymerization of [2-(Methacryloyloxy)ethyl]dimethyl-(3-sulfopropyl)ammonium hydroxide	5%	-60% captive bubble [75]	-	-	Tuned with UV irradiation time and number of printed layers
[185]	Regenerated cellulose UF membrane	Controlled surface graft polymerization of 1-allyl-3-vinylimidazolium bromide, 1-hexyl-3-vinylimidazolium bromide, and 1 butyl-3-vinylimidazolium chloride	-61.8%	-33% sessile drop [70]	59% [16.4]	From -13 mV to the highest 57 mV	Investigated three types of monomer and different initiator immobilization reaction time
[186]	Polyvinylidene difluoride hollow fiber UF membrane	Electron transfer−atom transfer radical polymerization of sulfobetaine methacrylate	-	-37% sessile drop [95]	14%	-	Water contact angle tuned with polymerization reaction time
[187]	Porous cellulosic UF membrane	Surface-initiated atom transfer radical polymerization of *tert*-butyl acrylate and 2-hydroxy ethyl acrylate	-	84% sessile drop [44]	-10.6% [8.5]	-	Water contact angle tuned with polymer brush layer molecular weight
[198]	Poly(vinyl chloride) UF membrane	Surface-initiated electron transfer-atom transfer radical polymerization of [2-(methacryloyloxy) ethyl] dimethyl-(3-sulfopropyl) ammonium hydroxide	22%	-17% sessile drop [99.2]	59% [17]	-	Tuned with grafting time
[189]	Polyvinylidene difluoride UF membrane	Surface-initiated atom transfer radical polymerization of N-isopropylacrylamide and poly (ethylene glycol) methacrylate	-	-40% sessile drop [96]	-10% [13.2]	-	Tuned with polymerization time and monomer solution concentration
[55]	Polyvinylidene difluoride UF membrane	Surface-initiated atom transfer radical polymerization of N-acryloyl morpholine	-	-77% sessile drop [110.9]	-	-94.7% [-26.4]	Tuned with grafting time
[25]	Polyamide TFC RO membrane	Surface-initiated activators regenerated electron transfer atom transfer radical polymerization of sulfobetaine methacrylate	-	-31.5% sessile drop [52]	106% [29.8]	39% (at pH 5.7) [-13]	Tuned with grafting time and initiator immobilization time
[197]	ESPA-HDR RO membrane	Redox-initiated graft polymerization of N-(3- sulfopropyl)-N-methacroyloxyethyl-N,N-dimethylammonium betaine, 2-hydroxyethyl methacrylate, poly(ethylene glycol) methacrylate, [2-(methacryloyloxy)-ethyl]trimethylammonium chloride, and methacrylate	5%	-22%~30% sessile drop [27]	-	-33.3%~66.7% (pH of 7) [-30]	Tuned with different types of monomers

[191]	SW30 XLE TFC RO membrane	Activators regenerated by electron transfer−atom transfer radical polymerization of acrylamide, sulfobetaine methacrylate, and [2-(methacryloyloxy)- ethyl] trimethylammonium chloride. Redox radical graft polymerization of acrylic acid. Direct grafting of polyethylenimine and 1H,1H,2H,2H-perfluorodecanethiol.	-	-66.7%~296.7% sessile drop [30]	-14%~10% [100]	The grafted membranes had zeta potential ranging from -16 to 5 mV at pH of 7 [-12.5]	Investigated three grafting approaches and multiple monomers
[193]	Polyamide RO membrane	UV polymerization of 2,2,3,4,4,4-Hexauorobutyl methacrylate and tobramycin	6%	-65%~53% sessile drop [75.1]	-12.5% [91.5]	32.5% [-42]	-
[192]	Polyamide TFC RO membrane	Atom transfer radical polymerization of 3-sulfopropyl methacrylate potassium	-	-81.9% sessile drop [58.5]	-7.5%~-20% [40]	-	Tuned with feed composition of reagents used for synthesis of polymer brush layer
[194]	Polyamide TFC RO membrane	Sequential surface treatment using acidic aqueous glutaraldehyde and monomethoxy-poly(ethylene glycol) solutions	6.8%	-19.2%~-29.3% sessile drop [59.8]	10.2%~46.8% [69.8]	20%~34.4% [-48.2]	Tuned with initial monomer solution concentration
[196]	Polyamide TFC RO membrane	Combination of plasma activation, plasma bromination and surface-initiated atom transfer radical polymerization of hydroxyethyl methacrylate, 2-methacryloyloxyethyl phosphorylcholine and [2-(methacryloyloxy)ethyl]-dimethyl-(3-sulfopropyl)ammonium hydroxide	11.6%	-18.7%~-51.6% sessile drop [51.9]	-	-	Tuned with grafting time and types of monomers
[195]	Polyamide TFC RO membrane	Surface-initiated atom transfer radical polymerization of [(2-methacryloyloxy)ethyl]dimethyl[3-sulfopropyl]ammonium hydroxide	4.2%	-37.8%~-68.9% sessile drop [45]	-60.9%~45.7% [92]	-	Tuned with initial monomer solution concentration
[49]	Polyamide TFC RO membrane	Atmospheric-pressure plasma-induced graft polymerization of acrylic acid	6%	-29.9% captive bubble [28.4]	7.8% [67.6]	-	-

[a] Percent change with a positive number indicates performance value of the modified membrane is greater than the base membrane, while a negative number indicates the opposite.

[b] Change (%) represent the change of membrane performance after modification relative to the base membrane, defined as $\Delta A=[(A_{modified}-A_{Base})/A_{Base}]\cdot 100\%$ for O/C, contact angle, water permeability, roughness and zeta potential (at pH of 7).

[c] Contributions of the studies other than performance alternation relative to the base membrane.

Table 2-7. Literature review (past 5 years) of surface tethered brush layer affecting UF and RO membrane performance[a,b]

Ref	Base membrane	Membrane surface modification method	Change (%) in water permeability[c] relative to base membrane [$L \cdot m^{-2} \cdot h^{-1} \cdot bar^{-1}$]	Change (%) in selectivity[d] relative to base membrane	Change (%) in fouling flux decline	Change (%) in permeability recovery	Other[e]
[182]	Polyvinylidene difluoride UF membrane	UV treatment polymerization of sulfobetaine methacrylate	-57%~62.5% [176]	25.8% rejection of BSA	-9.5% 3 cycles of 1h BSA fouling	3% pure water	Tuned membrane permeability with polymerization reaction time
[183]	Polyvinylidene difluoride UF membrane	Dopamine-initiated atom transfer radical polymerization of sulfobetaine methacrylate	-3%~47% [340]	-9% pore diameter [14.3 nm]	-7% three cycle 30 min BSA fouling	8% pure water	Investigated the difference between surface grafted and interior grafted membranes. Also tuned separation properties with polymerization reaction time
[184]	Polyethersulfone UF membrane	UV-mediated graft polymerization of [2-(Methacryloyloxy)ethyl]dimethyl-(3-sulfopropyl)ammonium hydroxide	-66%~-87% [513]	-11% MWCO [150 kDa]	-	-	Tuned with UV irradiation time. Improved fouling resistance was indicated by up to 82% reduced BSA adsorption and up to 73% reduced *P. aeruginosa* biofilm thickness
[185]	Regenerated cellulose UF membrane	Controlled surface graft polymerization of 1-allyl-3-vinylimidazolium bromide, 1-hexyl-3-vinylimidazolium bromide, and 1 butyl-3-vinylimidazolium chloride henceforth	-6%~108% [176]	75~96% BSA rejection [50%]	-	-	Investigated three types of monomer and different initiator immobilization reaction time Investigated electrical-responsive membrane performance
[186]	Polyvinylidene difluoride hollow fiber UF membrane	Electron transfer–atom transfer radical polymerization of sulfobetaine methacrylate	96%~560% [25]	-7.1% areal porosity [8%]	-3.3% one-month operation in gravity driven membrane dynamic fouling tests of sewage wastewater	-	Permeability and porosity tuned with polymerization reaction time
[187]	Porous cellulosic UF membrane	Surface-initiated atom transfer radical polymerization of *tert*-butyl acrylate and 2-hydroxy ethyl acrylate	-99%~250% [300]	79% Lysozyme rejection [18%]	-	-	Permeability and porosity tuned with polymer brush layer molecular weight
[198]	Poly(vinyl chloride) UF membrane	Surface-initiated electron transfer-atom transfer radical polymerization of [2-(methacryloyloxy) ethyl] dimethyl-(3-sulfopropyl) ammonium hydroxide	-36%~-53% [4500]	-28% average pore diameter [18 nm] 4% sodium alginate rejection [93%]	-	-	Tuned with grafting time

[188]	Regenerated cellulose UF membrane	Surface-initiated polymerization of 2-hydroxyethyl methacrylate	-	-7%~-40% MWCO [120 kDa] 5.6%~35.3% Dextran rejection [0%] 1%~37.4% BSA rejection [41%]	-	-	Investigated external and internal pore grafting Tuned with different pore filling solvents
[189]	Polyvinylidene difluoride UF membrane	Surface-initiated atom transfer radical polymerization of N-isopropylacrylamide and poly (ethylene glycol) methacrylate	43%~148% [31.4]	-0.23%~9% oil rejection [89.21%]	-13.3% 2h filtration of synthetic oily water	15% pure water	Tuned with polymerization time and monomer solution concentration
[190]	Regenerated cellulose UF membrane	Activator generated electron transfer atom transfer radical polymerization of glycidyl methacrylate	-	12%~59% BSA rejection [41%] 2%~30% dextran rejection [69%]	-	-	Tuned with grafting time and different pore filling solvents
[55]	Polyvinylidene difluoride UF membrane	Surface-initiated atom transfer radical polymerization of N-acryloyl morpholine	85%~212% [833]	-11%~-24% mean pore size [0.45 μm]	15% five cycle of 50 min oil/water emulsions	6% pure water backflush	Tuned with grafting time
[46]	Zirconia (ZrO_2)-based ceramic UF membrane	Surface-initiated free radical graft polymerization of poly(vinyl pyrrolidone)	-54% [130.7]	-	-11.5% 90 min Lysozyme fouling -24.6% 90 min BSA fouling	-	Investigated the impact of pH and ionic strength on membrane fouling performance with surface tethered polymer brush layer
[25]	Polyamide RO membrane	Surface-initiated activators regenerated electron transfer atom transfer radical polymerization of sulfobetaine methacrylate	-55.6% [2.7]	0.1% salt rejection [98.8%]	-27% 48h gypsum scaling	-	-
[191]	SW30 XLE TFC RO membrane	Activators regenerated by electron transfer–atom transfer radical polymerization of acrylamide, sulfobetaine methacrylate, and [2-(methacryloyloxy)- ethyl] trimethylammonium chloride. Redox radical graft polymerization of acrylic acid. Direct grafting of polyethylenimine and 1H,1H,2H,2H-perfluorodecanethiol.	4%~20% [2.5]	-0.6%~0.1% salt rejection [99.0%]	-3%~15% 1400 min silica scaling	-	Investigated three grafting approaches and multiple monomers
[193]	Polyamide RO membrane	UV polymerization of 2,2,3,4,4,4-Hexauorobutyl methacrylate and tobramycin	-10.8%~5.6% [3.5]	0.06%~0.1% salt rejection [98.99%]	-60% 3 cycle of 3.5h BSA fouling	48% pure water	-
[192]	Polyamide TFC RO membrane	Atom transfer radical polymerization of 3-sulfopropyl methacrylate potassium	3.5%~24.6% [5.7]	-0.9%~-2.1% salt rejection [97.6%]	-	-	Tuned with feed composition of reagents used for synthesis of polymer brush layer

[194]	Polyamide TFC RO membrane	Sequential surface treatment using acidic aqueous glutaraldehyde and monomethoxy-poly(ethylene glycol) solutions	-3.7%~-11.7% [3.0]	0.1%~0.5% salt rejection [98.1%	-15.2% 3 cycles of 20h filtration of industrial effluent	15.4% pure water	Tuned with initial monomer solution concentration
[196]	Polyamide TFC RO membrane	Combination of plasma activation, plasma bromination and surface-initiated atom transfer radical polymerization of hydroxyethyl methacrylate, 2-methacryloyloxyethyl phosphorylcholine and [2-(methacryloyloxy)ethyl]-dimethyl-(3-sulfopropyl)ammonium hydroxide	20%~45%	-	-	-	Tuned by different types of monomers
[195]	Polyamide TFC RO membrane	Surface-initiated atom transfer radical polymerization of [(2-methacryloyloxy)ethyl]dimethyl[3-sulfopropyl]ammonium hydroxide	-33.8%~-70.6% [6.8]	-1%~-3% salt rejection [97%]	-34.7%~-65.1% 20h biofouling filtration test	-	Tuned with grafting time
[49]	Polyamide TFC RO membrane	Atmospheric-pressure plasma-induced graft polymerization of acrylic acid	-40%~27% [3.37]	-1.0%~+0.8% salt rejection [98.4%]	-17% 24h BSA fouling	14% pure water	Tuned with plasma treatment and graft polymerization conditions

[a] Percentage change with a positive number indicates performance value of the modified membrane is greater than the base membrane, while a negative number indicates the opposite.

[b] Change (%) represent the change of membrane performance after modification relative to the base membrane, defined as $\Delta A=[(A_{modified}-A_{Base})/A_{Base}]\cdot 100\%$ for water permeability, pore size and solute permeability; and $\Delta A=A_{modified}-A_{Base}$ for solute rejection, fouling flux decline and permeability recovery.

[c] Water permeability coefficient L_p was evaluated with D.I. water, defined as $L_p=J_v/\Delta P$ where J_v is volumetric permeate flux and ΔP is the transmembrane pressure.

[d] Membrane selectivity is represented via membrane pore size, solute rejection, or solute permeability.

[e] Contributions of the studies other than performance alternation relative to the base membrane.

2.6 Responsive brushes

In previous studies, membrane modified with a tethered polyelectrolyte bush layer demonstrated stimuli-responsive physicochemical properties (i.e., surface charge, chemical functionality, surface hydrophilicity, electrostatic characteristics) [51, 52]. Such self-regulation of membrane permeability and selectivity via the flexible adjustment of pore sizes and surface properties allows the stimuli-responsive membranes to stand out from traditional membrane technologies [199]. The resulting stimuli-responsive smart membranes can then be used for a wide range of applications, including drug release, chiral separation, pollutants detection, graded sieving separation, biological separation, water treatment, tissue engineering, valve applications, and chemical sensors [199-202]. Self-regulated conformational changes of the tethered polymer brush layer may also influence membrane-solute affinity, and thus the feasibility of reducing membrane fouling propensity and improving membrane cleaning efficacy [52, 53].

External environmental stimuli, such as pH and ionic strength, can impact membrane properties primarily due to conformational changes of the tethered polymer brush layer (e.g., via extension/collapse of the tethered chains). For example, solution pH can trigger proton association-dissociation equilibrium (i.e., protonation and deprotonation) of the polyelectrolytes and lead to variation of charge, and thus conformational expansion and shrinkage [203]. As solution pH increases above the acidic polyelectrolytes pKa, the surface tethered polymer chains deprotonate, which further leads to chain swelling owing to electrostatic repulsion between the negatively charged segments [180]. On the other hand, under low pH conditions, protonation of the ionizable functional groups of the surface tethered polymer brush layer leads to chain deswelling (**Fig. 2-12**). In addition to electrostatic interaction, pH-responsive properties of weak polyelectrolyte brushes have also been associated with the adsorption-desorption equilibrium of hydronium or

hydroxide which leads to reorganization of the interchain hydrogen bond network [204]. Similar to solution pH, the charge screening effect of Na^+ and Cl^- ions also disrupts the electrostatic interactions among the charged polyelectrolyte chain segments [125, 181], leading to chain collapse with increasing solution ionic strength (**Fig. 2-12**). However, exceptions were reported for polyzwitterionic brushes which exhibit a strong "anti-polyelectrolyte effect" [201, 205]. Due to the presence of both positive and negative charges, zwitterionic polymer chains collapse in water and stretch in salt solutions [201, 205].

The conformational changes of tethered polymer brush layer (e.g., via extension/collapse of the tethered chains) alter membrane surface hydrophilicity. In most studies of responsive membranes, swelling of the membrane surface tethered polymer brush layer led to increased surface hydrophilicity (and thus lower membrane surface energy), and a more collapsed conformation led to the opposite effect [53, 125, 199, 206]. Such a correlation is attributed to the change of polymer solubility and/or water adsorption volume inside the polymer layer upon its conformational change [206]. Another explanation for the reversible switch of surface wettability is the entropically driven conformational change of surface tethered chains due to the changed hydrogen-bonding pattern [207].

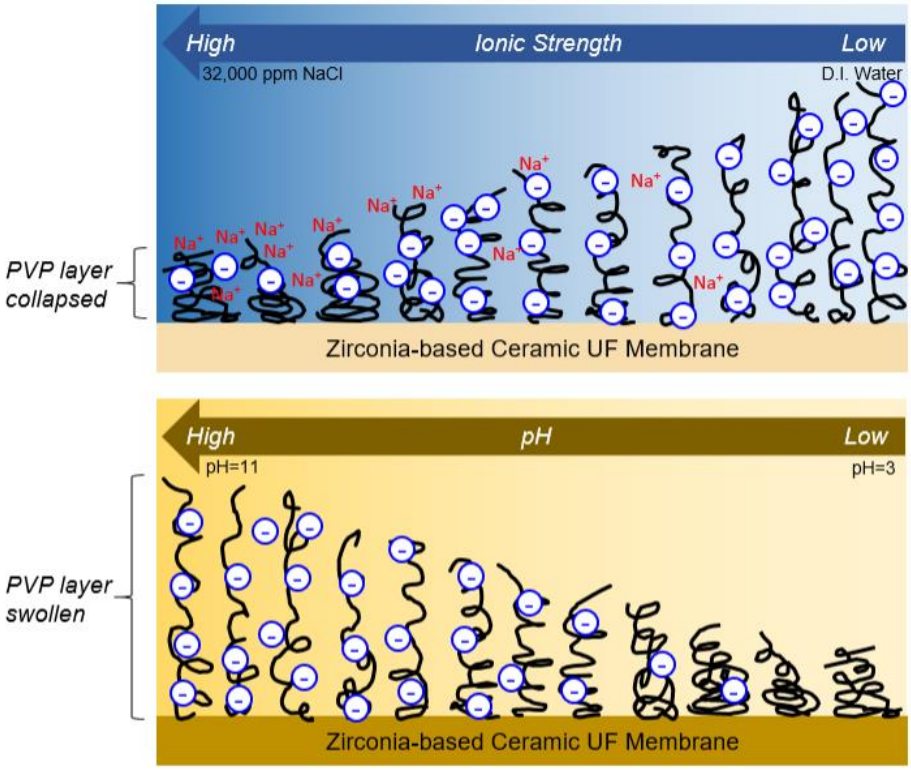

Figure 2-12. Illustration of the gradient responsive conformational change of the surface tethered poly(vinyl pyrrolidone) (PVP) chains on zirconia-based ceramic UF membrane at the range of ionic strength and pH (adapted from [46]).

More importantly, conformational changes of tethered polymer chains due to different degrees of swelling may trigger changes in membrane permeability and selectivity (**Table 2-8**). Indeed, swelling of tethered polymer brushes often correlates with increased membrane rejection but reduce permeate flux, while their collapse leads to the opposite behavior. Increased membrane rejection is at the cost of reduced membrane permeability, which is consistent with the typical membrane perm-selectivity tradeoff (**Table 2-9)**. Such alteration of porous UF membrane separation properties is attributed to the conformational change of polymer chains that are tethered onto the pore wall, hence narrowing ("close") or enlarging ("open") the membrane pores, as illustrated in **Fig. 2-13**. The stimuli-responsive polymer chains can thus act as an "on-off valve"

to regulate porous membrane permeability and selectivity, since both of these attributes are impacted by membrane pore size based on the "through-pore" mechanism [50, 145, 180, 208-217]. Consequently, for size-based membrane separation, tunable pore sizes via external environmental stimuli can serve to adjust the selectivity of a given membrane for efficient separation of target solutes of different sizes [199].

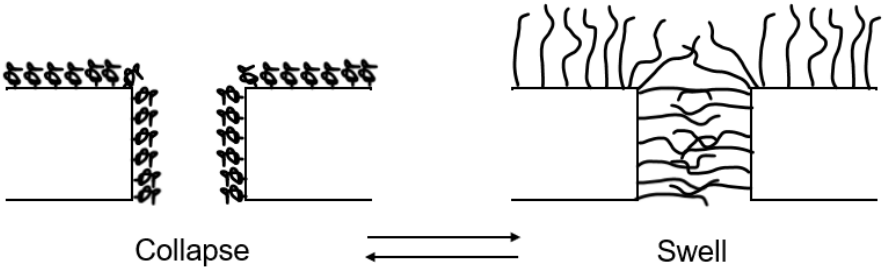

Figure 2-13. Schematic representation of the conformational change of polymer chains tethered in proximity or inside a membrane pore leading to narrowing ("close") or enlarging ("open") of the membrane pore.

Graft polymerization of methacrylic acid (MAA) onto PES using benzoyl peroxide (BPO) as a chemical initiator was reported for the synthesis of pH-responsive UF membranes [208]. The MAA grafted membranes demonstrated up to 77% decreased permeate flux (from 87 $L \cdot m^{-2} \cdot h^{-1}$ to 20 $L \cdot m^{-2} \cdot h^{-1}$) with pH increase from 2 to 10 and 8% increase of BSA rejection (from 91% to 99%) with pH increased from 4 to 8 [208]. A porous poly (vinylidene fluoride) UF membrane activated with low-pressure air plasma followed by graft polymerization of polyacrylamide (PAAm) and poly(acrylic acid) (PAA) also demonstrated permeability and solute rejection that are responsive to pH [145]. The PAA grafted membranes exhibited decreasing permeate flux from 0.31 $mL \cdot cm^{-2} \cdot min^{-1}$ to 0.03 $mL \cdot cm^{-2} \cdot min^{-1}$ and increased rejection up to 100%, during filtration of 0.1% blue dextran in citrate-phosphate buffer, as solution pH increased from 1.4 to 7.4 [145]. Phenolphthalein poly(ether sulfone) porous UF membrane grafted with a poly(methacrylic acid) layer via redox-initiated graft polymerization also demonstrated pH-responsive membrane permeability [50]. The

modified membrane showed decreased permeate flow rate (from 0.97 to 0.4 g/min) as the feed solution pH increased from 3 to 9, while the permeate water flux was practically constant (1.51 g/min) for the virgin membrane despite the pH change [50]. In another study, a polystyrene nanospheres UF membrane was surface nano-structured with spherical polyelectrolyte, poly(acrylic acid) brushes [180]. The resulting membranes exhibited decreased water flux (from 2261 to 726 $L \cdot m^{-2} \cdot h^{-1}$), and increased rejection for nanoparticles and dyes with different sizes as pH increased from 3.5 to 10.1 [180]. Poly(vinylidene fluoride-co-chlorotrifluoro-ethylene) UF membrane grafted with hydrophilic polymethacrylic acid side chains with different chain lengths enabled fractionation of nanoparticles with different sizes from the mixture using a single membrane varying solution pH [209]. The resulting membranes demonstrated decreasing pure water flux from 583.1 to 48.5 $L \cdot m^{-2} \cdot h^{-1}$ as the pH increased from 3 to 11, while membrane rejection increased from 71.6% to 90.3%, 72.8% to 96.4%, and 68.7% to 98.5% for poly(ethylene oxide) (~300 kDa), polystyrene microspheres (diameter of 20 nm), and polystyrene microspheres (diameter of 30 nm), respectively [209]. A pH-responsive UF membrane was also synthesized based on a commercial polysulfone UF membrane with the surface tethered poly(acrylic acid) brush layer via UV-initiated graft polymerization [211]. The grafted membrane demonstrated up to 26% decreased permeability coefficient as pH increased from 3 to 7 [211]. A similar trend was observed for a methacrylic acid grafted polyethersulfone UF membrane, which demonstrated up to 18.9% decreased pure water flux as pH increased from 1 to 9 [212]. In another study, end-functionalized poly(acrylic acid) was synthesized with reversible addition-fragmentation chain-transfer (RAFT) polymerization and attached to commercial polysulfone UF membranes [213]. The resulting membranes demonstrated 32.3-115% decreased pure water flux and up to 79% decreased *MWCO* as pH increased from 3 to 11 [213]. It was also shown that a commercial TFC-

PA membrane can become pH-responsive upon surface modification with a poly(acrylic acid) (PAA) brush layer, synthesized via surface-initiated atom transfer radical polymerization (SI-ATRP). The modified membranes demonstrated 20.6% permeate flux increase (from 68 $L \cdot m^{-2} \cdot h^{-1}$ to 82 $L \cdot m^{-2} \cdot h^{-1}$) as the feed solution pH decreased from 9 to 2 [51], relative to a pH-independent flux of ~72 $L \cdot m^{-2} \cdot h^{-1}$ for the base TFC-PA membrane [51]. It has been suggested that pH-responsiveness of the PAA grafted TFC-PA membrane may be due to swelling of the PAA chains at pH above their pKa (4.5, [156]), owing to electrostatic repulsion between chain segments, which can lead to increased membrane hydraulic resistance [46].

Similarly, a salt-responsive UF membrane can be achieved based on a polyethersulfone UF membrane with surface tethered zwitterionic poly(N-(3-sulfopropyl)-N-methacroyl-oxyethyl-N,N-dimethyl-ammonium betaine) and poly(2-carboxy-*N*,*N*-dimethyl-*N*-(2′-(methacryl-oyloxy)ethyl)ethan-aminium inner salt) layer synthesized via photo-initiated graft polymerization [215]. The grafted membrane exhibited decreased permeate flux with increasing electrolyte concentration for various salts (i.e., K_2SO_4, KH_2PO_4, KCl, and $KClO_4$). Among all tested salts, the most significant decrease in the grafted membrane permeate flux (by 36%) was observed for $KClO_4$ concentration increased from 0 to 125 mM [215].

Membrane stimuli-responsiveness can also be attained when multiple environmental conditions are simultaneously changed. For example, a thermo- and pH-responsive polypropylene microporous UF membrane can be prepared by photo-initiated RAFT polymerization of poly(N-isopropylacrylamide) and poly(acrylic acid) [210]. The modified membrane demonstrated decreased pure water flux (by up to 19.6% and 41.7%) as pH increased from 2 to 10 and temperature increased from 20°C to 60°C, respectively [210]. In another study, a pH- and salt-responsive porous poly(tetrafluoroethylene) UF membrane was synthesized by surface tethering

of a layer of poly(glutamic acid) [214]. The resulting membrane demonstrated decreased permeate flow rate (up to 23.5% and 13.8%) with increasing pH from 3 to 9 and decreasing NaCl ionic strength from 0.20 to 0 M [214]. Another dual-responsive UF membrane was achieved by grafting deblock copolymer (consists of PNIPAAm and poly-N,N-dimethyl-N-methacryloyloxyethyl-N-(3-sulfopropyl) ammonium betaine (PSPE)) onto a track-etched polyethylene terephthalate membranes via sequential surface-initiated atom transfer radical polymerization [216]. The modified membranes demonstrated 27% increased pore diameter (calculated based on Hagen-Poiseuille equation) with increasing temperature from 25°C to 40°C, and 22% reduced pore diameter as $KClO_4$ concentration increased from 0 to 100 mM [216].

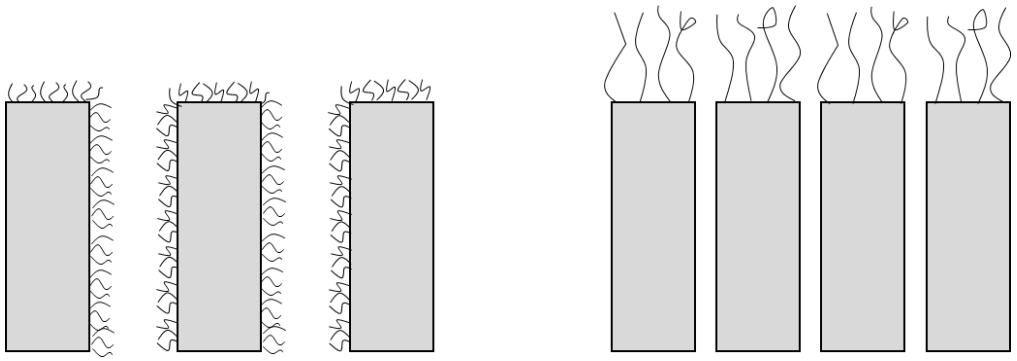

Figure 2-14. Schematic illustration of different locations of tethered polymer chains with respect to membrane pores: (a) complete tethered polymer chains coverage of the entire membrane surface (including pore), preferred for MF membranes with relatively large barrier pores (>50 nm; [218]), and (b) tethered polymer chains coverage of the external membrane surface, preferred for UF membranes with small pores (< 10 nm; [218]).

Most responsive membrane studies reported in the literature investigated the "through-pore" mechanism (**Fig. 2-13**) which is mainly observed for porous membranes (pore size >50 nm), in which polyelectrolyte chains were tethered inside the pores. Swelling of the chains triggered by environmental stimuli narrowed/blocked the membrane pores and thus led to increased membrane rejection but at the cost of reduced hydraulic permeability, consistent with the typical membrane perm-selectivity tradeoff. By contrast, the "through-polymer" mechanism of responsive membrane

is dominant for tight base membranes (pore size <10 nm) with sufficiently long surface tethered polyelectrolyte chains. In the above case there may be different effects on membrane performance via the reversible swelling/deswelling of the polymer brush layer [218], but these are largely unexplored. For example, a tubular carbon-supported ZrO_2 Carbosep M1 membrane (pore size of 6 nm) with poly(vinyl pyrrolidone) (PVP) chains, tethered mainly on membrane surface, demonstrated decreasing rejection lysozyme (Lys) from 24.4% to 0.5% as the solution pH increased from 3 to 10 [46]. In another study, a polyamide thin film composite RO membrane with surface tethered poly(acrylic acid) chains exhibited salt rejection decrease from 96% to 93% as feed solution pH increased from 3 to 11 [51]. In both cases, swelling of the surface tethered polymer chains (at basic conditions, pH>7, due to electrostatic repulsion between the chain segments), led to decreased membrane solute rejection.

The conformational changes of tethered polymer chains can also influence membrane-solute affinity, and the membrane's ability to bind and release a target compound [53]. As a result, self-regulated conformational changes of tethered polymer brush layer were also evaluated for control of surface hydrophilic/hydrophobic behavior, thus reducing membrane fouling propensity and facilitating a membrane self-cleaning ability [219, 220]. For example, a salt-responsive RO membrane was developed by grafting a zwitterionic polymer poly (4-(2-sulfoethyl)-1-(4-vinylbenzyl) pyridinium betaine) (PSVBP), via redox initiated graft polymerization, onto a commercial TFC-PA RO membrane (XLE, Filmtec Inc., USA) surface [219]. The PSVBP grafted membrane demonstrated measurable antifouling performance (~24% flux decline after 100 hr BSA solution (100 mg/L BSA and 2000 mg/L NaCl) filtration, relative to ~29% flux reduction, under the same filtration conditions, for the base TFC-PA RO membrane [219]. Membrane cleaning by alternating flushing with D.I. water and then saline solution (1.5 mg/L NaCl) of the PSVBP-grafted

and base TFC-PA membranes provided flux recovery of 90% and 75%, respectively [219]. The improvement in membrane cleaning efficacy was attributed to phase transition and conformational changes of the PSVBP brush manifested by tethered chains collapse at high salinity and swelling in D.I. water, thereby providing for the release of surface deposited foulants [219]. It was shown that tethering of three stimuli-responsive polymers, poly(sulfobetaine methacrylate) (PSBMA), poly(4-(2-Sulfoethyl)-1-(4-vinyl-benzyl) pyridinium betain) (PSVBP) and poly(N-isopropylacrylamide) (PNIPAM) onto the surface of a commercial TFC-PA RO membrane (XLE, Filmtec Inc., USA), via surface-initiated graft polymerization [220], enabled membrane responsiveness to changes in ionic strength and temperature. In the above study, the XLE membranes, modified PSBMA, PSVBP and PNIPAM, were of lower fouling propensity as indicated in BSA fouling tests (100 hr filtration with a solution of 0.1 g/L BSA and 2 g/L NaCl) that demonstrated a decline of 36%, 38%, and 40%, respectively, relative to 48% for the base XLE membrane [220]. Cleaning efficacy also improved upon switching the cleaning solution salinity from 0 g/L to 2 g/L NaCl and also periodically switching the feed temperature between 15°C and 35°C. The above cleaning approach led to flux recovery of 86.3%, 88.1% and 84.4% for the XLE membranes modified with PSBMA, PSVBP and PNIPAM, respectively, relative to only 66.3% flux recovery for the base XLE membrane [220].

Table 2-8. Summary of literature reported pH and ionic strength-responsive UF and RO membranes with surface tethered polymer brush layer.

Ref	Base Membrane	Polymer Brush	Stimuli	Responsive Properties
[208]	Polyether sulfone UF (3-25 nm pore size)	Poly(methacrylic acid)	pH	Decrease in permeate flux and increase in BSA rejection with pH
[145]	Poly (vinylidene fluoride) UF (220 nm pore size)	Polyacrylamide and poly(acrylic acid)	pH	Decrease in permeate flux and increase in dye rejection with pH
[50]	Phenolphthalein poly(ether sulfone) phase inversion porous membrane	Poly(methacrylic acid)	pH	Decrease in permeate flux with pH
[180]	Polystyrene nanospheres UF (100 nm pore size)	Poly(acrylic acid) (25-72 nm chain length)	pH	Decrease in permeate flux and increase in membrane rejection for nanoparticles and dyes with pH
[209]	Poly(vinylidene fluoride-co-chlorotrifluoro-ethylene) UF (10-36 nm pore size after grafting)	Poly(methacrylic acid)	pH	Decrease in permeate flux and increase in membrane rejection for poly(ethylene oxide) and polystyrene microspheres with pH
[210]	Polypropylene microporous membrane (100 nm pore size)	Poly(N-isopropylacrylamide) and poly(acrylic acid)	pH	Decrease in permeate flux with pH
[211]	Polysulfone UF (200 nm pore size)	Poly(acrylic acid)	pH	Decrease in membrane permeability with pH
[212]	Polyethersulfone UF	Poly(methacrylic acid)	pH	Decrease in permeate flux with pH
[213]	Polysulfone UF (10-35 nm pore size)	Poly(acrylic acid) (5-10 nm chain length)	pH	Decrease in both permeate flux and membrane molecular weight cutoff (pore size) with pH
[51]	Thin film composite polyamide RO	Poly(acrylic acid)	pH	Decrease in permeate flux and decrease in salt rejection with pH
[46]	Zirconia (ZrO2)-based ceramic UF (6 nm pore size)	Poly(vinyl pyrrolidone)	pH	Decrease in permeate flux and decrease in lysozyme rejection with pH

[214]	Porous poly(tetrafluoroethylene) membrane (100 nm pore size)	Poly(glutamic acid)	pH and ionic strength	Decrease in permeate flux with pH, and increase in permeate flux with ionic strength
[215]	Polyethersulfone UF (8 nm pore size)	Zwitterionic poly(N-(3-sulfopropyl)-N-methacroyl-oxyethyl-N,N-dimethyl-ammonium betaine) and poly(2-carboxy-*N*,*N*-dimethyl-*N*-(2′-(methacryl-oyloxy)ethyl)ethan-aminium inner salt)	Ionic strength	Decrease in permeate flux with ionic strength
[216]	Track-etched polyethylene terephthalate UF (110 nm pore size)	Poly(N-isopropylacrylamide) and zwitterionic poly-N,N-dimethyl-N-methacryloyloxyethyl-N-(3-sulfopropyl) ammonium betaine	Ionic strength	Decrease in pore diameter with $KClO_4$ concentration
[219]	Thin film composite polyamide RO	Poly (4-(2-sulfoethyl)-1-(4-vinylbenzyl) pyridinium betaine)	Ionic strength	Increased cleaning efficacy by alternating flushing with D.I. and saline water
[220]	Thin film composite polyamide RO	Poly(sulfobetaine methacrylate), poly(4-(2-Sulfoethyl)-1-(4-vinyl-benzyl) pyridinium betain) and poly(N-isopropylacrylamide)	Ionic strength	Increased cleaning efficacy by alternating flushing with different cleaning solution salinity

Table 2-9. Summary of literature reported explanations of pH and ionic strength-responsive membrane performance.

Change of environmental stimuli	**Change of membrane performance**	**Explanation**	**Ref**
Membranes with surface tethered polymer brush layers			
↑ pH	↑ Membrane permeability	Through-polymer mechanism: water diffuses through the interstices between swollen ionized polymer chains	[214, 221]
	↓ Membrane permeability	Through-pore mechanism: swelling of the polymer chains blocks/narrows the pores.	[46, 50, 51, 145, 180, 208-214]
	↑ Membrane rejection	Through-pore mechanism: swelling of the polymer chains blocks/narrows the pores.	[145, 180, 208, 209, 213]
	↓ Membrane rejection	There is no competition between sodium and hydrogen ions (the hydrogen ions have a greater charge-to-mass ratio and are more mobile compared to sodium ions)	[51]
↑ Ionic strength	↑ Membrane permeability	Through-pore mechanism: collapse of the polymer chains opens up the pores.	[214]
	↓ Membrane permeability	Through-pore mechanism: swelling of the polyzwitterionic chains blocks/narrows the pores.	[215]
	↑ Membrane rejection	Through-pore mechanism: swelling of the polyzwitterionic chains blocks/narrows the pores.	[216]
Base/commercial membranes			
↑ pH	↓ Membrane permeability	Decreased pore size due to conformational changes of the cross-linked membrane polymer structure.	[222]
		Decrease in electro-viscous effects.	[222]
	↑ Membrane rejection	Increased membrane surface charge density led to an	[13, 223-225]

		enhanced electrostatic interaction with charged solutes.	
↑ Ionic strength	↓ Membrane permeability	Increasing impact of the osmotic pressure difference across the membrane.	[226]
	↓ Membrane rejection	Charge screening by salt ions led to weakened Donnan potential.	[226-228]
		Pore swelling (i.e., increase in mean pore radius due to repulsion forces between counterions inside pores).	[228-233]
		Salting-out effect: partial dehydration of neutral organic solute size.	[228, 230-232, 234]
		Increase in mean pore size due to thinning of the hydration layer at the pore surface.	[228, 230]
		Stronger reduction of permeate flux through small pores, as compared with larger pores, leading to more solutes passing through larger pores.	[228, 233]
		Opening of membrane pores due to compression of the electrical double layer formed at the membrane surface.	[228, 235]
		Increased effective membrane thickness due to collisions between ions and neutral solutes, which would lengthen the moving path of solutes.	[228, 230]
		Change in molecular polarity of solutes.	[228, 235]

2.7 Summary

Despite the rapid growth of membrane-based desalination technology, there are still challenges in RO and UF process that limit further process efficiency improvement and cost reduction. The primary challenges include the barrier imposed by the permeability-selectivity tradeoff, need for removal of specific contaminants, and membrane fouling and scaling. Among the various surface modification approaches for improving membrane performance, membrane surface tethering with a hydrophilic polymer brush layer was shown to be a long-lasting, cost-efficient, and convenient approach to tailor membrane surface characteristics, tune membrane performance, and mitigate membrane fouling and scaling. Consequently, over the past few decades, extensive efforts have been devoted to investigate the impact of surface tethered polymer brush layers on membrane properties and performance. Namely, tailoring of membrane surface characteristics and tuning membrane performance can be achieved by manipulation of the polymer brush layer structures. For example, polymer brush layer density and thickness can be tuned by initiator immobilization and graft polymerization time, and initiator and monomer concentrations. However, there are still research areas that are less explored that require more comprehensive investigations that include, but are not limited to:

- The correlation between the structure of the surface tethered polymer brushes and the resulting modified membrane properties and performance;
- Systematic tailoring of membrane surface characteristics and membrane performance to overcome the typical perm-selectivity tradeoff;
- Impact of surface tethered polymer brush layers on RO membrane removal of specific contaminants and mineral scaling; and

- Effective scale-up of membrane surface modification approaches and fabrication of commercial-scale spiral-wound elements

Chapter 3 Modification of PSf membranes via AA Surface Graft Polymerization induced by Surface Activation with atmospheric pressure Air, He/O_2 and He plasmas

3.1 Overview

Polymeric ultrafiltration (UF) membranes are increasingly utilized for selective separations of suspended solids, colloids, emulsions, natural organic matters, macromolecules, bacteria, and viruses [40, 62]. Polysulfone (PSf) and its variants are widely used polymers for the synthesis of UF membrane due to their good thermal and chemical stability [236]. However, commercially available PSf UF membranes are typically limited in terms of the available ranges of membrane permeability and molecular weight cutoff (*MWCO*), and thus lack membrane selection for sharp separation tasks. Also, a major challenge is membrane fouling which leads to a decreased membrane flux, deterioration of membrane structure, and increased energy and maintenance costs [40, 42, 62]. Membrane separation properties and fouling characteristics are directly attributed to membrane surface characteristics (e.g., surface chemistry, charge, topography, porosity, and hydrophilicity) [40-42]. Thus, membrane surface modification has been pursued to both mitigate membrane fouling propensity and tune membrane performance [146, 156, 237-239].

Among the various UF membrane surface modification approaches, plasma surface treatment, generated based on various gases (e.g., helium, argon, nitrogen, hydrogen, oxygen, ammonia, nitrous oxide, carbon dioxide, water, and tetrafluoromethane [140]), has been increasingly explored for: (i) direct surface functionalization (e.g., implantation of hydrophilic OH, C-O, N-H_3, and C-O_x groups), (ii) creation of surface active group (e.g., peroxides) for subsequent polymer grafting or graft polymerization [240], and (iii) altering surface roughness [241, 242]. In contrast with plasma, which is based on more costly purified gases (e.g., He, Ar, O_2, CO_2), there has been

an interest in using air-based low-pressure [41, 140, 142-145] and corona discharge [40, 42, 62, 146-151]; the latter relying on ambient air at atmospheric pressure.

In the present work, the use of impinging atmospheric pressure Air plasma source (Air APP) is introduced, for the first time, for UF membrane surface activation to induce subsequent acrylic acid (AA) graft polymerization. Utilization of the lower-cost Air APP for surface activation, if effective, would be beneficial given the potential scalability of the approach.

The effectiveness of Air APP for PSf surface activation was first assessed for surrogate PSf membrane surfaces for surface activation to induce free-radical AA graft polymerization [149] relative to the use of He and He/O_2 APP. The impacts of both plasma surface treatment and AA graft polymerization were then evaluated with respect to changes in surface oxygen composition, surface hydrophilicity, surface topography, and surface zeta potential.

3.2 Experimental

3.2.1 Materials

PSf membrane (MUF-20K, Toray Membrane USA Inc., Poway, CA) with manufacturer reported 100 kDa *MWCO* was selected as the base membrane for surface nano-structuring (SNS) with tethered PAA layer. Also, a commercial PSf membrane (MUF-10K, Toray Membrane USA Inc., Poway, CA) was used for performance comparison. Both of the above membranes were obtained as flat sheets. Helium (99.999%) and oxygen (99.999%) gases (Airgas, Los Angeles, CA) were utilized for PSf surface plasma treatment, prior to graft polymerization, and nitrogen (99%) gas (Airgas, Los Angeles, CA) was used for PSf sample drying, graft polymerization degassing, and UF system feed tank pressurizing. Acrylic acid (99%, Sigma-Aldrich, St. Louis, MO) was the

hydrophilic monomer used for graft polymerization to form poly(acrylic acid) chains tethered onto the PSf surfaces, post-activation with atmospheric pressure plasma.

Relatively smooth surrogate PSf membrane surfaces were synthesized onto prime grade 4″ silicon ⟨100⟩ wafers to assess the impact of the tethered chains on surface topography. The wafers were first cleaned with sulfuric acid (96%) and aqueous hydrogen peroxide (30%) (KMG Electronic Chemicals, Inc., Houston, TX). A poly(ethyleneimine) (PEI, *Mw*~750,000) solution (50 wt% in H_2O, Sigma-Aldrich, St. Louis, MO) was spin coated onto the cleaned silicon wafer to form an adhesion layer. Immediately afterward, a solution of 0.25 wt% PSf (prepared using pellets of *Mw*~35,000; Sigma-Aldrich, St. Louis, MO) in chloroform (≥99.9%, Sigma-Aldrich, St. Louis, MO) was spin coated onto the PEI adhesion layer to form a PSf surface for nano-scale surface topography characterizations.

Membrane surface zeta potential measurements were conducted with a 0.001 M potassium chloride (Sigma-Aldrich, St. Louis, MO) aqueous solution with pH adjustment using 0.05 M hydrochloric acid and sodium hydroxide solutions (Fisher Scientific, Chino, CA). All solutions were prepared in D.I. water produced with a Milli-Q filtration system (Millipore Corp., San Jose, CA).

3.2.2 Preparation of PSf surrogate membrane surfaces

PSf surfaces on silicon wafer substrates were prepared following a previously established protocol [156] to create a smooth model PSf-PEI-Si membrane surface. Briefly, silicon wafers were prepared as 2 cm × 2 cm samples and then cleaned in a piranha solution (an aqueous mixture of 70 vol% sulfuric acid and 30 vol% hydrogen peroxide) at 90°C for 10 min to remove organic residues, followed by five cycles of D.I. water rinsing. Prior to PEI spin coating, each wafer sample

was washed with isopropanol and then D.I. water, followed by nitrogen blow drying. A 0.1 mL of 0.3 wt% aqueous PEI solution was dispensed onto the silicon substrate center, and the PEI adhesion layer (~2 nm) was formed by spin-coating (using a 790 Spinner with PWM32 controller, Headway Research Inc., Garland, TX) at 2500 rpm for 30 s. Subsequently, ~0.3 mL solution of 0.25 wt% PSf in chloroform was spin-coated (2500 rpm for 30 s) onto the PEI-Si surface. The PSf-PEI-Si surrogate membrane surface was then dried in a vacuum oven at 40°C for 24 h prior to further use.

3.2.3 Atmospheric pressure plasma-induced graft polymerization (APPIGP)

The tethered PAA layer was synthesized onto PSf surfaces via APPIGP PSf surface modification approach (**Appendix C**), which proceeds via the following sequential steps: (1) surface atmospheric pressure plasma treatment to generate free radicals on the substrate surface, (2) exposure of surface radicals to ambient air, when using He or He/O_2 plasma, to create peroxide groups (–O-O· or –O-O-H), and (3) thermal decomposition of peroxide bonds (O-O) that initiates acrylic acid free-radical graft polymerization (**Fig. 3-1**). This APPIGP process results in PAA chains that are covalently end-attached (tethered) to the PSf surface [156].

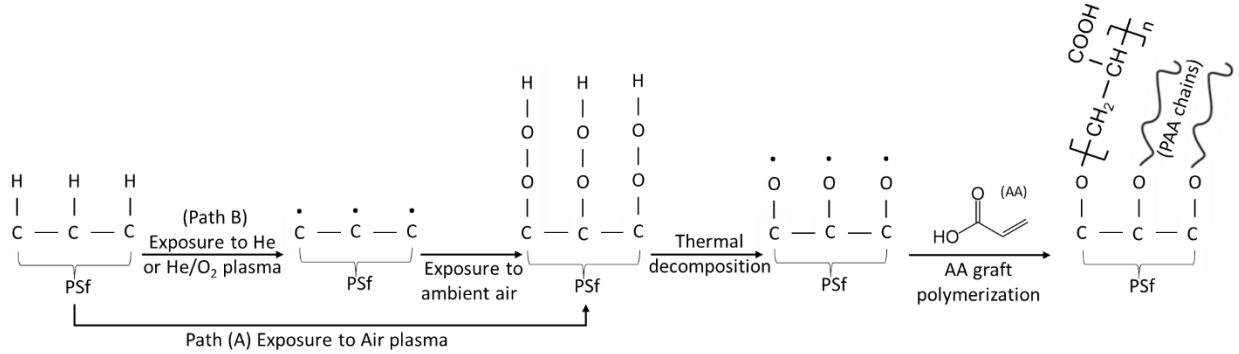

Figure 3-1. Schematics of the APPIGP process mechanisms where Path A designates surface treatment with Air APP and Path B is for surface treatment with either He or He/O_2 plasma.

Prior to surface activation, the PSf-PEI-Si surfaces were dried in a vacuum oven for a period of about 24 h. PSf surface activation was accomplished via atmospheric pressure plasma being either He, He/O_2 or Air plasma (**Table 3-1**). Atmospheric pressure Air plasma was dispensed via FG5001 Plasma Generator (Plasmatreat USA, Inc., Elgin, IL) operating with the frequency of 21 kHz, voltage of 280 V, and Plasma Cycle Time (PCT) of 100%. Atmospheric pressure plasma helium (He) and helium/oxygen (He/O_2) plasmas were dispensed via Atomflo™ 500 (Surfx Technologies Inc., Redondo Beach, CA) at the source gas flow rates of 45 L/min and 0.5 mL/min for He and O_2 gases, respectively, and RF power of 150 W. The plasma was discharged via dispensing jets installed on an XYZ scanning robot (Surfx Technologies Inc., Redondo Beach, CA). Surface activation was accomplished via 1-3 sequential plasma scans (*N*) at a speed of 100 mm/s and source-surface separation (*PSS*) distance in the range of 5-15 mm.

Table 3-1. Summary of plasmas properties information

Properties*	**Air Plasma**	**He/O_2 Plasma**	**He Plasma**
Gas supply composition	Compressed air	99% He + 1% O_2	100% He
Temperature in plasma (°C)	43-69°C	53-75°C	53-75°C
Percentage of gas ionized in plasma	1.0%	0.00001%	0.00001%
Reactive species in exit gas flow	Neutrals, ions and electrons	Neutrals	Neutrals

*Information provided by Surfx Technologies Inc.

Following APP activation, the PSf-PEI-Si substrates were immersed in aqueous AA monomer solutions ($[M]_o$ ~20 vol%) in 250 mL capped glass vials immersed in a constant temperature water bath at 70°C for 60 min. Nitrogen was bubbled into the reaction vials (via tubes inserted through the sealed vial caps) during graft polymerization to promote mixing and scavenge dissolved oxygen that could inhibit the graft polymerization reaction [156]. After the graft polymerization,

the PAA-PSf-PEI-Si surfaces were rinsed with D.I. water to remove unreacted species, and then dried in a vacuum oven at 40°C for 24 h prior to further surface characterization (**Sections 3.2.4.1-3.2.4.3**).

The two-step graft polymerization process was also carried out employing surface activation via Air APP for the synthesis of a tethered PAA layer onto a base PSf membrane (MUF-20K). The base membrane coupons were, kept in D.I. water for at least 24 h, and then thoroughly rinsed with D.I. water, and subsequently dried via an impinging nitrogen stream prior to surface activation with atmospheric pressure Air plasma. Following plasma activation, surface graft polymerization proceeded as per the protocol for the PSf-PEI-Si substrates. The resulting SNS-PAA-PSf membranes were kept in D.I. water for at least a 24 h period prior to their characterization.

3.2.4 Surface characterization

3.2.4.1 Surface chemistry

The surface atomic composition of the plasma treated and graft polymerized PSf surfaces was analyzed via X-ray photoelectron spectroscopy (XPS) performed using a Kratos Axis Ultra DLD (Kratos Analytical, Manchester, UK) with a monochromatic Al Kα source. High-resolution C 1s and O 1s spectra were obtained for the native and plasma treated PSf-PEI-Si surfaces. Survey scan and high-resolution C 1s spectra were obtained for both the native PSf-PEI-Si and PAA-PSf-PEI-Si surfaces activated with Air, He/O_2, and He APP and following AA graft polymerization. Survey XPS spectra were obtained by sweeping over 0–1000 eV electron binding energy with a resolution of 1 eV to obtain the surface atomic composition. Each of the survey spectra was the average of five survey scans with at least 6 replicates were performed for each membrane type. High resolution scans were obtained by averaging 20 scans (per replicate measurement) for C 1s peak

from 282 to 292 eV and O 1s peak from 526 to 538 eV with a resolution of 0.1 eV to characterize the composition of specific functional groups. The high resolution XPS spectra were subtracted by the Shirley-type background. Gaussian-Lorentz peak deconvolution was performed to estimate the binding energy shift of C 1s and O 1s. The specific XPS peak areas for the C 1s and O 1s scans were calculated via Casa peak fitting function. The peak area percentage was then used to quantify the relative presence of the specific functional group.

3.2.4.2 Surface topography

The surface roughness of PSf UF membrane is typically in the range of ~(24-44 nm; [243]) which is significantly greater relative to both the expected average tethered layer feature height (~3-10 nm) and its surface roughness (0.7-3 nm; [156]). Thus, in order to assess its local topography, the tethered PAA layer was synthesized onto a smooth PSf layer that was casted on a smooth silicon wafer substrate (**Section 3.2.2-3.2.3**). The native, plasma treated, and AA graft polymerized PSf surrogate membrane surfaces were then characterized via AFM, using a Bruker Dimension Icon Scanning Probe Microscope (Bruker, Santa Barbara, CA), as per a previously described protocol [156]. Briefly, the PSf-PEI-Si surfaces were immersed in D.I. water for 30 min to allow for equilibration prior to AFM characterizations using AFM probes (ScanAsyst-Fluid+, Bruker, Santa Barbara, CA) in Mechanical Force Tapping mode [244]. AFM topography was carried out, in D.I. water, for 1 μm×1 μm regions at 512×512-pixel resolutions, at a probe loading force ~1 nN and scan rates of 0.8 Hz. The root-mean-square surface roughness (R_{rms}) was determined from the AFM feature height (FH) data as $R_{rms} = \sqrt{\sum_i^N (Z_i - Z_{avg})^2 / N}$, where Z_i is the FH of the i^{th} data point, N is the total number of data points within the scanned area (1 μm×1 μm), and Z_{avg} is the average FH. Cross-sectional FH profiles were obtained from the FH data over

a 1 μm line across the surface. The tethered PAA layer dry thickness was determined from the AFM cross-sectional height profile in air, as per the protocol summarized below.

The PAA-PSf-PEI-Si surfaces were first scratched manually using a sharp metal needle to form multiple random and parallel scratches following previously described protocol [245] to expose the underlying silicon substrate. The scratched region was then scanned by AFM in air over an area of 10 μm × 10 μm at a scan rate of 1 Hz at 1 nN peak force. The layer thickness was then determined from the AFM cross-sectional height profile, indicated by the distance between two parallel lines representing silicon wafer surface and polymer layer surface (**Fig. 3-2**).

At least five replicates were performed for each thickness measurement to assess the possibility of local membrane surface heterogeneities. The total layer thickness for the PAA-PSf-PEI-Si surface was taken as the sum of the tethered PAA layer thickness and the PSf layer thickness. To specifically determine the tethered PAA layer thickness, the PSf layer thickness was measured by repeating the previous layer thickness measuring steps for the PSf-PEI-Si surface after APP surface treatment. Accordingly, the tethered PAA layer thickness was determined from $t_{PAA} = t_T - t_{PSf}$, where t_{PAA} is the tethered PAA layer thickness, t_T is the total layer thickness, and t_{PSf} is the polysulfone layer thickness.

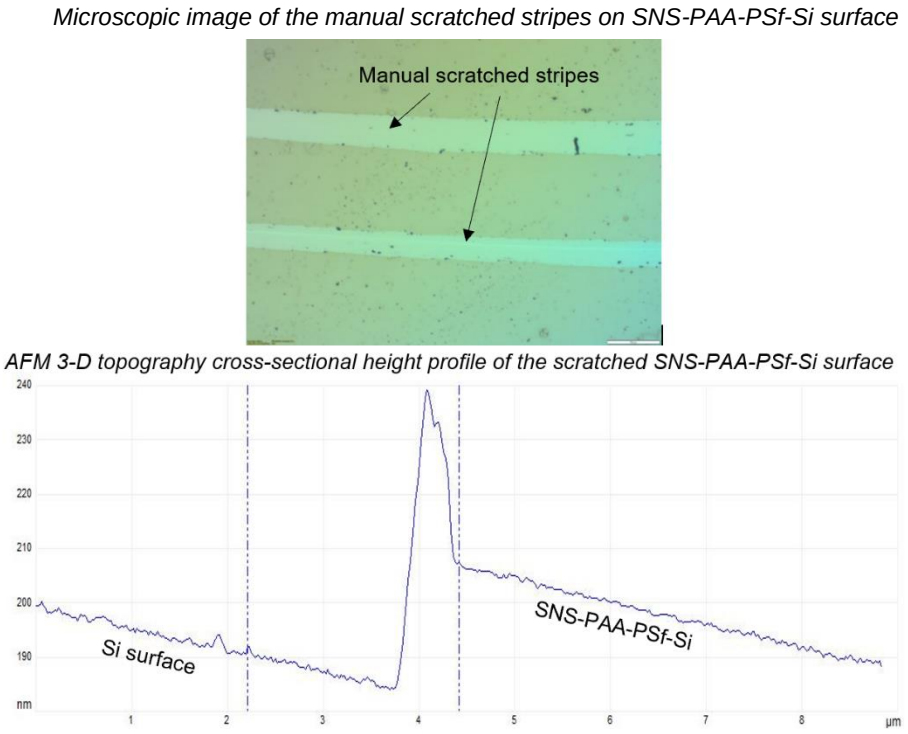

Figure 3-2. Manually scratched stripes of SNS-PAA-PSf-Si (top), and AFM 3-D topography cross-sectional height profile of the scratched area (bottom).

3.2.4.3 Surface hydrophilicity

Surface wettability of both the PSf membrane and PSf-PEI-Si surfaces was evaluated by sessile drop (SD) water contact angle measurements (θ) using an automated analyzer (DSA20; KRÜSS GmbH, Germany) [156]. SD water contact angle measurements were taken (at ~20°C) within 2 s following placement of a 1 µL D.I. water drop onto sample surfaces. The reported contact angles represent values averaged over measurements from at least 5 locations for each sample. The surface free energy of hydration (ΔG_{iw}) was then calculated using the Young-Dupré equation, $\Delta G_{iw} = -\gamma_w(1+\cos\theta_w)$, where γ_w is the surface energy of liquid water and θ_w is the water contact angle. It is noted that surfaces are typically considered to be hydrophilic when ΔG_{iw} < -113 mJ/m^2, and hydrophobic with ΔG_{iw} > -113 mJ/m^2 [246].

3.2.4.4 Surface zeta potential

Membrane surface charge was quantified using the SurPASS Electrokinetic Analyzer (Anton Paar GmbH, Graz, Austria) at ~20°C following a standard protocol (**Appendix B**). Zeta potential measurements were initially done at a 0.001 M potassium chloride solution at neutral pH, followed by titration with a 0.05 M NaOH solution incrementally increasing the pH from neutral to ~10 [247]. Subsequently, the zeta potential was determined in a 0.001 M KCl solution gradually decreasing the pH from 10 to 3 using 0.05 M HCl. The isoelectric point (i.e., pH at which surface charge is zero) was determined by the acquired zeta potential versus pH curves.

3.3 Results and Discussion

3.3.1 PSf surface functionalization

Effective free-radical graft polymerization of the polymeric surface requires the introduction of surface active groups via plasma surface treatment [248]. Of the three plasma types used in the present work, exposure of the PSf surface to Air plasma (containing 21% oxygen in its source air gas) has been reported to lead to the direct formation of surface peroxide groups [249]. The peroxide groups can then serve as the active groups to initiate AA graft polymerization [249, 250]. In contrast with the Air plasma, the He/O_2 plasma was produced with a gas stream containing only 1 vol% oxygen, while He plasma source gas is devoid of oxygen. However, once the He or He/O_2 plasmas treated PSf surface is exposed to air, conversion of surface radicals to peroxide groups can ensue [248]. Indeed, as shown by the XPS C 1s scan (characterizing the C-O, C-S, and C-C bonds), surface active sites were introduced to the PSf-PEI-Si surfaces post-treatment with Air, He/O_2, and He plasmas, as revealed by the increased presence of C-O bond by up to 20.3%, 2.6%,

and 2.3%, respectively; correspondingly, the presence of C-C bond decreased by 19.2%, 1.6%, and 2.1% (**Table 3-2** and **Fig. A-1, Appendix A**). Similarly, the XPS O 1s scan, characterizing C-O and O=S=O bonds, revealed the increased presence of C-O (by 6.6-39.5%) for all the three plasmas (i.e., Air, He/O_2, and He) treated PSf surfaces, which was also accompanied by decreased O=S=O presence of 6.6-39.5% (**Table 3-2**). Not surprisingly, the oxygen-containing active sites introduced onto the PSf-PEI-Si surfaces post-plasma treatment led to increased surface oxygen content. Indeed, the PSf surfaces treated with Air, He/O_2 and He plasmas revealed increased oxygen-to-carbon (O/C) ratio by 5.9%, 1.0%, and 0.2%, respectively (**Table 3-3**, **Figs. A-2** and **A-4, Appendix A**). The maximum increase of oxygen presence on the PSf surface was post-Air APP treatment. This result is plausibly due to the greater abundance of ionized oxygen species generated in the Air APP that are capable of oxidizing the PSf surface [251-253]. It is also argued that the decreased presence of C-C and O=S=O could be due to backbone breakage of the native PSf bulk material which has been reported to result from surface etching [249, 254]. Indeed, characterization of the Air APP treated PSf surface indicated a decrease in the presence of C-C and O=S=O by 19.2% and 39.5%, respectively (**Table 3-2**), relative to the native PSf surface. Correspondingly, the presence of C-C and O=S=O decreased by a lower percentage of 1.6%, 8.4% and 2.1%, 6.6% for the He/O_2 and He plasmas, respectively. SEM images of the different plasma treated PSf surfaces revealed dark streaks that could be indicative of surface etching, which was more pronounced for the Air plasma **(Fig. A-3, Appendix A**). Membrane performance characterization (**Chapter 5**), however, did not reveal deterioration of membrane performance presumably since plasma etching was restricted to the immediate upper PSf layer.

Table 3-2. XPS spectra of C 1s and O 1s scan peak area (%) for the native PSf-PEI-Si surface, and PSf surfaces treated with Air, He/O_2, and He plasmas [(a)].

Plasma	C 1s scan [(b)]			O 1s scan [I]	
	C-C	C-S	C-O	O=S=O	C-O
(Native)	82.17	5.90	11.93	53.16	46.84
Air APP	62.98	4.78	32.24	13.69	86.31
He/O_2 APP	79.58	5.96	14.46	44.79	55.21
He APP	80.09	5.75	14.16	46.64	53.36

[(a)] Plasma treatment was at a plasma source-substrate separation distance (PSS) of 10 mm, and one surface scan (N = 1).
[(b)] Peaks in C 1s spectra at 285 eV, 285.4 eV, 285.6 eV, 286.6 eV, and 289.2 eV correspond to aromatic/aliphatic carbons, C-C=O, C-S, C-O, and carboxylic acid groups, respectively [255].
[I] Peaks in O 1s spectra at 531.9 eV and 533.2 eV corresponds to O=S=O and C-O groups, respectively [255].

Table 3-3. The surface elemental atomic composition of PSf surfaces after plasma treatment with Air, He/O_2, and He plasmas and post-AA graft polymerization [(a)].

Plasma	PSf-PEI-Si				PAA-PSf-PEI-Si			
	C (%)	O (%)	S (%)	O/C (%)	C (%)	O (%)	S (%)	O/C (%)
(Native)	86.36	10.14	3.50	11.74	-	-	-	-
Air	82.15	14.46	3.39	17.60	81.15	16.02	2.83	19.74
He/O_2	85.57	10.88	3.55	12.71	79.46	18.14	2.40	22.83
He	86.25	10.24	3.51	11.87	81.72	16.03	2.55	19.62

[(a)] Plasma treatment was at a plasma source-substrate separation distance (PSS) of 10 mm, and one surface scan (N = 1). AA graft polymerization conditions: $[M]_o$ = 20 vol%, 70 °C, 1 h.

PSf surface treatment with Air plasma resulted in the greatest increase in surface oxygen composition relative to the He/O_2 and He plasmas. Thus, one would be tempted to expect a higher number density of tethered PAA chains on the PSf surface for AA graft polymerization post-Air plasma surface activation. Accordingly, a higher O/C ratio should be expected for the tethered PAA surface synthesized post-Air plasma surface activation. However, XPS surface

characterization showed that the O/C ratio rise post AA graft polymerization for the PSf surface treated with Air plasma was the lowest (2.1%) compared to 7.7% and 10.1% rise for the PAA surfaces synthesized post-surface activation with He and He/O_2 plasmas, respectively (**Table 3-3**, **Figs. A-2** and **A-4, Appendix A**). It is also noted that carboxylic acid and C-C=O groups were absent on the native PSf surface, but present after AA graft polymerization (**Fig. A-2, Appendix A**). The carboxylic acid group presence (0.6%) after AA graft polymerization of the PSf surface (post-activation with Air plasma) was 83.3% and 92.0% lower relative to PAA surfaces synthesized post-activation with He and He/O_2 plasmas, respectively (**Fig. A-2, Appendix A**).

The rise of both the O/C ratio and carboxylic acid group presence post-AA graft polymerization was the lowest for PAA layer formed post-Air plasma PSf surface activation; this despite the greater presence of oxygen-containing groups (relative to the other two plasmas) after surface treatment with Air APP. Thus, it is reasonable to surmise that not all the implanted oxygen-containing functional groups introduced by Air plasma were effective in inducing AA graft polymerization. Indeed, studies have shown that Air plasma treatment of polymeric surfaces (e.g., polypropylene hollow fiber microporous membrane [140], polyether sulfone (PES) UF membrane [62], and PES MF membrane [42]) can introduce various oxygen-containing functional groups (e.g., hydroxide, aldehyde, ketone, acid, and ester groups) [42, 62, 140, 249, 256, 257] other than the desired peroxides that are effective for initiating free-radical polymerization.

3.3.2 PSf surface topography

Surface roughness of the plasma treated PSf surface and average major peak separations distance increased by 100%, 24%, 39%, and 146%, 88%, 47%, respectively, upon surface treatment with the Air, He/O_2 and He plasmas. The average feature height (FH) remained essentially unchanged for the He plasma treated PSf surface, but increased by 112% and 26% for

the Air and He/O_2 plasma treated PSf surfaces, respectively. The above trend is consistent with a greater degree of Air plasma surface etching and implantation of oxygen-containing surface groups (**Section 3.3.1**) onto the PSf surfaces. Indeed, previous studies have reported aggressive surface etching [258-260] by plasma surface treatment, consistent with the observation of greater PSf surface roughness and average FH for the Air APP treated surface relative to the surfaces treated by the other two plasmas (**Fig. 3-3** and **Table 3-4**). Additional surface characterization data for the plasma treated PSf surfaces is provided in **Fig. 3-4** and **Fig. A-6, Appendix**.

Table 3-4. Surface roughness and average FH for the native PSf-PEI-Si and PAA-PSf-PEI-Si surfaces activated with Air, He/O_2 and He plasmas.

Plasma	PSf-PEI-Si			PAA-PSf-PEI-Si		
	Roughness (nm)	Average Feature Height (nm)	Average Major Peak[b] Separation Distance (nm)	Roughness (nm)	Average Feature Height (nm)	Average Major Peak Separation Distance (nm)
(Native)	0.33	1.80	17.3			
Air	0.66	3.82	42.5	1.26	4.91	54.1
He/O_2	0.41	2.26	32.6	0.73	2.81	20.6
He	0.46	1.79	25.4	1.26	4.81	63.9

[a] Plasma treatment conditions: *PSS* =10 mm, N = 1; Graft polymerization: $[M]_o$ = 20 vol%, 70 °C, 1 h); [b] Major peaks were taken to be at least 1/3 of the maximum peak height of the distribution [55];

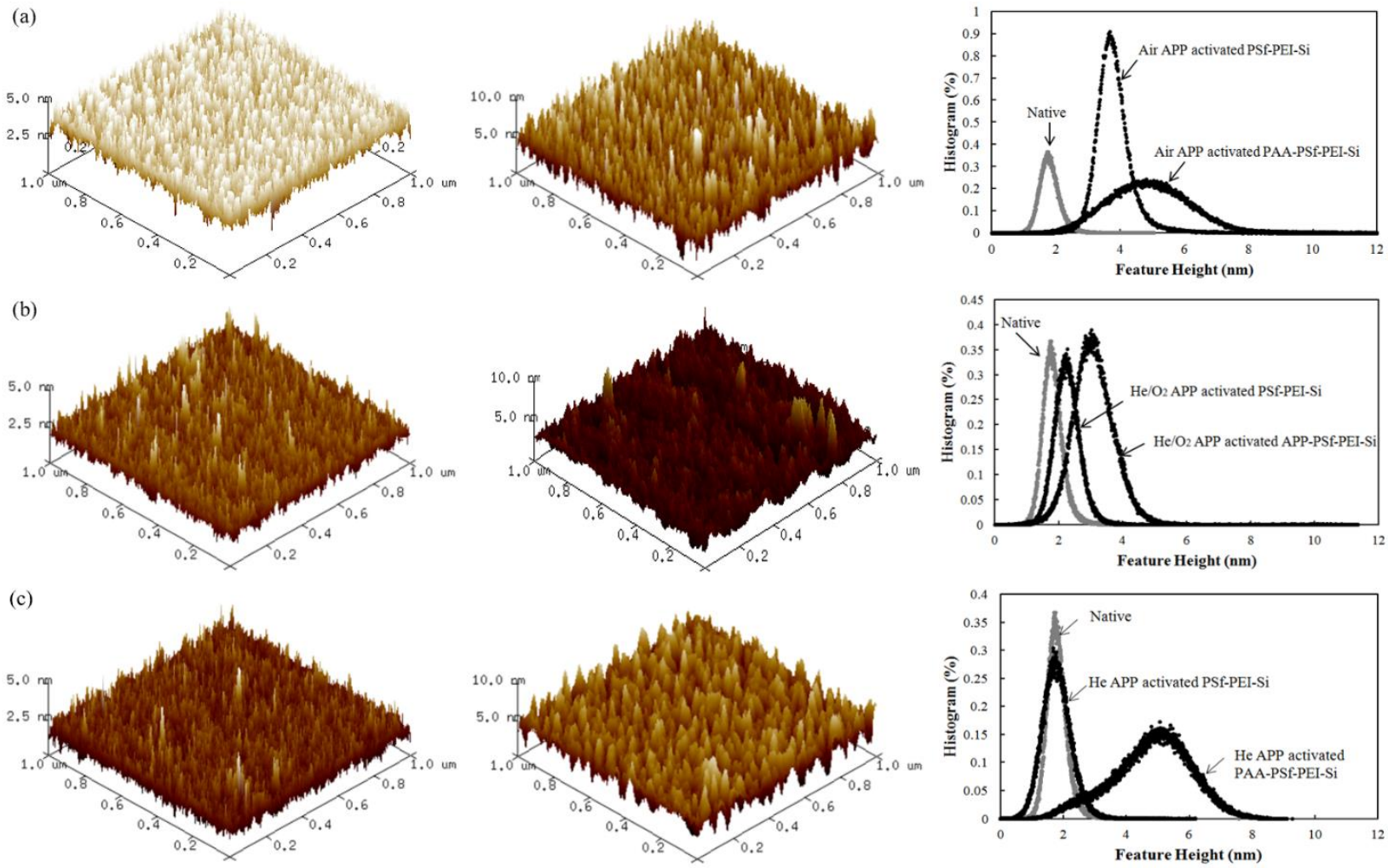

Figure 3-3. AFM 3-D topography for plasma treated PSf-PEI-Si surfaces (in D.I. water): (left), PAA-PSf-PEI-Si surfaces activated with plasma treatment followed by AA graft polymerization (middle), and the respective FH distributions (right) for (a) Air, (b) He/O_2, and (c) He APP.

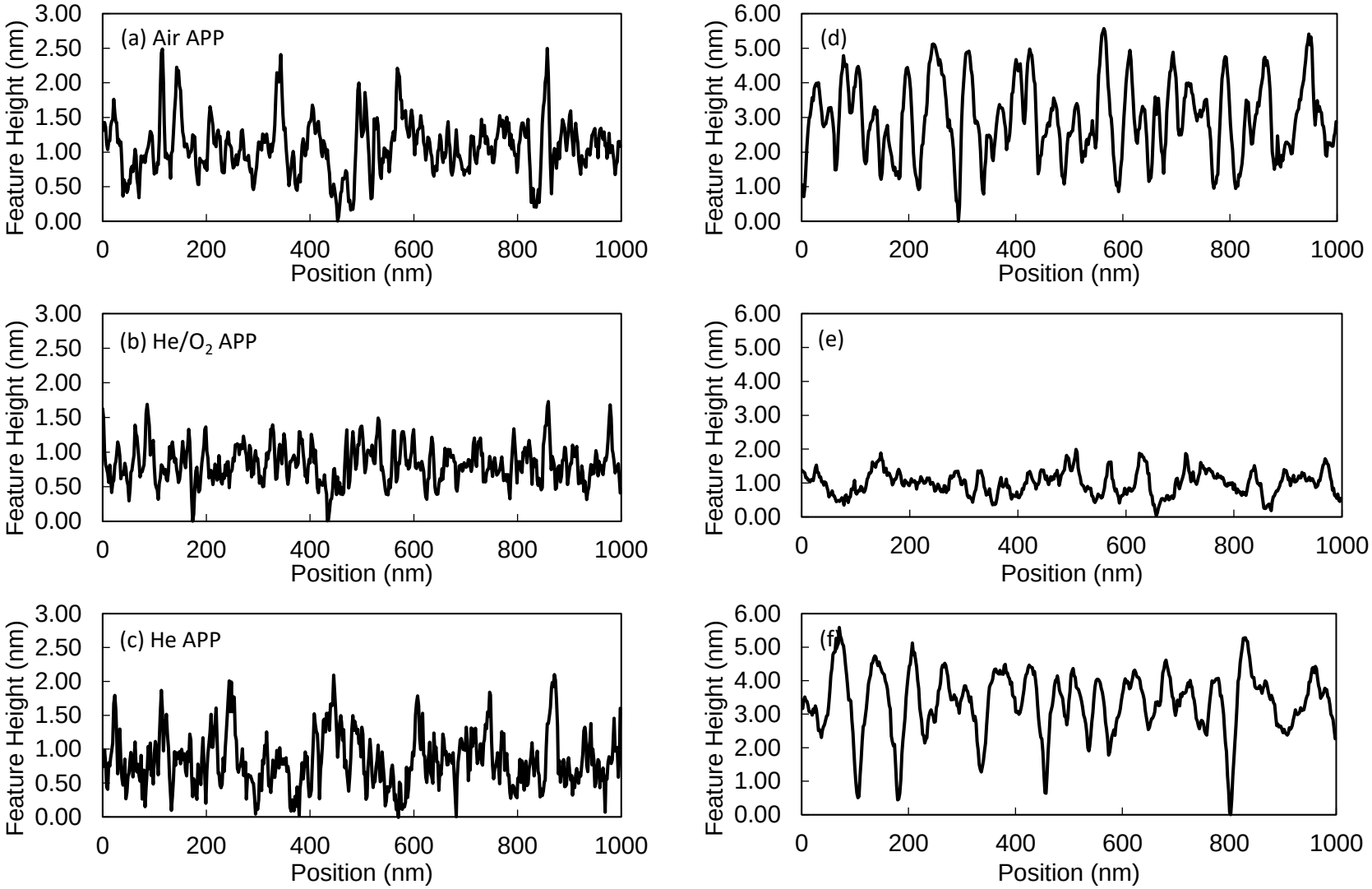

Figure 3-4. Cross-sectional AFM FH profiles obtained in D.I. water for PSf-PEI-Si surface after surface treatment with (a) Air APP, (b) He/O_2 APP, and (c) He APP, and corresponding AA graft polymerized PSf surfaces (d), (e) and (f).

Upon AA graft polymerization post-surface plasma treatment, the surface roughness and average FH of the PSf surfaces with tethered PAA chains increased, relative to the plasma treated PSf surfaces, by factors of 1.8-2.7 and 1.2-2.7, respectively (**Fig. 3-3** and **Table 3-4**). Such surface roughness increase is not surprising given that the tethered PAA layer consists of chains that are not uniform in size (as expected in free-radical polymerization) with chain-chain separation distance that has been reported to be in the range of 1.5-2.4 nm for the present reaction conditions [54].

Given the tethering of PAA chains onto the PSf surface, the FH distribution shifted toward higher values. The PAA layer thickness, as determined by AFM in air, which is a poor solvent for PAA, was greatest for the AA graft polymerized PSf surface post-activation by He/O_2 plasma (5.5 nm), followed by He (4.1 nm) and Air (3.6 nm) plasmas, respectively (**Fig. A-5, Appendix**). It is stressed that the rate of monomer addition is expected to be similar on any surface when chain growth is from a similar surface peroxide group resulting from APP surface treatment [45, 261]. Therefore, it is reasonable to expect that the tethered PAA layer thickness (**Fig. A-5, Appendix**) will be greater for a tethered PAA layer of higher surface chain number density [262]. Given the above, it may be reasonable to assume that the highest PAA layer thickness would be for the one synthesized post-Air plasma treatment of the PSf surface. This assertion would seem reasonable given that treatment of the PSf surface with Air plasma resulted in a greater O/C ratio (**Table 3-3**), a greater presence of C-O bond (**Table 3-2**), and a greater contact angle decrease (**Table 3-5**, **Section 3.3.3**) relative to PSf surface treated with the other two plasmas. Thus, one may be led to conclude that a higher surface number density of active oxygen-containing groups was available on the Air plasma treated surfaces which would serve as anchoring points for tethered chains. However, upon AA graft polymerization, the lowest relative O/C ratio increase (relative to the

other two plasmas) was for the PSf surface activated via Air plasma treatment (**Table 3-3**). In fact, the highest oxygen presence on the PAA-PSf-PEI-Si surface was for the AA graft polymerized PSf surface post-He/O_2 plasma treatment (**Table 3-3**). Given the above observations, it is reasonable to postulate that the highest number density of peroxide groups (for inducing AA graft polymerization), was for the PAA-PSf surface synthesized post-activation with He/O_2 plasma, followed by He and Air plasmas, consistent with the trend of PAA layer thickness.

3.3.3 PSf Surface contact angle

The change in PSf surface hydrophilicity due to surface plasma treatment is attributed to the implantation of hydrophilic functional groups [263] such as hydroxyl, carbonyl, carboxyl, and amino groups, whose surface number density directly impacts surface wettability [264]. Given the above, the greatest reduction in water contact angle was, as expected, for Air plasma (64.5 - 71.6%), as it led to increasing the surface oxygen content as ascertained from the XPS measurements composition that revealed increased C-O bond and O/C ratios (**Section 3.3.1**). Indeed, Air plasma treatment was the most effective (among the three evaluated plasmas) in reducing the contact angle (from 85.4^o to 30.3^o) within 1 scan (~0.4 s exposure time) (**Fig. 3-5**, **Table 3-5**).

Although this trend might suggest the mere use of plasma treatment to increase surface fouling resistance [265-268], the PSf water contact angle decrease post-plasma treatment was not permanent; the water contact angle increased over time upon exposure to air (**Table 3-5**; **Fig. 3-6**), a behavior consistent with previously reported studies [251, 258]. After exposure to air for 30 h, the water contact angle increased by 36.4%, 7.0%, and 3.3%, for the Air, He/O_2, and He plasma treated PSf-PEI-Si surfaces, respectively, relative to the native PSf surface contact angle (**Table 3-5**).

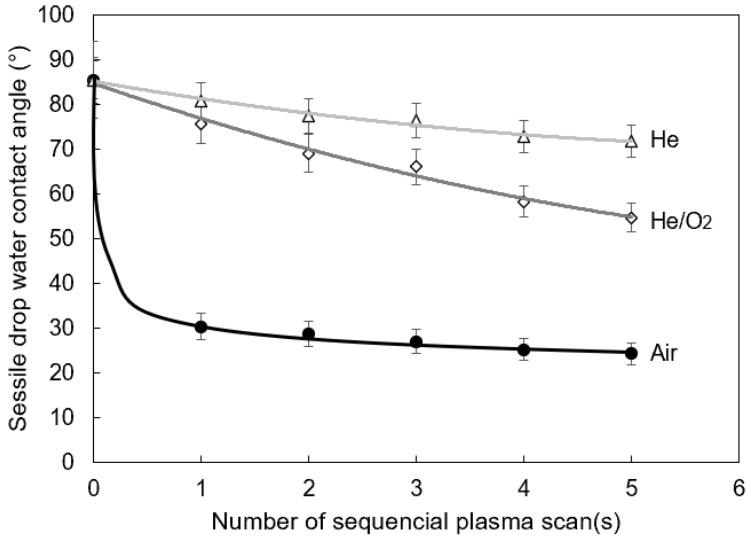

Figure 3-5. Sessile drop water contact angle of PSf surfaces (PSf-PEI-Si) treated with He, He/O_2, and Air plasmas at PSS of 10 mm and 1-5 sequential plasma scans (equivalent exposure time of 0.4-2 s).

Table 3-5. Sessile drop water contact angle and free energy of hydration(a) for the PSf and PAA tethered surfaces formed on silicon wafer substrates.

	PSf-PEI-Si		PAA-PSf-PEI-Si
Plasma	*Contact angle after plasma treatment*[(a)]	*Contact angle after 30 hrs exposure to ambient air, post-plasma treatment*	*Contact angle after AA graft polymerization*[(b)]
(Native)	*85.4±1.9º*		
Air	30.3±0.7º	54.3±1.0º	63.8±1.2º
He/O_2	75.6±1.6º	79.4±0.7º	69.0±1.3º
He	80.8±2.0º	82.6±1.0º	71.3±1.6º

(a) Plasma treatment conditions: *PSS* =10 mm, *N* = 1.
(b) Synthesized post plasma surface activation. Graft polymerization conditions: $[M]_o$ = 20 vol%, 70 °C, 1 h.

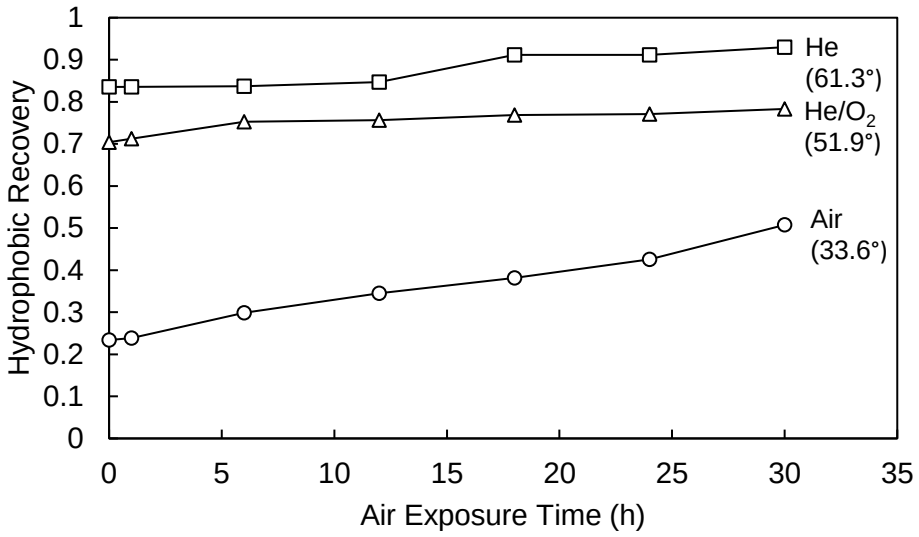

Figure 3-6. Stability of plasma treatments as indicated by hydrophobic recovery (i.e., ratio of sessile drop water contact angle measurements of the plasma treated Base-PSf membrane surface to the one of the original Base-PSf membrane surface) upon increased time of exposure to air after plasma treatment.

In contrast with the plasma treated PSf surface (**Fig. 3-5**; and **Table 3-5**), the PAA-PSf-PEI-Si surfaces did not reveal measurable degradation of surface hydrophilicity over the course of the study. This result is consistent with previous work on PSf modification via AA graft polymerization [269]. The above behavior is not surprising since the PAA layer is covalently tethered to the underlying PSf surface. However, the water contact angle for the AA graft polymerized PSf surfaces, synthesized post-activation with Air plasma, increased by 17.5% relative to the contact angle for the plasma treated PSf surface (even after exposure to ambient air) (**Table 3-5**). It is plausible that the above contact angle increase resulted from (a) lower tethered PAA chain number density, and (b) screening of hydrophilic surface groups (implanted via Air plasma treatment) by the PAA chains. In contrast to the PAA-PSf-PEI-Si surface synthesized post-Air plasma PSf surface activation, the water contact angles for PAA-PSf-PEI-Si surfaces synthesized post activation with He and He/O_2 plasmas were reduced by 11.8% and 8.7%, respectively, relative to the corresponding plasma treated PSf surfaces (**Table 3-5**). Nonetheless,

the water contact angle for the PAA-PSf-PEI-Si surface, synthesized via AA graft polymerization post-Air plasma activation of the PSf surface, was 7.5-10.5% lower relative to the tethered PAA synthesized post-activation with He and He/O_2 plasmas. Here we note that the PAA-PSf-PEI-Si surface synthesized via Air plasma surface activation was more hydrophilic (i.e., 6.2-9.2% greater negative surface free energy of hydration) compared to the surfaces synthesized based on PSf surface activation with He and He/O_2 plasmas (**Table 3-5**, **Fig. 3-7**). The above results suggest that the greater hydrophilicity of the PAA-PSf surface, which was synthesized post-surface activation by Air APP, is likely due to the combined outcome of both the hydrophilic tethered PAA chains and the remaining surface oxygen containing groups introduced by Air APP surface activation.

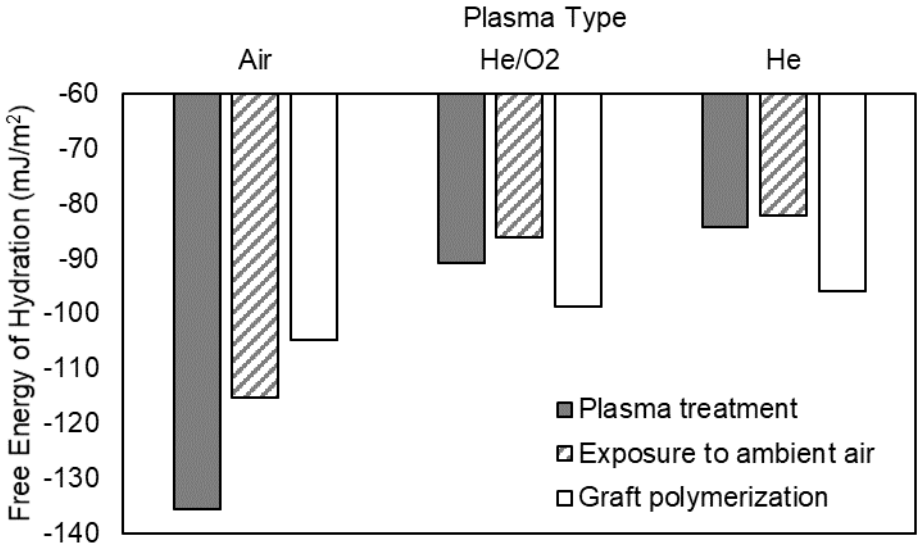

Figure 3-7. Free energy of hydration (**Section 3.2.4.3**) for native PSf and PAA-PSf-PEI surfaces formed on smooth silicon wafer substrates (calculated based on water contact angles; **Table 3-5**; Also, exposure to ambient air was for a period of 30 hrs).

3.3.4 PSf Surface Charge

Membrane surface zeta potential was evaluated as an added metric that typically serves to indicate the potential for membrane fouling [270]. Negative membrane surface zeta potential was

expected for the SNS-PAA-PSf membrane at pH above the point of zero charge (PZC), given the amphoteric behavior (i.e., deprotonation) of the tethered polyelectrolyte chains. Zeta potential of the PAA tethered membrane surface (**Fig. 3-8**) showed a trend of surface charge that switches from positive (at pH below the PZC) to increasingly negative (at pH above the PZC). Upon tethering of the PAA chains, the SNS-PAA-PSf membrane surface [271] with greater values of PZC are expected due to higher PAA pKa (~4.8, [156]) relative to the isoelectric point (IEP) of PSf (~3.2, [272]). The SNS-PAA-PSf membrane demonstrated a higher PZC value of 4.9 relative to 3.3 for the Native-PSf UF membrane (**Fig. 3-8**). A trend of greater negative surface zeta potential for the SNS-PAA-PSf membrane relative to the Native-PSf was encountered at pH>6. For the SNS-PAA-PSf surface, the variability of surface zeta potential with pH is expected to be governed by the carboxyl groups introduced by the tethered chains. It is estimated that for the range of tethered PAA chain sizes (*Mw*~19,000-56,000) synthesized under the present reaction conditions [54], about ~260-780 carboxyl groups are introduced per tethered chain. With an estimated PAA chain-chain separation of 1.5-2.4 nm [54], the area number density of carboxyl groups is in the range of 45-347 per square nanometer. Thus, increased electrostatic repulsion (relative to the Native-PSf surface) should be expected between the PAA-modified membrane surface and negatively charged foulant molecules (i.e., BSA and sodium alginate) at the above pH range; hence, the lower fouling propensity of the SNS-PAA-PSf membrane relative to the Native-PSf membrane (**Chapter 7**).

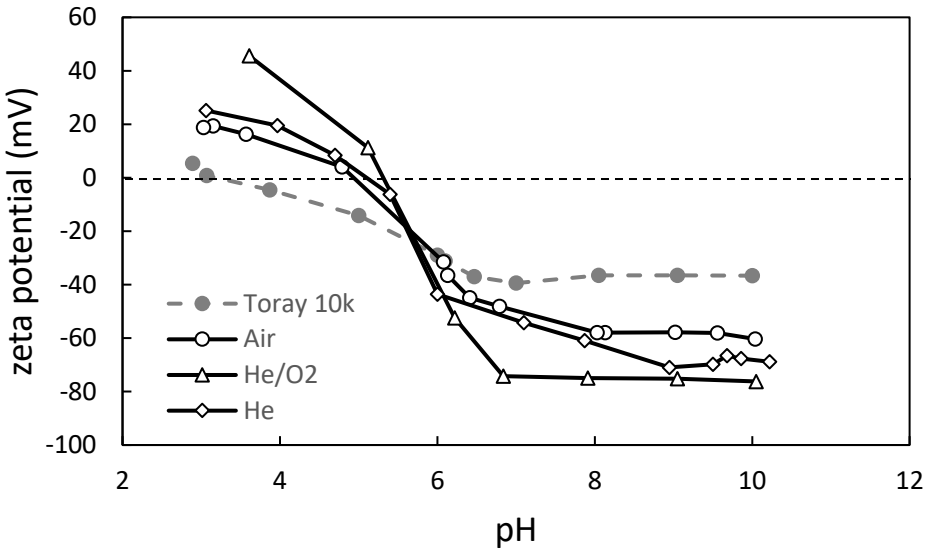

Figure 3-8. Comparison of zeta potential variation with pH for the SNS-PAA-PSf membranes, synthesized via AA graft polymerization post-surface activation (with different plasmas) of the base PSf membrane (Toray MUF-20K), compared with a tight commercial UF membrane (Toray MUF-10K).

3.4 Conclusions

Surface nano-structuring of polysulfone (PSf) substrate and ultrafiltration (UF) membranes via acrylic acid (AA) graft polymerization to form a tethered polyacrylic acid (PAA) layer was investigated systematically with respect to surface activation with atmospheric pressure Air, He and He/O_2 plasmas. Among the three plasmas, PSf surface treatment with Air plasma resulted in the highest degree of surface hydrophilicity (as indicated by the lowest surface energy). XPS analysis revealed that PSf surfaces that were treated with Air plasma had the highest O/C ratio suggesting that this plasma resulted in a higher surface concentration of oxygen-enriched functional groups. AA graft polymerization, post-surface activation by the three plasmas, further increased the surface O/C ratio which was the highest for the He/O_2 plasma followed by Air and He plasmas. However, the highest hydrophilicity remained highest for the PSf surface tethered with PAA chains post-activation with Air plasma. The above results indicate that surface hydrophilicity is governed by the combination of presence of surface oxygen groups resulting from

plasma treatment and the surface density of tethered PAA chains. Given the greater negative zeta potential (at pH >~6) for the tethered PAA-PSf surface synthesized post-activation with He/O_2 and He plasmas relative to Air plasma, it is reasonable to conclude that the former surface had a lower number density of PAA chains.

Chapter 4 Tuning the Performance of Surface Nano-structured UF Membranes Surface Activated by He/O_2 APP

4.1 Overview

There is a growing demand for the UF membrane purification and fractionation of high-value biomolecules from complex mixtures including proteins, peptides, and polysaccharides [61]. The separation performance of UF membranes is typically quantified in terms of molecular weight cut-off (*MWCO*) [64, 65], defined as the approximate molecular weight (*Mw*) of solute which is rejected by the membrane to a level of 90% [273]. However, commercially available UF membranes typically cover a limited range of *MWCO* needs [61], and hence sharp separation remains a challenge [4, 61, 274]. In this regard, it is of interest to tune UF membrane *MWCO* and hydraulic permeability.

In recent years various approaches to membrane surface modifications have been proposed for tunning UF membrane performance [55, 58, 275]. Results from existing studies provide sufficient evidence to suggest that the performance of UF membranes modified with tethered hydrophilic chains is affected by the type of polymer used, modification conditions, and base membrane choice. To date, however, membrane modifications via APPIGP were explored focusing primarily on reducing PES UF membrane fouling propensity and enhancing membrane cleaning efficacy [54, 57, 58], typically tested with model foulants (e.g., lysozyme, alginic acid, immunoglobulin G, and BSA). The reported data clearly showed that membrane hydraulic permeability decreases while solute rejection increases (or *MWCO* decreases) upon UF membrane modification with tethered hydrophilic polymer chains. However, previous studies have not systematically addressed the feasibility of UF membrane performance (i.e., hydraulic permeability and *MWCO*) tunability via adjustment of surface activation and graft polymerization conditions. The available studies have

generally revealed increased solute rejection (or reduced *MWCO*) with decreased hydraulic permeability (e.g., [57]). Here we contend that although surface modification with tethered chains reduces membrane hydraulic permeability, through a proper choice of the base UF membrane it should be possible to arrive at the desired hydraulic permeability and *MWCO* combination.

Accordingly, the present study presents a systematic investigation of PSf UF membrane hydraulic permeability (L_p) and *MWCO* tuning via surface nano-structuring with a tethered poly (acrylic acid) (PAA) layer. The PAA surface layer was synthesized via a two-step approach consisting of surface activation with He/O_2 APP followed by free radical GP. The APPIGP approach was selected as it was shown to provide the means for creating a high surface density of tethered chains on both PSf and polyamide surfaces [49, 54]. A systematic evaluation of the impact of APP activation and GP conditions on membrane performance was then undertaken demonstrating membrane performance tuning capability that allows overcoming the typical UF hydraulic permeability – *MWCO* tradeoff.

4.2 Experimental

4.2.1 Materials

Prime grade 4″silicon ⟨100⟩ wafers were utilized as a base for preparing model surfaces with PAA chains tethered onto a pre-coated layer of PSf. Sulfuric acid (96%) and aqueous hydrogen peroxide (30%) (KMG Electronic Chemicals, Inc., Houston, TX) were used for preliminary silicon wafer cleaning to remove organic residues. The cleaned silicon wafer was spin coated with Poly(ethyleneimine) (PEI, Mw~750,000) solution (50 wt% in H_2O, Sigma-Aldrich, St. Louis, MO) to form an adhesion layer. A PSf layer was then formed on top of the PEI layer by spin coating a PSf solution prepared from 0.25 wt% PSf pellets (Mw~35,000, Sigma-Aldrich, St. Louis, MO)

dissolved in chloroform (⩾99.9%, Sigma-Aldrich, St. Louis, MO). Acrylic acid (99%, Sigma-Aldrich, St. Louis, MO) monomer was used for graft polymerization to modify the PSf surfaces which were post-activated with atmospheric pressure plasma. Helium (99.999%) and oxygen (99.999%) gases (Airgas, Los Angeles, CA) were used for plasma treatment sources, and nitrogen (99%) gas (Airgas, Los Angeles, CA) was used for substrate surface drying, graft polymerization degassing, and UF filtration feed tank pressurizing.

Polyethylene glycol (PEG, *Mw* from 2,000 to 35,000 Da, Sigma-Aldrich, St. Louis, MO) was used for membrane *MWCO* characterization. Deionized (D.I.) water, produced by Milli-Q filtration system (Millipore Corp., San Jose, CA), was used for all reaction and model solutions. Solution pH adjusted using 0.1 N sodium hydroxide solution (Fisher Scientific, Chino, CA), was monitored using a pH meter (Oakton pH 110 Meter; Cole-Parmer, Vernon Hills, IL). PSf membrane sheets (MUF-10K and MUF-20K, Toray Membrane USA Inc., Poway, CA), with manufacturer reported 10 kDa and 100 kDa *MWCO*, respectively, were selected as the base membranes to illustrate the feasibility for UF membrane performance tuning with tethered PAA chains.

4.2.2 Preparation of PSf surrogate membrane surfaces

Tethered PAA layer feature heights and surface roughness were of the order of 1-8 nm and 0.6-1.3 nm, respectively [54], and these values are respectively lower by factors of about 4 and 15 relative to typical UF membrane surfaces [276, 277]. Therefore, for atomic force microscopy (AFM) characterization of the tethered chains, a PAA layer was synthesized onto a relatively smooth PSf surfaces spin cast onto a silicon wafer substrate following a previously established protocol [48, 54, 278] to form a smooth model PAA-PSf-Si surface. Briefly, the silicon wafers were first cut into 1.5 cm × 1.5 cm square samples using Small Sample Cleaving Pilers (GC-SS-

100, LatticeGear, Beaverton, OR) and cleaned in a piranha solution (an aqueous mixture of 70 vol% sulfuric acid and 30 vol% hydrogen peroxide) at 90°C for 10 min, followed by five cycles of thorough rinsing with D.I. water. Prior to spin coating, each wafer piece was washed with isopropanol and D.I. water, followed by nitrogen drying (in the UCLA Nanolab class 100 cleanroom). A PEI adhesion layer was then formed on the cleaned silicon wafer substrates by spin coating (using 790 Spinner with PWM32 controller; Headway Research Inc., Garland, TX) 0.1 mL of a 0.3 wt% aqueous PEI solution (centrally placed using a pipet onto the substrate surface) at 2500 rpm for 30 s. Immediately afterward, the PEI-Si surfaces were spin coated with about 0.1 mL of a 0.25 wt% PSf solution in chloroform at 2500 rpm for 30 s to form a ~26 nm PSf layer (AFM dry thickness measurement in ambient air). The PSf surrogate membrane surfaces (PSf-PEI-Si) were then dried in a vacuum oven at 40°C for 24 h prior to further use.

4.2.3 Atmospheric pressure-induced graft polymerization (APPIGP)

The tethered PAA layer was synthesized onto PSf surfaces via a two-step process (**Appendix C**) consisting of (1) PSf surface activation via exposure to APP, followed by (2) free-radical graft polymerization of AA in an aqueous monomer solution [54, 278]. PSf surface activation was accomplished following a previously established protocol [279] using a helium/oxygen (He/O_2) APP system (Atomflo™ 500; Surfx Technologies Inc., Redondo Beach, CA) operated at helium and oxygen flow rates of 45 L/min and 0.5 L/min, respectively, with low plasma discharge temperature (53-75°C) generated at 150W RF power. The PSf-PEI-Si surfaces were activated via 1-3 sequential plasma scans (*N*) and source-surface separation (*PSS*) distance range of 5, 10, or 15 mm.

Following APP activation, the PSf-PEI-Si substrates were placed in 250 mL glass reaction vessels containing the aqueous AA monomer solutions. The vessels were placed in a constant water bath at 50-90°C for 30-60 min. The initial monomer concentration $[M]_o$ was varied in the range of 15-25 vol% and solution pH was varied in the range of 1.8-13.5, adjusted using 0.1 N NaOH aqueous solution. Nitrogen was injected (via a thin tubing loop with small holes poked with needles) at the bottom of the vessels during graft polymerization to promote mixing and scavenge dissolved oxygen that could inhibit the polymerization reaction [280]. After the graft polymerization step, the PAA-PSf-PEI-Si surfaces were rinsed with D.I. water to remove unreacted species, and then dried in a vacuum oven at 40°C for 24 h prior to further AFM characterization (**Section 4.2.4.1**).

The above two-step graft polymerization process was also applied to synthesize a PAA layer onto the base PSf membranes. The base PSf membranes (MUF-10K and MUF-20K) were kept in D.I. water for 24 h, thoroughly rinsed with D.I. water, and subsequently dried via an impinging nitrogen stream prior to surface activation with plasma. Following plasma activation, surface graft polymerization proceeded as per the protocol described in **Section 4.2.3**. Scanning electron microscope (SEM) membrane characterization was carried out for the membranes post-drying in a vacuum oven at 40°C for 24 h. Performance characterization (i.e., hydraulic permeability and *MWCO* determination) of each membrane was conducted after its immersion in D.I. water for at least a 24 h period.

4.2.4 Surface Characterization

4.2.4.1 Surface topography

Native PSf and PAA-PSf-PEI-Si surrogate membrane surfaces were characterized via AFM using a Bruker Dimension Icon Scanning Probe Microscope (Bruker, Santa Barbara, CA). AFM obtained topography was determined under D.I. water with ScanAsyst-Fluid+ probes in Mechanical Force Tapping mode [244, 278]. Prior to AFM characterization, surrogate membrane surfaces were immersed in D.I. water for 30 min for equilibration. AFM topography images of size 1 μm×1 μm with 512×512-pixel resolutions were obtained with loading force ~1 Nn at scan rates of 0.8 Hz. The root-mean-square surface roughness (R_{rms}) can be calculated from the AFM feature height (FH) data as $R_{rms} = \sqrt{\sum_i^N (Z_i - Z_{avg})^2 / N}$, where Z_i is the FH of i^{th} data point, N is the total number of data points within the 1 μm×1 μm topography image size, and Z_{avg} is the average FH. Also, cross-sectional FH profiles were created from the FH data over a 1 μm line across the surface topography images.

4.2.4.2 Membrane surface and cross-section images

Aerial surface (top-view) and cross-section of both the Base-PSf and SNS-PAA-PSf membranes were imaged via SEM (Zeiss Supra VP40, Carl Zeiss AG, Oberkochen, Germany) with an accelerating voltage of 10 keV and a spot size of 100-10,000 nm. The top-view SEM images were carried out to assess the membrane pore shape, size, and distribution. Cross-sectional SEM images were obtained by a freeze-fracture method, whereby the membranes were rapidly frozen in liquid nitrogen and cracked using the edge of a glass plate. The membranes were then affixed to standard SEM sample stubs with double-sided carbon tape and sputter-coated

(Hummer® 6.6 Sputter Coater, Anatech USA, Sparks, NV) with a thin film of gold (Au) to prevent charging during SEM characterization.

4.2.4.3 Surface wettability

Surface wettability of both the UF membranes and model PAA-PSf-Si surfaces was evaluated by sessile drop (SD) contact angle measurements [54, 281-284] using an automated drop shape analyzer (DSA20; KRÜSS GmbH, Germany). SD water contact angle measurements were taken within 2 s following placement of 1 µL D.I. water drops onto sample surfaces. The reported contact angles represent averaged values based on measurements for at least 5 locations for each sample.

4.2.5 Performance Characterization

4.2.5.1 Hydraulic permeability

Membrane water permeability was evaluated in a 50 mL dead-end stirred UF cell (Amicon 8050, Millipore Corporation, Burlington, MA) in which the installed membrane coupons had an active area of 13.4 cm^2 (**Appendix D**). The stirred membrane cell was fed D.I. water from an 800 mL nitrogen pressurized feed tank. Prior to determining membrane hydraulic permeability, membrane samples were compacted with D.I. water at 3.5 bar (~50 psi) and ~20°C for 3 h until the permeate flux stabilized. Water flux ($J_v = Q_p / A$, in which Q_p and A are the permeate flow rate and membrane area, respectively) was determined over an applied pressure range of 0-3.5 bar (0-50 psi), using an in-line liquid flow meter (SLS-1500, Sensirion AG, Switzerland). Water permeability (L_p) was determined from the slope of a linear plot of water flux versus transmembrane pressure (i.e., $L_p = J_v / \Delta P$, where ΔP is the applied transmembrane pressure). The experimental uncertainty in the determined hydraulic permeability values was assessed based on

the flow and pressure measurements accuracy with the relevant error bars reported in the presented data. It is noted that all membrane hydraulic permeabilities were reported for D.I. water at ~20°C, and thus the membrane hydraulic resistance is given by $R_m = 1/(\mu \cdot L_p)$, where μ is solution viscosity ($\mu = 0.001 Pa \cdot s$ for the current study).

4.2.5.2 Molecular weight cutoff

The molecular weight cutoff (*MWCO*), defined as the solute *Mw* rejected by the membrane at a level of 90% [273], was determined for each membrane using a series of commonly used PEG fractions [285, 286] of *Mw* in the range of 2,000 to 35,000 Da. Each solute rejection experiment was conducted using aqueous (D.I. water) 1 g/L PEG solutions. All *MWCO* experiments were carried out in the stirred membrane cell at ~20°C, at the same initial permeate flux of 9 $L \cdot m^{-2} \cdot h^{-1}$ (~5.3 $gallon \cdot ft^{-2} \cdot day^{-1}$). The membrane and UF filtration system (stirred membrane cell and feed reservoir) were both thoroughly rinsed with D.I. water after each PEG filtration run.

PEG concentrations in the feed (C_f) and in the permeate (C_p) were determined by a Total Organic Carbon (TOC) Analyzer (Aurora 1030W, OI Analytical, College Station, TX). The solute observed (nominal) rejection for each PEG fraction was calculated as $R_o = (1 - C_p / C_f) \times 100\%$. Subsequently, the observed rejection for different *Mw* of PEG fraction was correlated with the PEG *Mw*, serving to determine the *Mw* fraction corresponding to 90% rejection which was then designated as the membrane *MWCO*. The experimental uncertainty in the determined *MWCO* for a given membrane was assessed based on the accuracy of the TOC measurements (±2%) with the relevant *MWCO* error bars reported in the presented data.

4.3 Results and Discussion

4.3.1 AFM characterization of tethered PAA layer on surrogate PSf membrane substrate

Surface topography of the PAA-PSf-PEI-Si surfaces was evaluated via AFM 3D imaging (**Figure 4-1** and **Table 4-1).** The topography of the PAA tethered surfaces (He/O_2 plasma surface activation at *PSS*=10 mm, *N*=1 and AA graft polymerization at 70°C for 1 h reaction time) were clearly impacted by the initial monomer concentration over the evaluated range of $[M]_o$=15-25 vol%. Upon PAA modification, surface roughness of the PSf surfaces increased by a factor of ~2.1-10.1, and the average FH increased by ~1.7-5.8 fold. More importantly, over the range of monomer concentrations, the brush-like structure of the tethered PAA (**Figure 4-1**) appeared to display minima in both surface roughness and average FH at monomer concentration of 20 vol% (**Table 4-1**). In contrast, the FH distribution was broader at monomer concentrations above and below 20 vol% (**Figure 4-2**) appearing as aggregated (and less-uniform) structures. It is noted that tethered polymer chain length and grafted polymer chain density should increase with the initial monomer concentration owing to the increased rate of monomer addition [49, 54]. However, at elevated monomer concentration, polymer chains that may have formed in the bulk solution can terminate with growing surface chains or active sites which would then lower the chain grafting density [49]. Indeed, the above results are consistent with previous work in which chain surface number density was reported to reach a maximum with respect to the initial monomer concentration [54].

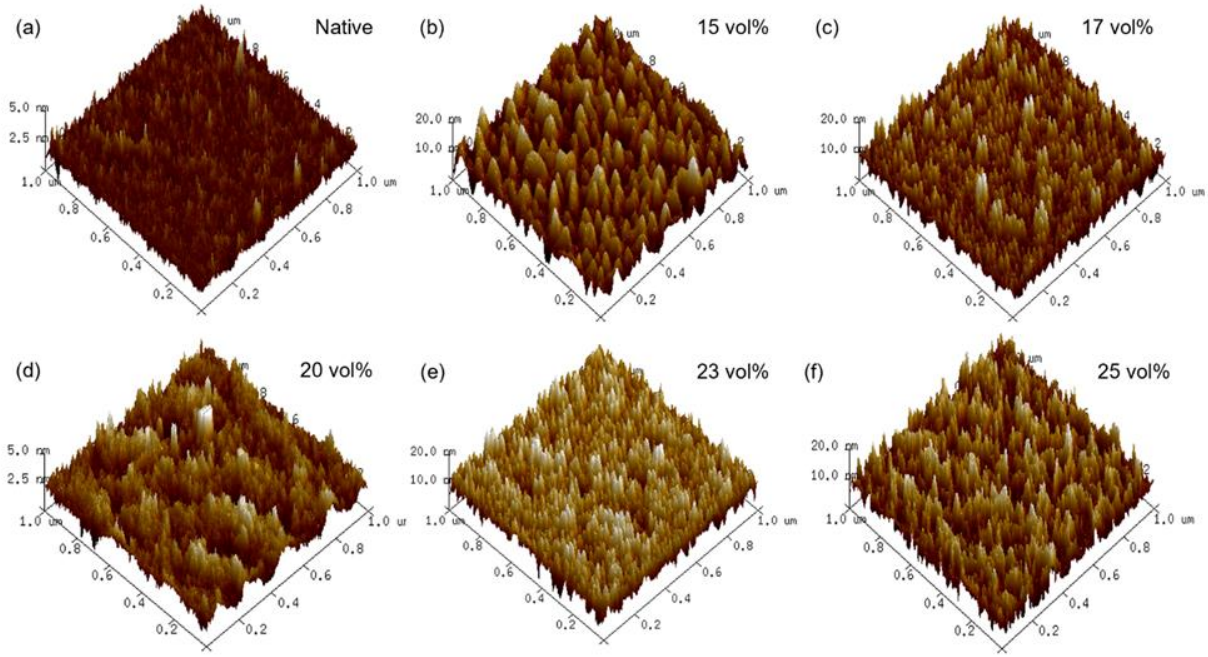

Figure 4-1. AFM derived topography images (under D.I. water) of (a) native PSf-PEI-Si surface and PAA-PSf-PEI-Si surfaces synthesized via APPIGP: surface activation with He/O_2 plasma treatment (*PSS*=10 mm, N=1), followed by AA graft polymerization at initial monomer concentration ($[M]_o$) of (b) 15 vol%, (c) 17 vol%, (d) 20 vol%, (e) 23 vol%, and (f) 25 vol% at 70°C for 1 h.

As shown in the AFM cross-section profile (**Figure 4-3**), the average major peak separation distance was the shortest (21.1 nm) for the tethered PAA layer synthesized at an initial monomer concentration of 20 vol% (**Table 4-1**). The above separation distance between major peaks was up to 81.8% and 70.6% lower compared to the highest and lowest monomer concentrations of 25 and 15 vol%, respectively. For the above initial monomer concentrations, the PAA-PSf-PEI-Si surfaces revealed lower density of surface major peaks with peak-peak separations over the range of 72.0-115.5 nm. The observed trends indicated in **Figure 4-1, Figure 4-2** and **Figure 4-3** confirmed that by setting a target initial monomer concentration for the graft polymerization reaction, the tethered PAA layer structure can be tuned. As discussed in **Sections 4.3.2.1-4.3.2.4**, the performance of SNS-PAA-PSf membranes can be tuned via adjustments of APP and graft polymerization conditions.

Table 4-1. Surface roughness, average FH and average major peak separation distance for the native PSf-PEI-Si and PAA-PSf-PEI-Si surfaces.

$[M]_o$ (vol%) (pH)[a]	PAA-PSf-PEI-Si*		
	R_{rms} (nm)	Average FH (nm)	Average Major Peak[b] Separation Distance (nm)
(Native)	*0.33*	*1.8*	*17.3*
15 (2.0)	3.33	10.4	72.0
17 (2.0)	2.50	8.7	63.8
20 (1.9)	0.71	3.1	21.1
23 (1.7)	2.62	8.4	43.2
25 (1.6)	2.82	9.0	115.5

[a] Initial monomer concentration and pH for AA graft polymerization;
[b] Major peak is defined as those above ~30% of the maximum peak height;
* PAA-PSf-PEI-Si surfaces were synthesized via APPIGP: surface activation with He/O_2 plasma treatment (PSS=10 mm, N=1), followed by AA graft polymerization at initial monomer concentration ($[M]_o$) in the range of 15-25 vol% at 70°C for 1 h.

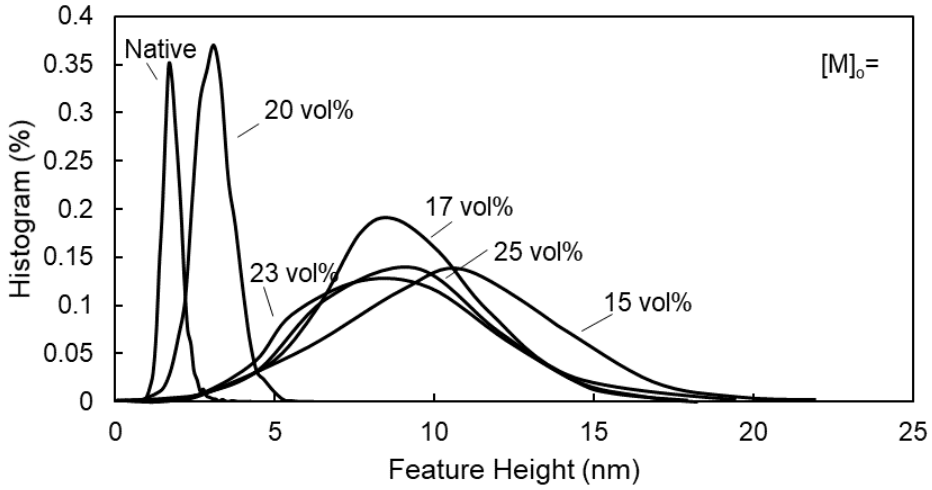

Figure 4-2. AFM derived surface FH distributions (under D.I. water) of native PSf-PEI-Si surface and PAA-PSf-PEI-Si surfaces synthesized via APPIGP: surface activation with He/O_2 plasma treatment (PSS=10 mm, N=1), followed by AA graft polymerization at initial monomer concentration ($[M]_o$) in the range of 15-25 vol% at 70°C for 1 h.

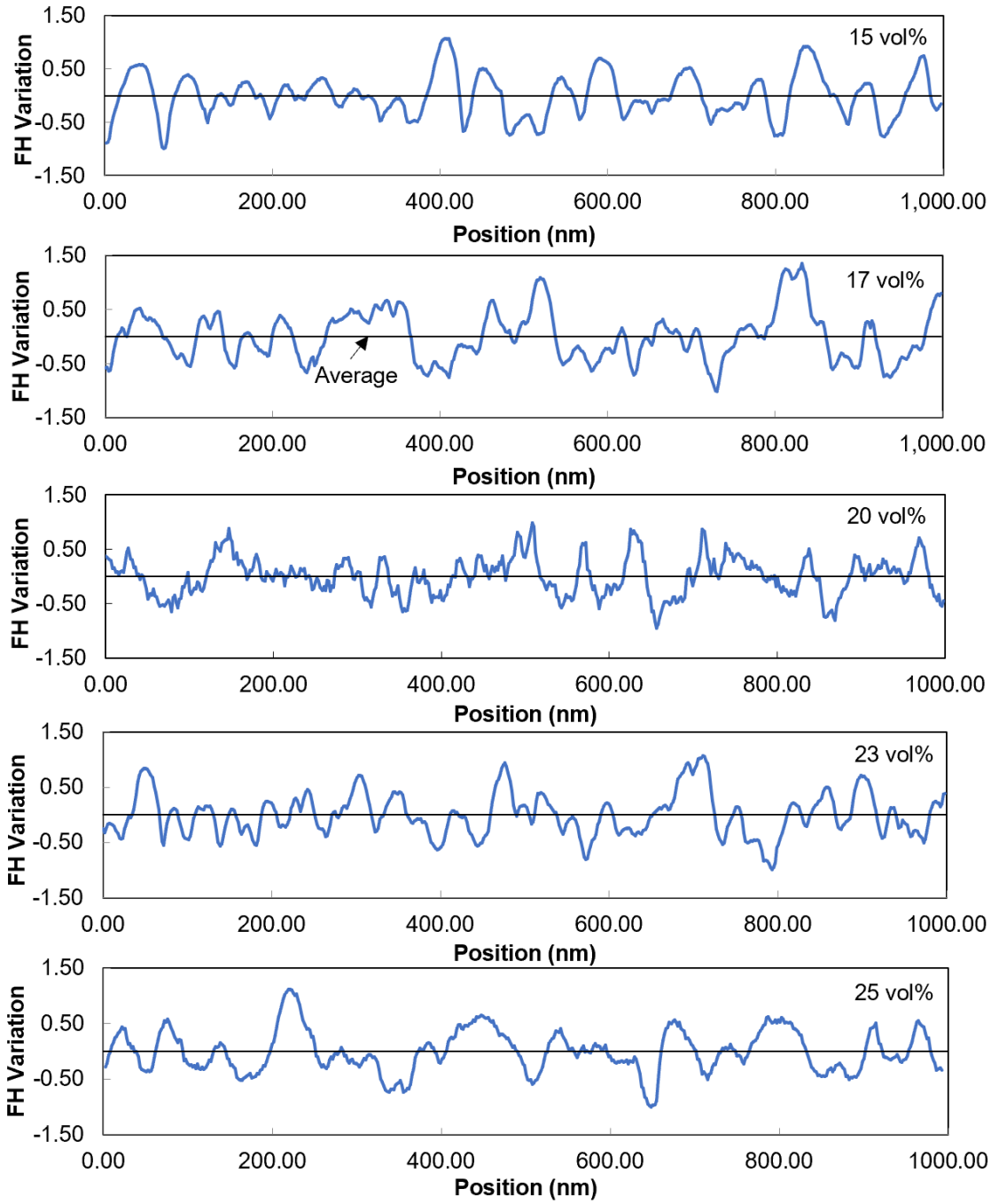

Figure 4-3. Cross-sectional AFM FH profiles (in water) with respect to the average FH of PAA-PSf-PEI-Si surfaces activated with He/O_2 plasma treatment (PSS=10 mm, N=1), followed by AA graft polymerization (70°C for 1 h) at $[M]_o$ of (a) 15 vol%, (b) 17 vol%, (c) 20 vol%, (d) 23 vol%, and (e) 25 vol%.

4.3.2 SNS-PAA-PSf membranes

The tethered PAA surface layer is expected to alter the underlying PSf membrane hydraulic permeability and *MWCO* owing to pore narrowing and blockage. As illustrated in the examples of SEM top-view of the base PSf and SNS-PAA-PSf membranes (**Figure 4-4**), the tethered PAA layer led to a visible reduction of the number density of large pores (dark circular regions in **Figure 4-4**) and thus reduced average pore size (**Table 4-2** and **Table 4-3**). As illustrated in **Figure 4-4**, surface modification was restricted to the upper active layer of the membrane, with no observable alteration of the larger pores in the support structure. The above observation is consistent with the assertion that graft polymerization is unlikely to have occurred inside the membrane pores, given that plasma treatment was confined to the surface of the membrane which was not wetted prior to graft polymerization. Given the estimated average pore size of 6.3 and 2.9 nm for the base MUF-20K and MUF-10K base UF membranes (**Table 4-2** and **Table 4-3**), respectively, one should expect that PAA chains would also be grafted in the vicinity and to some extent near the pore opening regions of the looser UF base membrane (**Table 4-2**). Here we note that it was previously estimated that for the tethered PAA layer, which was graft polymerized at a similar range of initial monomer concentration, surface tethered chain-chain separation distance was ~1.5-1.7 nm [54]. Thus, a PAA layer at such short, tethered chain-chain separation distance should be expected to impact the resulting SNS membrane performance relative to the base membrane. Accordingly, a greater change in SNS-PAA-PSf membrane performance should be expected relative to the looser UF base membrane as discussed in **Sections 4.3.2.5**.

Membrane hydraulic permeability and *MWCO* are expected to decrease upon AA graft polymerization. Such hydraulic permeability and *MWCO* reductions are attributed to the added hydraulic resistance imparted by the PAA layer which effectively narrows or may block pore

openings. We note that the SNS-PAA-PSf membranes, synthesized with base membranes of MUF-20K and MUF-10K (**Table 4-2** and **Table 4-3**), demonstrated up to 79% and 96% water permeability and *MWCO* reduction, respectively, corresponding to membranes #33 and #21 (**Table 4-2**). The increased membrane hydraulic resistance and decreased *MWCO* due to the tethered PAA layer, depend, to a degree, on the base membrane pore size distribution and the tethered layer structure which is governed by the plasma surface activation and GP conditions. The reduction of the average pore size (estimated as per **Figure A-10, Appendix A**) reduction for the SNS-PAA-PSf membranes was 46.0-66.7% and up to 27.6% relative to the corresponding MUF-20K and MUF-10K base membranes, respectively (**Table 4-2** and **Table 4-3**).

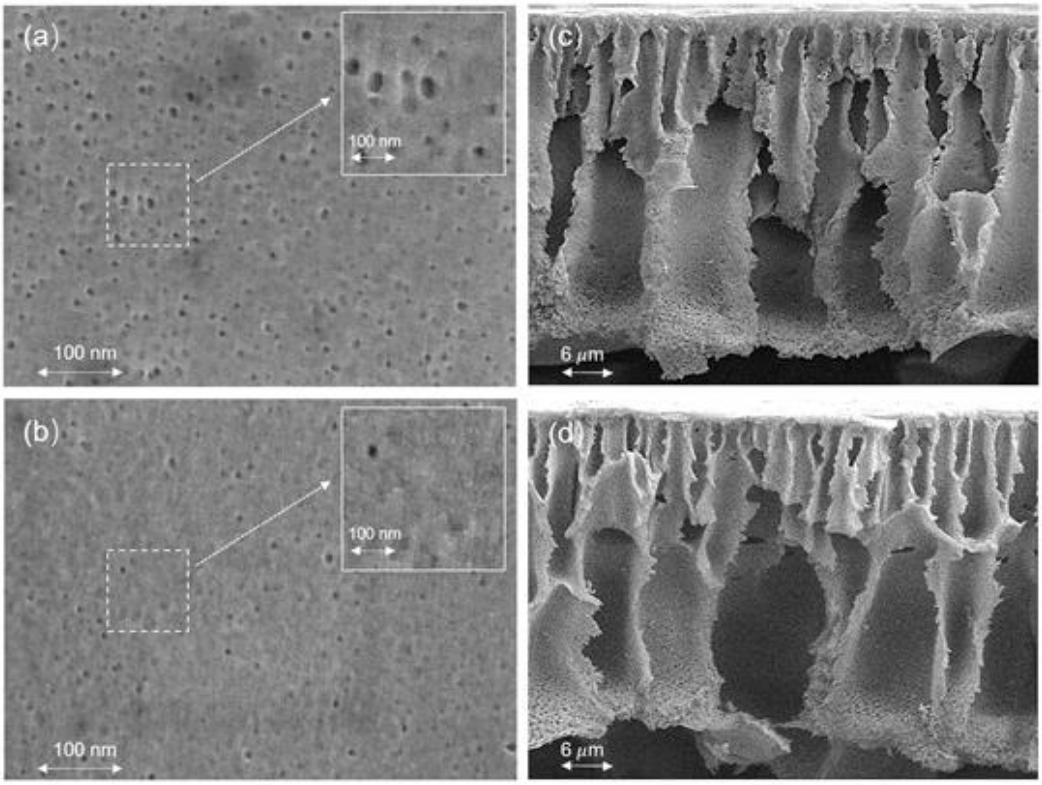

Figure 4-4. SEM top surface images of (a) PSf base membrane MUF-20K, and (b) SNS-PAA-PSf membrane, also cross section images of (c) PSf base membrane MUF-20K, and (d) SNS-PAA-PSf membrane.

Table 4-2. Performance of SNS-PAA-PSf membranes synthesized at various plasma and graft polymerization conditions, based on the MUF-20K membrane.

Membrane	He/O_2 plasma		Graft polymerization				Separation properties		
	PSS Distance[a] (mm)	*N*[b]	Time (min)	Temperature (°C)	$[M]_o$ (vol%)	pH[c]	Permeability[d] ($L \cdot m^{-2} \cdot h^{-1} \cdot bar^{-1}$)	*MWCO*[e] (kDa)	Pore size[f] (nm)
1 (Base)	-	-	-	-	-	-	37.4	100	6.3
2	5	1	60	70	20	1.9	21.3	10.5	2.9
3	5	2	60	70	20	1.9	18.2	10.5	2.9
4	5	3	60	70	20	1.9	24.8	7.7	2.6
5	10	1	60	70	20	1.9	16.0	6	2.4
6	10	2	60	70	20	1.9	16.9	6.8	2.5
7	10	3	60	70	20	1.9	17.1	7	2.5
8	15	1	60	70	20	1.9	23.5	11	3.0
9	15	2	60	70	20	1.9	20.7	8	2.7
10	15	3	60	70	20	1.9	19.0	7	2.5
11	10	1	30	70	20	1.9	32.4	10	2.9
12	10	1	45	70	20	1.9	18.8	8	2.7
13	10	1	60	50	20	1.9	32.8	7.5	2.6
14	10	1	60	60	20	1.9	26.6	7	2.5
15	10	1	60	80	20	1.9	12.9	9	2.8
16	10	1	60	90	20	1.9	12.3	10	2.9
17	10	1	60	70	15	2.0	18.3	9	2.8
18	10	1	60	70	19	1.9	18.1	7	2.5
19	10	1	60	70	21	1.8	13.5	3.9	2.1
20	10	1	60	70	22	1.7	14.3	5.8	2.4
21	10	1	60	70	25	1.6	16.3	6	2.4
22	5	3	60	70	17	1.9	35.4	11	3.0
23	5	3	60	70	19	1.9	32.2	9.6	2.8
24	5	3	60	70	21	1.8	30.8	10.5	2.9
25	5	3	60	70	22	1.7	33.0	12.5	3.1
26	10	1	60	70	21	3.6	20.5	5.3	2.3
27	10	1	60	70	21	4.0	29.2	10	2.9
28	10	1	60	70	21	4.7	43.3	11	3.0
29	10	1	60	70	21	5.9	28.5	11.5	3.0
30	10	1	60	70	21	8.2	19.5	10	2.9
31	10	1	60	70	21	13.5	7.8	5.3	2.3

[a] *PSS* – plasma source-surface separation distance.

[b] Number of sequential plasma surface scans (*N*), each scan performed at a speed of 100 mm/s.

[c] The AA solution pH beyond the natural monomer solution pH was adjusted using 0.1 N NaOH solution.

[d] Water permeability coefficient (L_p) was determined (uncertainty ± 5.4%) with D.I. water after membrane compaction under 3.5 bar (50 psi) pressure for 3 hours at ~20°C.

[e] Molecular weight cutoff (*MWCO*) was determined using PEG molecular weight fractions (**Section 4.2.5.2**) in the range of 2,000-35,000 Da (uncertainty of ± 4%). The solute rejection vs *Mw* curves for selected SNS-PAA-PSf membranes are shown in **Figure A-11, Appendix A**.

[f] Pore size estimated based on *MWCO* – pore diameter correlation (d_p=1.3095 × $MWCO^{0.3409}$; **Figure A-10, Appendix A.**

Table 4-3. Performance of SNS-PAA-PSf membranes synthesized at various plasma and graft polymerization conditions, based on the MUF-10K membrane [(1)]

Membrane	He/O_2 plasma		AA graft polymerization				Separation properties		
	PSS Distance[a] (mm)	*N*[b]	Time (min)	Temperature (°C)	$[M]_o$ (vol%)	pH[c]	Permeability[d] ($L \cdot m^{-2} \cdot h^{-1} \cdot bar^{-1}$)	*MWCO*[e] (kDa)	Pore size[f] (nm)
1 (Base)	-	-	-	-	-	-	23.2	10	2.9
2	15	1	60	70	20	1.9	23.1	7.7	2.6
3	15	2	60	70	20	1.9	11.5	5.8	2.4
4	15	3	60	70	20	1.9	14.2	7.5	2.6
5	10	1	60	70	20	1.9	16.0	7.5	2.6
6	5	1	60	70	20	1.9	10.2	5.8	2.4
7	15	2	50	70	20	1.9	18.3	8	2.7
8	15	2	40	70	20	1.9	15.5	7.7	2.6
9	15	2	30	70	20	1.9	10.2	4	2.1
10	15	2	20	70	20	1.9	12.6	9.7	2.8
11	15	2	30	70	17	1.9	22.0	8	2.7
12	15	2	30	70	18	1.9	23.5	10	2.9
13	15	2	30	70	21	1.8	14.6	6.9	2.5

[(1)] All superscripts refer to the same table footnotes listed in **Table 4-2**.

4.3.2.1 Effect of plasma treatment conditions

Surface activation of PSf substrates by APP has been shown to be impacted by the exposure time to plasma (governed by the number of surface scans and scan speed) and plasma-surface separation (*PSS*) distance. The above plasma exposure conditions affect the number density of surface-active sites (and thus the grafted chain density), while surface etching can occur at excessive exposure to plasma [45, 49]. Thus, a wide range of membrane performance can result, for given GP conditions, depending on the specific conditions of APP surface activation. Indeed, membrane L_p range of 16.0-24.8 $L \cdot m^{-2} \cdot h^{-1} \cdot bar^{-1}$ and *MWCO* range of 6-11 kDa were achieved (**Figure 4-5** and **Table 4-2**) for PSf UF membranes with tethered PAA layer synthesized (at $[M]_o$=20 vol% at 70°C for 1h) post He/O_2 plasma PSf surface treatment at 1-3 scans and *PSS* distance of 5-15 mm. Surface activation efficiency is diminished at long *PSS* distance, and as a consequence, lower surface chain density is attained upon graft polymerization, consistent as has been reported in previous work [49]. On the other hand, at short *PSS* distance, plasma surface

etching may lead to pore enlargement while the tethered PAA chains reduce pore size (**Table 4-2)**. Indeed, as shown in **Figure 4-5**, for a given number of plasma exposure scans, membrane hydraulic permeability and *MWCO* are lower by up to 31.9% and 83.3%, respectively, at *PSS* distance of 10 mm relative to membrane performance at *PSS* of 15 mm and 5 mm.

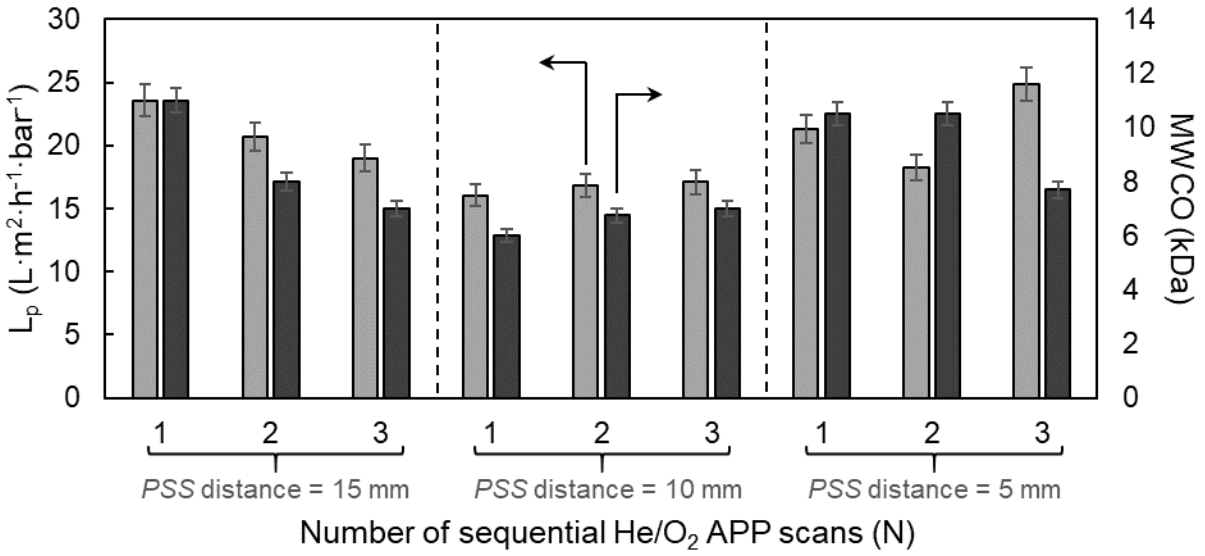

Figure 4-5. Dependence of SNS-PAA-PSf membranes (utilizing MUF-20K base membrane) hydraulic permeability (L_p) and *MWCO* on surface activation conditions (i.e., plasma source-surface (*PSS*) distance and number of sequential He/O_2 APP scans (*N*).

The interplay between plasma treatment source-surface separation distance and number of sequential scans is complex. As shown in **Figure 4-5**, for a given *PSS* distance, the hydraulic permeability and *MWCO* can either increase or decrease with the number of plasma scans. For example, at *PSS* of 15 mm, membrane L_p and *MWCO* decreased by 19.1% and 36.4%, respectively, as the number of scans increased from 1 to 3. At *PSS* of 5 mm, *MWCO* was lower by 26.7% for the membranes synthesized (via GP) post 3 scans of plasma surface activation relative to a single scan. On the other hand, at *PSS* of 10 mm the membrane L_p and *MWCO* increased by 6.9% and 16.7%, respectively, for base membranes graft polymerized post-plasma activation, as

the number of plasma scans increased from 1 to 3. Given the present study's focus on fine tuning membrane performance with the aim targeting the lowest *MWCO* range, plasma treatment at *PSS* of 10 mm and a single plasma source scan, which led to the lowest SNS-PAA-PSf membrane *MWCO (*6 kDa), were selected for subsequent demonstration of the impact of graft polymerization conditions on membrane performance tuning.

4.3.2.2 Effect of graft polymerization reaction temperature

Graft polymerization conditions such as temperature, initial monomer concentration and solution pH have been shown to impact the tethered layer chain density and chain length distribution [49, 287]. Over the temperature range of 50-90°C, the resulted SNS-PAA-PSf membranes water permeabilities were in the range of 12.3-32.8 $L \cdot m^{-2} \cdot h^{-1} \cdot bar^{-1}$ and *MWCO* in the range of 6-10 kDa (**Table 4-2** and **Figure 4-6**). As shown in **Figure 4-6**, SNS-PAA-PSf membranes *MWCO* appear to display a minimum with respect to the reaction temperature (at ~70°C). It is stressed that, although the rate of free radical polymerization increases with temperature [288, 289], premature chain termination (i.e., by combination or disproportionation) can occur at a higher temperature, thereby increasing the ratio of termination to propagation rates for the grafted polymer chains [261]. As a consequence, one should expect that the tethered chains will reach a maximum length with respect to temperature [287] and correspondingly a minimum *MWCO* will be attained for the SNS-PAA-PSf membranes which, in the present case, was 6 kDa in the vicinity of ~70°C. Although with increased temperature, thermal monomer initiation in the bulk solution should increase the probability of polymer grafting (i.e., "grafting to"), the decomposition of surface peroxide groups will also increase with rising temperature [287]. Thus, the tethered PAA layer thickness and chain density will increase with temperature and thus lead to

lower membrane hydraulic permeability (~62.5% decrease over the temperature range of 50°C to 90°C) as shown in **Figure 4-6**.

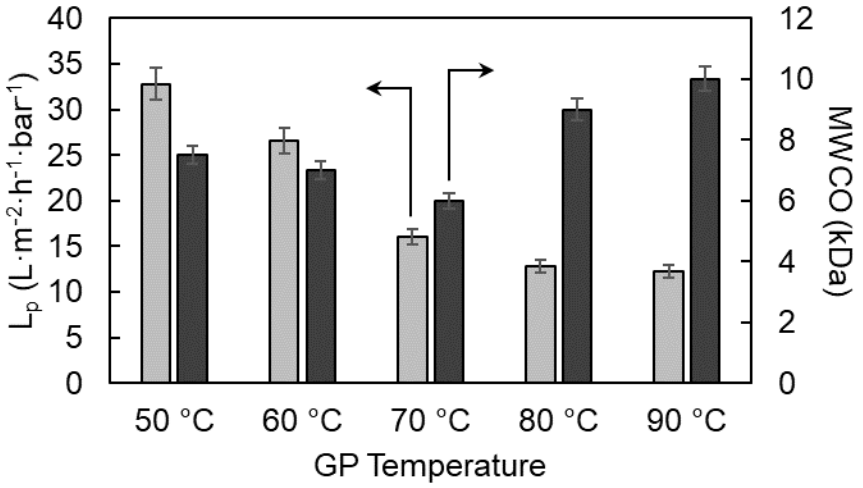

Figure 4-6. Effect of graft polymerization (GP) temperature on membrane hydraulic permeability (L_p) and *MWCO* for SNS-PAA-PSf membranes (utilizing MUF-20K base membrane).

4.3.2.3 Effect of initial monomer concentration

Tuning of the SNS-PAA-PSf membrane hydraulic permeability and *MWCO* can also be accomplished by adjusting the initial monomer concentration which impacts the resulting tethered polymer chain length [49]. In the current study, the reaction time of 60 min was determined to be sufficient, for the range of employed monomer concentrations, to achieve the sought UF performance. It is noted that SNS-PAA-PSf membranes synthesized at a shorter graft polymerization time had both higher hydraulic permeability and *MWCO* (**Figure 4-7**). As illustrated in **Figure 4-8** and **Table 4-2**, for the case of Toray MUF-20K base membrane, whose surface was activated via He/O_2 APP treatment at two different conditions (*PSS*=10 mm, *N*=1 and *PSS*=5 mm, *N*=3), the resulting SNS-PAA-PSf membranes had performance range of L_p =13.5-35.4 L·m^{-2}·h^{-1}·bar^{-1} and *MWCO*=3.9-12.5 kDa over the initial monomer concentration range of 15-25 vol%. With increased initial monomer concentration, a higher rate of monomer addition is

expected resulting in longer chains (i.e., thicker tethered polymer layer) [287]. On the other hand, excessively high initial monomer concentration can lead to early termination of growing tethered chains, due to chain transfer and termination with radical chains that may form in the bulk solution [49]. The above can thus result in nonuniform tethered layer thickness and possibly lower surface number density of the long chains. Therefore, it is not surprising that there are minima of both membrane L_p (13.5 $L \cdot m^{-2} \cdot h^{-1} \cdot bar^{-1}$) and *MWCO* (3.9 kDa) with respect to the initial monomer concentration (21 vol%), as shown in the example for membranes graft polymerized post-APP surface activation at *PSS*=10 mm and *N*=1. Similar behavior was observed for SNS-PAA-PSf membranes synthesized via graft polymerization, post He/O_2 APP treatment at *PSS*=5 mm and *N*=3, for which the membrane L_p and *MWCO* had minima of 21.3 $L \cdot m^{-2} \cdot h^{-1} \cdot bar^{-1}$ and 10.5 kDa, respectively, at $[M]_o$=20 vol% (**Figure 4-8**). The slight difference in monomer concentrations at which the L_p and *MWCO* minima were encountered for the SNS-PAA-PSf membranes were due to the difference in APP surface activation conditions (**Figure 4-5**). The above examples illustrate that fine tuning membrane performance can be attained by a combination of APP membrane activation and initial monomer concentration in the graft polymerization step.

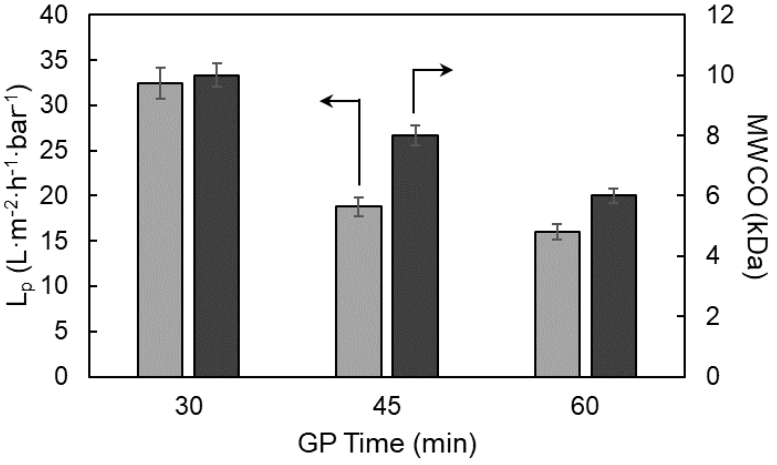

Figure 4-7. Dependence of SNS-PAA-PSf membranes (based on MUF-20K membrane) hydraulic permeability (L_p) and *MWCO* on graft polymerization time.

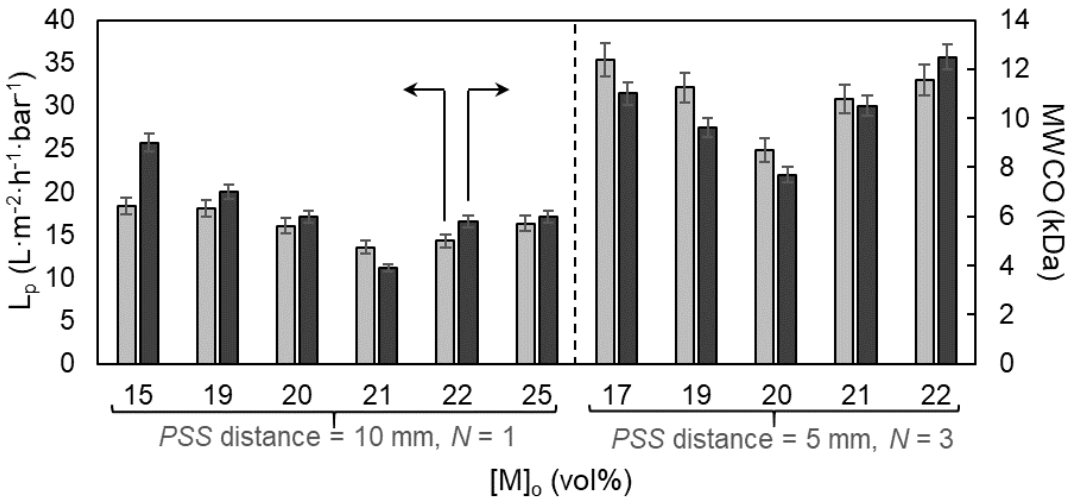

Figure 4-8. Effct of initial monomer concentration on membrane hydraulic permeability (L_p) and *MWCO* for SNS-PAA-PSf membranes (utilizing MUF-20K base membrane).

AFM surface characterization of the PAA-PSf-PEI-Si surfaces revealed minima of surface roughness, average FH, and average major peak separation distance (**Figure 4-1, Figure 4-2, Figure 4-3,** and **Table 4-1**), with respect to the initial monomer concentration, at $[M]_o$~20 vol%. Correspondingly, the minima of SNS-PAA-PSf membrane water permeability and *MWCO* were also found at $[M]_o$ of ~20-21 vol% (**Figure 4-8**), suggesting that SNS-PAA-PSf membrane performance correlates with the above tethered brush layer surface characteristics. At monomer concentrations above and below the membrane performance minima (i.e., in terms of hydraulic permeability and *MWCO*), the surface tethered PAA chain density and layer thickness decreased and thus led to lower membrane resistance and higher *MWCO*. Given that the tethered chains surface density and thickness, which have an impact on the resulting SNS-PAA-PSf membrane performance, are governed by the polymerization and APP surface activation conditions, it is feasible to tailor SNS-PAA-PSf membrane performance through tuning of the above membrane synthesis conditions.

4.3.2.4 Effect of initial monomer solution pH

The resulting SNS-PAA-PSf membrane performance was most affected by the initial pH of the graft polymerization monomer solution. Membranes derived graft polymerization at monomer solution pH in the range of 1.8-13.5, had L_p and *MWCO* ranges of 7.8-43.3 $L \cdot m^{-2} \cdot h^{-1} \cdot bar^{-1}$ and 3.9-11.5 kDa, respectively (**Figure 4-9** and **Table 4-2**), both demonstrating maxima with respect to the monomer solution pH. The maxima of SNS-PAA-PSf membrane hydraulic permeability (43.3 $L \cdot m^{-2} \cdot h^{-1} \cdot bar^{-1}$) and *MWCO* (11.5 kDa) were achieved at initial monomer solution pH of 4.7 and 5.9, respectively (pKa for AA is about 4.2, relative to pKa~4.5 for PAA [290]). The above results can be rationalized by noting the monomer becomes more ionized [291] as the pH increases toward the AA pKa (~4.2). Correpondingly, increased AA monomer ionization will impede the rate of graft polymerization [292] as the reaction solution pH approaches the monomer pKa. It is also noted that the isoelectric point for the PAA tethered membrane surface, which depends on the tethered chains graft density, has been reported to be in the pH range of 4-6 [293, 294]. Accordingly, as the isoelectric point is approached, the formed tethered PAA chains would be in a more collapsed configuration, and hence a potentially lower degree of monomer accessibility to active chain ends. Given the above, it is reasonable to expect that as the graft polymerization solution pH approaches the range of 4-6, shorter tethered chains will form, and thus both membrane hydraulic permeability and *MWCO* would correspondingly increase. Accordingly, it is not surprising that the SNS-PAA-PSf membranes displayed hydraulic permeability reduction up to 82.0% and 68.8% as the monomer solution pH increased above and decreased below pH~4.7 (i.e., within the range of the pKa of AA and isoelectric point of PAA), respectively. Similarly, membrane *MWCO* reduction was of up to 53.9% and 66.1% as the monomer solution pH increased above and decreased below pH of 5.9, respectively.

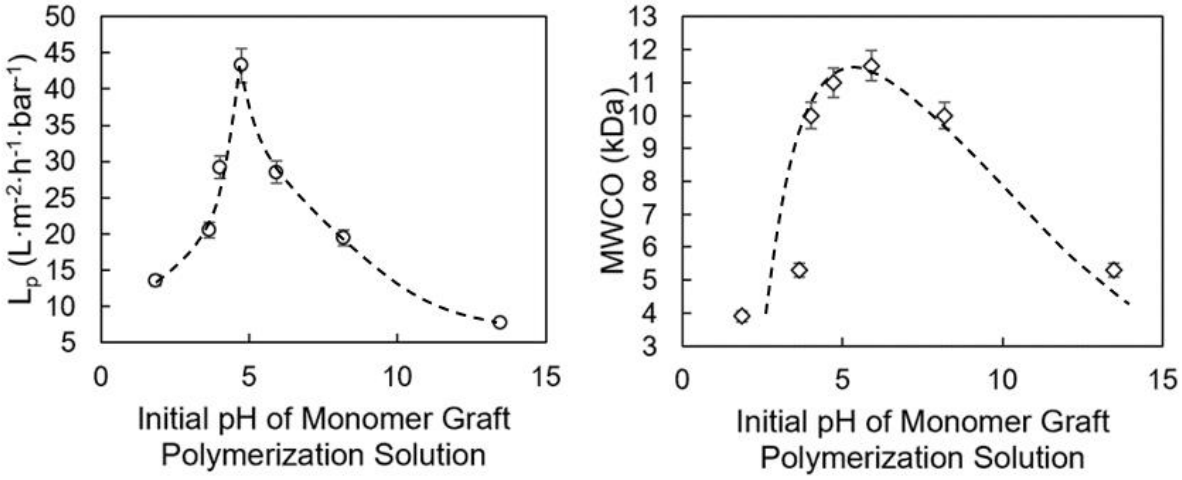

Figure 4-9. The effect of initial monomer solution pH on (a) membrane hydraulic permeability (L_p) and (b) *MWCO* for SNS-PAA-PSf membranes (prepared using base membrane MUF-20K).

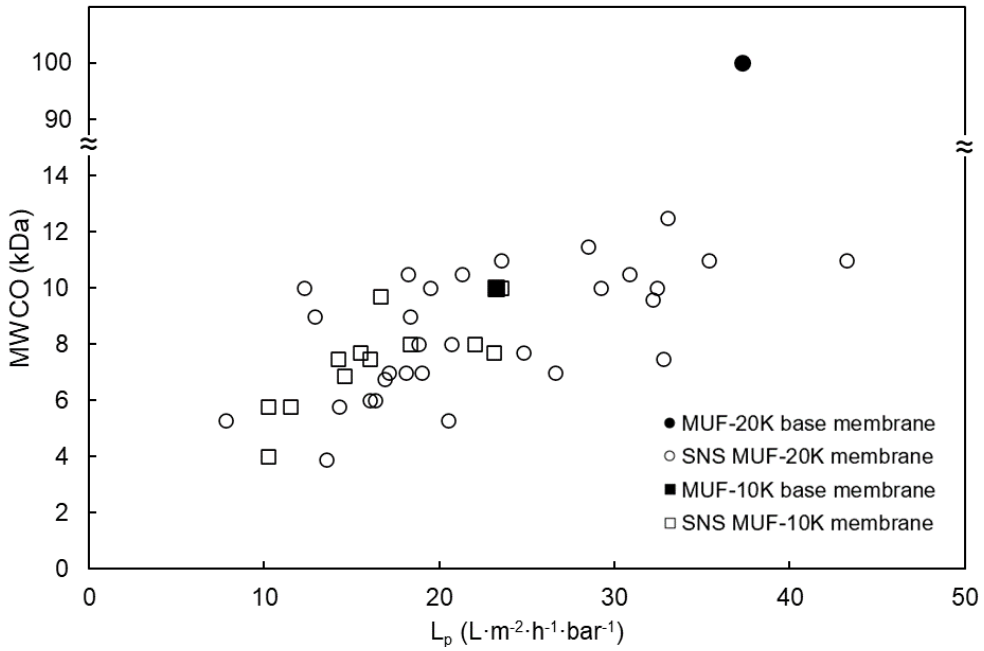

Figure 4-10. Dependence of membrane performance (*MWCO* and hydraulic permeability) tunability range of SNS-PAA-PSf membranes derived based on two different UF base membranes: (a) MUF-10K and (b) MUF-20K. SNS-PAA-PSf membrane performance was tuned by adjustment of various plasma and graft polymerization conditions.

4.3.2.5 Impact of base membrane on SNS-PAA-PSf membrane performance

Previous studies have suggested that narrowing of UF membrane pores by surface grafted polymers contributes directly to both reduced water permeance and *MWCO* [141]. Therefore, the

pore structure of the base membrane (and thus its hydraulic permeability and *MWCO*) will impact the resulting membrane performance upon graft polymerization. One should expect that a UF base membrane of sufficiently high membrane hydraulic permeability and *MWCO (*MUF-20K) would enable tuning SNS-PAA-PSf membranes with a broader range of membrane performance. For example, with the MUF-20K base membrane, the derived SNS-PAA-PSf membranes were with hydraulic permeability and *MWCO* ranges of 7.8-43.3 $L \cdot m^{-2} \cdot h^{-1} \cdot bar^{-1}$ and 3.9-12.5 kDa, respectively, relative to the corresponding performance of L_p =37.4 $L \cdot m^{-2} \cdot h^{-1} \cdot bar^{-1}$ and *MWCO*=100 kDa for the base membrane (**Table 4-2**; **Figure 4-10**). On the other hand, with a tighter UF base membrane (MUF-10K), one can synthesize SNS-PAA-PSf membranes that are tuned at a finer resolution but with lower and narrower ranges of L_p (10.2-23.5 $L \cdot m^{-2} \cdot h^{-1} \cdot bar^{-1}$) and *MWCO* (4-10 kDa) (**Table 4-3**; **Figure 4-10**), relative to the corresponding base membrane performance of L_p=23.2 $L \cdot m^{-2} \cdot h^{-1} \cdot bar^{-1}$ and *MWCO*=10 kDa. Here it is stressed that the relative membrane hydraulic permeability and *MWCO* reductions, upon AA graft polymerization, were higher for SNS-PAA-PSf membranes derived based on the looser UF base membrane relative to a tighter one (**Table 4-2** and **Table 4-3; Figure 4-10)**. For example, AA graft polymerization onto the more permeable MUF-20K base membrane resulted in SNS-PAA-PSf membranes that had more significant reductions in both L_p (up to 79.1%) and *MWCO* (up to 96.1%). By comparison, SNS-PAA-PSf membranes synthesized using a tighter base membrane (MUF-10K) displayed a lower degree of L_p and *MWCO* reduction of up to 56.2% and 60.0%, respectively. As revealed in the present study, the hydraulic resistance due to the tethered chains appears to be dominant in reducing the hydraulic permeability. It is possible, however, that increased hydrophilicity imparted by the tethered hydrophilic PAA layer, as verified by contact angle measurements (**Table 4-4**) and consistent with previous work on PAA tethered layers on PSf, may lead to decreased hydraulic

resistance and thus compensate, to some degree, for the increased resistance due to the added layer of tethered chains. Indeed, in a number of cases, the hydraulic permeability of the SNS-PAA-PSf membranes was within ±1.3-5.3 % (Membranes #22, **Table 4-2** and Membranes #2, #11, and #12, **Table 4-3**) of the values of their respective base membranes which can be considered to be within the experimental uncertainty. The *MWCO* for the same membranes was about the same or lower relative to the base membranes. A striking example is Membrane #22 (**Table 4-2**) for which the *MWCO* was reduced by about a factor of nine, while the hydraulic permeability was reduced by merely 5.3% (within the range of experimental uncertainty). It is interesting to note that in one particular case, SNS-PAA-PSf Membrane #28 (**Table 4-2**), synthesized from base membrane MUF-20K, had somewhat higher hydraulic permeability (by ~16%), but displayed significantly lower (by 89%) *MWCO* relative to the base MUF-20K membrane. As shown in the summary of the different SNS-PAA-PSf membranes (**Table 4-2** and **Table 4-3**) membrane performance can be tuned by the tethered layer synthesis conditions as further discussed in **Section 4.3.3**.

4.3.3 Tailored membrane performance summary

Given that the tethered PAA layer properties (i.e., chain surface number density and length) are governed by APP surface activation and graft polymerization conditions, one has a wide array of synthesis parameters that can be adjusted to tune SNS-PAA-PSf membrane performance. For the present choice of base membranes, SNS-PAA-PSf membranes were synthesized with performance that spanned a hydraulic permeability range of 7.8-43.3 $L \cdot m^{-2} \cdot h^{-1} \cdot bar^{-1}$ and *MWCO* range of 3.9-12.5 kDa. The qualitative trends of tuning SNS-PAA-PSf membrane performance, in terms of hydraulic permeability and *MWCO*, with APP surface activation conditions (i.e., *PSS* distance and *N*) and graft polymerization conditions (reaction temperature, initial monomer

concentration, and monomer solution pH) are summarized in **Table 4-5**. One can fine tune the SNS-PAA-PSf membrane performance by adjusting the above synthesis parameters. Minima of hydraulic permeability and *MWCO* were observed with respect to APP surface activation conditions (i.e., *PSS* distance and *N*), and initial monomer concentration. In contrast, hydraulic permeability and *MWCO* maxima were observed for SNS-PAA-PSf membranes with respect to the graft polymerization initial monomer solution pH. The existence of both maximum and minimum membrane hydraulic permeability and *MWCO* values were due to multiple competing factors that affect PSf surface activation and free radical polymerization kinetics. A noted exception to the above is that as the graft polymerization temperature increased (within the current evaluated range), the hydraulic permeability of the synthesized SNS-PAA-PSf membranes continued to decrease.

Through a judicious choice of the base membrane and SNS-PAA-PSf synthesis conditions, it should be possible to potentially overcome (to some degree) the hydraulic permeability-rejection (or *MWCO*) tradeoff (i.e., improving membrane hydraulic permeability without sacrificing *MWCO*). To quantify the ability to fine-tune membrane performance in terms of the attainable hydraulic permeability-*MWCO* performance, the separations performance data (**Table 4-2**) are shown in **Figure 4-11**. SNS-PAA-PSf membranes were synthesized with essentially the same *MWCO* performance but over a wide hydraulic permeability range (**Figure 4-11a**) or a given hydraulic permeability over a range of *MWCO* (**Figure 4-11b**). For example, starting with the base MUF-20K membrane, SNS-PAA-PSf membranes of permeability of 13.2 $L \cdot m^{-2} \cdot h^{-1} \cdot bar^{-1}$ and 32.8 $L \cdot m^{-2} \cdot h^{-1} \cdot bar^{-1}$ were derived with target *MWCO* ranges of 3.9-9 kDa (membranes #15 and 19 from **Table 4-2**) and 7.5-12.5 kDa (membranes #11, 13, 23 and 25 from **Table 4-2**), respectively. In another example, SNS-PAA-PSf membranes of *MWCO* of 5.3 kDa and 10 kDa were produced

(starting with the same MUF-20K base membrane) with hydraulic permeability ranges of 7.8-20.5 $L \cdot m^{-2} \cdot h^{-1} \cdot bar^{-1}$ (membranes #26 and 31 from **Table 4-2**) and 12.3-32.4 $L \cdot m^{-2} \cdot h^{-1} \cdot bar^{-1}$ (membranes #11, 16, 27, and 30 from **Table 4-2**), respectively.

Table 4-4. PSf and SNS-PAA-PSf surface hydrophilicity measured via sessile drop (SD) water contact angle.

No.	Membrane Surface		SNS-PAA-PSf-Si Substrate (Surrogate model membrane surface[a])	
	SD water Contact Angle (°)	Uncertainty (°)	SD Water Contact Angle (°)	Uncertainty (°)
Base-PSf	66.3[b]	±1.8	89.4[c]	±1.9
SNS-PAA-PSf 1[d]	52.1	±2.1	44.5	±1.6
SNS-PAA-PSf 2[e]	57.2	±1.5	57.3	±2.2
SNS-PAA-PSf 3[f]	60.6	±1.7	75.5	±1.7

[a] Model PSf-PEI-Si surface and the SNS-PAA-PSf-Si surfaces post APPIGP surface modification. The synthesis procedure is given in **Section 4.2.2**.

[b] Base-PSf membrane here refers to the Toray MUF-20K membrane, which is also the base membrane used to synthesis the SNS-PAA-PSf membranes 1, 2, and 3. A similar SD water contact angle for the native PSf membrane surface was previously reported in [295].

[c] Base-PSf surrogate membrane surface refers to the native PSf-PEI-Si surface. A similar SD water contact angle for PSf-PEI-Si surface was previously reported [54].

[d] SNS-PAA-PSf 1 surface was synthesized via He/O_2 plasma activation (N=1, *PSS*=5 mm), followed by graft polymerization at $[M]_o$=20 vol%, pH = 1.9 at 70°C for 1h. Membrane performance data are given in **Table 4-2**, membrane #2.

[e] SNS-PAA-PSf 2 surface was synthesized via He/O_2 plasma activation (N=1, *PSS*=10 mm), followed by graft polymerization at $[M]_o$=20 vol%, pH = 1.9 at 70°C for 1h. Membrane performance data are given in **Table 4-2**, membrane #5.

[f] SNS-PAA-PSf 3 surface was synthesized with He/O_2 plasma activation (N=1, *PSS*=15 mm), followed by graft polymerization at $[M]_o$=20 vol%, pH = 1.9 at 70°C for 1h. Membrane performance data are given in **Table 4-2**, membrane #8.

Table 4-5. Summary of the trend of SNS-PAA-PSf membranes L_p and *MWCO* with respect to surface nano-structuring (APP and GP) conditions.

Membrane surface nano-structuring conditions	L_p	*MWCO*	Relevant Figure
Number of sequential plasma exposure scans (*N*)	minimum exists as combination with *PSS*	minimum exists as combination with *PSS*	Fig. 5
Plasma source-surface separation (*PSS*) distance	minimum exists	minimum exists	Fig. 5
GP temperature	Decreases with increasing temperature	minimum exists	Fig. 6
$[M]_o$	minimum exists	minimum exists	Fig. 7
Initial monomer solution pH	maximum exists	maximum exists	Fig. 8

Starting with a loose UF base membrane (**Table 4-2**, **Figure 4-10**), it should be possible to derive SNS-PAA-PSf membranes of a hydraulic permeability similar to that of a commercial tight UF base membrane, but with a wide range of tailored *MWCO*. For example, SNS-PAA-PSf membranes #2, 8, 9, and 26 (**Table 4-2**) produced using base membrane MUF-20K, had a similar hydraulic permeability range as the commercial MUF-10K membrane but tailored (targeted) *MWCO* over the range of 5.3-11 kDa (i.e., 47% lower to 10% higher relative to the MUF-10K membrane). It should also be feasible to tune the SNS-PAA-PSf membranes to attain the target *MWCO* of a tight UF commercial base membrane but with a wide range of target water permeability. For example, SNS-PAA-PSf membranes #11, 16, 27, and 30 (**Table 4-2**) had essentially the same *MWCO* as the commercial MUF-10K UF membrane, but with water permeability range of 12.3-32.4 $L \cdot m^{-2} \cdot h^{-1} \cdot bar^{-1}$ (i.e., 47% lower to 39.7% higher compared to MUF-10K membrane).

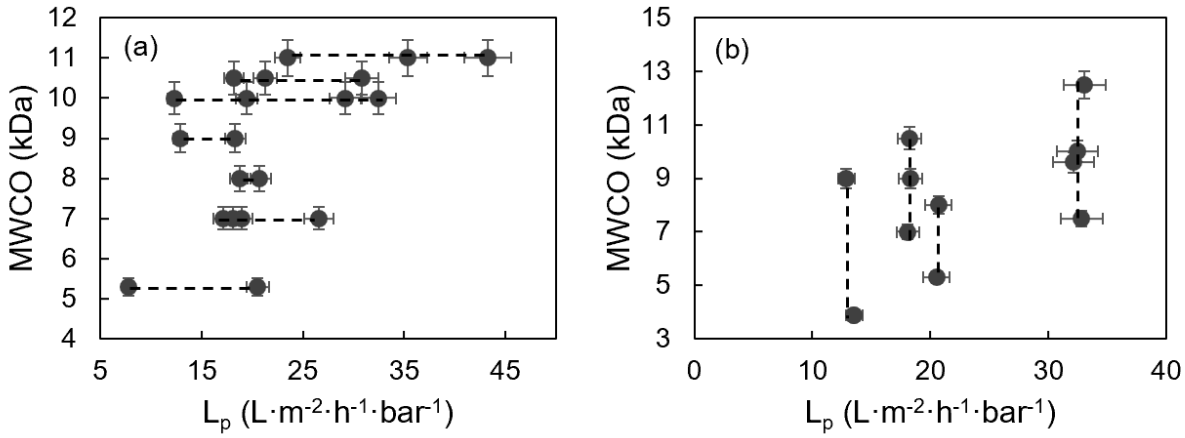

Figure 4-11. Mapping of *MWCO* and hydraulic permeability of SNS-PAA-PSf membranes (synthesized utilizing base membrane MUF-20K) at various plasma and graft polymerization conditions that achieve (a) a range of hydraulic permeability at a target *MWCO*, and (b) a range of *MWCO* at essentially the same hydraulic permeability.

Another approach to visualizing the tradeoff for the SNS-PAA-PSf and other reported modified UF membranes [296-298] is shown in **Figure 4-12a.** For the *MWCO* range of 5.3-12.5 kDa the SNS-PAA-PSf membranes displayed higher hydraulic permeability (by a factor of ~2-30) relative to reported literature data for modified membranes. The above *MWCO* is lower by 25.0-95.6% relative to other reported membranes, for the hydraulic permeability range of 7.8-43.3 L·m^{-2}·h^{-1}·bar^{-1}. A more distinct visualization of the difference in membrane performance is shown in **Figure 4-12b** in which the variation of the tradeoff ratio of $L_p/MWCO$ with hydraulic permeability. For example, the utilization of such hydraulic permeability-*MWCO* tradeoff measure visually accentuated the gain in hydraulic permeability relative to the decrease in attained *MWCO*. The ability to tailor the SNS-PAA-PSf membrane performance over $L_p/MWCO$ ratio range of 1.2-4.4 L·m^{-2}·h^{-1}·bar^{-1}·kDa^{-1} (with the highest more than doubled the reported literature values shown in **Figure 4-12b**) was achieved over a hydraulic permeability range of 23.2-32.8 L·m^{-2}·h^{-1}·bar^{-1}. In other words, APPIGP tuning of suitable UF base membranes can allow us to attain a significantly

lower *MWCO* for a given hydraulic permeability, and, in part, overcoming the hydraulic permeability-*MWCO* tradeoff barrier.

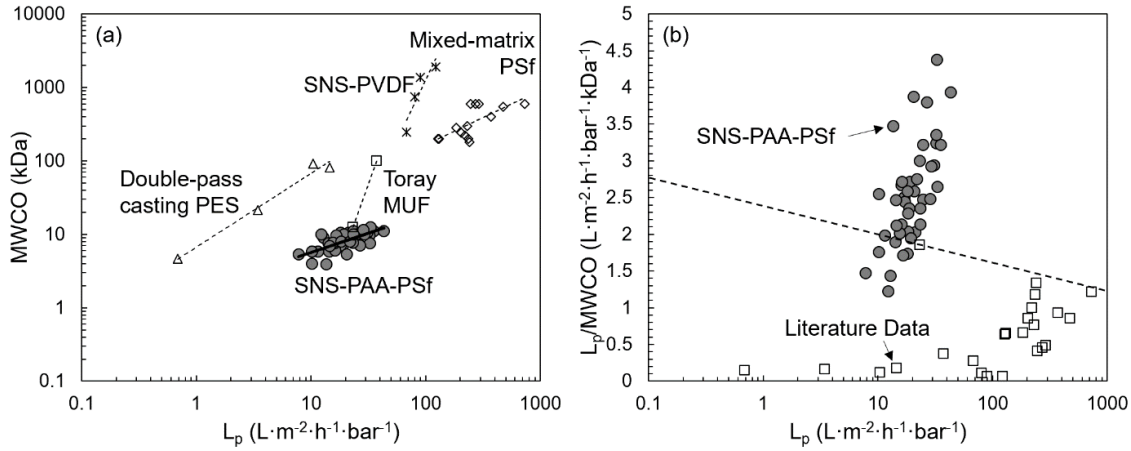

Figure 4-12. Comparison of SNS-PAA-PSf membranes performance, at various plasma and graft polymerization conditions, and for other modified and the present commercial base UF membranes (Toray-MUF: 10K and 20K), demonstrating (a) tradeoff relationship between membrane *MWCO* and hydraulic permeability, and (b) $L_p/MWCO$ ratio vs the water permeability.

4.4 Conclusions

Tailoring the performance of polysulfone (PSf) ultrafiltration (UF) membrane, via surface modification with tethered hydrophilic polymer chains, was evaluated in a systematic investigation in which base membranes were modified by atmospheric pressure plasma (APP) induced graft polymerization (GP) of acrylic acid (AA). UF membrane performance tuning was achieved, with respect to hydraulic permeability and molecular weight cutoff (*MWCO*), by adjustment of APP surface treatment and graft polymerization conditions. The SNS-PAA-PSf exhibited both membrane hydraulic permeability and *MWCO* minima with respect to the graft polymerization initial AA monomer concentration. Here we note that AFM analysis of the tethered PAA layer topography, on a relatively smooth model PSf surface substrate, revealed tethered PAA layer surface roughness, feature height, and major peak separation distance that also displayed minima

with respect to the initial monomer concentration at about the same level (i.e., 20 vol%) at which the minima of membrane hydraulic permeability and *MWCO* were also observed.

It was shown, for the first time, that PAA surface-nano-structured (SNS) PSf membranes' performance can be tuned to achieve a range of *MWCO* (spanning a factor of 1.5-2.3 in magnitude) for a given hydraulic permeability or conversely a hydraulic permeability range (spanning a factor of 1.1-2.6 in magnitude) for a given *MWCO*. Relative to other reported modified UF membranes, at a comparable *MWCO* range of 5.3-12.5 kDa, the SNS-PAA-PSf membranes had a higher hydraulic permeability by a factor of ~2-30. While the current results suggest a feasible means of tuning UF membranes, admittedly application of the present approach, beyond that of specialized small-scale applications, would require process adaptation and optimization that consider technical and economic scalability.

Chapter 5 PSf UF Membrane Performance Tuning via APPIGP surface activated by Air and He plasmas

5.1 Overview

It was shown in **Chapter 4** that PSf UF membrane performance can be tuned via AA graft polymerization, induced by surface activation with He/O_2 APP. It was also shown that PSf UF membranes could be synthesized with a molecular weight cutoff (*MWCO*) range for essentially the same water permeability, and a range of permeabilities for a given *MWCO* [156]. In addition to the above plasma treatment and AA graft polymerization conditions, the types of plasma used for surface activation can also be used to tune membrane performance. Moreover, such an approach of UF membrane performance tuning requires purified gases and thus is not attractive for scale up of the process to large membrane areas. In this regard, utilization of the lower-cost Air APP for surface activation, if effective, would be beneficial given the potential scalability of the approach.

Air plasma has other desirable advantages, such as: (1) effectiveness in hydrophilic modification via surface implantation of oxygen-containing polar groups [140]; (2) improvement of surface biocompatibility by introducing nitrogen-containing radicals [299]; (3) introduction of ampheric surface character and thus enhancement of membrane fouling resistance [140]; (4) generation of high-density ions [154, 300] and thus polar groups on the membrane surface, which may be active for inducing post-reactions; and most importantly (5) reduction in system complexity and operating cost given the operation with ambient air [150, 263, 301].

As was shown in **Chapter 3**, among the tested atmospheric pressure Air, He, and He/O_2 plasmas, PSf surface treatment with Air plasma resulted in the highest degree of surface hydrophilicity and oxygen composition suggesting that this plasma resulted in a higher surface

concentration of hydrophilic oxygen-enriched functional groups [278]. Consequently, the feasibility of tuning the surface nano-structured (SNS) membrane performance with surface tethered polyacrylic acid (PAA) brush layer, synthesized post Air plasma, was investigated with respect to hydraulic permeability and molecular weight cutoff (*MWCO*). Atmospheric pressure Air plasma surface activation conditions were varied (*PSS*=5-15 mm, *N*=1-3). The resulting membrane performance tunability was then compared with the SNS-PAA-PSf membrane surface activated by He/O_2 plasma from **Chapter 4**.

5.2 Experimental

5.2.1 Materials

PSf membrane (MUF-20K, Toray Membrane USA Inc., Poway, CA) with manufacturer reported 100 kDa *MWCO* was selected as the base membrane for surface nano-structuring (SNS) with tethered PAA layer. Also, a commercial PSf membrane (MUF-10K; Toray Membrane USA Inc., Poway, CA) was used for performance comparison. Both of the above membranes were obtained as flat sheets. Nitrogen (99%) gas (Airgas, Los Angeles, CA) was used for PSf sample drying, graft polymerization degassing, and UF system feed tank pressurizing. Acrylic acid (99%, Sigma-Aldrich, St. Louis, MO) was the hydrophilic monomer used for graft polymerization to form poly(acrylic acid) chains tethered onto the PSf surfaces, post-activation with atmospheric pressure plasma. All solutions were prepared in deionized (D.I.) water produced with a Milli-Q filtration system (Millipore Corp., San Jose, CA). Polyethylene glycol (PEG, *Mw* from 2,000 to 35,000 Da, Sigma-Aldrich, St. Louis, MO) was used for membrane *MWCO* characterization.

5.2.2 Atmospheric pressure plasma-induced graft polymerization (APPIGP)

The tethered PAA layer was synthesized onto the base PSf UF membrane (MUF-20K) via a two-step process (**Appendix C**), comprising of PSf membrane surface activation via exposure to APP, followed by AA free-radical graft polymerization [55, 156, 278]. The base membrane coupons were, kept in D.I. water for at least 24 hr, and then thoroughly rinsed with D.I. water, and subsequently dried via an impinging nitrogen stream prior to surface activation with plasma. PSf membrane surface activation was accomplished using FG5001 Plasma Generator (Plasmatreat USA, Inc., Elgin, IL), which was operated with the frequency of 21 kHz, voltage of 280 V, and Plasma Cycle Time (PCT) of 100%. The plasma was discharged via dispensing jets installed on an XYZ scanning robot (Surfx Technologies Inc., Redondo Beach, CA). Surface activation was accomplished via 1-3 sequential plasma scans (*N*) at a speed of 100 mm/s and source-surface separation (*PSS*) distance in the range of 5-15 mm.

Following APP activation, the membranes were immersed in aqueous AA monomer solutions ($[M]_o$ ~20 vol%) in 250 mL capped glass vials immersed in a constant temperature water bath at 70°C for 60 min. Nitrogen was bubbled into the reaction tubes (via tubes inserted through the sealed tube caps) during graft polymerization to promote mixing and scavenge dissolved oxygen that could inhibit the graft polymerization reaction [55]. After the graft polymerization, the resulting membranes were kept in D.I. water for at least a 24 hr period prior to their characterization.

5.2.3 UF Performance characterization

Membrane performance was evaluated with circular membrane coupons (active area of 13.4 cm^2) in a dead-end filtration configuration consists of a 50 mL stirred UF cell (Amicon 8050,

Millipore Corporation, Burlington, MA) interfaced with an 800 mL feed tank pressurized using nitrogen (**Appendix D**). Membrane hydraulic permeability coefficient and *MWCO* were determined as per a previously reported protocol [55, 156, 278]. Briefly, the membrane samples were first compacted with D.I. water at 3.5 bar (~50 psi) and ~20°C for a 3 hr period prior to performance characterization.

Water flux ($J_v=Q_p/A$, in which Q_p and A are the permeate flow rate and membrane area, respectively) was determined over an applied pressure range of 0-3.5 bar (0-50 psi). The permeate flow rate was determined using an in-line liquid flow meter (SLS-1500, Sensirion AG, Switzerland) with a maximum deviation of ±5% from the measured value. The pressure, set via a pressure regulator (Type 90, Control Air Inc., Amherst, NH), was measured using a pressure gauge (33HP99, Grainger, Lake Forest, IL) with a maximum measurement error of ±0.4% of the full scale reading of 60 psi. The hydraulic permeability coefficient (L_p) was then determined from the slope of water flux versus transmembrane pressure (i.e., $L_p = J_v / \Delta P$, where ΔP is the applied transmembrane pressure) [46].

The molecular weight cutoff (*MWCO*), defined as the solute *Mw* rejected by the membrane at a level of 90% [55], was determined for each membrane using 1 g/L aqueous solutions of PEG fractions with *Mw* in the range of 2,000 – 35,000 Da. PEG concentrations in the feed (C_f) and in the permeate (C_p) were determined by a Total Organic Carbon (TOC) Analyzer (Aurora 1030W, OI Analytical, College Station, TX) with a maximum measured value uncertainty of ±2%. The observed (nominal) rejection (i.e., $R_o = (1 - C_p / C_f) \times 100\%$) for the different PEG fractions was correlated with the PEG *Mw*, serving to determine the *Mw* fraction corresponding to 90% rejection which was then designated as the membrane *MWCO*. All *MWCO* determinations were carried out

at the same initial permeate flux of 9 $L \cdot m^{-2} \cdot h^{-1}$ (~5.3 $gallon \cdot ft^{-2} \cdot day^{-1}$). Both the membrane and the UF filtration system were thoroughly rinsed with D.I. water after each filtration run.

5.3 Results and Discussion

5.3.1 Influence of surface plasma treatment on SNS-PAA-PSf membrane performance

Surface modification of PSf UF membranes, via surface activation with Air APP followed by acrylic acid (AA) graft polymerization, enabled tuning of membrane performance (i.e., hydraulic permeability coefficient and *MWCO*). SNS-PAA-PSf UF membranes were synthesized at different levels of performance (**Fig. 5-1** and **Table 5-1**) depending on the chosen plasma type and plasma surface activation conditions (e.g., plasma source-surface separation distance (*PSS*) and the number of sequential scans (*N*)). It is stressed that the membrane permeability and *MWCO* for the SNS-PAA-PSf membranes modified based on Air APP surface activation did not increase relative to the base PSf UF membrane (**Table 5-1**). Therefore, it is reasonable to conclude that Air APP surface treatment did not lead to surface etching that would have degraded membrane performance. It is also possible that graft polymerization ameliorated the impact of membrane etching by providing effective "pore filling."

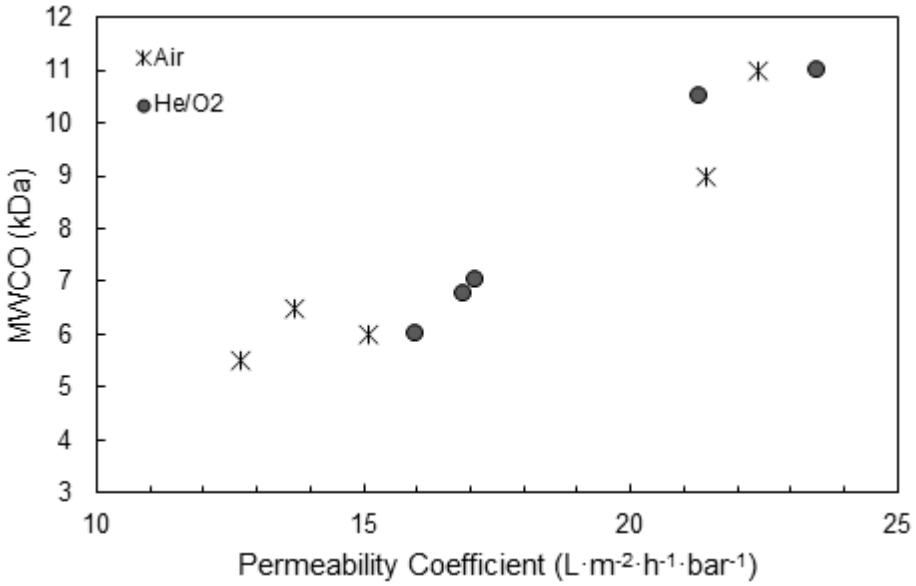

Figure 5-1. Permeability coefficient and *MWCO* for the SNS-PAA-PSf membranes synthesized via surface activation Air APP over a range of different operating conditions. Also shown are data from [156] for SNS-PAA-PSf UF membranes synthesized via AA graft polymerization post-surface activation with He/O_2 plasma. (Membrane synthesis conditions and performance data are provided in **Table 5-1**).

Over the range of plasma surface activation conditions, the SNS-PAA-PSf membranes had permeability coefficient (L_p) and *MWCO* in the ranges of 12.7-23.5 $L \cdot m^{-2} \cdot h^{-1} \cdot bar^{-1}$ and 5.5-11 kDa, respectively (**Fig. 5-1**). Both L_p and *MWCO* for the SNS-PAA-PSf membranes were reduced by 37.2%-66.0% and 89-94.5%, respectively, relative to the base PSf UF membrane (**Table 5-1**). The above trends are attributed to the added hydraulic resistance and pore narrowing (or blocking) due to the tethered PAA chains [156]. As shown in **Fig. 5-1**, the above range of UF membrane performance is similar to previously reported results for SNS-PAA-PSf membranes (based on Toray MUF-20K PSf UF membrane), synthesized via AA graft polymerization post-surface activation with He/O_2 plasma [156]. The previous approach, however, requires the utilization of high purity helium and oxygen gases relative to the significantly lower cost membrane surface modification with atmospheric pressure Air plasma.

Table 5-1. Summary of performance for the SNS-PAA-PSf[a] and commercial PSf membranes.

No.	Plasma Treatment Conditions			Membrane Properties		
	Type	*PSS* Distance[b] (mm)	*N*[c]	Permeability[d] ($L \cdot m^{-2} \cdot h^{-1} \cdot bar^{-1}$)	*MWCO*[e] (kDa)	Pore Size[f] (nm)
MUF-20K (Base)	-	-	-	37.4	100	6.3
MUF-10K	-	-	-	23.2	10	2.9
1	Air	15	1	21.4	9	2.8
2	Air	10	1	13.7	6.5	2.5
3	Air	5	1	22.4	11	3.0
4	Air	10	2	15.1	6	2.4
5	Air	10	3	12.7	5.5	2.3
6[g]	He/O_2	15	1	23.5	11	3.0
7[g]	He/O_2	10	1	16.0	6	2.4
8[g]	He/O_2	5	1	21.3	10.5	2.9
9[g]	He/O_2	10	2	16.9	6.8	2.5
10[g]	He/O_2	10	3	17.1	7	2.5

[a] AA graft polymerization conditions: $[M]_o$ = 20 vol% at 70 °C for 1 h; [b]*PSS* - plasma source-surface separation distance; [c] No. of sequential plasma surface scans (*N*) each performed at a speed of 100 mm/s; [d] Hydraulic permeability coefficient (L_p) determined (uncertainty ± 5.4%) with D.I. water (post membrane at 3.5 bar (50 psi) pressure for 3 hours at ~20°C; [e] Molecular weight cutoff (*MWCO*) determined (estimated error: ± 4%) using PEG Mw fractions (2,000-35,000 Da) ; [f] Pore size estimated based on *MWCO* - pore diameter data provided in [302] described by the correlation $d_p = 1.3095 \times MWCO^{0.3409}$ nm [156]); [g] Adapted from [156]. Note: SNS-PAA-PSf membranes are at the low pore size range of UF membranes [303].

Table 5-2. Cost analysis of the research grade SNS-PAA-PSf membrane coupon synthesis. The use of Air plasma can lead to significant cost reduction relative to He/O_2 plasma.

Items	Air plasma ($/coupon)	He/O_2 plasma ($/coupon)
Plasma Process		
Plasma gas(es)[a]	-	1.85
Electricity	0.06	0.08
Total	*0.06*	*1.93*
Graft Polymerization		
Base membrane sheet	0.03	0.03
AA	0.55	0.55
Nitrogen	1.06	1.06
Electricity (26.71 ¢/kWh)	0.26	0.26
Total	*1.90*	*1.90*
SUM	1.96	3.83

[a]The entire plasma treatment process (i.e., controller tuning, robot movement) can take 40-70 s depending on the number of sequential pass(es).

5.3.2 Cost analysis and future scale-up expectations

Based on the knowledge of the feasibility of applying Air APP in membrane surface modification (**Chapters 3** and **5**), cost analysis for the SNS-PAA-PSf membrane synthesis was carried out. The use of Air plasma should significantly reduce the cost of membrane surface activation relative to the generation of plasma with purified gases. Compared to He/O_2 plasma, the use of Air APP indeed reduces the cost of PSf surface activation by a factor of ~32, which lead to the reduction of the overall membrane synthesis cost by up to 48.8%. It is noted the total cost of research grade SNS-PAA-PSf membrane synthesis price is around $1.96-3.83/coupon, calculated based on the material/chemicals and electricity usage for surface modification of PSf UF membranes. Nitrogen bubbling cost accounted for 28-54% of the total cost. In this regard, it is expected that for commercial production, nitrogen could be generated at a much lower cost via membrane gas separation of air to produce nitrogen. Also, the cost of AA monomer at bulk quantities should be significantly lower.

Membrane surface activation with Air APP followed by acrylic acid (AA) graft polymerization, enabled tuning of membrane performance (i.e., hydraulic permeability coefficient and *MWCO*). SNS-PAA-PSf UF membranes were synthesized at different levels of performance (**Fig. 5-1** and **Table 5-1**) depending on the selected plasma type and plasma surface activation conditions (e.g., plasma source-surface separation distance (*PSS*) and the number of sequential scans (*N*)). It is stressed that the membrane permeability and *MWCO* for the SNS-PAA-PSf membranes modified based on Air APP surface activation did not increase relative to the base PSf UF membrane (**Table 5-1**). Therefore, it is reasonable to conclude that Air APP surface treatment did not lead to surface etching that would have degraded membrane performance. It is also possible that graft polymerization ameliorated the impact of membrane etching by providing effective "pore filling."

Over the range of plasma surface activation conditions, the SNS-PAA-PSf membranes had permeability coefficient (L_p) and *MWCO* in the ranges of 12.7-23.5 $L \cdot m^{-2} \cdot h^{-1} \cdot bar^{-1}$ and 5.5-11 kDa, respectively (**Fig. 5-1**). Both L_p and *MWCO* for the SNS-PAA-PSf membranes were reduced by 37.2%-66.0% and 89-94.5%, respectively, relative to the base PSf UF membrane (**Table 5-1**). The above trends are attributed to the added hydraulic resistance and pore narrowing (or blocking) due to the tethered PAA chains [156]. As shown in **Fig. 5-1**, the above range of UF membrane performance is similar to previously reported results for SNS-PAA-PSf membranes (based on Toray MUF-20K PSf UF membrane), synthesized via AA graft polymerization post-surface activation with He/O_2 plasma [156]. The previous approach, however, requires the utilization of high purity helium and oxygen gases relative to the significantly lower cost membrane surface modification with atmospheric pressure Air plasma.

5.4 Conclusions

Tuning of PSf UF membrane performance (i.e., *MWCO* and permeability coefficient) via Air APP induced graft polymerization was shown to be feasible while avoiding performance degradation due to etching by this type of plasma. For the same graft polymerization conditions, the SNS-PAA-PSf membranes synthesized post-surface activation by Air plasma demonstrated the greatest reductions in both L_p and *MWCO*, relative to the base PSf UF membrane. It is noted surface nano-structuring of the PSf UF membrane with tethered PAA, relying on surface activation with atmospheric Air and He/O_2 plasmas, enabled the synthesis of membranes with *MWCO* range of 5.5-12 kDa over a corresponding permeability range of 12.7-27.4 $L \cdot m^{-2} \cdot h^{-1} \cdot bar^{-1}$, which followed the expected permeability solute rejection tradeoff. The cost efficiency of using Air plasma in PSf UF membrane surface modification was also significantly improved demonstrated with cost reduction by a factor of ~32 relative to He/O_2 plasmas for plasma process only, and by

up to 48.8% for the entire membrane synthesis process. In closure, there is merit in exploring its scalability given the utilization of air as a low cost plasma source gas.

Chapter 6 Stimuli-Responsive PSf UF Membrane with Self-Adaptive Membrane Performance and Surface Wettability

6.1 Overview

Stimuli-responsive membranes refer to the membranes with physicochemical properties (i.e., surface charge, chemical functionality, surface hydrophilicity, electrostatic characteristics) and perm-selectivity adjusted (reversibly) in response to environmental stimuli such as pH, ionic strength, temperature, light, and electrical and magnetic fields [51, 52]. Standing out from the traditional membrane technologies [199], stimuli-responsive smart membranes have been proposed for use in a wide range of applications including drug release, chiral separation, pollutants detection, graded sieving separation, bioseparation, water treatment, tissue engineering, and chemical sensors [199-202].

Responsive membranes can be synthesized by tethering polyelectrolyte chains onto the surface of the target base membrane. The tethered chains can undergo conformational change (e.g., extension/collapse) so as to alter membrane performance. For example, a change in solution pH can trigger proton association-dissociation equilibrium (i.e., protonation and deprotonation) of the polyelectrolytes [203]. As solution pH increases above the acidic polyelectrolytes pKa, the surface tethered polymer chains deprotonate, leading to chain swelling owing to electrostatic repulsion between charged segments [180]. At low pH, on the other hand, protonation of the ionizable functional groups of the surface tethered polymer brush layer leads to chain collapse. Swelling of the surface tethered polyelectrolyte chains at high pH was reported in a previous study that the mixed polymer brush consisting of poly(*N*-isopropyl acrylamide) and poly(acrylic acid) (PAA) tethered on a wafer surface had thickness (14-43 nm) increased by factors of 2.3-2.9 as pH increased from 3 to 8 [304]. It was also demonstrated that PAA brush layer tethered on the

polystyrene-coated glass substrates had surface feature (aggregates) height increased by a factor of ~2.2 as pH increased from 2 to 10 [305]. Tethered polyelectrolyte chains also respond to changes in solution ionic strength due to charge screening by Na^+ and Cl^- ions that disrupt electrostatic interactions among the charged polyelectrolyte chain segments [125, 181], leading to chain collapse with increasing solution ionic strength. The collapse of polyelectrolyte chains at high ionic strength was confirmed in a previous study in which PAA chains tethered onto polysulfone (PSf) surrogate surface had surface roughness (0.83 nm) and equilibrium thickness (13 nm) reduced by ~35% and ~91%, respectively, in 35 g/L NaCl solution relative to 1.28 nm and 145 nm in D.I. water [54]. Swelling of the surface tethered polymer chains can lead to increased surface hydrophilicity (and thus lower membrane surface energy), while chain collapse will lead to increased surface hydrophobicity [53, 125, 199, 206], attributed to the change of polymer solubility (i.e., polymer-water interaction parameter) and water adsorption volume (i.e., the volume fraction of water) inside the polymer layer [306].

Conformational changes of the tethered polymer chains due to different degrees of swelling may lead to changes in membrane permeability and selectivity (**Table 2-7**, **Chapter 2**). The responsive membrane separation behavior has been attributed to two mechanisms: "through-pore" and "through-polymer" (**Fig. 6-1**). The "through-pore" mechanism has been widely explored in the literature [50, 145, 180, 208-217], focusing on porous membranes with pore size > 50 nm [218]. For the above pore size range, tethered polyelectrolyte chains whose average length is significantly smaller compare to the base membrane pore size, may be tethered both onto the external membrane surface and inside the pores. The tethered chains act as an "on-off valve" to regulate porous membrane permeability and selectivity, and where chain swelling and collapse lead to narrowing ("close") or enlarging ("open") of the membrane pores. Consequently, for size-based membrane

separation, tunable membrane pore sizes can be achieved via external environmental stimuli [199]. For example, graft polymerization of methacrylic acid (MAA) onto PES using benzoyl peroxide (BPO) as a chemical initiator resulted into pH-responsive UF membranes, which demonstrated an 8% increase in BSA rejection (from 91% to 99%) at the cost of up to 77% decreased permeate flux (from 87 $L \cdot m^{-2} \cdot h^{-1}$ to 20 $L \cdot m^{-2} \cdot h^{-1}$) with pH increase from 2 to 10 [208]. In another study, end-functionalized poly(acrylic acid) chains were synthesized with reversible addition-fragmentation chain-transfer (RAFT) polymerization and attached to commercial polysulfone UF membranes [213]. The resulting membranes demonstrated 32.3-115% decreased pure water flux and up to 79% decreased *MWCO* as pH increased from 3 to 11 [213]. With the "through-pore" mechanism, the responsive membranes achieved increased membrane permeability but at the cost of reduced membrane solute rejection; thus, leading to the typical membrane perm-selectivity tradeoff [50, 145, 180, 208-217].

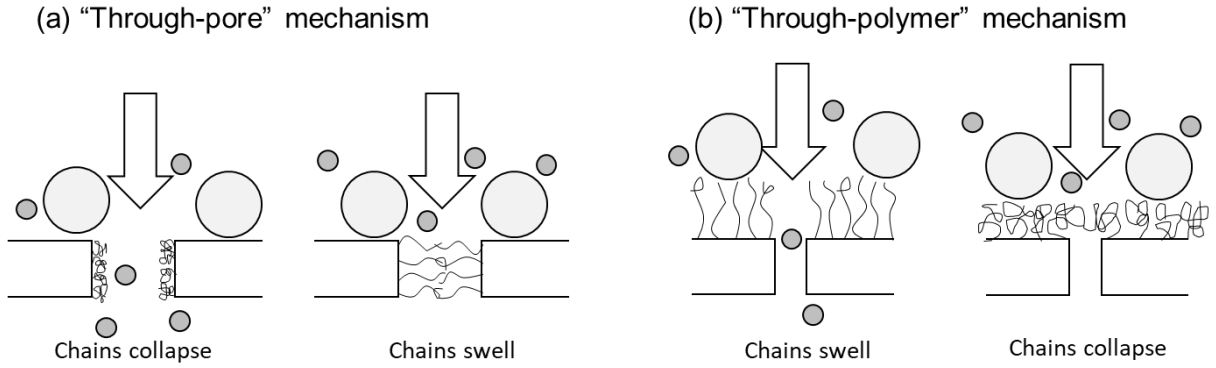

Figure 6-1. Schematics of (a) "through-pore" mechanism and (b) "through-polymer" mechanism of responsive membrane tethered with polyelectrolyte chains.

The "through-polymer" mechanism (**Fig. 6-1**), is demonstrated for nonporous or tight porous membranes with pore size <10 nm [218]. Polyelectrolyte chains of average chain length that is significantly greater compared to the base membrane pore size are expected to be mainly tethered on the external membrane surface. Swelling of polymer chains that are tethered onto the external

membrane surface could lead to exposure of the underlying membrane pores and thus decreased membrane rejection. Collapse of the chains (form mushroom-like structure [125, 307]) leads to membrane pore narrowing or blocking, and thus increases membrane rejection. For example, tubular carbon-supported ZrO_2 Carbosep M1 membrane (pore size of 6 nm) with poly(vinyl pyrrolidone) (PVP) chains tethered onto the membrane surface demonstrated decreasing lysozyme (Lys) rejection from 24.4% to 0.5% upon swelling of the tethered chains as the solution pH increased from 3 to 10 [46]. In another study, a nonporous polyamide (PA) thin-film composite (TFC) RO membrane with surface tethered poly(acrylic acid) chains exhibited salt rejection that decreased from 96% to 93% upon swelling of the tethered PAA chains as solution pH increased from 3 to 11 [51]. In both cases, swelling of surface tethered polymer chains (at basic conditions, pH>7), due to electrostatic repulsion between the chain segments, led to decreased membrane rejection, as expected for the "through-polymer" mechanism. Unlike membrane rejection, which mainly depends on membrane pore size, membrane permeability can be affected by various other factors including surface hydrophilicity and tethered polymer layer thickness [156]. Consequently, there is a possibility that the typical membrane perm-selectivity tradeoff can be overcome via the "through-polymer" mechanism, but this has not been previously investigated.

In order to assess the feasibility to overcome the typical membrane perm-selectivity tradeoff via the responsive membrane "through-polymer" mechanism, pH and ionic strength-responsive UF membranes were evaluated with respect to membrane intrinsic resistance and molecular weight cutoff (*MWCO*). The responsive membranes were synthesized by tethering PAA onto PSf UF membranes via atmospheric pressure plasma-induced graft polymerization (APPIGP). A commercial PSf UF membrane, having sufficiently large water permeability coefficient and *MWCO*, was surface nano-structured (SNS) via AA graft polymerization induced by atmospheric

pressure He/O_2 plasma surface activation. To ensure the application of the responsive membrane "through-polymer" mechanism, plasma and graft polymerization conditions were selected as per previous studies [54, 156] in which synthesized tethered PAA chains had an average length (96-145 nm) up to 23 folds greater compared to base membrane pore size (~6.3 nm). Thus, the PAA chains were expected to be tethered primarily onto the external membrane surface. Tuning of SNS-PAA-PSf membrane surface hydrophilicity, intrinsic resistance, and polyethylene glycol (PEG) *MWCO* as compared to the Native-PSf membrane was achieved over a range of solution pH and ionic strength. In addition, the feasibility of overcoming the typical membrane perm-selectivity tradeoff via the "through-polymer" mechanism of the responsive membranes was also evaluated.

6.2 Experimental

6.2.1 Materials

PSf membrane sheets (MUF-10K and MUF-20K, Toray Membrane USA Inc., Poway, CA), with manufacturer reported 10 kDa and 100 kDa *MWCO*, respectively, were selected as the base membranes for surface modification and as a reference membrane for comparison. Acrylic acid (99%, Sigma-Aldrich, St. Louis, MO) monomer was used for graft polymerization to modify the base PSf membrane which was post-activated with atmospheric pressure plasma. Helium (99.999%) and oxygen (99.999%) gases (Airgas, Los Angeles, CA) were used for plasma treatment sources, and nitrogen (99%) gas (Airgas, Los Angeles, CA) was used for substrate surface drying, graft polymerization degassing, and UF filtration feed tank pressurizing. The molecular weight cutoff (*MWCO*) of each UF membrane was characterized using polyethylene glycol (PEG, *Mw* from 1,000 to 35,000 Da, Sigma-Aldrich, St. Louis, MO). Sodium chloride (NaCl, ≥99.0%, Fisher Scientific, Chino, CA) was used to adjust solution ionic strength. 0.1 N

hydrochloric acid and sodium hydroxide solutions (Fisher Scientific, Chino, CA) were used to adjust the solution pH. All experiments were conducted using deionized (D.I.) water.

6.2.2 Atmospheric pressure-induced graft polymerization (APPIGP)

The tethered PAA layer was synthesized onto the PSf surface via atmospheric pressure He/O_2 plasma surface activation, followed by AA free-radical graft polymerization as per the protocol described elsewhere [49, 156, 278]. Membrane coupons (with an active area of 13.4 cm^2) were extracted from the base membrane sheet (Toray MUF-20K), immersed in D.I. water for at least 24 hr, and subsequently dried by blowing nitrogen over the surface using a polytetrafluoroethylene (PTFE) nitrogen/drying gun (International Polymer Solutions, Inc., Irvine, CA). PSf membrane surface activation was then accomplished using a helium/oxygen (He/O_2) APP with helium and oxygen flow rates of 45 L/min and 0.5 L/min, respectively, and the scanning speed of 100 mm/s. The plasma was generated using the Atomflo™ 500 APP system (Surfx Technologies Inc., Redondo Beach, CA) at 150W RF power. The base PSf membrane surface was activated via 2 sequential plasma scans (*N*) and a source-surface separation (*PSS*) distance of 15 mm (plasma exposure time of ~1 s). The selection of plasma type and plasma treatment conditions for the PSf UF base membranes were based on previously derived membrane performance tuning setting [156]. The resulting SNS-PAA-PSf membrane had water permeability coefficient and *MWCO* within the same range as the Native-PSf membrane (MUF-10K), and thus their stimuli-responsive changes in membrane performance are comparable.

The plasma-activated base PSf membranes were placed in 250 mL glass reaction vessels containing the 20 vol% aqueous AA monomer solutions (pH = 1.9) [156]. The capped glass vessels were immersed in a constant temperature water bath at 70°C for 60 min. Nitrogen was bubbled

into the monomer solution (via a perforated tube) at the bottom of the vessels during graft polymerization to promote mixing and scavenge dissolved oxygen that could inhibit the polymerization reaction [280]. Subsequent to the graft polymerization step, the surface nano-structured membranes were rinsed with D.I. water. The resulting membranes were then immersed in D.I. water for at least 24 hr prior to further characterizations.

6.2.3 Membrane Surface Hydrophilicity

The variation of surface wettability of SNS-PAA-PSf and Native-PSf membranes (with a surface area of 13.4 cm^2) with solution pH and ionic strength was evaluated by captive bubble (CB) water contact angle measurements [156] using an automated drop shape analyzer (DSA20; KRÜSS GmbH, Germany). The membranes were immersed in the target aqueous solutions (pH range of 3-11 and NaCl concentration of 0-32 g/L) at room temperature (~20°C) for at least 30 min prior to CB water contact angle measurement. Water contact angles were measured within 2 s of dispensing a 6 µL air bubble onto the immersed membrane surfaces using a 'J'-shaped needle. Contact angles were measured for at least 5 locations for each sample, and the reported values represent the average of each set of measurements.

Membrane free energy of hydration (ΔG_{iw}) was calculated using Young-Dupré equation, $\Delta G_i = -\gamma(1+\cos\theta)$, where γ is the surface tension of the liquid and θ is the contact angle. Surface tension (γ) of aqueous solutions with different pH and ionic strengths used in the present study is given in **Table 6-2**.

Surface CB contact angle uniformity of the 15 cm × 15 cm Native-PSf membrane sheets was evaluated by characterizing six 5 cm × 5 cm membrane coupons extracted from different sections of the membrane sheets (**Fig. A-7, Appendix**). The membrane surface CB contact angle

uniformity measure (*f*) was defined as $f = (1 - sd / \bar{x}) \times 100\%$, in which $\bar{x}$ and *sd* are the average value and standard deviation of the membrane surface CB contact angle.

6.2.4 Membrane Performance Characterization

The SNS-PAA-PSf and Native-PSf (MUF-10K) membranes hydraulic permeability coefficient and PEG *MWCO* were characterized over a pH range of 3-11, and NaCl concentration up to 32 g/L. Feed solution pH, adjusted using 0.1 N HCl and 0.1 N NaOH, was monitored using a pH meter (Oakton pH 110 Meter; Cole-Parmer, Vernon Hills, IL). Solution ionic strength, adjusted using NaCl, was measured using a hand-held conductivity sensor (WD-35604-00, OAKTON, Chicago, IL).

The membrane hydraulic permeability coefficient and PEG *MWCO* were determined following a previously established protocol [156, 278]. Briefly, the performance of UF membrane was evaluated in a dead-end stirred UF cell (Amicon 8050, Millipore Corporation, Burlington, MA), where the active membrane area was 13.4 cm^2. Membrane permeate flow rate was determined using an in-line liquid flow meter (SLS-1500, Sensirion AG, Switzerland). Post membrane compaction at 3.5 bar (~50 psi) and ~20°C for 3 hr, the membrane hydraulic permeability coefficient (L_p) was determined from the slope of a linear plot of water flux versus transmembrane pressure (i.e., $L_p = J_v / \Delta P$, where ΔP is the applied transmembrane pressure, J_v is the permeate water flux defined by $J_v = Q_p / A$, in which Q_p and A are the permeate flow rate and membrane area, respectively). Membrane hydraulic resistance was then calculated as $R_m = 1/(\mu \cdot L_p)$, where μ is the solution viscosity (**Table 6-1**).

UF membrane PEG *MWCO* was determined using a series of PEG *Mw* fractions [285, 286] in the range of 1,000 - 35,000 Da. All PEG *MWCO* determinations were carried out using 1 g/L PEG

solution at the same initial permeate flux of 9 $L \cdot m^{-2} \cdot h^{-1}$ (~5.3 $gallon \cdot ft^{-2} \cdot day^{-1}$). PEG concentrations in the feed (C_f) and permeate (C_p) streams were determined by a Total Organic Carbon (TOC) Analyzer (Aurora 1030W, OI Analytical, College Station, TX). The solute observed (nominal) rejection for each PEG fraction was calculated as $R_o = (1 - C_p / C_f) \times 100\%$. Subsequently, the observed rejection for different *Mw* of PEG fraction was correlated with the PEG *Mw*. The *Mw* fraction corresponding to 90% rejection was then designated as the membrane PEG *MWCO*. Membrane pore size was calculated based on the membrane PEG *MWCO* using the empirical correlation of $d_p = 1.3095 \times MWCO^{0.3409}$ [156]. It is noted that the impact of concentration polarization is small in a similar UF stirred cell setting, where the difference between membrane intrinsic rejection (R_i) and observed rejection (R_o) is less than 3% [308].

6.3 Results and Discussion

In order to investigate the stimuli-responsive membrane properties governed by the "through-polymer" mechanism, sufficiently long PAA chains relative to the base membrane pore size (~6.3 nm) were synthesized onto the external membrane surface. It was previously reported [54] that surface tethered PAA chains, synthesized under the presently selected plasma and graft polymerization conditions, should have an average length of 96-145 nm and sufficiently high ratio of chain length to base membrane pore size (15.2-23.0).

The SNS-PAA-PSf membrane demonstrated stimuli-responsive membrane intrinsic resistance and PEG *MWCO* over the present experimental range of pH (3-11) and ionic strength (0-547 mM). For example, the intrinsic membrane resistance and PEG *MWCO* decreased by 28.7% and 77.5%, respectively, for the SNS-PAA-PSf membrane as solution ionic strength increased from 0 to 547 mM. Over the above pH and ionic strength ranges, SNS-PAA-PSf membrane intrinsic resistance

and PEG *MWCO* were in the range of 1.37 - 1.61×10^{13} m^{-1} and 1.8 - 15.0 kDa, respectively (**Table 6-1**). Comparatively, the Native-PSf membrane exhibited narrower ranges of membrane resistance R_m of 0.74 - 2.29×10^{13} m^{-1}, and PEG *MWCO* of 10.0 - 16.8 kDa in response to the tested range of solution pH and ionic strength. More importantly, a decrease in both intrinsic membrane resistance and PEG *MWCO* was observed for the SNS-PAA-PSf membrane at low pH (~3) or high ionic strength (~547 mM), owing to the surface tethered PAA chains being in more collapsed conformation; thus overcoming the typical tradeoff between membrane permeability coefficient and selectivity. It is argued that swelling of the surface tethered PAA chains, triggered by the increase in solution pH or decrease in ionic strength, is also implied by the SNS-PAA-PSf membrane surface energy decreased of ~21.6% (from -114.5 to -139.2 mJ/m^2) relative to constant surface energy for the native PSf membrane, with deviation from the average within ±5% (**Table 6-2**). The greater change in SNS-PAA-PSf membrane surface energy is attributed to the conformational change of tethered polyelectrolytes upon change of solution pH and ionic strength and thus a change in water adsorption volume within the polymer brush layer [53, 125, 199, 206].

Table 6-1. Membrane hydraulic permeability coefficient and PEG *MWCO* for Native-PSf and SNS-PAA-PSf membranes in response to NaCl concentration and pH.

Aqueous environment	μ (Pa·s)	Native-PSf Membrane [c]						SNS-PAA-PSf Membrane [d]					
		L_p ($L \cdot m^{-2} \cdot h^{-1} \cdot bar^{-1}$) [e]	R_m (m^{-1}) [f]	R_m^o	*MWCO* (kDa) [g]	$MWCO^o$	Pore Size (nm)	L_p ($L \cdot m^{-2} \cdot h^{-1} \cdot bar^{-1}$)	R_m (m^{-1})	R_m^o	*MWCO* (kDa)	$MWCO^o$	Pore Size (nm)
Ionic strength (mM) [a]													
0	0.001000	23.2	1.55×10^{13}	1.000	10.0	1.000	2.9	20.7	1.74×10^{13}	1.000	8.0	1.000	2.7
2	0.001000	23.2	1.55×10^{13}	1.000	10.1	1.010	2.9	22.7	1.59×10^{13}	0.912	7.6	0.954	2.6
17	0.001002	23.1	1.55×10^{13}	1.004	10.4	1.040	2.9	23.8	1.51×10^{13}	0.869	7.2	0.900	2.6
171	0.001020	22.3	1.59×10^{13}	1.021	11.4	1.140	3.0	24.5	1.44×10^{13}	0.830	4.4	0.554	2.2
547	0.001064	21.1	1.61×10^{13}	1.035	15.3	1.530	3.3	27.2	1.24×10^{13}	0.715	1.8	0.225	1.6
pH [b]													
3	0.001000	26.2	1.37×10^{13}	1.000	14.6	1.000	3.3	48.7	7.38×10^{12}	1.000	6.9	1.000	2.5
5	0.001000	25.1	1.44×10^{13}	1.047	13.8	0.945	3.2	37.4	9.62×10^{12}	1.303	7.9	1.145	2.7
7	0.001000	23.2	1.55×10^{13}	1.130	10.0	0.685	2.9	20.7	1.74×10^{13}	2.355	8.0	1.159	2.7
9	0.001000	23.8	1.51×10^{13}	1.101	10.5	0.719	2.9	17.7	2.03×10^{13}	2.754	9.6	1.391	2.8
11	0.001000	24.9	1.45×10^{13}	1.054	16.8	1.151	3.4	15.7	2.29×10^{13}	3.108	15.0	2.174	3.3

[a] Aqueous solution ionic strength adjusted with NaCl.

[b] Aqueous solution pH adjusted with 0.1N HCl and NaOH solutions.

[c] Commercial PSf UF membrane (Toray MUF-10K).

[d] The SNS-PAA-PSf membrane is synthesized based on a commercial PSf UF membrane (Toray MUF-20K) surface modified by atmospheric pressure He/O_2 plasma treatment (*PSS*=15 mm, *N*=2), followed by AA graft polymerization ($[M]_o$=20 vol%, 70°C, 1 hr).

[e] Membrane hydraulic permeability coefficient measured following the protocol described in **Section 6.2.4**.

[f] Membrane intrinsic resistance calculated based on membrane hydraulic permeability coefficient and solution viscosity (**Section 6.2.4**).

[g] Membrane PEG *MWCO* determined using a series of PEG *Mw* fractions, following the protocol in **Section 6.2.4**.

Table 6-2. Membrane surface captive bubble (CB) water contact angle for Native-PSf and SNS-PAA-PSf membranes at different pH and salt concentrations

Membrane no.	Aqueous Environment	Surface tension[a] (mN/m)	Native-PSf Membrane			SNS-PAA-PSf Membrane		
			CB contact angle (°)	Uncertainty (°)	Surface energy[b] (mJ/m^2)	CB contact angle (°)	Uncertainty (°)	Surface energy[b] (mJ/m^2)
Ionic Strength (mM)								
1	0	72.8	50.5	± 2.5	-119.1	43.4	± 2.0	-125.7
2	2	72.8	55.0	± 1.9	-114.6	45.6	± 2.1	-123.8
3	17	72.8	50.5	± 1.9	-119.1	48.1	± 1.9	-121.4
4	171	73.0	48.0	± 1.7	-121.9	51.2	± 1.8	-118.8
5	547	73.5	50.4	± 1.5	-120.4	56.1	± 1.9	-114.5
pH								
6	3	72.8	46.4	± 1.9	-123.0	41.6	± 2.1	-127.3
7	5	72.8	44.0	± 1.8	-125.2	43.6	± 1.9	-125.5
8	7	72.8	50.5	± 2.5	-119.1	43.4	± 2.0	-125.7
9	9	72.8	47.7	± 1.7	-121.8	36.5	± 1.4	-131.3
10	11	72.8	45.4	± 2.1	-123.9	24.3	± 1.8	-139.2

[a] The surface tensions of the listed solutions are given in **Table A-1, Appendix A**.

[b] Membrane surface energy calculated following the protocol described in **Section 2.3**.

6.3.1 Salinity-responsive membrane performance

In response to increased solution ionic strength over the range of 0-547 mM (NaCl), the SNS-PAA-PSf membrane exhibited 28.7% decreased membrane intrinsic resistance (from 1.74 to 1.24×10^{13} m^{-1}) and 77.5% decreased PEG *MWCO* (from 8.0 to 1.8 kDa) (**Table 6-1**). Changes in SNS-PAA-PSf membrane permeability coefficient and PEG *MWCO* are associated with the conformational change (i.e., swelling/collapse) of the tethered polyelectrolyte chains in response to solution ionic strength [46]. The surface tethered PAA chains are expected to be in more collapsed conformation at high ionic strength due to charge screening by the salt ions (Na^+) that reduce electrostatic repulsion among the charged chain segments [180]. Previous work has shown [54] that the surface tethered PAA chains collapse in saline water, as implied by 91% decline of the PAA layer thickness (from 145 nm in D.I. water to 13 nm in saline water with 35 g/L NaCl). Also, the collapsed PAA brush layer at high solution ionic strength (547 mM) should have reduced water adsorption volume. The above behavior is consistent with the 29.3% increase in surface contact angle in aqueous solutions with targeted pH and ionic strength, adjusted using HCl/NaOH, and NaCl, respectively, relative to in D.I. water (**Fig. 6-2**, **Table 6-2**).

The swelling of the tethered PAA chains (at low solution ionic strength) corresponds to increased PEG *MWCO*, and the collapse of the chains (at high solution ionic strength) corresponds to the decreased PEG *MWCO*, consistent with the expectation of the "through-polymer" transport mechanism. Collapsed PAA chains at high solution ionic strength (547 mM) are expected with increased chain size/radius [125, 307] that leads to screening the underlying membrane pores, thus, leading to narrowed membrane effective pore size and decreased membrane PEG *MWCO*. At low solution ionic strength (e.g., D.I. water), the swollen PAA chains should be in a more extended configuration leading to exposure of the underlying membrane surface including the pores, and

thus increased membrane PEG *MWCO* (**Fig. 6-5**). Unlike the membrane PEG *MWCO* which is mainly a function of membrane pore size (UF separation is based on size exclusion [156]), and the membrane hydraulic permeability coefficient may be affected by the tethered polymer layer thickness. The observed increase of the SNS-PAA-PSf membrane intrinsic hydraulic resistance with swelling of the tethered PAA chains (at low solution ionic strength), can be explained by the increased PAA layer thickness which leads to greater resistance to water transport through the membrane. In contrast, for Native-PSf membrane, only a negligible (~3.9%) intrinsic membrane resistance (**Table 6-1** and **Fig. 6-3**) increase was observed as the feed solution ionic strength increased from 0 to 547 mM. Deviation of the Native-PSf membrane surface contact angle from the average (50.9˚) was within ±5% (**Table 6-2** and **Fig. 6-2**), and also within the Native-PSf membrane uniformity measure of surface CB contact angle (92.8%; **Figure A-7, Appendix A**). The above results suggest that there was no significant conformational change of the surface of the Native-PSf membrane in response to solution ionic strength, which is as expected for the PSf membrane material. The significant increase in PEG *MWCO* (53%; from 10 to 15.3 kDa) for the Native-PSf membrane with the rise in the solution ionic strength from 0 to 547 mM (**Table 6-1** and **Fig. 6-4**) can be possibly explained by the corresponding reduction of the hydrated size of the PEG molecule. The above is consistent with previous work [234] in which it was reported that partial dehydration of PEG molecules (with Stokes radius of ~0.45-0.6 nm) is induced by the surrounding ions (i.e., at the presence of 0.1-1 M KCl, LiCl, and $MgCl_2$). Increased concentration of the above salts led to PEG effective molecular size reduction by 9-22% and PEG rejection decrease by 40% for the rigid non-swelling nanofiltration ceramic membrane [234].

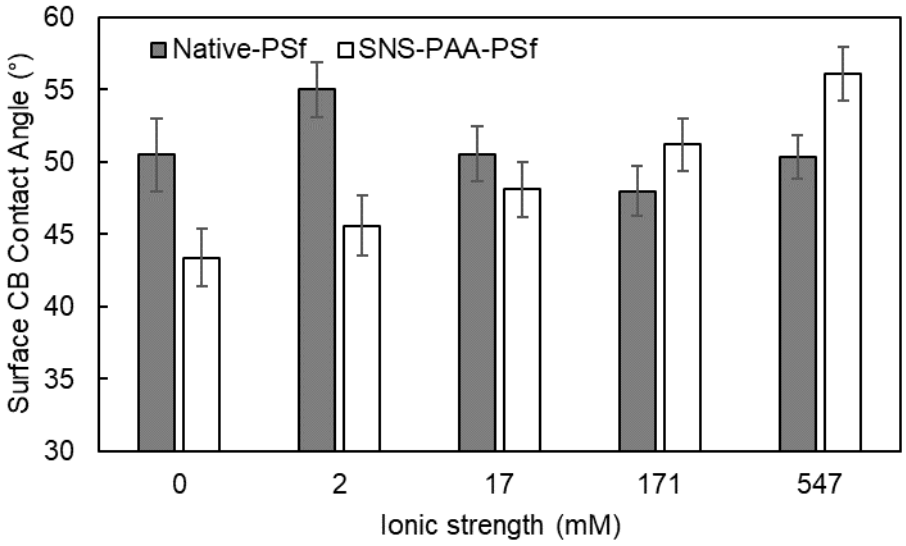

Figure 6-2. Dependence of the surface captive bubble contact angle for the Native-PSf and SNS-PAA-PSf membranes on solution ionic strength (0 - 547 mM) at pH of 7.

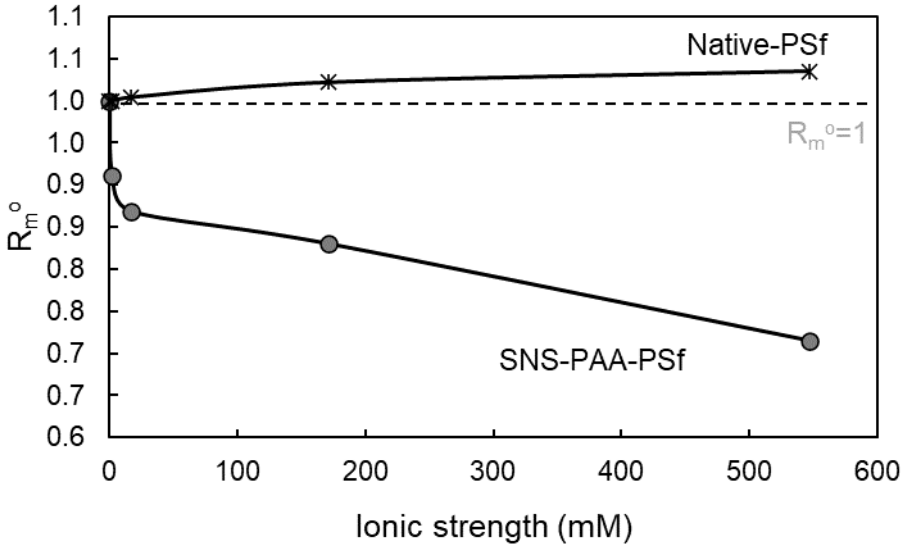

Figure 6-3. Normalized intrinsic membrane resistance of Native-PSf and SNS-PAA-PSf membranes over solution ionic strength in the range of 0 - 547 mM at constant pH of 7.

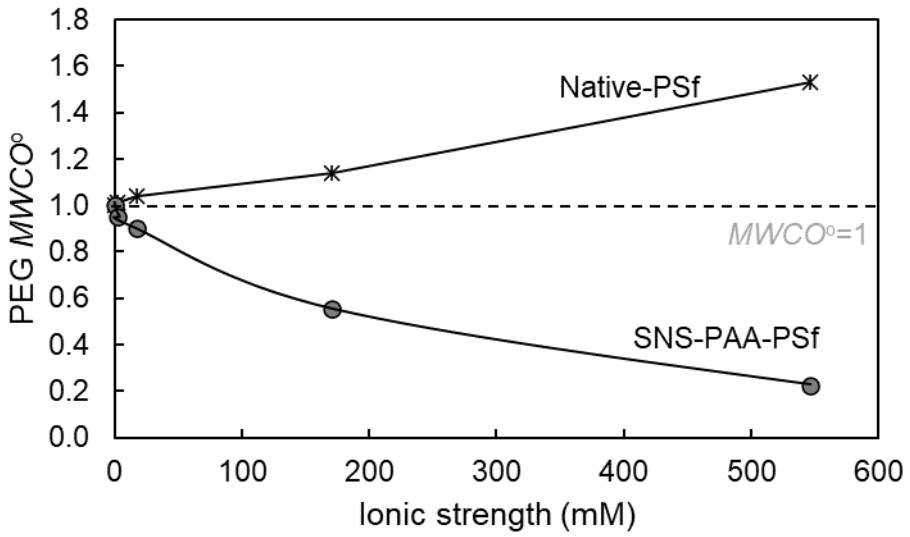

Figure 6-4. Normalized PEG *MWCO* of Native-PSf and SNS-PAA-PSf membranes over solution ionic strength range of 0 - 547 mM at pH of 7.

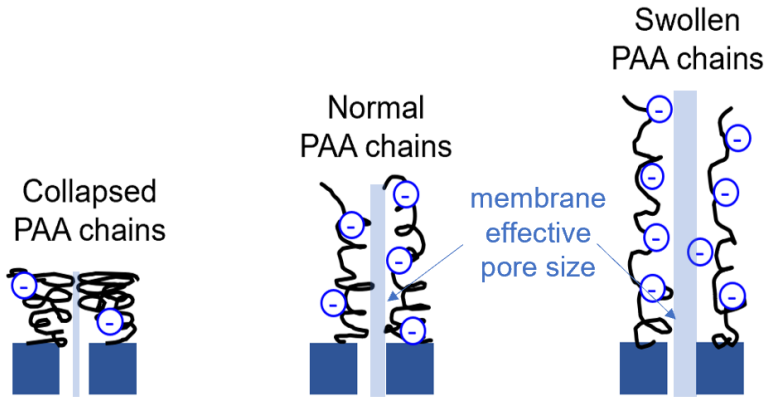

Figure 6-5. Illustration of tethered chains in the proximity of a membrane pore under collapsed (left), swollen (right) and "normal" (middle) conditions.

6.3.2 pH-responsive performance

The SNS-PAA-PSf membrane exhibited pH-responsive performance as indicated by increased R_m and PEG *MWCO* by factors of ~3.1 and 2.2, respectively, as the solution pH increased from 3 to 11 (**Figs. 6-7** and **6-8**, **Table 6-1**). The pH-responsiveness of membrane performance is also associated with the conformational change (i.e., swell/collapse) of the surface tethered PAA chains [180] upon protonation/deprotonation of the ionizable side group (i.e., carboxylic acid group). At

pH greater than the pKa of PAA (~4.8, [156]), the PAA contained carboxylic acid groups are ionized to $-COO^-$ and protons [309], and the electrostatic repulsion between chain segments (i.e., $-COO^-$ groups) leads to a more extended conformation of the tethered PAA chains. It is noted that the surface contact angle and surface energy for SNS-PAA-PSf membrane were reduced by 31.3% and 14%, respectively, as the pH increased from 3 to 11 (**Table 6-1** and **Fig. 6-6**). The above behavior is consistent with the expected swelling of the tethered PAA chains with increased pH. As reported in previous studies [53, 125, 199, 206], swelling of the polymer brush layer corresponds to increased surface hydrophilicity due to the greater of polymer solubility and/or water adsorption volume within the polymer layer.

pH-responsive SNS-PAA-PSf membrane performance is consistent with the "through-polymer" mechanism. Swelling of the PAA chains (at a high solution pH of 11 relative to 3) corresponded to increased PEG *MWCO* (~15.0 kDa) and their collapse corresponded to decreased PEG *MWCO* (~6.9 kDa). Increased membrane pore size (from 2.5 to 3.3 nm) with solution pH is ascribed to the swollen chains exposing the underlying membrane pores (**Figs. 6-1** and **6-4**). Unlike the membrane PEG *MWCO* which mainly depends on membrane pore size (UF separation is based on size exclusion [156]), the membrane hydraulic resistance increased with the tethered polymer layer thickness (**Fig. 6-7**), due to the greater resistance to water transport through the membrane.

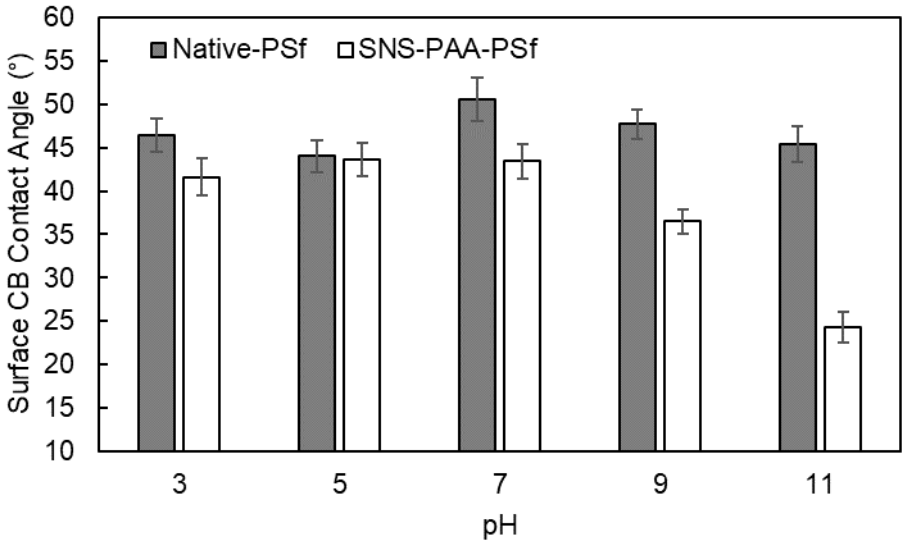

Figure 6-6. Dependence of Native-PSf and SNS-PAA-PSf membranes surface captive bubble contact angle on solution pH (3 - 11).

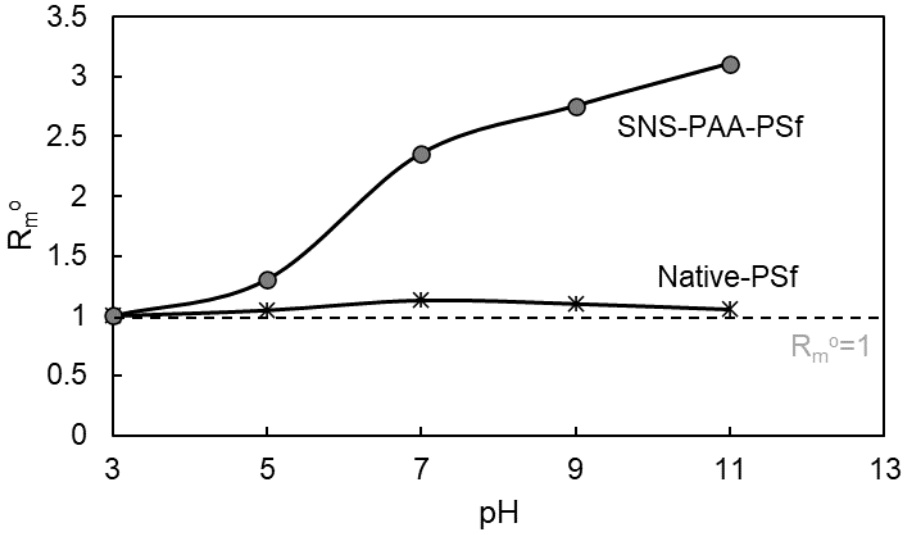

Figure 6-7. Normalized intrinsic membrane resistance for Native-PSf and SNS-PAA-PSf membranes over solution pH range of 3-11.

It is noted that the Native-PSf membrane performance was also observed with ranges of R_m 1.37 - 1.55×10^{13} m^{-1}, and PEG *MWCO* 10 - 16.8 kDa as solution pH varied from 3 to 11 (**Table 6-1**). Both the maximum hydraulic membrane resistance and minimum membrane PEG *MWCO*,

of 1.55×10^{13} m^{-1} and 10.0 kDa, respectively, were observed at pH 7 (**Figs. 6-6** and **6-7**). However, the surface contact angle of the Native-PSf membrane remained unchanged over the pH range of 3-11 (**Fig. 6-6** and **Table 6-2**), with a deviation from the average surface CB contact angle (46.8˚) within ±5%, which is also within the Native-PSf membrane uniformity measure of surface CB contact angle (92.8%; **Figure 6-5**). The pH-responsive intrinsic resistance and PEG *MWCO* of the Native-PSf membrane may be attributed to the structural/chemical degradation of the Native-PSf membrane active layer at extreme pH conditions, and thus decreased membrane resistance and increased PEG *MWCO*.

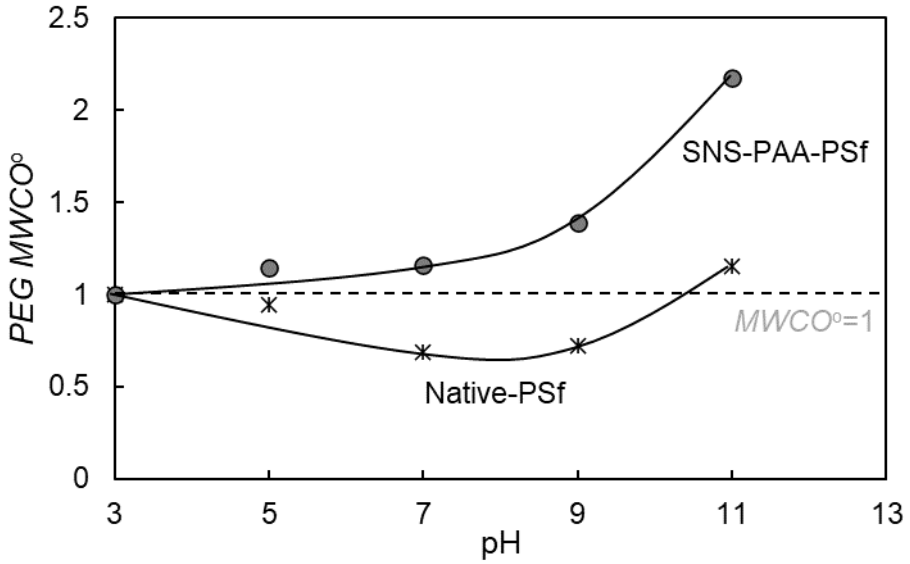

Figure 6-8. Normalized PEG *MWCO* of Native-PSf and SNS-PAA-PSf membranes over solution pH range of 3-11.

6.3.3 Self-regulated membrane performance and surface wettability

The SNS-PAA-PSf membrane demonstrated pH and ionic strength-responsive intrinsic membrane resistance and PEG *MWCO*. Increased intrinsic membrane resistance (by 210% and 40%) and greater PEG *MWCO* (by factors of 2.2 and 4.4) are observed for the SNS-PAA-PSf membrane with increasing pH (from 3 to 11) and decreasing ionic strength (from 547 mM to 0

mM), respectively (**Sections 6.3.1** and **6.3.2**). Consequently, with the present experimental range of solution conditions (i.e., pH 3-11, and ionic strength 0-547 mM), a wide performance range (i.e., R_m 0.74 - 2.29×10^{13} m^{-1}, and PEG *MWCO* 1.8 - 15.0 kDa) was achieved for the tested SNS-PAA-PSf membrane (**Fig. 6-9**). The wide range of responsive performance tuning for the SNS-PAA-PSf membrane is significant with the potential for enabling the sharp separation, purification, and fractionation of desired products of different *Mw* such as proteins, peptides, and polysaccharides [61, 156]. It is noted that the Native-PSf membrane also demonstrated a measure of pH and ionic strength-responsive performance, albeit for much narrower ranges (i.e., R_m 1.37 - 1.61×10^{13} m^{-1}, and PEG *MWCO* 10.0 - 16.8 kDa).

The responsive SNS-PAA-PSf membrane also demonstrated decreased intrinsic membrane resistance (equivalent to increased membrane throughput) that was accompanied by PEG *MWCO* decreased (equivalent to increased membrane selectivity) in response to increased solution ionic strength or reduced solution pH (**Table 6-1**). Accordingly, increase of both the permeability coefficient (up to 68% lower R_m) and selectivity (up to 77% lower PEG *MWCO*) of the SNS-PAA-PSf membrane is achieved when the surface tethered PAA chains are expected with more collapsed conformation (at pH ~3 or ionic strength ~547 mM), thus overcoming the typical tradeoff between membrane permeability coefficient and selectivity.

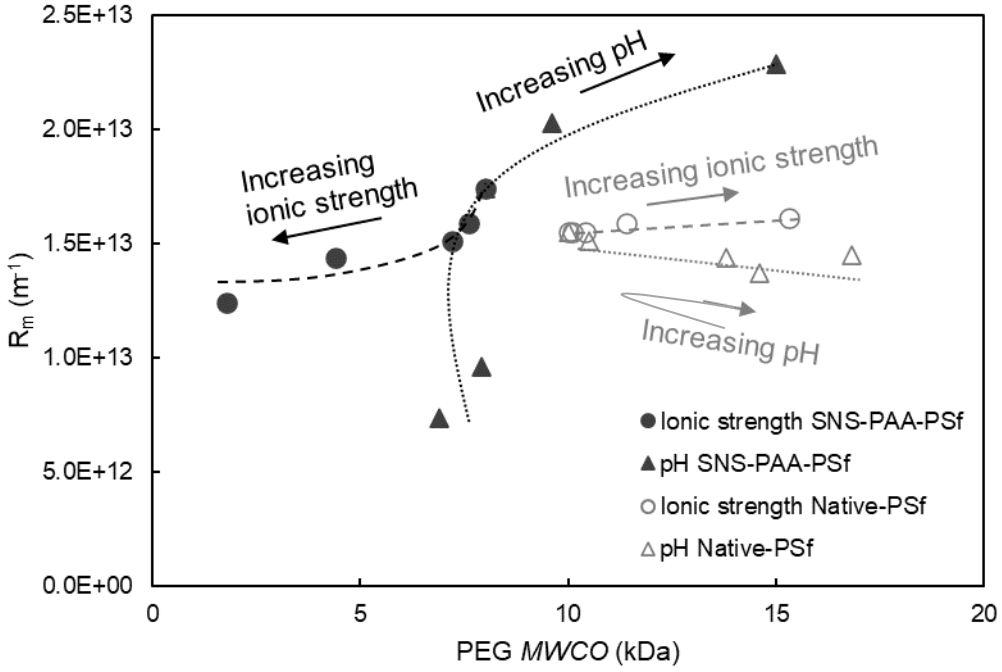

Figure 6-9. Mapping of PEG *MWCO* and intrinsic membrane resistance of the SNS-PAA-PSf and Native-PSf membranes by adjusting solution ionic strength and pH. (Raw data: **Table 6-1**)

SNS-PAA-PSf membrane also demonstrated surface hydrophilicity that varied in response to solution pH and ionic strength. For the tested ranges of pH (3-11) and ionic strength (0-547 mM), a wide range of surface energy (-114.5 to -139.2 mJ/m^2), relative to ~120.8 mJ/m^2 for the Native-PSf membrane (**Fig. 6-10**, **Table 6-2**). The change of SNS-PAA-PSf membrane surface energy is attributed to the responsive conformational change of the surface tethered PAA chains in response to changing solution pH or ionic strength. Swelling of PAA chains (at high pH and low ionic strength) leads to increased surface hydrophilicity (lower surface energy), and the collapse of PAA chains (at low pH and high ionic strength) leads to increased surface hydrophobicity (higher surface energy) [53, 125, 199, 206]. Controlling of membrane surface hydrophilicity via external stimuli can potentially reduce membrane fouling propensity and enhance membrane self-cleaning [26, 28, 219, 220, 265-268, 278].

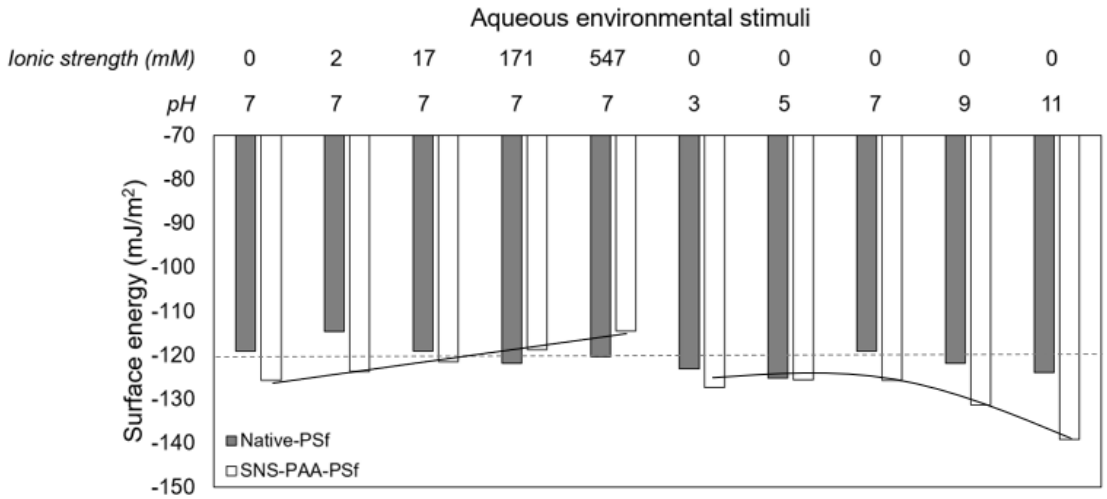

Figure 6-10. Membrane surface hydrophilicity (i.e., surface energy) of both Native-PSf (MUF-10K) and SNS-PAA-PSf membranes variation with solution ionic strength and pH. (Raw data: **Table 6-2**).

6.4 Conclusions

Dual-responsive (i.e., pH and ionic strength) PSf UF membrane was synthesized with surface tethered PAA chains via atmospheric pressure plasma-induced graft polymerization (APPIGP). To assess the "through-polymer" mechanism of the responsive membranes, commercial PSf UF membranes were surface nano-structured (SNS) with sufficiently long PAA chains (~96-145 nm as determined in a previous study [49]) relative to the base membrane pore size (~6.3 nm [156]). Accordingly, the PAA chains were expected to be tethered mainly on the external membrane surfaces. In response to increased ionic strength (from 0 to 547 mM), the resulting SNS-PAA-PSf membrane exhibited 28.7% decreased membrane intrinsic resistance and 77.5% decreased PEG *MWCO*. The SNS-PAA-PSf membrane also exhibited pH-responsive performance as indicated by increased R_m and PEG *MWCO* by factors of ~3.1 and 2.2, respectively, as the solution pH increased from 3 to 11. The changes in SNS-PAA-PSf membrane hydraulic resistance and PEG *MWCO* are attributed to the conformational expansion and shrinkage of the surface tethered PAA chains via electrostatic interactions among the charged chain segments caused by proton association-

dissociation equilibrium (i.e., protonation and deprotonation) and charge screening, respectively. In response to both stimuli, swelling of the tethered PAA chains corresponded to increased PEG *MWCO* which is attributed to exposure of the underlying membrane pores when the chains are in more extended conformations, consistent with the "through-polymer" transport mechanism.

Compared to the Native-PSf membrane, the SNS-PAA-PSf membrane also demonstrated greater sensitivity to the aqueous environment and thus its performance tuning was achieved over a wider range (i.e., R_m 0.74 - 2.29×10^{13} m^{-1}, and PEG *MWCO* 1.8 - 15.0 kDa) relative to R_m 1.37 - 1.61×10^{13} m^{-1}, and PEG *MWCO* 10.0 - 16.8 kDa for the Native-PSf membrane. More importantly, the decreased intrinsic membrane resistance and PEG *MWCO* (equivalent to increase in both membrane throughput and selectivity) for the SNS-PAA-PSf membrane was achieved simultaneously when the PAA chains are in more collapsed conformation (at low pH and high ionic strength), and thus overcoming the typical tradeoff between membrane permeability coefficient and selectivity. A range of surface energy from -114.5 to -139.2 mJ/m^2 was also observed for the SNS-PAA-PSf membrane, relative to essentially invariant Native-PSf membrane (deviation from the average within ±5%), in response to both solution pH and ionic strength. Control of the membrane surface hydrophilic/hydrophobic behavior using external stimuli, enabled reduction of membrane fouling and can serve for the design of self-cleaning membrane surfaces.

Chapter 7 Reduced PSf UF Fouling Propensity with A Surface Tethered PAA Brush Layer

7.1 Overview

It was shown previously that surface tethered hydrophilic polymer brush layer can reduce membrane fouling propensity attributed to the partial mobility (due to Brownian motion) of the tethered PAA chain segments which also screen the underlying membrane surface [45-47, 310, 311]. Increased membrane surface hydrophilicity also effectively reduces the hydrophobic interaction between membrane surface and foulant molecules and thus mitigates surface adsorption or deposition [26, 28, 265-268].

Membrane fouling characteristics are directly attributed to membrane surface characteristics (e.g., surface chemistry, charge, topography, and hydrophilicity) [40-42], which can be tuned by membrane surface activation using different types of plasmas (i.e., Air, He/O_2, and He; **Chapter 3**) followed by AA graft polymerization. Among the three tested plasmas, a greater level of hydrophilicity was attained for the surrogate PSf membrane surfaces treated by Air APP and subsequently AA graft polymerized, relative to the corresponding surfaces synthesized via surface activation with He and He/O_2 plasmas (**Chapter 3**). It is thus expected that SNS-PAA-PSf membrane surface that is activated by Air APP should have superior fouling resistance and cleaning efficacy.

Accordingly, the effectiveness of Air APP for PSf surface activation was assessed with respect to its impact on membrane fouling propensity and cleaning efficacy. The fouling propensity and cleaning efficacy of the SNS-PAA-PSf membrane were evaluated using the model foulants, BSA and sodium alginate. In addition, the resulting membrane fouling properties were assessed in relation to the membrane surface characteristics (i.e., surface hydrophilicity, surface topography, surface charge, and surface composition; **Chapter 3**).

7.2 Experimental

7.2.1 Materials

PSf membrane (MUF-20K, Toray Membrane USA Inc., Poway, CA) with manufacturer reported 100 kDa *MWCO* was selected as the base membrane for surface nano-structuring (SNS) with tethered PAA layer. Also, a commercial PSf membrane (MUF-10K; Toray Membrane USA Inc., Poway, CA) was used for performance comparison. Both of the above membranes were obtained as flat sheets. Nitrogen (99%) gas (Airgas, Los Angeles, CA) was used for PSf sample drying, graft polymerization degassing, and UF system feed tank pressurizing. Acrylic acid (99%, Sigma-Aldrich, St. Louis, MO) was the hydrophilic monomer used for graft polymerization to form poly(acrylic acid) chains tethered onto the PSf surfaces, post-activation with atmospheric pressure plasma. All solutions were prepared in deionized (D.I.) water produced with a Milli-Q filtration system (Millipore Corp., San Jose, CA). Formamide (Fisher Scientific, Chino, CA), diiodomethane (⩾99%, Fisher Scientific, Chino, CA) and deionized (D.I.) water were used for surface energy characterization via contact angle measurements. Alginic acid sodium salt from brown algae (Sigma-Aldrich, St. Louis, MO) and BSA (⩾98%, Sigma-Aldrich, St. Louis, MO) was a model foulant for the ultrafiltration fouling tests. Sodium alginate filtration tests were conducted with 32 g/L sodium chloride (⩾99.0%, Fisher Scientific, Chino, CA) aqueous solutions. BSA was dissolved in phosphate-buffered saline (PBS) solution prepared with 8 g/L sodium chloride, 0.2 g/L potassium chloride, 1.44 g/L sodium phosphate (diabasic, anhydrous, Sigma-Aldrich, St. Louis, MO), and 0.24 g/L potassium phosphate (monobasic, Fisher Scientific, Chino, CA). Solution pH was adjusted using 0.1 M hydrochloric acid (HCl) and 0.1 M sodium hydroxide (NaOH) solution (Fisher Scientific, Chino, CA) and determined using a pH meter (Oakton pH 110 Meter; Cole-Parmer, Vernon Hills, IL).

7.2.2 Atmospheric pressure plasma-induced graft polymerization (APPIGP)

The tethered PAA layer was synthesized onto PSf surfaces via atmospheric pressure He/O_2 plasma PSf membrane surface activation followed by AA free-radical graft polymerization following a previously established protocol [55, 156, 278]. The Base-PSf UF membrane (MUF-20K) was immersed in D.I. water for at least 24 hr, and subsequently dried via an impinging nitrogen stream prior to surface activation with plasma. Air plasma was dispensed via FG5001 Plasma Generator (Plasmatreat USA, Inc., Elgin, IL) operating with the frequency of 21 kHz, voltage of 280 V, and Plasma Cycle Time (PCT) of 100%. The plasma was discharged via dispensing jets installed on an XYZ scanning robot (Surfx Technologies Inc., Redondo Beach, CA). Surface activation was accomplished via single sequential plasma scan (*N*) at a speed of 100 mm/s and source-surface separation (*PSS*) distance in the range of 10 mm.

Following APP activation, the Base-PSf membranes were placed in 250 mL glass reaction vessels containing the 20 vol% aqueous AA monomer solutions (pH = 1.9). The vessels were placed in a constant water bath at 70°C for 60 min. Nitrogen was injected (via a thin tubing loop with small holes poked with needles) at the bottom of the vessels during graft polymerization to promote mixing and scavenge dissolved oxygen that could inhibit the polymerization reaction [280]. After the graft polymerization step, the SNS-PAA-PSf membrane surfaces were rinsed with D.I. water to remove unreacted species. Performance characterization (i.e., hydraulic permeability and *MWCO* determination) of each membrane was conducted after its immersion in D.I. water for at least a 24 hr period.

7.2.3 Surface hydrophilicity

Surface wettability of both the PSf membrane and membrane surrogate surfaces was evaluated by sessile drop (SD) water contact angle measurements (θ) using an automated analyzer (DSA20; KRÜSS GmbH, Germany) [55, 156, 278]. SD water contact angle measurements were taken (at ~20°C) within 2 s following placement of a 1 µL D.I. water drop onto sample surfaces. The reported contact angles represent values averaged over measurements from at least 5 locations for each sample. The surface free energy of hydration (ΔG_{iw}) was then calculated using the Young-Dupré equation, $\Delta G_{iw} = -\gamma_w(1+\cos\theta_w)$, where γ_w is the surface energy of liquid water and θ_w is the water contact angle. It is noted that surfaces are typically considered to be hydrophilic when ΔG_{iw} < -113 mJ/m^2, and hydrophobic with ΔG_{iw} > -113 mJ/m^2 [246].

The SNS-PAA-PSf membrane surface contact angles were also obtained for formamide and diiodomethane to determine the dispersive/non-polar Lifshitz-van der Waals component, γ^{LW}, and the polar Lewis acid-base component (γ^{AB}) representing dipole-dipole Coulomb interactions and hydrogen bonding [312, 313] contributions to the membrane surface energy [25, 314]. Surface energy components for all three liquids [315] are listed in **Table 7-1**. These two surface energy components were estimated following the X-DLVO theory described in [25, 315]:

$$\gamma^{\mathrm{AB}} = 2\sqrt{\gamma^{+}\gamma^{-}} \qquad [7\text{-}1]$$

$$\gamma^{\mathrm{TOT}} = \gamma^{\mathrm{LW}} + \gamma^{\mathrm{AB}} \qquad [7\text{-}2]$$

$$\left(1+\cos\theta\right)\ \gamma_{\mathrm{l}}^{\mathrm{TOT}} = 2\left(\sqrt{\gamma_{\mathrm{s}}^{\mathrm{LW}}\gamma_{\mathrm{l}}^{\mathrm{LW}}} + \sqrt{\gamma_{\mathrm{s}}^{+}\gamma_{\mathrm{l}}^{-}} + \sqrt{\gamma_{\mathrm{l}}^{+}\gamma_{\mathrm{s}}^{-}}\right) \qquad [7\text{-}3]$$

where γ^{TOT} is the total surface tension, γ^{LW} is the nonpolar (Lifshitz-van der Waals, LW) component of surface tension, γ^{AB} is the polar (Lewis acid-base, AB) component of surface tension, γ^{+} and γ^{-} are the electron acceptor and donor parameters, respectively, and θ is the contact angle. The

subscript *s* and *l* denote the solid (membrane) surface and liquid, respectively. The LW component represents mainly Keesom orientation force, Debye induction force and London dispersion force, while the AB component represents electron-donor-electron-acceptor interactions between polar moieties in a polar media [312, 313]. The AB component of membrane surface energy can then be divided into electron acceptor (γ^+) and donor (γ^-) parameters.

Table 7-1. Surface tension of liquids used in contact angle measurements[a].

Liquid	γ_l (mN/m)	γ_l^d (mN/m)	γ_l^p (mN/m)
D.I. Water	72.8	22.2	50.6
Formamide	58.4	19.8	38.6
Diiodomethane	50.8	6.7	44.1

[a] γ_l is the surface tension of liquid, γ_l^d , γ_l^p are the dispersive and polar components of liquid surface tensions. Data from [142, 316, 317].

The Gibbs free energy change (ΔG) was calculated as the difference between the Gibbs free energies of the two surfaces are adsorbed and desorbed to each other, to indicate whether the interaction between two surfaces is attractive (i.e., ΔG<0) or repulsive (i.e., ΔG>0) [313]. The free energy of cohesion represents the membrane-membrane interfacial interaction. The greater absolute value of negative free energy of cohesion implies the stronger surface hydrophobicity [318]. While free energy of adhesion represents the energy needed for the adhesion of the foulant (i.e., BSA in this study) and membrane surface is calculated using surface energy of both pristine and BSA fouled membrane surface. In principle, when the free energy of adhesion is negative, membrane fouling would be spontaneous due to the attractive force between the foulant molecule and membrane surface. When the free energy of adhesion is positive, there is repulsive force between the foulant and membrane; thus, membrane fouling would require additional factor/energy such as permeate flux [313]. Both free energy of cohesion and adhesion consists of polar (AB) and nonpolar (LW) components and can be calculated via:

$$\Delta G_{h_0}^{\mathrm{TOT}} = \Delta G_{h_0}^{\mathrm{LW}} + \Delta G_{h_0}^{\mathrm{AB}} \quad [7\text{-}4]$$

$$\Delta G_{h_0}^{\mathrm{LW}} = 2\left(\sqrt{\gamma_{\mathrm{l}}^{\mathrm{LW}}} - \sqrt{\gamma_{\mathrm{m}}^{\mathrm{LW}}}\right)\left(\sqrt{\gamma_{\mathrm{c}}^{\mathrm{LW}}} - \sqrt{\gamma_{\mathrm{l}}^{\mathrm{LW}}}\right) \quad [7\text{-}5]$$

$$\Delta G_{h_0}^{\mathrm{AB}} = 2\sqrt{\gamma_{\mathrm{l}}^{+}}\left(\sqrt{\gamma_{\mathrm{m}}^{-}} + \sqrt{\gamma_{\mathrm{c}}^{-}} - \sqrt{\gamma_{\mathrm{l}}^{-}}\right) + 2\sqrt{\gamma_{\mathrm{l}}^{-}}\left(\sqrt{\gamma_{\mathrm{m}}^{+}} + \sqrt{\gamma_{\mathrm{c}}^{+}} - \sqrt{\gamma_{\mathrm{l}}^{+}}\right) - 2\left(\sqrt{\gamma_{\mathrm{m}}^{+}\gamma_{\mathrm{c}}^{-}} + \sqrt{\gamma_{\mathrm{c}}^{+}\gamma_{\mathrm{m}}^{-}}\right) \quad [7\text{-}6]$$

where ΔG is the free energy of adhesion. The subscripts *m*, *l* and *c* denote membrane, bulk liquid and foulants, respectively.

7.2.4 Fouling resistance

Membrane performance was evaluated with circular membrane coupons (active area of 13.4 cm^2) in a dead-end filtration configuration consists of a 50 mL stirred UF cell (Amicon 8050, Millipore Corporation, Burlington, MA) interfaced with an 800 mL feed tank pressurized using nitrogen (Error! Reference source not found.). The membrane samples were first compacted with D .I. water at 3.5 bar (~50 psi) and ~20°C for a 3 hr period prior to performance characterization. Water flux ($J_v = Q_p / A$, in which Q_p and A are the permeate flow rate and membrane area, respectively) was determined over an applied pressure range of 0-3.5 bar (0-50 psi). The permeate flow rate was determined using an in-line liquid flow meter (SLS-1500, Sensirion AG, Switzerland) with a maximum deviation of ±5% from the measured value. The pressure, set via a pressure regulator (Type 90, Control Air Inc., Amherst, NH), was measured using a pressure gauge (33HP99, Grainger, Lake Forest, IL) with a maximum measurement error of ±0.4% of the full scale reading of 60 psi. The hydraulic permeability coefficient (L_p) was then determined from the slope of water flux versus transmembrane pressure (i.e., $L_p = J_v / \Delta P$, where ΔP is the applied transmembrane pressure) [46, 278].

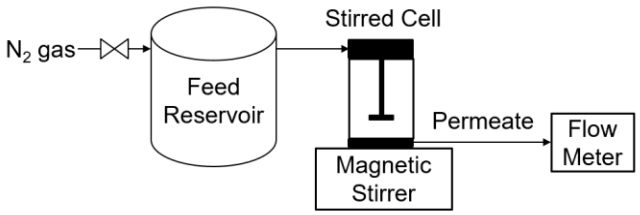

Figure 7-1. Configuration of the UF filtration system.

Fouling propensity and cleaning effectiveness for the SNS-PAA-PSf membranes were evaluated in fouling stress tests. The fouling tests were carried out with solutions of high concentration (1 g/L) of BSA and sodium alginate as model foulants. Fouling tests with BSA were conducted with PBS solutions and sodium alginate at high salinity (32 g/L NaCl). Filtration tests were carried out at an initial permeate flux of 9 $L \cdot m^{-2} \cdot h^{-1}$ (~5.3 $gallon \cdot ft^{-2} \cdot day^{-1}$), which is within the typical permeate flux range for UF seawater pretreatment [319]. The observed foulant rejection for the different membranes, $R(\%) = (1 - C_p / C_f) \times 100$, in which C_p and C_f are the foulant concentrations in the permeate and feed solution, respectively, determined during the initial state of each fouling test. BSA and sodium alginate concentrations in the feed and permeate streams were determined using UV-Vis (HP 8452A Diode Array Spectrophotometer, Hewlett-Packard, Palo Alto, CA) at λ=278 and 220 nm, respectively.

Prior to each protein solution filtration test, the membrane hydraulic resistance, R_m (m^{-1}), was determined using D.I. water, determined from Darcy's law, $J_{PW} = \Delta P / \mu R_m$, where ΔP (bar) is the transmembrane pressure, and μ (kg/m·s) represents viscosity. Here we note that the hydraulic permeability is related to the membrane hydraulic permeability coefficient as $L_p = 1/\mu R_m$. The total membrane filtration resistance [46, 278] at the end of each fouling test (R_T) was taken to be the linear sum of the hydraulic intrinsic membrane resistance, R_m, irreversible fouling resistance

(R_{irrev}), and cake layer buildup (reversible) foulant layer (R_{cake}) (i.e., $R_T = R_m + R_{cake} + R_{irrev}$). At the end of each fouling test, the membrane was backwashed with D.I. water at twice the initial permeate flux (i.e., 18 $L \cdot m^{-2} \cdot h^{-1}$) for 2 min. The hydraulic resistance of the backwashed membrane was then redetermined with D.I. water, thereby allowing quantification of the combined intrinsic membrane and irreversible fouling resistances expressed as $R_T^{'} = R_m + R_{irrev}$. Subsequently, R_{cake} and R_{irrev} were determined given the calculated values of R_T and $R_T^{'}$.

7.3 Results and Discussion

Upon Air APP treatment of the PSf membrane, the water contact angle was reduced from 66.3° (Native-PSf membrane) to 15.5° (**Table 7-2**). Subsequent AA graft polymerization led to SNS-PAA-PSf membrane for which the water contact angle was 19% lower relative to the Native-PSf membrane (**Table 7-2**). Given that the free energy of hydration (ΔG_{iw}) for the SNS-PAA-PSf membrane was lower than the critical hydrophilicity threshold of -113 mJ/m^2 [246], this membrane can be classified as hydrophilic [246].

Table 7-2. Sessile drop water contact angle and free energy of hydration for the Native-PSf, plasma treated and SNS-PAA-PSf membranes.

Membrane	Contact Angle (º)	Uncertainty (º)	Free energy of hydration (mJ/m^2)
Native-PSf[(a)]	66.3	1.8	-102.1
Air APP treated PSf membrane[(b)]	15.5	1.9	-143.0
SNS-PAA-PSf[(c)]	53.7	2.2	-115.9

[(a)] MUF-10 K UF membrane (**Table 5-1, Chapter 5**).

[(b)] Native-PSf membrane treated with Air APP (*PSS* =10 mm, N = 1)

[(c)] PSf-UF membrane with tethered PAA layer (Surface activation by Air APP (*PSS* =10 mm, N = 3) followed by AA graft polymerization ($[M]_o$ = 20 vol%, 70 C, 1 h).

The increases in total surface energy (γ^{TOT}) and its two components (γ^- and γ^{AB}) as shown in **Table 7-3** have been correlated with improved membrane antifouling performance [320] and thus lead to the expectation of reduced fouling propensity of the SNS-PAA-PSf membrane. The polar component of the surface energy (γ^{AB}) for the SNS-PAA-PSf membrane increased by a factor of 6.6 upon surface modification with the tethered PAA layer (**Table 7-3**), consistent with the hydrophilicity improvement as quantified by the reduced surface free energy of hydration (**Table 7-2**). Also, the electron donor (γ^-) part of the polar surface energy component (γ^{AB}) increased by a factor of ~133 relative to the Native-PSf membrane (**Table 7-3**). The increase in the above metrics correlates with membrane surface polarity post-AA graft polymerization and can be attributed to the introduction of negatively charged carboxyl groups of the tethered PAA chains [148].

The repulsive (positive) free energy of AB component ($\Delta G^{AB}_{cohesion}$) and the less attractive (negative value reduced by ~90%) total free energy of cohesion ($\Delta G^{TOT}_{cohesion}$) of the SNS-PAA-PSf relative to the Base-PSf membrane indicating improved surface wettability to form hydration shells [318] and thus enhancing membrane fouling resistance (**Figure 7-2**). The much lower total free energy of adhesion ($\Delta G^{TOT}_{adhesion}$) by ~80% as well as the AB component ($\Delta G^{AB}_{adhesion}$) by ~90% for the SNS-PAA-PSf membrane suggested the lower attractive interaction between membrane surface and foulant molecules (i.e., BSA), indicating reduced membrane surface protein adsorption [313].

Table 7-3. Contact angle and surface energy parameters of Native PSf membrane (MUF-10K) and SNS-PAA-PSf membrane.

	Native membrane	SNS-PAA-PSf membrane
(a) Contact angle (°) measured with different probe liquids (n=3)		
Water	77.1±1.6	41.6±1.5
Formamide	48.6±1.3	21.0±1.3
Diiodomethane	23.9±0.9	29.2±1.8
(b) Membrane surface energy parameters (mJ/m^2) (n=3)*		
γ^{LW}	46.50±0.09	44.67±0.29
γ^+	4.82±0.09	0.91±0.03
γ-	0.13±0.02	30.35±0.41
γ^{AB}	1.60±0.09	10.50±0.12
γ^{TOT}	48.10±0.18	55.17±0.30

* γ^{TOT} is the total surface energy, γ^{LW} is the nonpolar (Lifshitz-can der Waals, LW) surface energy component, γ^{AB} is the polar (Lewis acid-base, AB) surface energy component, γ^+ and γ^- are the electron acceptor and electron donor parameters, respectively.

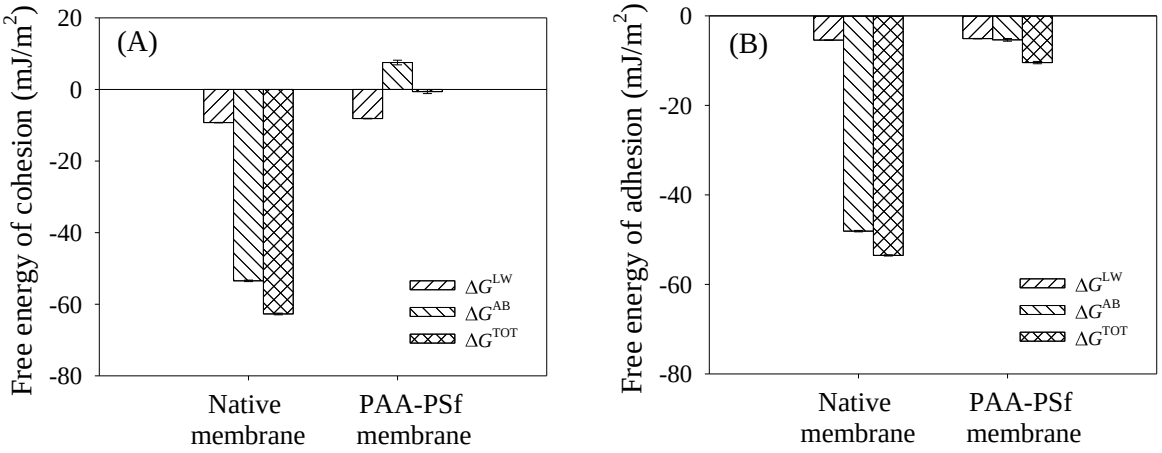

Figure 7-2. (A) Membrane surface free energy of cohesion and its components, and (B) free energy of adhesion between membrane surface and the foulants (contact angle measured on the BSA fouled membranes).

The fouling propensity of the SNS-PAA-PSf membrane was assessed via fouling filtration stress tests with the model foulants BSA and the smaller size sodium alginate. All filtration tests commenced at the same initial permeate flux. For BSA (Mw=66.4 kDa), the SNS-PAA-PSf

membrane fouling propensity was compared to a commercial PSf UF membrane (MUF-10K) having similar BSA rejection (96.1%) to the SNS-PAA-PSf membrane (96.3%) (**Table 7-4**). Filtration tests with the much smaller sodium alginate (*Mw*=1-5 kDa), having a significantly lower membrane rejection relative to BSA (**Table 7-4**), were also carried for the native and SNS-PAA-PSf membranes to assess the potential for pore fouling blockage.

Table 7-4. Membrane hydraulic resistance, *MWCO*, and rejection of BSA and sodium alginate for the Base-PSf (MUF-20K), Native-PSf (MUF-10K), and SNS-PAA-PSf membranes.

Membranes	Membrane hydraulic Resistance (m^{-1})	Molecular Weight Cutoff (kDa)	Foulant Rejection[(d)] (%)	
			BSA	Sodium Alginate
Base-PSf (MUF-20K)[(a)]	8.1×10^{12}	100	92.3	47.2
Native-PSf (MUF-10K)[(b)]	1.3×10^{13}	10	96.1	70.9
SNS-PAA-PSf [(c)]	6.9×10^{13}	6.5	96.3	84.6

[(a)] Membrane modified to synthesize the SNS-PAA-PSf membrane (**Section 7.2.2**).
[(b)] Unmodified commercial membrane for comparison with the SNS-PAA-PSf membrane.
[(c)] PSf UF Membrane with tethered PAA chains (**Table 5-1, Chapter 5)**.
[(d)] Foulant rejection determined per the protocol in **Section 7.2.4**.

Filtration of the BSA solution (**Section 7.2.4**) with the SNS-PAA-PSf membrane was accompanied by a lower overall filtration resistance increase of ~10.5% (after 2 h filtration) relative to 26.3% resistance increase for the commercial PSf UF membrane (Toray MUF-10K) (**Fig. 7-3a**). Previous studies have argued that the lower fouling propensity imparted by tethered hydrophilic polymer chains is attributed, in part, to the partial mobility (due to Brownian motion) of the tethered PAA chain segments and screening of the underlying membrane surface [45-47, 310, 311]. It is also noted that at the operating pH (~7) for the present fouling tests, the negative zeta potential for the SNS-PAA-PSf membrane surface was greater (by 26%) relative to the native PSf membrane (**Fig. 3-8, Chapter 3**). Thus, greater repulsion of the negatively charged BSA molecules from the membrane surface is expected for the SNS-PAA-PSf membrane. A greater

degree of surface hydrophilicity for the SNS-PAA-PSf membrane was observed relative to the Native-PSf membrane (indicated by 13.5% lower free surface energy of hydration, and 14.7% and 556.3% greater surface energy and its polar component, respectively).

It is stressed that effective cleaning of the BSA fouled SNS-PAA-PSf membrane was achieved via simple D.I. water backwash (for 2 min) resulting in 100% permeability recovery, relative to ~81.5% recovery for the Native-PSf membrane. Given the residual (irreversible) BSA fouling resistance for the native PSf membrane (**Table 7-5**), more aggressive chemical cleaning would be needed to restore the original membrane permeability. Here we note that the greater cleaning efficacy achieved with the SNS-PAA-PSf membrane is not surprising given the higher hydrophilicity (**Table 7-2**), surface negative charge (**Fig. 3-8, Chapter 3**), and screening of the PSf surface by the tethered PAA chains that also lower the probability for foulant surface adsorption [47, 310, 311, 321].

Fouling filtration tests with sodium alginate, which had a significantly lower membrane rejection relative to BSA (**Table 7-5**), indicated a similar fouling resistance increase of up to 43% and 47% (after 2 hr filtration) for the SNS-PAA-PSf and Native-PSf membrane membranes, respectively (**Fig. 7-3b**). It is plausible that sodium alginate fouling within the membrane pores was more pronounced for the Native-PSf membrane. This may have led to a somewhat higher degree of fouling for the SNS-PAA-PSf membrane, which has smaller pores as suggested by the higher sodium alginate rejection (84.6% relative to 70.9% for the native PSf membrane; **Table 7-4**). Cleaning efficacy, however, was significantly higher for the SNS-PAA-PSf membrane having 100% permeability recovery upon simple backwash with D.I water. In contrast, the same cleaning procedure for the native PSf membrane achieved permeability recovery of only 66%. The above comparison of fouling and cleaning performance with sodium alginate further indicates that the

tethered PAA chains were effective in screening the underlying membrane surface and preventing membrane pore fouling.

Table 7-5. Intrinsic membrane resistance (R_m), reversible fouling resistance (R_{rev}) and irreversible fouling resistance (R_{irrev}) for Commercial PSf (Toray MUF-10K) membrane and SNS-PAA-PSf[(a)] membrane post 2 hr filtration with BSA[(b)] (in PBS solution) and sodium alginate[(b)] in a high salinity aqueous solution.

Membrane	R_m **(m^{-1})**	R_{rev} **(m^{-1})**	R_{irrev} **(m^{-1})**	R_{Total} **(m^{-1})**
BSA Filtration				
Native-PSf (MUF-10K)	1.3×10^{13}	4.9×10^{11}	3.0×10^{12}	1.6×10^{13}
SNS-PAA-PSf (Air APP)	6.9×10^{13}	7.3×10^{12}	-	7.6×10^{13}
Sodium Alginate Filtration				
Native-PSf (MUF-10K)	1.3×10^{13}	5.0×10^{12}	6.6×10^{12}	2.5×10^{13}
SNS-PAA-PSf (Air APP)	6.9×10^{13}	5.1×10^{13}	-	1.2×10^{14}

[(a)] SNS-PAA-PSf membrane synthesized using a Base-PSf membrane (MUF-20K) via AA graft polymerization ($[M]_o$=20 vol%, 70°C, 1 hr) post-surface activation with atmospheric pressure Air plasma (*PSS* =10 mm, N = 1); [(b)] BSA fouling stress tests conducted with 1 g/L BSA in PBS solution (pH=7.4, ~20°C); [(c)] Sodium alginate fouling stress tests conducted with 1 g/L sodium alginate in aqueous 32,000 mg/L NaCl solution).

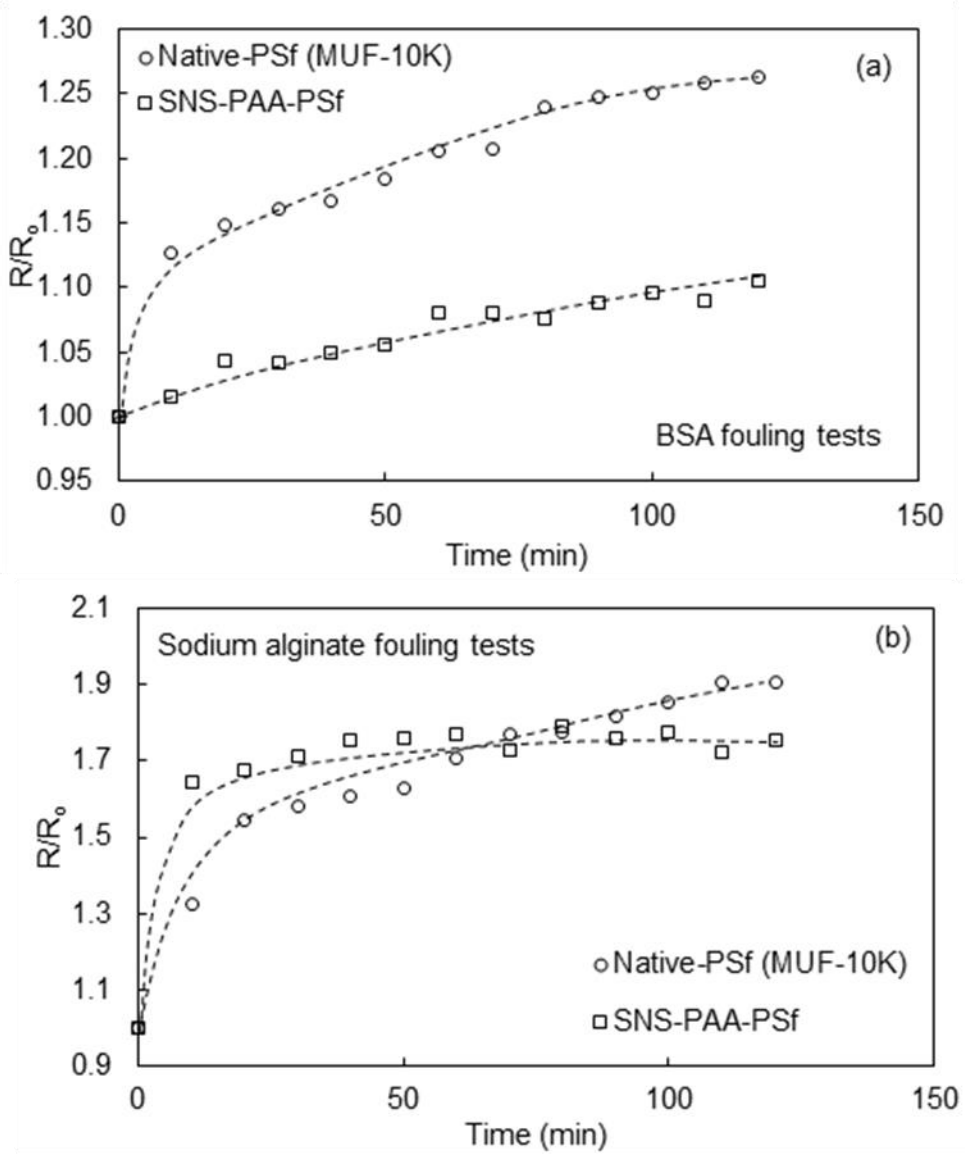

Figure 7-3. Normalized overall UF membrane resistance for fouling stress tests comparing the SNS-PAA-PSf and a commercial UF membranes for (a) BSA filtration of 1 g/L BSA in PBS aqueous solution at pH 7.4 for 2 h, and (b) filtration of 1 g/L sodium alginate saline solution (with 32 g/L NaCl) at pH 7 for 2 h. All fouling tests were at the same initial flux (9 $L \cdot m^{-2} \cdot h^{-1}$). The SNS-PAA-PSf synthesis conditions: Air APP treatment at *PSS* =10 mm and *N* = 1; AA graft polymerization at $[M]_o$ = 20 vol% and 70 °C for 1 h.

7.4 Conclusions

The SNS-PAA-PSf membrane demonstrated improved surface hydrophilicity, increased polar component of the surface energy, and lower foulant-membrane attractive interaction (as indicated by membrane surface free energy of adhesion), which supports the expectation of reduced fouling

propensity. As expected, the SNS-PAA-PSf membrane demonstrated reduced flux decline during the filtration of bovine serum album (BSA) attributed to the partial mobility (due to Brownian motion) of the tethered PAA chain segments which also screen the underlying membrane surface. Flux declines was observed during filtration SNS-PAA-PSf membrane of sodium alginate, and was within a range similar to that formed for Native-PSf membrane. Higher foulant rejection can lead to greater membrane surface accumulation of the foulant molecules and thus more severe cake layer buildup, which can offset the beneficial impact of the surface tethered PAA layer in reducing membrane fouling propensity. For both BSA and sodium alginate fouling tests, the SNS-PAA-PSf membrane demonstrated much better cleaning efficacy relative to the Native-PSf membrane as indicated by greater permeability recovery.

Chapter 8 Selective RO membrane with a surface tethered polymer brush layer for enhanced rejection of nitrate, boron, and arsenic

8.1 Overview

To alleviate the global water crisis, the low-cost and high-efficiency reverse osmosis (RO) process is increasingly used for both seawater (SW) and brackish water (BW) desalination to produce potable drinking water [117]. RO membranes are effective for the removal of salt ions, but have low rejection for ions such as nitrate, boron, and arsenic that are of concern due to their toxicity [87, 322]. Nitrate presence in drinking water has been reported to lead to methemoglobinemia (baby blue syndrome) causing reduced oxygen transport to bodily tissues [87]. Chronic arsenic exposure is associated with a wide variety of adverse health effects such as cancer, skin lesions, diabetes, and cardiovascular and neurological disease [323, 324]. Boron is known to be toxic to various plants [325], and while its chronic toxicity impacts from drinking boron-contaminated water have not been clearly established, it has been reported to have reproductive and developmental [87]. Both the World Health Organization (WHO) and the United States Environmental Protection Agency (EPA) have set strict drinking water standards for the above contaminants with the recommended maximum contamination level of 45 mg NO_3^-/L, 0.5 mg/L, and 10 μg/L, for nitrate, boron, and arsenic (sum of As (III) and As (V)), respectively [170, 172, 220].

Removal of the above ions from water to meet the above drinking water standard represents a challenge in RO desalination. The high salt rejecting TFC-PA RO membranes (with above 99% NaCl rejection) have a lower rejection in the ranges of 40-98% [326-328], 12-96% [10, 117, 329], 5-99% [102, 105, 330], 68-99% [105, 331] for nitrate, boron, As (III), and As (V), respectively (**Table 8-1**). While, for example, the maximum total boron concentration in seawater could amount

up to about 15 g/L [14]. To comply with the safe drinking water standard and reduce boron concentration below 0.5 mg/L in the treated permeate stream [15], a minimum RO boron rejection of 97% is required. This indicates that the level of the above solute rejections by commercial RO membranes are insufficient for reducing contaminant concentrations in contaminated water supplies in order to meet the drinking water quality requirements under normal operational conditions [11].

Table 8-1. Summary of membrane rejections for nitrate, boron, As (III), and As (V) for commercial PA BWRO and SWRO membranes (both flat sheet and spiral-wound elements) selected removal for (detailed literature review summary table* in **Section 2.1.3.2**).

Selected Removal	Flat sheet membrane	Spiral wound module
Nitrate [a]	40.4-97.7%	65-98%
Boron [b]	12-91%	70-96%
As (III) [c]	61-99%	5-85%
As (V) [d]	68-98%	92-99%

[a] Feed concentration of 18-1000 mg/L NO_3^- or 13-42.5 mg/L NO_3-N.

[b] Feed concentration of 1-8.6 mg/L boron.

[c] Feed concentration of 12-100 μg/L total arsenic (sum of As (III) and As (V)).

* Literature reported RO membrane rejections of nitrate, boron, As (III), and As (V) are provided in **Tables 2-1**, **2-2**, and **2-3**. The tables report on the membrane model and configurations (both flat-sheet and spiral-wound element), feed solution concentration and pH, membrane solute rejection, and the reference number of the studies.

The traditional approaches to increasing RO membrane removal of these contaminants include adjusting feedwater pH, increasing operating pressure, optimizing process flow, diluting the RO permeate, using multi-pass RO, implementing processes such as adsorption, ion exchange, oxidation, coagulation, precipitation, electrodialysis, and biological denitrification [10-13, 81, 117]. Although effective, these methods can lead to significant increases in both capital and operational costs [117]. For example, it was reported that RO rejection of boron increased from 40-60% under normal operating conditions to 99.5% when solution pH was increased to 11 [15].

Increased RO boron rejection at high solution pH is due to both dissociation of the boric acid ($B(OH)_3+H_2O \rightarrow B(OH)_4^-+H^+$) and molecule hydration, resulting in the formation of an ion with a negative charge and a larger radius [79]. Higher membrane boron rejection can thus be explained by both size exclusion and charge repulsion. However, the issue with the above approach is that it leads to increased operating costs (due to the use of additional chemicals), and the challenge of a brine stream disposal.

As an alternative, various approaches to modifying TFC-PA membranes have been explored to increase RO membrane rejection for boron (from 58-83% to 76-93%, [156, 332, 333]) and nitrate (from 92% to 95%, [334]). Tuning membrane rejection of the above contaminants has been advanced by targeting critical factors that affect solute transport enabled via membrane surface modification (**Table 8-2**). For example, increased boron rejection was achieved for a commercial TFC-PA RO membrane module (Dow SW30) by surface grafting of polyethylenimine (PEI) and subsequently adsorbed with glutaric dialdehyde (GA) to form a crosslinked network [156]. Boron rejection (feed concentration of 5-22 ppm) by the modified membrane increased from 76.65% to 90.14% [156] which was attributed to increased surface hydrophilicity. However, the improvement of membrane boron rejection was accompanied by 58% reduction in water permeability [156]. Improved membrane boron rejection was also achieved by adsorbing 4-nitrobenzenesulfonyl chloride (NBS) onto a commercial TFC RO membrane (SW30-4040, Dow) [332]. The resulting membrane's boron rejection (for feed boron concentration of 5 ppm) increased from 83.1% to 93.1% relative to the base membrane; however, this was at the cost of 62% reduction of the membrane hydraulic permeability. Greater boron rejection which was achieved in the above study was attributed to enhanced steric hindrance by the embedded NBS and synergistic exclusion effect by -SO3H groups [332]. In-situ modification of commercial TFC-PA RO membranes (SWC5 max

and SWC4B, Hydranautics) to increase boron rejection was also achieved by the incorporation (coupling) of aliphatic amines "plug" that can chemically or physically bind to the selective PA layer [329]. The modified membranes demonstrated reduced boron passage (the ratio of permeate and feed boron concentrations) by a factor of 2–4 (feed concentration of 5 ppm), but this was at the expense of 18-80% flux reduction [329]. In-situ modification of spiral-wound TFC-PA RO (LE and SW30 from Dow, and ESPA-1 from Hydranautics) membranes via persulfate/metabisulfite redox couple-initiated free-radical graft polymerization of 2-Hydroxyethyl methacrylate (HEMA), ethylene glycol dimethacrylate (EGDMA), or methyl methacryalte (MM) also led to increased boron rejection to 76-80% (determined for boron feed concentration of 5 ppm) relative to 58% for the base membrane [333]. The above study also conjectured that the improvement in boron rejection was primarily due to sealing of less selective areas ("defects") inherently present in the base TFC-PA RO membrane. Finally, it is noted that the mere treatment of a commercial TFC-PA RO membranes (Merlin, AG, and BW30LE) with sodium hypochlorite (4,000 ppm exposure for 15 min) was reported to increase membrane boron rejection (for boron feed concentration of 0.5 mg/L) from 17.4% to 27.9% [335]. The above boron rejection improvement was attributed to increased membrane hydrophilicity and higher negative surface charge; the consequence was increased electrostatic repulsion between the membrane surface and the negatively charged ions, as well as tightening of the polyamide active layer associated with the membrane chlorine treatment [335]. In spite of the extensive efforts to increase RO membrane boron rejection, only one study investigated the membrane surface modification approach to increase RO membrane nitrate rejection. It was demonstrated that grafting of a TFC-PA RO membrane (BW30, Filmtec Inc., USA) with a hydrophilic polyamidoamine (PAMAM) dendrimer, followed by embedding a graphene oxide (GO) nanosheet within the grafted layer increased

membrane nitrate rejection (evaluated for feed concentration of 1000 mg/L $NaNO_3$) from 92% to 95% [334]. To date, the impact of membrane surface modification via tethered polymer chains on RO membrane rejection of arsenic (both As(III) and As(V)) has not been reported in the research literature.

Table 8-2. Summary of the proposed key factors affecting solute rejection performance imparted by tethered hydrophilic polymers

Factors	Mechanisms	Modification Approaches	References
Surface charge	Increased negative membrane surface charge provides greater electrostatic repulsion of negatively charged ions.	Hypochlorite treatment	[335]
Surface hydrophilicity	Increased membrane surface hydrophilicity leads to greater hydrated membrane water fraction, which then affects the membrane water/salt transport.	Hydrophilic polymer grafting followed by embedding nanosheets	[334]
		Membrane surface grafting to form a crosslinked network	[156]
		Hypochlorite treatment	[335]
Steric hindrance	Increased membrane hydraulic resistance altered diffusivity and solubility of the solutes in the membrane.	Embedding of molecular plugs between the PA chains	[329, 332]
		Hypochlorite treatment	[335]
		Membrane surface free-radical graft polymerization	[333]
Surface screening	Formed a barrier on top of membrane active layer to reduce/eliminate solute/base membrane affinity.	Hydrophilic polymer grafting followed by embedding nanosheets	[334]
		Membrane surface free-radical graft polymerization	[333]

Accordingly, a systematic investigation was undertaken of the impact of surface tethered PAA brush layer on TFC-PA RO membrane rejection of nitrate, boron, As (III), and As (V). The approach consisted of a commercial BWRO polyamide membrane (Toray 73AC) surface nano-structuring with PAA brush layer via the APPIGP approach [49, 336]. Subsequently, SNS-PAA-PA membrane rejections for nitrate, boron, As (III), and As (V) were characterized at neutral pH (within the surface water pH range of 6.5 to 9 reported by the US EPA) and compared to the rejection performance of three commercial RO membranes.

8.2 Experimental

8.2.1 Materials

A commercial BWRO flat sheet membrane (73AC, Toray Membrane USA Inc., Poway, CA) was selected as the base membrane for membrane surface nano-structuring. A commercial SWRO flat sheet membrane, also from Toray (82V, Toray Membrane USA Inc., Poway, CA), and a widely-used SWRO membrane, (Dow SW30HR, Dow Filmtec Inc., Midland, MI) were selected for membrane performance comparison (**Table 8-3**).

Deionized (D.I.) water produced by Milli-Q filtration system (Millipore Corp., San Jose, CA) was used in all experiments. Acrylic acid (99%, Sigma-Aldrich, St. Louis, MO) monomer was selected for PA surface graft polymerization after surface activation by atmospheric pressure plasma treatment. 0.1 N hydrochloric acid (HCl) and sodium hydroxide (NaOH) solutions (Fisher Scientific, Chino, CA) were used to adjust the solution pH. Helium (99.999%) and oxygen (99.999%) gases (Airgas, Los Angeles, CA) were used as the atmospheric pressure plasma sources. Nitrogen (99%) gas (Airgas, Los Angeles, CA) was used for membrane surface drying prior to plasma surface activation, and for monomer solution degassing during graft polymerization.

Potassium nitrate (KNO_3, Laboratory Grade, Carolina Biological Supply, Burlington, NC), boric acid (H_3BO_3, ≥99.5%, Sigma-Aldrich, St. Louis, MO), sodium arsenite ($AsNaO_2$, Reagent Grade, Fisher Scientific, Chino, CA), and sodium arsenate dibasic heptahydrate ($Na_2HAsO_4 \cdot 7H_2O$, ≥98%, Sigma-Aldrich, St. Louis, MO) were used to determine membrane rejection of nitrate, boron, and arsenic (III and V charge), respectively.

Table 8-3. Commercial membrane performance reported by the manufacturers.

Membrane	Toray 82V (*Flat sheet*)	Toray 73AC (*Flat sheet*)	Dow SW30 * (*Spiral wound*)
Type	SWRO	BWRO	SWRO
Permeability ($L \cdot m^{-1} \cdot h^{-1} \cdot bar^{-1}$)	0.83	3.35	0.71[a]
Salt (NaCl) Rejection (%)	99.7	99.8	99.4[a]

[a] Permeability and salt rejection were determined based on the following test conditions: 32,000 ppm NaCl, pressure of 800 psi (55 bar), 25°C and 5% recovery. Permeability for the commercial elements may vary +/-20% according to the manufacturer's specification.

* The Dow SW30 membrane had literature reported nitrate rejection of 94% [88], boron rejection of 70-92% [78, 97-99], and arsenic rejection of (77-96% for As(III) and 90-96% for As(V); [80, 101, 103]).

8.2.2 Atmospheric pressure-induced graft polymerization (APPIGP)

The protocol for polyamide membrane surface nano-structuring followed the optimized approach reported previously [49]. Briefly, the Base-PA membrane sheets were kept in D.I. water for > 24 h. Prior to surface plasma treatment, membrane coupons (with active areas of 42 cm^2) were rinsed with D.I. water and blow-dried with compressed nitrogen. Membrane surfaces were plasma-activated through exposure to atmospheric pressure plasma (APP) using helium (He) APP system (Atomflo™ 500; Surfx Technologies Inc., Redondo Beach, CA) via 2 sequential plasma scans (*N*) and plasma-surface separation (*PSS*) distance of 10 mm (**Appendix C.2**). The plasma stream was delivered onto the membrane surface from a source head mounted on an XYZ scanning robot (Surfx Technologies LLC, Redondo Beach, CA) as illustrated in a previous study [336]. He APP was operated at a helium flow rate of 45 L/min generated at 150W radio frequency (RF) power. Immediately following APP activation, each membrane sample was immersed in a 250 mL glass reaction vessel containing the aqueous AA monomer solutions to initiate the free radical polymerization reaction on the membrane surface. The initial monomer concentration $[M]_o$ was set to 21 vol% and solution pH was adjusted to 6 using 0.1 N NaOH aqueous solution. The vessel containing the surface activated membrane was immersed in the monomer solution and then placed

in a constant water bath at 70°C for 60 min with nitrogen injected at the bottom to to both scavenge dissolved oxygen that could inhibit the graft polymerization reaction [156], and also provide for added mixing [336]. After graft polymerization, the membrane was thoroughly rinsed and stored in D.I water for at least 24 h prior to further characterization.

8.2.3 Membrane selective removal

Membrane performance characterization with respect to membrane solute rejection (for nitrate, boron, and arsenic) was conducted using a laboratory plate-and-frame RO (PFRO) membrane recirculation unit [49]. The PFRO system (**Fig. 8-1**) consisted of a rectangular flow cell (CF042D; Sterlitech Corp., Kent, WA) having an active membrane area of 42 cm^2 and dimensions of the flow channel of 8.5 cm (L) x 3.9 cm (W) x 0.08 cm (H), a positive displacement pump (Hydra-Cell; Wanner Engineering Inc., Minneapolis, MN), a 15 L feed tank and a refrigerated bath circulator (RTE-221, NESLAB Instruments Inc., Newington, NH). Transmembrane pressure was adjusted using a back-pressure valve (MCJ-050AB-3-1335G4Y; Hanbay Inc., Virginia Beach, VA) at the RO unit concentrate exit, and monitored via a pressure transmitter (Model A-10; WIKA Instrument LP, Lawrenceville, GA). The concentrate and permeate volumetric flow rates were monitored with a liquid flow sensor (Model 101-7; McMillan, Georgetown, TX) and a digital liquid flow meter (Model 5025000; GJC Instruments Ltd., UK), respectively. Feed solution temperature was maintained at 20.0±0.2 °C using the refrigerated bath circulator, monitored with a temperature probe (Go!Temp; Vernier Software & Technology, Beaverton, OR).

Prior to the determination of membrane rejection of nitrate, boron, and arsenic, the membrane coupons were compacted with D.I. water, under a transmembrane pressure (ΔP) of 58.6 bar (~850 psi) at a crossflow velocity of 49 cm/s and temperature of 20°C, for 24 h allowing the permeate

flux to stabilize. Membrane solute rejection was determined with model feed solutions at a crossflow velocity of 49 cm/s, a transmembrane pressure of 55.2 bar (~800 psi), and temperature of 20°C. Permeate samples were collected after the permeate flux was stabilized ~30 min. At the above operating conditions, the permeate flux was 25.5 $L \cdot m^{-2} \cdot h^{-1}$ such that the *CP* modulus in the present PFRO cell was at or below 1.3 [336].

The nitrate feed solution of ~60 ppm NO_3 concentration was prepared by dissolving KNO_3 in D.I. water. The feed and permeate NO_3 concentrations were measured using a hand-held digital nitrate sensor (eXact iDip® Process Water Professional Test Kit, Industrial Test Systems, Inc., Rock Hill, SC). The boron feed solution of ~3 ppm boron was prepared using H_3BO_3 and D.I. water. The arsenic feed solution of ~750 ppb concentration (As (III) or As (V)) was prepared by dissolving $AsNaO_2$ and $HAsNaO_4 \cdot 7H_2O$, respectively, in D.I. water. The feed and permeate concentrations of boron, As (III), and As (V) were measured using an Inductively Coupled Plasma Mass Spectrometer (ICP-MS, Perkin Elmer NexION 2000). It is noted that the feed concentrations of nitrate, boron, As(III), and As(V) were set within their measured concentration ranges in natural water. The pH of all model feed solutions was adjusted to 7 using 0.1 N HCl and 0.1 N NaOH and monitored using a pH meter (Oakton pH 110 Meter; Cole-Parmer, Vernon Hills, IL). Between each solute membrane rejection test, membrane cleaning was carried out by flushing the PFRO system with D.I. water at a transmembrane pressure of 21.4 bar (~310 psi) and crossflow velocity of 49 cm/s for 30 min.

The observed membrane solute rejection was calculated as $R_o = (1 - C_p / C_f) \times 100\%$, where C_p and C_f are permeate and feed stream solute concentrations, respectively. The intrinsic membrane solute rejection was determined as $R_i = (1 - C_p / C_m) \times 100\%$, where C_m is the average solute concentration at the membrane surface. C_m was estimated from the simple film model [337, 338],

$CP = \left(C_m - C_p\right) / \left(C_b - C_p\right) = exp\left(J_v / k\right)$, where C_b is the bulk solute concentration, and k is the feed-side solute mass transfer coefficient. Combining the simple film model and the membrane solute flux expression, $J_s = C_p \cdot J_v = B \cdot \left(C_m - C_p\right)$ [49], leads to the equation $ln\left(J_v \cdot (1 - R_o) / R_o\right) = J_v / k + ln(B)$, where B is the solute transport coefficient [72]. By varying the permeate flux, the value of k can then be obtained from a plot of $ln\left(J_v \cdot (1 - R_o) / R_o\right)$ vs J_v, where *1/k* is the slope and *ln(B)* is the y-intercept of the linear plot.

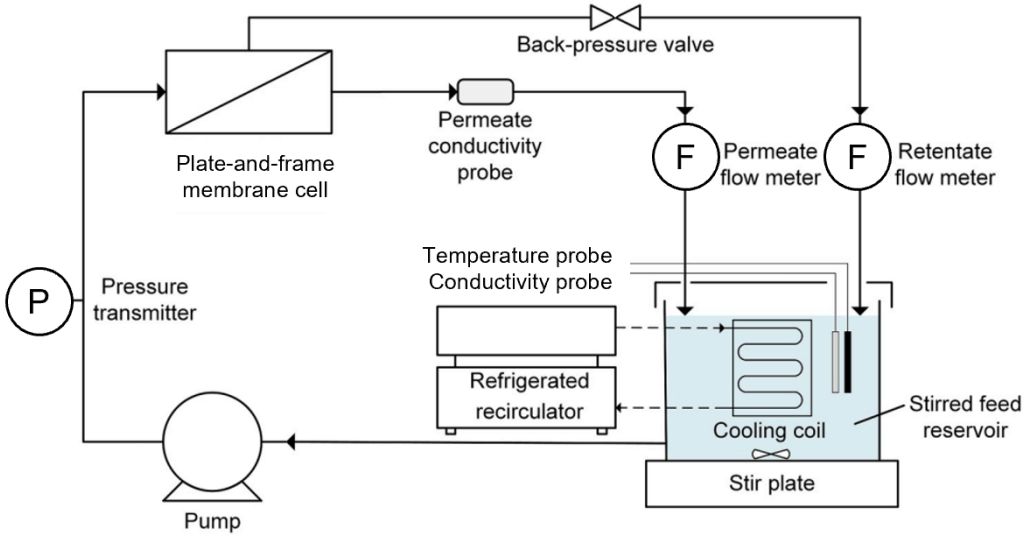

Figure 8-1. Configuration of the laboratory plate-and-frame RO (PFRO) membrane test unit (adapted from [49]).

8.3 Results and Discussion

The SNS-PAA-PA membrane demonstrated increased rejection for nitrate, boron, As (III), and As (V), compared to the commercial Dow SW30, Toray SWRO, and Base-PA membranes (**Fig. 8-2**). The increased SNS-PAA-PA membrane rejection for the above contaminants is consistent with its increased observed salt rejection (from 99.0% to 99.3%) as reported in a previous study [336], while its water permeability coefficient (1.69 $L \cdot m^{-1} \cdot h^{-1} \cdot bar^{-1}$) remained within the range for commercial SWRO membranes (**Table 8-4**). Upon tethering of PAA chains, the base membrane

observed nitrate rejection increased from 97.1% to 98% while the intrinsic rejection was elevated from 98.2% to 98.6%. The SNS-PAA-PA membrane also exhibited higher observed nitrate rejection relative to the commercial seawater RO membranes (Dow SW30 and Toray SWRO) by 0.9-1.2% and 0.4-0.8% higher R_o and R_i, respectively (**Table 8-5**). The SNS-PAA-PA membrane also displayed observed rejections for boron, As (III), and As (V), of 90.7%, 96%, and 99.6%, respectively, relative to 76.8-84.9%, 87.3-92.1%, and 94.5-97.2% for the tested commercial RO membranes (**Fig. 8-2** and **Table 8-5**). The SNS-PAA-PA membrane intrinsic rejections for boron, As (III), and As (V) were also 1.4-4.1% higher than for the commercial RO membranes. It is noted that the SNS-PAA-PA membrane is of increased solute rejection and it is capable of producing safe drinking water by treating feedwater of up to 2250 mg/L nitrate, 3.8 mg/L boron, or 182-1667 µg/L arsenic, which is not uncommon for highly contaminated water sources [339-341]. It was reasoned in previous studies that the modifying tethered polymer surface layer seals the microscopic defects (>0.5 nm; [342]) present in the polyamide membrane active layer; thus leading to increased membrane rejection via the size exclusion [167, 343, 344]. Previous studies have also reported improved salt rejection of commercial membranes after modification by surface tethering of PAA brush layer [49], surface coating of polyalkylene oxide [343], polyethylene glycol-based hydrogels [344] and polydopamine [167]. Given the above, the increased membrane removal of the above four solutes upon membrane surface grafting of the PAA brush is as expected.

It is noted nitrate, boron, As(III) and As(V) appear as NO_3^-, $B(OH)_3$, $HAsO_2$, and $HAsO_4^{2-}$ in aqueous solutions at neutral pH, with molecular weight of 62 Da, 62 Da, 108 Da, and 140 Da, respectively. Boron and As(III) are nonionic at neutral pH [78, 79, 81, 85]. Hence their rejection by membranes (via size exclusion) should increase owing to their increased molecular complex size. Consistent with the above are the higher observed (nominal) and intrinsic membrane

rejections obtained for $HAsO_2$ (87.3-94.5% and 91.9-96.0%), compared to the lower *Mw* $B(OH)_3$ (76.8-86.8% and 86.0-90.7%) for all four membranes (**Table 8-5**).

Table 8-4. Membrane water and salt permeability coefficients, and observed and intrinsic salt rejections [(a)].

Membrane [(b)]	L_p ($L \cdot m^{-1} \cdot h^{-1} \cdot bar^{-1}$)	B ($L \cdot m^{-2} \cdot h^{-1}$)	R_o (%)	R_i (%)
SNS-PAA-PA	1.69	0.15	99.3	99.5
Dow SW30	1.60	0.25	98.9	99.2
Toray SWRO	1.33	0.24	99.0	99.2
Base-PA	2.91	0.24	99.0	99.3

[(a)] Raw data obtained from [336].
[(b)] SNS-PAA-PA, Toray SWRO, and Base-PA membrane coupon samples were extracted from the commercial flat membrane sheets. The Dow SW30 membrane coupon sample was extracted from a membrane sheet taken from a commercial spiral wound element (Dow Filmtec SW30-2514).

Table 8-5. Membrane rejection of Nitrate, Boron, Arsenite, and Arsenate.

Membrane	**Nitrate**		**Boron**		**Arsenite**		**Arsenate**	
	R_o (%)	R_i (%)	R_o (%)	R_i (%)	R_o (%)	R_i (%)	R_o (%)	R_i (%)
Dow SW30	97.1	98.0	84.9	89.3	92.1	94.6	97.2	98.1
Toray SWRO	96.8	97.8	83.2	88.0	88.4	91.9	94.5	96.2
Base-PA	97.1	98.2	76.8	86.0	87.3	92.5	95.6	97.5
SNS-PAA-PA	98.0	98.6	86.8	90.7	94.5	96.0	99.4	99.6

The increased SNS-PAA-PA membrane rejection is also linked to its greater negative surface zeta potential of -54 mV for this membrane, relative to -38 mV for the commercial PA membranes at neutral pH [278, 345]. As a result, increased electrostatic repulsion between the tethered PAA membrane surface and the negatively charged solute ions should be expected. Since nitrate and As(V) exist as charged ions, NO_3^- and $HAsO_4^{2-}$, at neutral pH, their membrane rejection is governed by both electrostatic (Donnan) exclusion and size exclusion [81, 85]. Thus, the higher membrane rejection of nitrate and As(V) relative to boron and As(III) are as expected for all of the tested membranes.

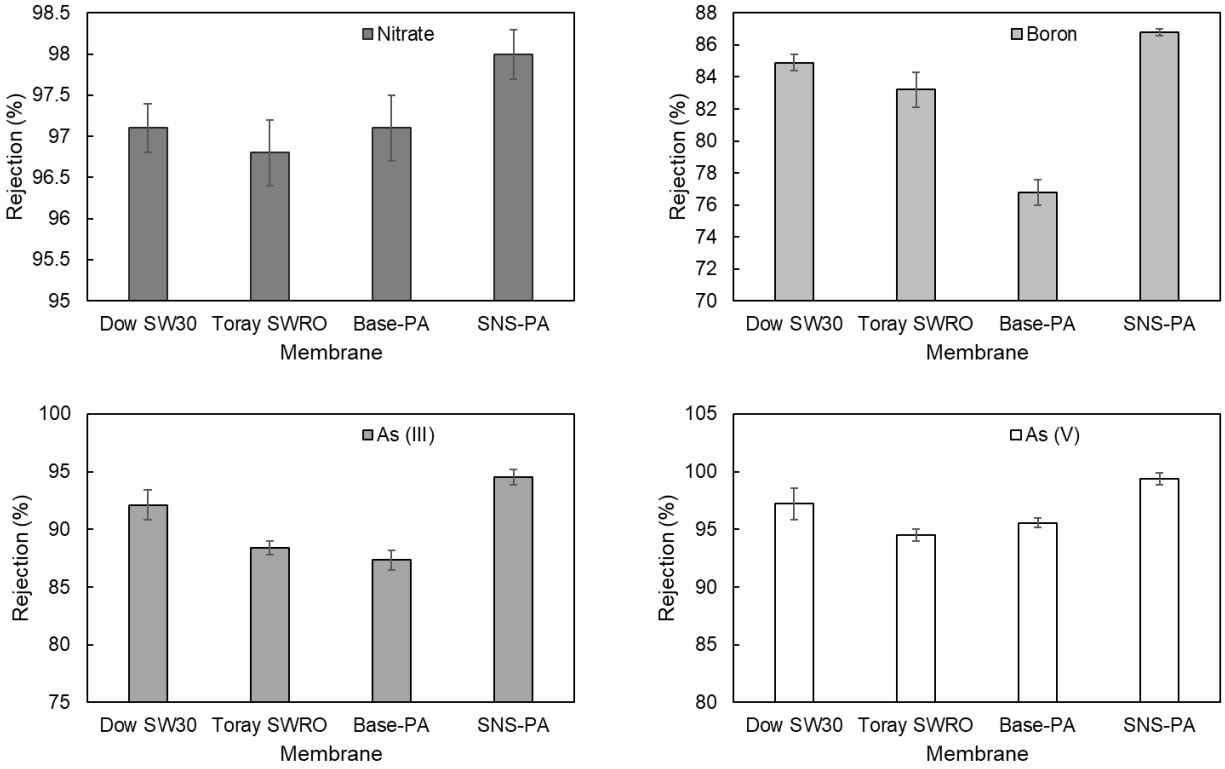

Figure 8-2. Rejection of nitrate, boron, As (III), and As (V) for SNS-PAA-PA membrane as compared to the commercial Dow SW30, Toray SWRO, and Base-PA membranes. (Feed solutions: 60 ppm NO_3 prepared using KNO_3, 3 ppm boron prepared using H_3BO_3, 750 ppb As (III) prepared using $AsNaO_2$, and 750 ppb As (V) prepared using $HAsNaO_4 \cdot 7H_2O$). Characterization conditions: crossflow velocity: 49 cm/s, permeate flux: 25.5 $L \cdot m^{-2} \cdot h^{-1}$, transmembrane pressure: 55.2 bar (~800 psi), and temperature: 20°C).

8.4 Conclusions

A thin-film composite (TFC) polyamide (PA) RO membrane with surface tethered poly(acrylic acid) (PAA) layer was synthesized via atmospheric pressure plasma-induced graft polymerization (APPIGP). This surface nano-structured (SNS) membrane demonstrated greater membrane removal of nitrate, boron, As(III), and As(V) relative to a commercial BWRO membrane surface. The superior removal of the above contaminants by the SNS-PAA-PA membrane was indicated by rejections of 98.0%, 90.7%, 96%, and 99.6%, for nitrate, boron, As (III), and As (V), respectively, relative to 96.8-97.1%, 76.8-84.9%, 87.3-92.1%, and 94.5-97.2% for the commercial

RO membranes (i.e., Base-PA, Dow SW30, and Toray SWRO). The above results suggest that there is merit for further tuning of SNS-PAA-PA membrane to improve rejections of above contaminants under field conditions.

Chapter 9 Impact of PAA Brush Layer on RO Membrane Scaling Propensity

9.1 Overview

The productivity of reverse osmosis (RO), which is one of the most widely used brackish water desalination technologies, is often limited by membrane surface mineral scaling. Membrane scaling occurs when the solubility limits of sparingly soluble salts (i.e., $CaCO_3$, $CaSO_4$, $BaSO_4$, $SrSO_4$, and silica) present in the feed water and within the RO feed channels are exceeded [18-21]. Even when the sparingly soluble salt concentrations in the raw feed are within their solubility ranges, concentration polarization, which is governed by membrane selectivity, permeate flux, and operating crossflow velocity (**Section 2.1.2.2**), leads to higher solute concentration near and at the membrane surface than in the bulk solution, and can thus result in supersaturation within the RO elements [25, 106]. Membrane mineral scaling can lead to permeate flux decline, and increased operation and maintenance costs (to maintain constant process productivity) due to higher consumption of energy, system downtime, membrane cleaning and replacement [18, 36]. Moreover, the presence of mineral scale formed on the membrane surface can also physically damage the membrane active layer and thus resulting in the loss of product quality and membrane selectivity [22, 24, 25, 347].

Current strategies to mitigate the adverse impact of mineral scaling include the use of antiscalants, adjustment of feedwater pH, frequent cleaning, and optimization of operational conditions such as cross-flow velocity and permeate flux [36]. Although the above approaches are effective, they represent increased operational complexity [36]. For example, the use of antiscalants and adjustment of feedwater pH introduce additional chemicals and thus lead to an added challenge for brine stream management [33]. Frequent cleaning requires plant shutdown or taking the membrane system offline (from hours to days), leading to reduced overall water treatment

plant capacity. As an alternative, the engineering of membrane surfaces to achieve improved scaling resistance has been an area of growing interest. It was previously demonstrated that membrane surface characteristics (e.g., surface charge, surface morphology, surface chemistry) can affect membrane scaling propensity, especially the rate of mineral crystal nucleation and scale surface adhesion [18, 36-38]. It was observed that membranes with lower surface roughness had greater ease of membrane surface silica scale removal [348]. Membranes with positive surface charge had more severe silica scaling than the negatively charged membranes due to the latter repulsion of like-charged species [191]. However, only limited surface modification approaches were conducted for reducing scaling of RO membrane [47, 108, 349], and the existed studies have focused mainly on gypsum scaling.

Assessment of the benefit of tethered PAA chains on PA-TFC membranes for reducing surface scaling were addressed in the dissertation study. The synthesized SNS-PAA-PA membrane had salt selectivity at a level comparable to the commercial Dow SW30 membrane [49]. The scaling propensity of the SNS-PAA-PA membrane was evaluated for both gypsum and calcium carbonate model solutions and compared to the base PA membrane, and two other commercial SWRO membranes (i.e., Toray SWRO and Dow SW30, **Chapter 8**). Gypsum and calcium carbonate were selected as model scalants representing alkaline and non-alkaline scaling, respectively, which are the two most commonly encountered membrane mineral scaling in desalination processes [116, 350-352]. Scanning electron microscope (SEM) images were obtained for both scaled and D.I. water cleaned membrane surfaces to provide direct measures of gypsum and calcium carbonate surface scaling. Post scaling tests, membrane cleaning was conducted to assess the degree of permeability restoration by re-dissolving mineral crystals (i.e., gypsum) and removing the loosely bound/attached mineral crystals via fluid shear. Membrane rejection, calculated based on the feed

and permeate conductivity, was also monitored during the filtration of gypsum and calcium carbonate to assess the impact of scale buildup on membrane surface on membrane salt rejection.

9.2 Experimental

9.2.1 Materials

A commercial PA-TFC BWRO membrane flat sheet (73AC, Toray Membrane USA Inc., Poway, CA) with sufficiently high water and salt permeability coefficients was selected as the base membrane for membrane surface nano-structuring. Two commercial flat sheet membranes, Toray SWRO (82V, Toray Membrane USA Inc., Poway, CA) and Dow SW30 (SW30HR, Dow Co., Midland, MI), were selected for comparison (**Table 8-3, Chapter 8**).

The base membrane surface nano-structuring was achieved with acrylic acid (99%, Sigma-Aldrich, St. Louis, MO) graft polymerization initiated by atmospheric pressure He plasma surface activation. A 0.1 N NaOH aqueous solution prepared in D.I. water using 50% w/w sodium hydroxide solution (Fisher Scientific, Chino, CA) was used to adjust the monomer solution pH. Helium (99.999%) and oxygen (99.999%) gases (Airgas, Los Angeles, CA) were used as atmospheric pressure plasma treatment sources, and nitrogen (99%) gas (Airgas, Los Angeles, CA) was used for membrane surface drying prior to plasma surface activation, and monomer solution degassing during graft polymerization.

Sodium chloride (NaCl, ≥99.0%, Fisher Scientific, Chino, CA) was used to adjust the scaling solution saturation level. Calcium chloride dihydrate ($CaCl_2$, Certified ACS, Fisher Scientific, Chino, CA), sodium sulfate (Na_2SO_4, Certified ACS, Fisher Scientific, Chino, CA), and sodium bicarbonate ($NaHCO_3$, ≥99.5%, Acros Organics, Freehold, NJ) were used to prepare model

solutions of gypsum and calcium carbonate, in order to assess membrane mineral scaling propensity.

9.2.2 Atmospheric pressure-induced graft polymerization (APPIGP)

The protocol for polyamide membrane surface nano-structuring was optimized in a previous study [49] to increase SNS-PAA-PA membrane salt selectivity to a level comparable to the Dow SW30 membrane. Briefly, the Base-PA membrane sheets were kept in D.I. water for over 24 h. Prior to membrane surface plasma treatment, membrane samples (with active areas of 42 cm^2) were extracted from the Base-PA membrane sheets, rinsed with D.I. water, and blow-dried with compressed nitrogen. Membrane surfaces were plasma-activated through exposure to atmospheric pressure plasma (APP) using helium (He) APP system (Atomflo™ 500; Surfx Technologies Inc., Redondo Beach, CA) via 2 sequential plasma scans (*N*) and source-surface separation (*PSS*) distance of 10 mm (**Appendix C.2**). He APP was operated at a helium flow rate of 45 L/min generated at 150W RF power. The plasma source head was translated over the area of the Base-PA membrane via the scanning robot at a speed of 100 mm/s. Immediately afterward, membrane samples were immersed in 250 mL glass reaction vessels containing the aqueous AA monomer solutions to initiate surface free radical polymerization. The initial monomer concentration $[M]_o$ was set to 21 vol% and solution pH was adjusted to 6 using 0.1 N NaOH aqueous solution. The vessels were then placed in a constant water bath at 70°C for 60 min with nitrogen bubbled into the monomer solution (via a perforated tube) to both scavenge dissolved oxygen that could inhibit the graft polymerization reaction and provide for added mixing [280]. The above plasma treatment and AA graft polymerization conditions were previously determined to achieve SNS-PAA-PA membranes with an average salt permeability coefficient and water permeability of 0.15±0.02 $L \cdot m^-$

$^{2}\cdot h^{-1}$ and 1.69±0.18 $L\cdot m^{-1}\cdot h^{-1}\cdot bar^{-1}$, respectively, and nominal salt rejection of 99.3±0.1% [49]. It is noted that the above performance is within the acceptable range for seawater desalination when compared with commercial membranes [73, 336]. After the graft polymerization step, the membrane was thoroughly rinsed and stored in D.I water for > 24 h prior to further characterization.

9.2.3 Surface scanning images

Scanning electron microscope (SEM) (Zeiss Supra VP40, Carl Zaiss AG, Oberkochen, Germany) was used to obtain visualized images of membrane surfaces [46, 156, 278]. Prior to characterization, membrane samples were rinsed with D.I. water and dried in a vacuum oven at 40°C for 24 h. The fully dried samples were sputter-coated (Hummer® 6.6 Sputter Coater, Anatech USA, Sparks, NV) for 3 min to form a thin film of Gold (Au). The sputter coat process is to prevent surface charging during SEM characterization. SEM scanning was carried out with an accelerating voltage of 10 keV and a spot size of 100-10,000 nm. All images were obtained with a working distance of 5 mm and magnification of 15,000.

9.2.4 Performance Characterization

9.2.4.1 Permeability

Membrane performance characterization was conducted using a laboratory plate-and-frame RO (PFRO) membrane recirculation unit described in **Section 8.2.3, Chapter 8**. Prior to the determination of the water permeability coefficient, membranes of dimensions of 11.2 cm × 5.6 cm and active areas of 42 cm^2 were compacted with D.I. water under a transmembrane pressure (ΔP) of 58.6 bar (~850 psi) at crossflow velocity of 49 cm/s and temperature controlled at 20°C until the permeate flux stabilized (typically within 24 hours). Pure water flux was determined by

measuring permeate flow rate over the transmembrane pressure range of 34.5-58.6 bar (500-850 psi) with an in-line liquid flow meter ((Model 101-7; McMillan, Georgetown, TX). Permeate water flux was calculated by $J_v = Q_p / A$, where Q_p is the permeate flow rate, and A is the active membrane area. Membrane D.I. water permeability coefficient was determined as $L_p = J_v / \Delta P$.

9.2.4.2 Mineral scaling

Prior to the mineral scaling tests, the membranes were compacted and the clean membrane permeability coefficient ($L_p = 1/\mu R_m$) was determined with D.I. water as described in **Section 9.2.4.1**, where μ is water viscosity and R_m is intrinsic membrane resistance. The membrane mineral scaling propensity was assessed with gypsum and calcium carbonate model solutions, at a crossflow velocity of 49 cm/s and initial permeate flux of 39.4 $L \cdot m^{-2} \cdot h^{-1}$, in a total recycle mode (i.e. permeate and retentate streams were continuously recirculated to the feed reservoir) with temperature controlled at 20°C for a 24-h period. The operational conditions were chosen to keep the initial membrane surface concentration polarization module (*CP*) below 1.3 (**Eqn. 2-12, Chapter 2**). The saturation levels were quantified in terms of saturation index, defined as $SI_x = IAP / K_{sp,x}$, where *IAP* is the ion activity product and $K_{sp,x}$ is the solubility product for the mineral salt x (e.g., where $x = c$ is $CaCO_3$ (as calcite) and $x = g$ is gypsum). Synthetic model solutions were prepared with compositions representative of the major ions in the agricultural drainage field water source (recipe from a previous study [353]). The synthetic model solution for gypsum scaling test comprised of 11.29 mM $CaCl_2$ and 58.43 mM Na_2SO_4, with the addition of 11.09 mM NaCl to reach the field source water saturation level with respect to gypsum. The saturation index of gypsum (SI_g) in the bulk solution and at the membrane surface were 1.0 and 1.7, respectively. The membrane surface saturation index was calculated given the *CP* value at the

membrane surface (~1.3 for the present operational conditions). The synthetic model solution for the calcium carbonate scaling tests comprisds of 11.29 mM $CaCl_2$, 4.02 mM $NaHCO_3$, and 156.31 mM NaCl; the saturation indices of calcite (SI_c) in the bulk solution and on the membrane surface were 6.3 and 10.6, respectively. The initial pH levels for the above synthetic model solutions were 5.7 and 7.9, respectively, and the salinity was 2,611 mg/L total dissolved solids (TDS) for both model solutions. After each scaling test, D.I. water was circulated (for 30 minutes) through the membrane system (~20°C) at a cross flow velocity of 49 cm/s and transmembrane pressure of 21.4 bar (~310 psi) for a period of 30 min. Following membrane cleaning, the water permeability coefficient ($L_p^{'} = \frac{1}{\mu(R_m + R_{scale})}$) was again determined with D.I. water, where R_{scale} is the membrane scaling resistance. The membrane cleaning efficacy was then quantified as the permeability recovery, defined as: $L_p \ Recovery = (L_p^{'} / L_p) \times 100\%$.

9.2.4.3 Membrane rejection

The feed and permeate conductivity were monitored using conductivity probes (Vernier Software & Technology, Beaverton, OR) during the 24 hr scaling tests with both gypsum and calcium carbonate model solutions to evaluate the change of membrane nominal rejection (R_o). Membrane salt rejection (for NaCl equivalent TDS) was calculated as $R_o = (1 - C_p / C_f) \times 100\%$ where C_f and C_p are the feed and permeate stream conductivity levels respectively.

To evaluate the contribution of membrane flux decline during the scaling tests to the change of membrane TDS rejection, membrane rejection (R_o) is expressed as a function of permeate flux (J_v) and intrinsic membrane rejection ($R_i = (1\text{-}C_p/C_m)\times 100\%$), where C_m is the membrane surface concentration. As an intrinsic membrane property, R_i is not a function of permeate flux and thus should remain constant if the membrane is intact. As a result, the average concentration

polarization (CP) module, $\overline{CP} = \frac{\overline{C_m} - \overline{C_p}}{\overline{C_b} - \overline{C_p}} = \exp\left(\frac{J_v}{k}\right)$, where *k* is the mass transfer coefficient, can be expressed as $\overline{CP} = \frac{R_i}{1-R_i} / \frac{R_o}{1-R_o} = \Psi / \frac{R_o}{1-R_o} = Z$, where $\Psi = \frac{R_i}{1-R_i}$ and $Z = \exp\left(\frac{J_v}{k}\right)$. Further reorganization of the equation will then lead to $R_o = \frac{\Psi / Z}{1 + \Psi / Z}$. It is also reasonable to invoke the approximation of $\overline{C_b} \cong C_f$ given the low element recovery (<1%) and high membrane rejection (>99%).

9.3 Results and Discussion

The scaling propensity of the SNS-PAA-PS membrane was assessed based on gypsum and calcium carbonate scaling tests and compared to scaling of three commercial RO membranes (i.e., Dow-SW30, Toray SWRO, and Base-PA) under the same operating conditions. During the 24 hr RO desalting tests for the gypsum and calcium carbonate model solutions, permeate flux decline (**Fig. 9-1**) was observed for both SNS-PAA-PA and commercial RO membranes as the consequence of surface crystallization and/or bulk crystallization [21]. Crystal scale formation on the membrane surface may block the surface (by surface crystallization) and/or the buildup of a cake layer (by bulk crystallization) can represent an additional mass transfer that can reduce membrane permeate flux [38, 354]. Indeed, the gypsum and calcium carbonate crystals that formed on the membrane surface, at the end of RO scaling tests, were observed as illustrated in the SEM images (**Figs. 9-2** and **9-3**). Gypsum crystals with both needle-shaped structure (i.e., orthorhombic or hexagonal prismatic) [354, 355], and rosette arrangements (consisting of gypsum needles growing from a core region) were observed (**Figs. 9-2** and **9-3**). The above two gypsum crystal morphologies are reported to be the characteristic features of bulk crystal deposition and surface crystallization,

respectively [25, 36, 356]. Here it is noted, based on SEM images, both surface and bulk crystallization mechanisms occurred during the gypsum scaling test. For calcium carbonate, only the layered rhombohedral calcite (anhydrous) [38, 357] crystal morphology was observed (**Fig. 9-3**). Calcite is known to be the most stable crystal morphology of calcium carbonate [358] and can form an adherent scale layer on the membrane surface and thus it has been reported as being more difficult to clean [359] via simple water flushing.

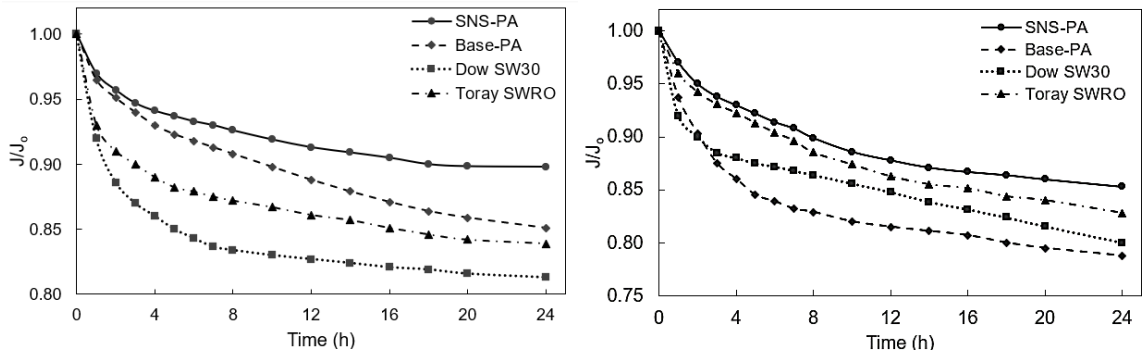

Figure 9-1. Flux decline for the SNS-PAA-PA membrane after 24 h gypsum scaling (left) and calcium carbonate scaling (right) tests, also showing the corresponding flux decline curves for the commercial membranes of Dow SW30, Toray SWRO, and Base-PA membranes. (Gypsum feed solution pH of 5.7, membrane surface saturation index of gypsum SI_g=1.3; Calcium carbonate feed solution pH of 7.9, membrane surface saturation index of calcite SI_c=6.9).

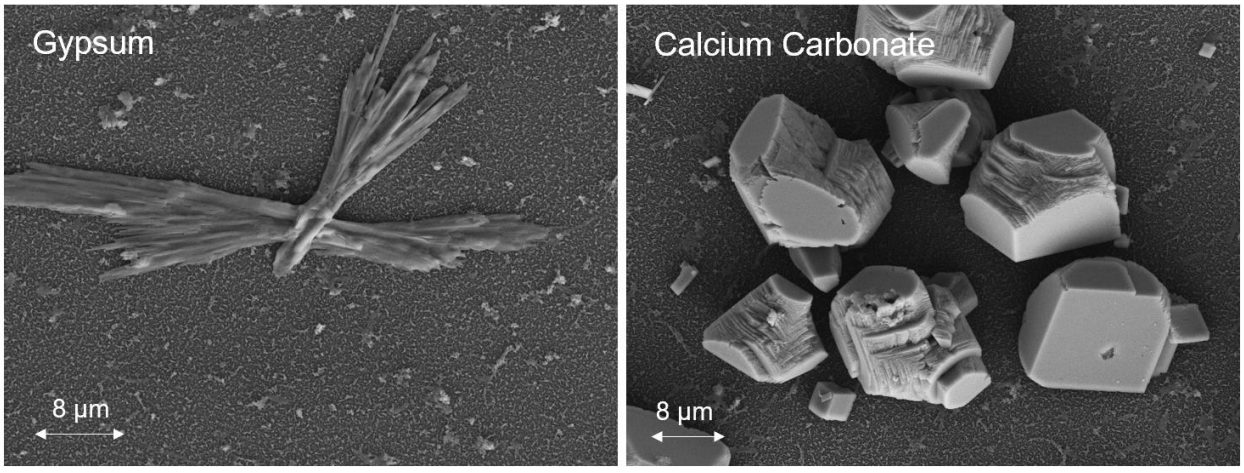

Figure 9-2. SEM top-view images of the gypsum (left) and calcium carbonate (right) scaled SNS-PAA-PA membrane surfaces, at the end of the 24 hr scaling tests. (Membrane surface saturation index of gypsum SI_g=1.3; membrane surface saturation index of calcite SI_c=6.9).

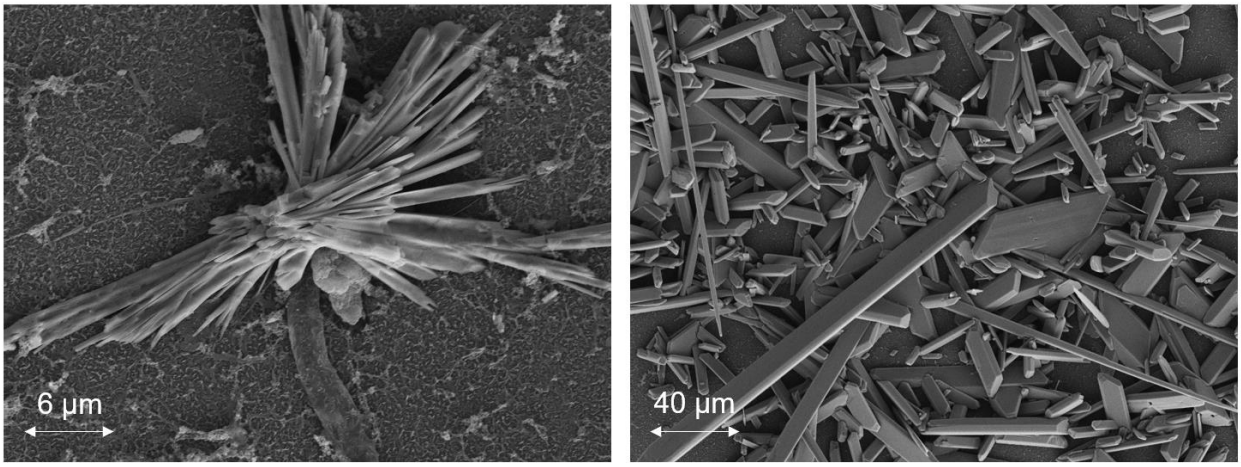

Figure 9-3. SEM top-view images of the two different structures of gypsum crystals, i.e., rosette arrangements consisting of gypsum needles growing from a core region (left) and needle-shaped structure (right), scaled on Dow SW30 and Toray SWRO membranes, respectively, at the end of the 24 hr scaling tests.

The surface-bound hydrophilic PAA chains were effective in reducing membrane scaling propensity attributed to efficient surface screening of the underlying membrane surface [46]. In addition, partial mobility of the chain segments is likely to have reduced the probability of nuclei and/or crystallite attachment to the end-grafted hydrophilic polymer layer surface [46, 108]. Indeed, the SNS-PAA-PA membrane demonstrated lower flux decline (~11%) relative to 14-19% for the commercial BWRO (i.e., Base-PA) and SWRO (i.e., Dow SW30 and Toray SWRO) membranes during the 24 hr filtrations of both gypsum and calcium carbonate model solutions (**Fig. 9-1**). Similarly, during the 24 hr desalting of calcium carbonate, the SNS-PAA-PA membrane demonstrated flux decline of 15% relative to 17-21% for the commercial Dow-SW30, Toray SWRO, and Base-PA membranes (**Fig. 9-1**).

The gypsum scaled SNS-PAA-PA membrane was flushed with D.I. water for 30 min (at crossflow velocity of 49 cm/s) to assess the degree of scaled membrane permeability restoration by re-dissolving the gypsum crystals and removing loosely bound/attached mineral crystals via fluid shear [360]. Gypsum crystals had moderate solubility in water (2.53 g/L at 20°C; [361]) and thus can be both re-dissolved and sheared to reach 100% membrane permeability recovery. Calcium

carbonate scaled SNS-PAA-PA membrane, however, demonstrated ~94% permeability recovery and ~4.3% membrane surface calcium carbonate scale coverage post 30 min D.I. water cleaning due to the negligible calcium carbonate solubility in water at room temperature (~0.015 g/L; [362]). As a result, calcium carbonate crystals, unlike gypsum, were more likely to be removed via fluid flow. Among the four tested membranes, the least surface density of calcite crystals was observed on the D.I. water cleaned SNS-PAA-PA membrane surface after 24 hr calcium carbonate scaling test (**Fig. 9-4**). The above observations indicated that calcium carbonate crystals were loosely bound/attached to the SNS-PAA-PA membrane surface. The above is attributed to effective surface screening by the tethered hydrophilic PAA brush layer, which reduces the likelihood of direct interactions between the mineral crystals and the membrane surface. Moreover, partial mobility (i.e., Brownian motion) of the tethered PAA chain segments reduced the likelihood of direct interaction (and thus strong adhesion force) between the mineral crystals and membrane surface [108]. It is noted that the tethered PAA brush layer was in a collapsed configuration in the scaling model solutions (2,611 mg/L TDS) due to the charge screening effect by salt ions [201, 363] and reduced chain-chain or segment-segment repulsion [364]. During D.I. water cleaning, however, the tethered PAA chains transformed into a more extensive/swollen conformation due to the electrostatic repulsion among the charged PAA chain segments, and thus crystals release/detachment was likely promoted (i.e., "self-cleaning" properties of the responsive membrane). It is also noted that the calcite crystals formed on the Base-PA membrane were of significantly smaller size (of ~1 μm) relative to 3-10 μm on the Dow SW30, Toray SWRO and SNS-PAA-PA membranes, but with ~100-150 times greater crystal surface number density (**Fig. 9-4**), possibly due to the difference in membrane surface properties [38, 107, 359]. It is postulated that a greater density of nucleation site (initial creation of a solid species formed by molecular

agglomeration from which the scale crystals can continue to grow [365]) was formed on the Base-PA membrane relative to Dow SW30, Toray SWRO, and SNS-PAA-PA membranes. However, the dependence of membrane surface density of formed nucleation sites on surface characteristics such as surface topography, hydrophilicity and charge is yet unclear [36].

Upon 30 min D.I. water cleaning, 100% permeability recovery was also observed for calcium carbonate scaled commercial membranes (i.e., Dow SW30, Toray SWRO, and Base-PA; **Table 9-1**). The above behavior is odd for the calcium carbonate scaled commercial RO membranes, which demonstrated insufficient cleaning as indicated by the remained of calcite scale on the membrane surfaces after D.I. cleaning, as indicated by 40.5-59.9% membrane surface calcium carbonate scale coverage (**Fig. 9-4**). The possible explanation for the above insufficient membrane cleaning, but still reaching 100% permeability recovery could be due to damage to the membrane surface active layer caused by the high degree of scaling, which is supported by the loss of membrane selectivity over the filtration time (**Figs. A-12** and **A-13, Appendix A**).

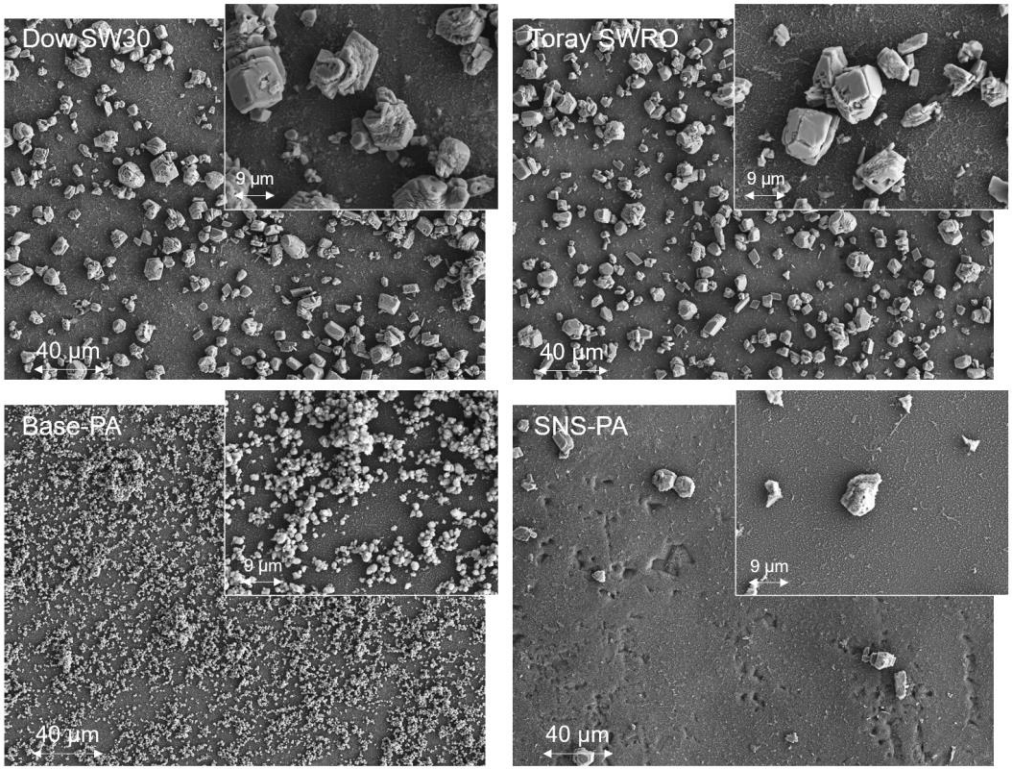

Figure 9-4. SEM top-view images of SNS-PAA-PA membrane after 24 h calcium carbonate scaling test, followed by 30 min D.I. water flushing, compared to selected commercial membranes (Dow SW30, Toray SWRO, and Base-PA). The shown level of membrane surface calcium carbonate scale coverage is 40.5%, 59.9%, 57.8%, and 4.3% for Dow SW30, Toray SWRO, Base-PA, and SNS-PAA-PA membranes, respectively.

Table 9-1. Summary of gypsum and calcium carbonate scaling and cleaning test results for membrane coupons [(a)]

Membrane	Scalant	J/J_o	$R_o/R_{o,o}$	$L_p/L_{p,o}$
Dow SW30	Gypsum	0.81	0.942	1.00
Toray SWRO	Gypsum	0.84	0.988	0.98
Base-PA	Gypsum	0.85	0.982	0.92
SNS-PAA-PA	Gypsum	0.89	0.994	1.00
Dow SW30	Calcium Carbonate	0.80	0.864	1.00
Toray SWRO	Calcium Carbonate	0.83	0.955	1.00
Base-PA	Calcium Carbonate	0.79	0.917	1.00
SNS-PAA-PA	Calcium Carbonate	0.85	0.973	0.94

[(a)] J/J_o – flux/initial flux; $L_p/L_{p,o}$ – permeability coefficient/initial permeability coefficient.

Membrane nominal rejection (calculated based on feed and permeate solution conductivity) decline (by 0.6-13.6%) was observed for all four tested PA TFC RO membranes over the 24 h gypsum and calcium carbonate scaling tests (**Figs. A-12** and **A-13, Appendix A**). For all four tested membranes (if remained intact), membrane intrinsic rejection ($R_i = (1-C_p/C_m)\times 100\%$), an intrinsic membrane property, can be assumed constant regardless of the operating conditions, of 99.5%, 99.2%, 99.3%, and 99.2% for the SNS-PAA-PA, Toray SWRO, Base-PA, and Dow SW30 membranes, respectively [336]. Membrane surface concentration (C_m), as reasoned in **Section 9.2.4.3**, decreases with decreased permeate flux. Consequently, at the end of the 24 hr desalting of gypsum and calcium carbonate, the four tested membranes' surface concentrations (C_m) were predicted to decrease by 6.0-10.7% and 8.5-12.0%, respectively, relative to the initial values (**Table 9-2**). From the constant membrane intrinsic rejection, the permeate TDS concentration and the membrane nominal TDS rejection can be predicted at the end of the 24 hr filtration of gypsum and calcium carbonate model solutions (**Table 9-2**). However, these predicted final membrane TDS rejections are overall 0.03-14.63% greater than the actual measurements (**Figs. A-12** and **A-13, Appendix A**), indicating that increased concentration polarization caused by membrane scaling flux decline cannot fully explain the observed loss of membrane rejection. More importantly, due to the formation of the scale crystals on the membrane surface, local solution concentrations reduce from supersaturation to saturation at the surface of the scale crystals, and thus leading to even higher predicted membrane nominal TDS rejection.

Table 9-2. Predicted membrane surface TDS concentration, permeate TDS concentration, and nominal membrane TDS rejection for all four tested membranes at the end of 24 hr filtration of gypsum and calcium carbonate model solutions [a].

Membrane	Gypsum [b]				Calcium Carbonate [c]			
	C_m [d] (mg/L)	C_p (mg/L)	R_i [e]	R_o	C_m [d] (mg/L)	C_p (mg/L)	R_i [e]	R_o
Dow SW30	4271	34	99.2%	98.7%	4239	34	99.2%	98.7%
Toray SWRO	4339	35	99.2%	98.7%	4311	34	99.2%	98.7%
Base-PA	4374	31	99.3%	98.8%	4209	29	99.3%	98.9%
SNS-PAA-PA	4506	23	99.5%	99.1%	4385	22	99.5%	99.2%

[a] The flux declines of the four tested membranes at the end of 24 hr filtration tests were given in **Fig. 9-1**.

[b] The composition of the gypsum model solution is described in **Section 9.2.4.2**, and the feed TDS concentration (C_f) is 2611 mg/L.

[c] The composition of the calcium carbonate model solution is described in **Section 9.2.4.2**, and the feed TDS concentration (C_f) was 2611 mg/L.

[d] Membrane intrinsic rejection was a function of permeate flux as $C_m = \frac{Z \cdot C_f}{R_i + (1 - R_i) \cdot Z}$, where $Z = \exp\left(\frac{J_v}{k}\right)$, derived from **Section 9.2.4.3**.

[e] As an intrinsic property, membrane intrinsic rejection can be assumed constant if the membranes were intact during the scaling tests. The membrane intrinsic rejection for the four tested membranes was reported in a previous study [336].

The possible decrease in membrane TDS rejection over the 24 hr scaling tests could be due to physical damage of the membrane active layer due to the crystal growth within the membrane active layer. Although not previously explored for RO membrane surfaces, membrane physical damage as a consequence of scaling has been widely reported for membrane distillation (MD) [347]. Indeed, it was observed in previous studies that scale crystals may penetrate through and even damage the active layer during their growth (i.e., formed defects (e.g. cracks) on the membrane surface [347]). The physical damage of the MD membrane due to mineral scaling was also associated with an impaired distillate quality and/or 0.8-6% lower membrane TDS rejection [24, 347, 366-370].

SNS-PAA-PA membrane with surface tethered PAA brush layer demonstrated the least rejection loss as compared to the commercial membranes over the 24 h scaling tests of both gypsum and calcium carbonate scaling. The lowest rejection decline during the 24 h RO gypsum scaling

tests was observed for the SNS-PAA-PA membrane (by ~0.6%) relative to 1.5%-5.7% for the commercial RO membranes (Dow SW30, Toray SWRO, and Base-PA). Similarly, during the 24 h calcium carbonate scaling tests, membrane TDS rejection (based on solution conductivity) of the tested commercial RO membranes (Dow SW30, Toray SWRO, and Base-PA) declined 4.4%-13.5%, relative to only 2.7% for the SNS-PAA-PA membranes (**Fig A-13, Appendix A**). The least permeate quality loss of the SNS-PAA-PA membrane is postulated to be due to the surface tethered PAA layer effective screening of the membrane active layer which was thus less prone to be penetrated by the mineral crystals.

9.4 Conclusions

Surface tethered polyacrylic acid (PAA) brush layer was synthesized onto a commercial polyamide (PA) brackish water reverse osmosis (BWRO) membrane (i.e., Base-PA) via atmospheric-pressure plasma-induced graft polymerization (APPIGP). The surface nanostructured (SNS) RO membrane (i.e., SNS-PAA-PA) demonstrated reduced scaling propensity as quantified by the lowest flux decline at the end of 24 hr RO desalting of both gypsum and calcium carbonate relative to the commercial SWRO (i.e., Dow SW30 and Toray SWRO) and BWRO (i.e., Base-PA) membranes. The SNS-PAA-PA membrane demonstrated both the lowest scaling propensity among all four tested membranes and 100% permeability recovery, attributed to the tethered PAA layer effectively screening the membrane surface. Although deterioration of permeate quality (increased permeate conductivity) was observed for all four membranes, the SNS-PAA-PA membrane demonstrated the least degree selectivity loss. Indeed, only 0.6% and 2.7% rejection loss was observed for the SNS-PAA-PA membrane at the end of the 24 hr filtration of gypsum and calcium carbonate model solutions, respectively, compared to 1.2-5.8% and 4.5-13.6% rejection loss for the commercial RO membranes. The lowest rejection loss of the SNS-PAA-PA membrane implies that

the surface tethered PAA brush layer may effectively screen/protect the membrane active layer making it less prone to damage by excessive formation of mineral crystals.

Chapter 10 Scaleup of APPIGP for the Fabrication of Spiral Wound RO Elements

10.1 Overview

Despite the extensive knowledge base regarding membrane surface modifications, most studies have focused on laboratory-scale demonstrations with small flat sheet membrane coupons [66], typically having a working area in the range of 4-18.6 inch^2 [49, 371-373]. Here we note that for a target RO membrane modification approach to be commercially viable, it must be scalable to an area sufficiently large for the fabrication of spiral-wound elements (>720 inch^2). Moreover, membrane modification should provide a high degree of performance uniformity across the membrane sheet [374]. To date, however, whole element scalability of RO membrane surface modifications has been demonstrated only for in-situ surface coating [166-168], surface grafting [26], and chemically-initiated free-radical graft polymerization [169-172] of commercial spiral wound RO elements.

An alternative to in-situ RO membrane element modification (via graft polymerization, surface grafting or coating) is ex-situ graft polymerization modification of RO membrane sheets prior to RO element fabrication. In this approach, modified RO membrane sheets are assembled to fabricate spiral-wound elements. There are various approaches to surface initiate graft polymerization [45] and their scale-up potential is critical for handling sufficiently large membrane surface area needed for the manufacturing of spiral-wound elements. In this regard, it has been previously shown that atmospheric-pressure plasma (APP)-induced graft polymerization (APPIGP), utilizing helium, oxygen, argon, hydrogen, air, and their mixtures, have been utilized for membrane surface activation [156, 278]. APPIGP has the potential for scale-up to a large membrane surface given: (a) a short surface activation time (~1-2 seconds) to form a high surface density of free-radials to initiate graft polymerization of a suitable vinyl monomer, (b) surface

activation at atmospheric pressure in ambient air, and (c) a reasonable graft polymerization time (30-60 minutes) that can be achieved in a continuous process. It is argued the plasma treatment step can be scaled-up to treat a large area membrane surface as required for the construction of spiral wound elements. It has also been shown that the APPIGP approach provides a route to overcoming the typical permeability-selectivity tradeoff [49, 156]. However, the scale-up of the approach to enable the fabrication of spiral-wound elements has not been previously demonstrated.

In the present study, the potential scalability of APPIGP (using helium plasma for surface activation) to surface modify polyamide (PA) thin-film composite (TFC) RO membrane was assessed for fabrication of small commercial-scale spiral wound elements (2.5" diameter and 21" length). A commercial brackish water (BW) RO membrane was selected as the base membrane that was then surface nano-structured (SNS) with a tethered layer of poly(acrylic acid) (PAA) via APPIGP. Previous studies have shown that SNS-PAA-PA membranes have a low fouling propensity and can potentially overcome the typical permeability-selectivity tradeoff [49]. Accordingly, large SNS-PAA-PA flat sheet membranes (30" × 24") were prepared via a two-step process consisting of APP base membrane surface activation (using a plasma source mounted on an XYZ scanning robot), followed by graft polymerization in a shallow graft polymerization reactor. Uniformity of membrane performance (i.e., water permeability and salt rejection) across the SNS-PAA-PA membrane sheet was evaluated and compared to the Base-PA (a commercial BWRO membrane). Fouling propensities of the SNS-PAA-PA membrane and selected commercial membranes were then evaluated, in both flat sheet coupons and spiral-wound elements, via filtration of solutions of bovine serum album (BSA) and sodium alginate as model foulants.

10.2 Experimental

10.2.1 Materials

Flat sheet PA-based TFC membranes (73AC and 82V), supplied by Toray Membrane USA Inc. (Poway, CA), and commercial Dow SW30-2514 spiral-wound elements, obtained from Filmtec Inc. (Edina, MN) were utilized for evaluating surface modification uniformity, spiral-wound element fabrication, and evaluating separation performance and fouling properties. Helium (99.999%) gas for plasma generation, and nitrogen (99.5%) gas for membrane surface drying and purging the monomer solutions during graft polymerization, were obtained from Airgas (Los Angeles, CA). Acrylic acid (99%, Sigma-Aldrich, St. Louis, MO) was the monomer for membrane surface graft polymerization. Monomer solution pH was adjusted using sodium hydroxide solution (50% w/w, Fisher Scientific, Chino, CA). All test solutions were prepared using ultra-pure deionized (D.I.) water. The flat-sheet coupon and spiral-wound membrane element salt rejection (**Section 10.2.6.1** and **10.2.6.4**) was determined using sodium chloride (≥ 99.0%, Fisher Scientific, Chino, CA). Alginic acid sodium salt from brown algae (Sigma-Aldrich, St. Louis, MO) and BSA (≥98%, Sigma-Aldrich, St. Louis, MO) were used as model foulants to characterize the fouling resistance of both the coupon membranes and the spiral wound elements. Both foulant model solutions were prepared in an aqueous saline solution of 32 g/L sodium chloride (≥99.0%, Fisher Scientific, Chino, CA).

10.2.2 Scaled-up plasma surface activation

Polyamide TFC brackish water reverse osmosis (BWRO) flat sheet membrane rolls (73 AC) were supplied by Toray Membrane USA Inc. (Poway, CA) and utilized as the base membrane onto which the tethered PAA layer was synthesized. Prior to plasma surface activation, the Base-PA

membrane sheets (31” × 25” each) were freshly cut from the manufacturer supplied roll and then fully immersed in D.I. water for 24 hr. Subsequently, the Base-PA membrane sheet was mounted onto an aluminum plate (31” × 25” × 0.2”) which ensured that the membrane sheet remained flat during the surface activation and graft polymerization steps (**Sections 10.2.2** and **10.2.3**). The active side of the base membrane sheet was dried by blowing nitrogen over the surface using a polytetrafluoroethylene (PTFE) nitrogen/drying gun (International Polymer Solutions Inc.; Irvine, CA).

Plasma surface activation of each Base-PA membrane sheet was accomplished with an APP system consisting of a plasma source system (AtomfloTM 500) with a coolant control module and a 3-inch linear source head (produces 79 mm × 0.4 mm beam). The plasma stream was delivered onto the membrane surface from the source head mountd on an XYZ scanning robot (Surfx Technologies LLC, Redondo Beach, CA). The plasma source head was translated over the area of the Base-PA membrane via the scanning robot at a speed of 100 mm/s. Helium plasma was generated at a helium flow rate of 45 L/min and radio frequency (RF) power of 150 W. Plasma treatment of each 30” × 24” base membrane sheet was accomplished with two repeated scans at a plasma source-substrate separation (*PSS*) distance of 10 mm. The above plasma treatment conditions were previously determined to be optimal for TFC-PA membranes surface activation with helium plasma [49] for subsequent AA graft polymerization.

10.2.3 Scaled-up graft polymerization

10.2.3.1 Scaled-up graft polymerization system

Membrane surface AA graft polymerization (GP) of 30” × 24” base PA membrane sheets was carried out post-plasma surface activation (**Section 10.2.2**) using a high density polyethylene

(HDPE) rectangular shallow reactor having dimensions of 32” × 26” × 2” (**Fig. 10-1**). The plasma-treated membrane sheet (affixed to an aluminum plate) was placed inside the reactor with the active side facing down (toward the reactor’s bottom) to ensure contact with the monomer solution in the reactor channel. The monomer solution was recirculated through the reactor using a peristaltic pump (EW-77600-62 and EW07594-10, Cole-Parmer, Vernon Hills, IL). Prior to being fed to the shallow GP reactor, the monomer solution was pumped through a stainless-steel coil, immersed in a circulation water bath (ColeParmer; Vernon Hills, IL), that was connected to the inlet (T connection) of a stainless-steel distribution pipe, wrapped with a heating cable (3631K22, McMaster-Carr; Santa Fe Springs, CA). The water bath and the pipe heating cable served to keep the monomer solution temperature at 70°C and minimize heat loss.

The monomer solution was then fed to the reactor via a 0.25” inner diameter 316 stainless steel manifold with 11 evenly distributed inlet jets (3404K78 and 2491K24, McMaster-Carr; Santa Fe Springs, CA). A similar manifold was installed at the reactor’s exit. A three-way diverting valve was installed between the reactor outlet and peristaltic pump to introduce the monomer solution to the reactor prior to initiating the graft polymerization.

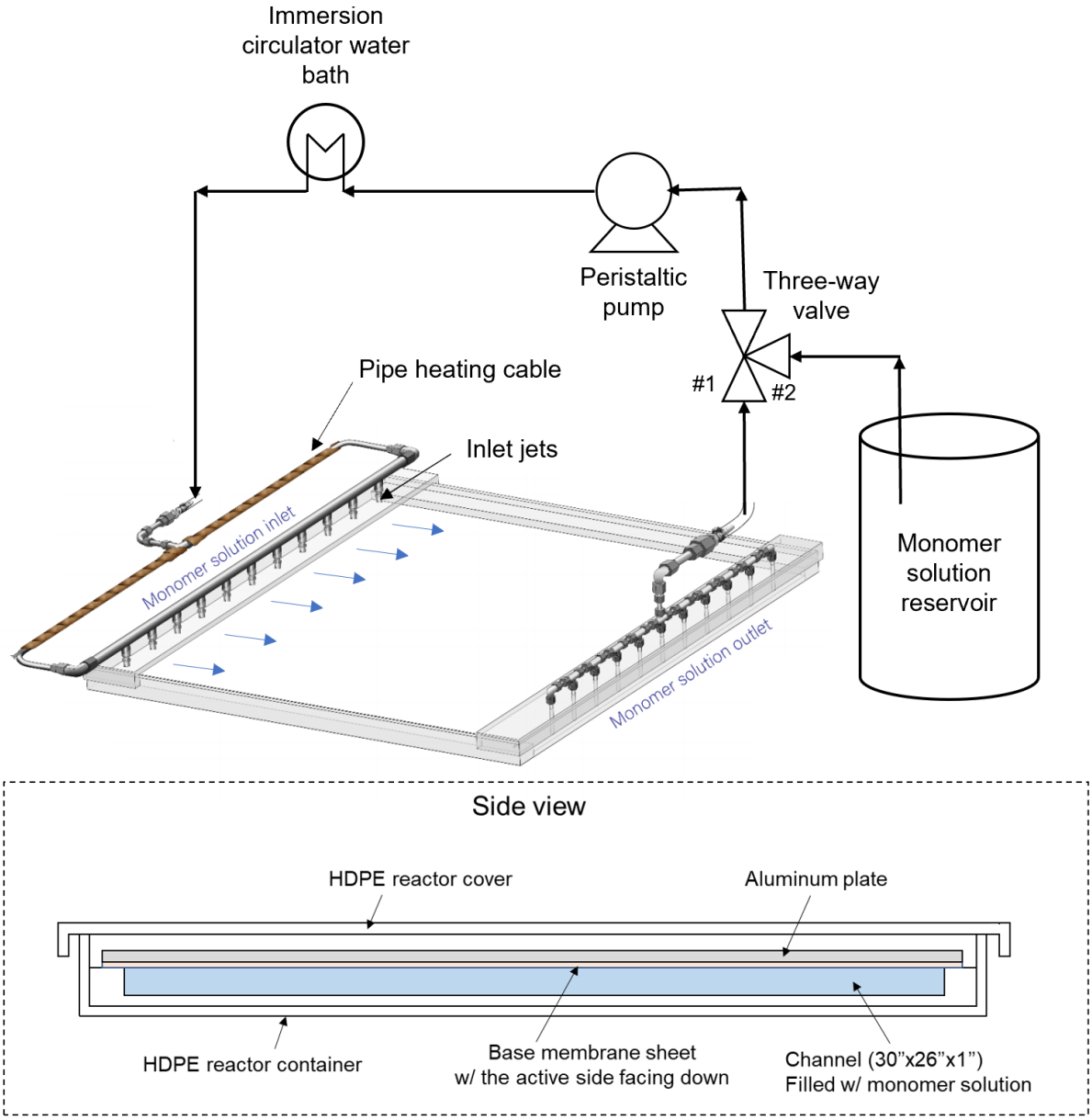

Figure 10-1. (Top) Graft polymerization reactor system schematic, and (Bottom) arrangement of membrane placement in the reactor.

10.2.4.2 Graft polymerization procedure

Graft polymerization of acrylic acid (AA) onto each Base-PA membrane sheet was carried out at an initial AA monomer concentration of 20 vol% and pH of 6 for 1 hr at 70°C. At the above reaction conditions, previous work has shown that SNS-PAA-PA membranes, with the same base PA membrane, had an average salt permeability coefficient and water permeability of 0.15±0.02

$L \cdot m^{-2} \cdot h^{-1}$ and 1.69±0.18 $L \cdot m^{-1} \cdot h^{-1} \cdot bar^{-1}$, respectively, and nominal salt rejection of 99.3±0.1% [49]. It is noted that the above performance is within the acceptable magnitude for seawater desalination when compared with commercial membranes (salt rejection>99%; [73]).

The monomer solution was prepared with the pH (monitored with an Oakton pH 110 meter; Oakton Instruments, Vernon Hills, IL) adjusted from its initial level of 1.9 to 6 using ~2.1 L aqueous NaOH solution (50% w/w). Subsequently, nitrogen was bubbled into the monomer solution (via a perforated tube), in a 25 L feed reservoir, to both scavenge dissolved oxygen that could inhibit the graft polymerization reaction [156] and provide for added mixing. The surface activated Base-PA membrane sheet (affixed to an aluminum plate) was then placed inside the scaled-up graft polymerization reactor system with the active side facing down (**Fig. 10-1**). Subsequently, circulation of the monomer solution through the reactor system was initiated. The addition of NaOH to the monomer solution led to a temperature rise to ~70°C, and this temperature was maintained during the polymerization period (**Section 10.2.3.2**). Graft polymerization was terminated by pumping the monomer solution out from the reactor, removing the SNS-PAA-PA membrane sheet from the reactor, and thoroughly rinsing it under a D.I. water stream. The SNS-PAA-PA membrane sheet was then removed from the aluminum plate, rolled and stored (immersed) in D.I. water.

10.2.4 Spiral-wound element fabrication

Spiral wound elements (2.5” outer diameter and 21” length) were fabricated at the facility of Toray Membrane USA Inc. (Poway, CA). Two membrane sheets were glued to form a membrane leaf and a feed spacer sheet (0.028” thick) was inserted in-between the glued membrane sheets to form the RO feed-side channel. Each SNS-PAA-PA element was fabricated using two membrane

leaves, separated by a sheet of permeate carrier/spacer (Tricot, 0.01" thick), then wrapped around a central permeate collection tube (**Fig. 10-2**). The freshly rolled membrane sheets were encased in a fiberglass shell with each end-capped with an anti-telescoping fitting. The resulting total active membrane area of the SNS-PAA-PA spiral-wound elements was estimated to be 0.92 m^2 (~9.9 ft^2).

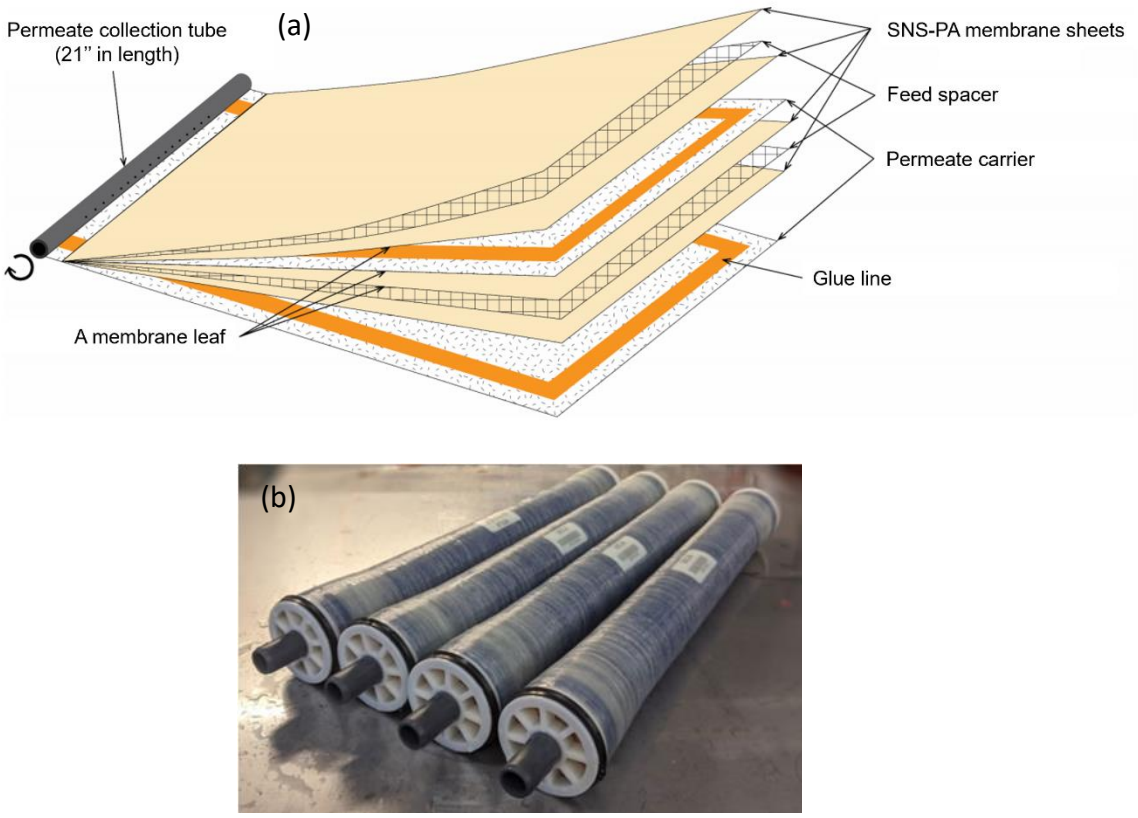

Figure 10-2. (a) Assembly of a spiral wound element using the SNS-PAA-PA membrane sheets, and (b) SNS-PAA-PA spiral wound membrane elements (**Section 10.2.4**).

Spiral wound elements of the same size as the SNS-PAA-PA elements were also fabricated using commercial membrane sheets (Toray 73AC and 82V; **Table 10-2**). This was done to provide a direct comparison of element performance to allow assessment of possible performance variability due to variations in the membrane element fabrication process (**Table 10-1**). The membrane element fabricated using the Toray 73AC membrane sheet was denoted as the Base-PA

element. Two additional elements, fabricated using Toray 82V membrane sheets, a commercial SWRO membrane from Toray, was denoted as Toray SWRO #1 and #2 (**Table 10-1**). The performance of the above fabricated spiral wound elements was also compared with three commercial SWRO elements (Dow Filmtec SW30-2514) of approximately the same element dimensions.

Table 10-1. RO spiral wound elements [a] used in the study

Spiral wound elements	Membrane sheet used	Fabrication Approach
SNS-PAA-PA #1	SNS-PAA-PA	**Section 10.2.4**
SNS-PAA-PA #2		
SNS-PAA-PA #3		
Toray SWRO #1 [b]	Toray 82V	
Toray SWRO #2 [b,c]		
Base-PA [b]	Toray 73AC	
Dow SW30 #1	Commercial elements [d]	
Dow SW30 #2		
Dow SW30 #3		

[a] Elements dimensions: 2.5" (diameter) × 21" (length)
[b] Spiral wound elements fabricated with commercial flat membrane sheets via the same protocol used for the SNS-PAA-PA elements (**Section 10.2.4**).
[c] Fabricated the second spiral wound element using the Toray 82V commercial flat membrane sheet to assess the consistency of the spiral wound element fabrication process.
[d] Obtained from Dow Inc.

Table 10-2. Comparison of performance of SNS-PAA-PA membrane with commercial membranes[(a)]

Membrane	Toray 82V (*Flat sheet*)	Toray 73AC (*Flat sheet*)	Dow SW30 (*Spiral wound*)	SNS-PAA-PA[(b)] (*Flat sheet*)
Type	SWRO	BWRO	SWRO	SWRO
Permeability ($L \cdot m^{-1} \cdot h^{-1} \cdot bar^{-1}$)	0.83	3.35	0.71[b]	1.69[c]
Salt (NaCl) Rejection (%)	99.7	99.8	99.4[b]	99.3[c]

[a] Based on manufacturer reported performance data
[b] Permeability and salt rejection were determined based on the following test conditions: 32,000 ppm NaCl, pressure of 800 psi (55 bar), 25°C and 5% recovery rates. Permeate flows for individual elements may vary +/-20%.
[c] Data obtained from a previous study [49] with the test conditions of: (i) D.I. water, pressure of 500-850 psi (34.5-58.6 bar), 20°C; (ii) 32,000 ppm NaCl, pressure of 800 psi (55 bar), 20°C.

10.2.5 Membrane surface characterization

10.2.5.1 Surface scanning images

The membrane surfaces were imaged using a scanning electron microscope (SEM) (Zeiss Supra VP40, Carl Zaiss AG, Oberkochen, Germany). All images were obtained with a working distance of 5 mm and 15,000× magnification. Prior to imaging, membrane samples were rinsed with D.I. water and dried in a vacuum oven at 40°C for 24 h. The dried samples were sputter-coated (Hummer® 6.6 Sputter Coater, Anatech USA, Sparks, NV) for 3 min to form a thin Gold (Au) film. SEM scanning was carried out with an accelerating voltage of 10 keV and a spot size of 100-10,000 nm.

10.2.5.2 Surface hydrophilicity

The membrane surfaces were imaged using a scanning electron microscope (SEM) (Zeiss Supra VP40, Carl Zaiss AG, Oberkochen, Germany). All images were obtained with a working distance of 5 mm and 15,000× magnification. Prior to imaging, membrane samples were rinsed with D.I. water and dried in a vacuum oven at 40°C for 24 h. The dried samples were sputter-coated (Hummer® 6.6 Sputter Coater, Anatech USA, Sparks, NV) for 3 min to form a thin Gold (Au) film. SEM scanning was carried out with an accelerating voltage of 10 keV and a spot size of 100-10,000 nm.

10.2.6 Membrane performance evaluation

10.2.6.1 Coupon membrane separation properties

Membrane performance, determined using membrane coupons (extracted from 30” × 24” membrane sheets), was evaluated, in terms of the water permeability coefficient (L_p), salt transport

coefficient (B), nominal (i.e., "observed") salt rejection (R_o), and intrinsic salt rejection (R_i). Membrane performance tests were conducted using a laboratory plate-and-frame RO (PFRO) membrane test system following a previously established protocol [49]. Briefly, the RO membrane coupons were compacted, over a 24 hr period, with D.I. water at 58.6 bar (~850 psi) transmembrane pressure (ΔP), and crossflow velocity of 49 cm/s at temperature of 20°C, to reach a stabilized permeate flow rate. The permeate salt concentration (C_p) was determined using a conductivity probe (Vernier Software & Technology, Beaverton, OR). Permeate flow rate (Q_p) was measured, over a transmembrane pressure range of 34.5-58.6 bar (500-850 psi), with an in-line liquid flow meter ((Model 101-7; McMillan, Georgetown, TX).

The membrane D.I. water permeability coefficient (L_p) for a given flat sheet membrane coupon was determined from the slope of the linear plot of permeate flux ($J_v=Q_p/A$) versus ΔP (i.e., where $J_v= L_p \Delta P$) for filtration tests with D.I. water, where A is the active membrane area. Subsequently, the membrane coupon was compacted using an aqueous 32,000 ppm NaCl under flow conditions at a transmembrane pressure of 55.2 bar (~800 psi) at 20°C until the permeate flux and permeate conductivity stabilized (typically within 24 hours). The membrane nominal salt rejection ($R_o=(1-C_p/C_f)\times 100\%$) was then evaluated at a crossflow velocity of 49 cm/s and permeate flux of 25.5 $L\cdot m^{-2}\cdot h^{-1}$, where C_p and C_f are the salt concentrations of the permeate and feed solutions, respectively. The intrinsic membrane salt rejection was determined from $R_i=(1-C_p/C_m)\times 100\%$, where C_m is the salt concentration at the membrane surface. C_m was estimated from the simple film-model [337, 338], $CP=(C_m-C_p)/(C_b-C_p)=exp(J_v/k)$, where C_b is the bulk salt concentration, and k is the solute (salt) mass transfer coefficient. Combining the simple film-model and the membrane salt flux expression, $J_s=C_p\cdot J_v=B\cdot(C_m-C_p)$ [49], leads to the equation $ln(J_v\cdot(1-R_o)/R_o)=J_v/k+ln(B)$, where B is the solute transport coefficient [72]. The value of k can then be

obtained from a plot of $ln(J_v \cdot (1-R_o)/R_o)$ vs J_v, where $1/k$ is the slope and $ln(B)$ is the y-intercept of the linear plot.

10.2.6.2 Coupon membrane fouling performance

Fouling tests with membrane coupons were conducted with 0.1 g/L BSA or sodium alginate in an aqueous 32 g/L NaCl solution, at crossflow velocity of 11 cm/s and initial permeate flux of 25.5 $L \cdot m^{-2} \cdot h^{-1}$, over a period of 24 h. Fouling tests at the same initial water permeate flux ensured the same initial hydrodynamics for each of the fouling tests, and thus a similar initial rate of foulants deposition [26]. Membrane fouling resistance and cleaning efficacy were assessed following a previously described protocol [46, 49]. Briefly, permeate flux decline, defined as $FD_i = 1 - J_{v,t} / J_{v.o}$, where $J_{v,t}$ and $J_{v,o}$ designate the permeate fluxes at time *t* and 0, respectively, was followed over the filtration period. At the termination of each fouling filtration test, D.I. water was circulated (for 30 minutes) through the membrane system at a transmembrane pressure of ~17 bar and crossflow velocity of 17 cm/s. Following the above membrane cleaning step, the water permeability coefficient ($L_{p,t}$) was again determined with D.I. water. Membrane cleaning efficacy was then quantified in terms of the percent permeability recovery, i.e., $L_{p,\mathrm{Recovery}} = (L_{p,t} / L_{p,o}) \times 100\%$.

The clean membrane permeability coefficient, L_p, was determined using D.I. water (**Section 10.2.6.1)** prior to each fouling test, and the corresponding intrinsic membrane hydraulic resistance, R_m, was determined from the relation $L_p = 1/\mu R_m$, where μ is the water viscosity (20°C in the current study). At the end of each fouling test, a determination was made of the membrane overall hydraulic resistance (R_T) being the sum of the intrinsic membrane resistance (R_m), irreversible fouling (R_{irrev}), and reversible cake layer (R_{cake} or R_{rev}) resistances, i.e., $R_T = R_m + R_{cake} + R_{irrev}$,

whereby the fouling resistance is given by $R_{fouling} = R_{cake}+R_{irrev}$. After membrane cleaning with D.I. water, the total residual hydraulic resistance, $R_T' = R_m + R_{irrev}$, was determined from which R_{irrev} was then calculated given R_m, and subsequently, R_{cake} was quantified given the overall hydraulic resistance (R_T).

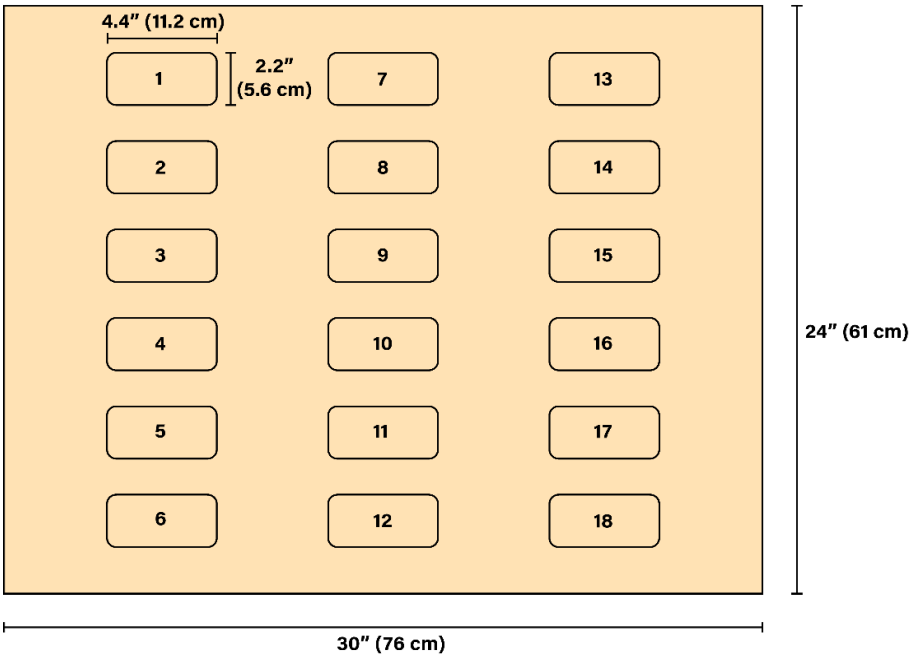

Figure 10-3. Illustration of the locations of individual membrane coupons, each measuring 11 cm × 5.6 cm (4.4" × 2.2") extracted from a large membrane sheet 76 cm × 61 cm (30" × 24") for performance uniformity testing. (Note that a portion of the edge area of the membrane sheet was trimmed when combining sheets for the production of the spiral-wound element).

10.2.6.3 Performance uniformity of the scaled up membrane sheet

Performance uniformity of the 30" × 24" SNS-PAA-PA and Base-PA membrane sheets was evaluated by characterizing eighteen 4.4" × 2.2" membrane coupons extracted from the different sections of the large membrane sheets (**Fig. 10-3**). A membrane sheet performance uniformity measure (f) was defined as $f_i = (1 - sd_i / \overline{x}_i) \times 100\%$, in which subscript i designates the performance variable, and $\overline{x}_i$ and sd_i are the average value and standard deviation of the performance parameter.

Performance of each coupon membrane was characterized following the protocol described in **Section 10.2.6.1**.

10.2.6.4 Water and salt permeability coefficients of spiral-wound elements

10.2.6.4.1 Spiral-wound RO test system

The separation performance of the spiral wound RO elements was evaluated using a mobile and modular RO system (**Fig. 10-4**) capable of processing up to 4.5 m^3/day feed water at operating pressure up to about 103.4 bar (1,500 psi). The RO system was capable of accommodating an RO element of 2.5" in diameter and 21" in length. The feed was delivered from a 450 L (120 gallon) feed tank via a booster pump (JM3460, Baldor, St, Louis, MO) and a high pressure RO feed pump (5 frame plunger pump 351, CAT Pumps, Minneapolis, MN) to the pressure vessel. The feed pressure was controlled using an adjustable actuated 2-way valve (MCJ-050AB, Hanbay, Torrance, VA) installed at the retentate stream exit. Both the permeate and retentate streams were recycled back to the feed tank. The retentate stream was first passed through two chillers (1171-P, VWR Scientific Products, Irvine, CA; and 1/2 HP Penguin Water Chiller, Penguin Chillers, Knoxville, TN) such that the operational temperature was maintained at 20°C.

The feed, permeate, and concentrate pressures were monitored using pressure transducers (A-10, WIKA, Lawrenceville, GA). Flow sensors were used to monitor the flow rates of the concentrate (3-2537-1C-P0, GF Signet, El Monte, CA) and permeate streams (101 Liquid Flo-Sen, McMillan, Georgetown, TX). Feed and permeate conductivities were monitored with inline GF Signet conductivity meters (El Monte, CA) 3-2850-52-42V and 3-2850-52-41V, respectively.

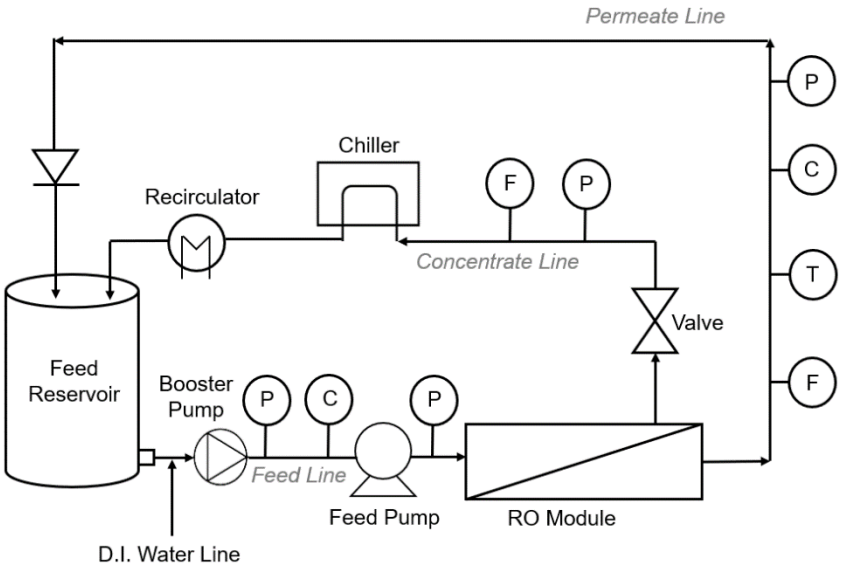

Figure 10-4. Configuration of the RO system for testing spiral-wound elements. (Sensors: P – pressure transducer, C – conductivity meter, T – thermometer, and F – flow meter.)

10.2.6.4.2 Spiral-wound RO membrane performance characterization

Spiral-wound membrane performance was characterized after membrane D.I. water compaction under a transmembrane pressure (ΔP) of 58.6 bar (~850 psi), and crossflow velocity of 11.4 cm/s at 20°C for 24 hr (a sufficient period for the permeate flux to stabilize). Element water and salt permeability coefficients were determined as per **Section 10.2.6.1**. For the spiral-wound RO elements, membrane intrinsic salt rejection was estimated as an average value for the entire element. The element permeate water flux can be expressed as shown in previous studies [70, 375-377]:

$$J_v = L_p\left[\Delta P - \pi_o \frac{\ln(1-Y)}{Y}\cdot\overline{CP} + \pi_o\cdot(1-R_o)\right] \quad (1)$$

where $\overline{\pi_o}$ is the feed osmotic pressure, $\overline{CP}$ is the average concentration polarization modulus in RO membrane element, and Y is the element recovery given by $Y = Q_p / Q_f$, where Q_p and Q_f are

permeate and feed flow rates, respectively. Substitution of the expression for *CP* and salt flux (**Section 10.2.6.1**) into Eqn. (1) leads to the following equation:

$$\frac{\left[\Delta P - \frac{J_v}{L_p} + \pi_o \cdot (1 - R_o)\right] \cdot R_o}{\pi_o \cdot J_v \cdot (1 - R_o)} = \frac{1}{B} \cdot \frac{\ln(1-Y)}{Y} \quad (2)$$

The membrane solute transport coefficient *B* can thus be estimated by plotting the left-hand side of Eqn. (2) vs. ln(1-Y)/Y, where *1/B* is the linear slope. Finally, the intrinsic salt rejection (**Section 10.2.6.1**) for the spiral-wound element was calculated given the expressions for the salt flux, as $\overline{C_m} = C_p \cdot J_v / B + C_p$, where the relation of $J_s = C_p J_v$ was utilized.

10.2.6.5 Element fouling resistance and cleaning efficacy

The fouling propensity and cleaning efficacy of the fabricated SNS-PAA-PA elements were evaluated and compared to a commercial SWRO element of about the same dimensions (Dow SW30-2521). Membrane fouling resistance and cleaning efficacy were assessed following a previously described protocol (**Section 10.2.6.2**). Fouling tests were carried out with 0.1 g/L BSA and 0.1 g/L sodium alginate in a high salinity (32 g/L NaCl) aqueous solution. Filtration tests were carried out over a 24 hr period at an initial permeate flux of 25.5 $L \cdot m^{-2} \cdot h^{-1}$ (~15 $gallon \cdot ft^{-2} \cdot day^{-1}$) and cross flow velocity of 11.4 cm/s. These operating conditions were set to be consistent with the flat-sheet coupon membrane characterization (**Section 10.2.6.2**). At the termination of each fouling filtration test, D.I. water was circulated through the membrane system at a transmembrane pressure of ~17 bar and crossflow velocity of 17 cm/s for 30 min. Following the above membrane cleaning step, the pure water permeability coefficient (**Section 10.2.6.1**) was again determined with D.I. water.

10.3 Results and Discussion

10.3.1 SNS-PAA-PA membrane sheet performance uniformity

The uniformity of membrane surface modification, across a membrane sheet, is a critical factor that impacts membrane performance and hence the viability for modification process scale-up. The performance range for the 18 membrane coupons, extracted from the SNS-PAA-PA 30" × 24" membrane sheet (**Fig. 10-3**), was within L_p = 1.67-2.32 $L \cdot m^{-1} \cdot h^{-1} \cdot bar^{-1}$, B = 0.13-0.21 $L \cdot m^{-2} \cdot h^{-1}$, and R_i = 99.4-99.6%. By comparison, the Base-PA (Toray 73AC) membrane displayed a somewhat wider variability of L_p (2.46-3.20 $L \cdot m^{-1} \cdot h^{-1} \cdot bar^{-1}$), B (0.15-0.32 $L \cdot m^{-2} \cdot h^{-1}$), and R_i (99.0-99.6%) (**Fig. 10-5**). The uniformity measure (**Section 10.2.6.3**) for the SNS-PAA-PA membrane sheets (**Sections 10.2.2** and **10.2.3**) was 89.7%, 84.9%, and 99.9% for L_p, B, and R_i, respectively (**Fig. 10-5** and **Table 10-3**). The uniformity measure of B and R_i for the SNS-PAA-PA membrane sheet (30" × 24") (**Section 10.2.6.3**) was greater by 8.2% and 0.1%, respectively, relative to the Base-PA membrane sheet (**Table 10-3**). It is noted that of the 18 coupons extracted from the Base-PA membrane sheet, four coupons (positions #8, 9, 10, and 14; **Fig. 10-5**) had B values that were 25-60% greater than the average value; this result suggests the possible existence of defects in the base membrane's PA active layer. In contrast, higher performance uniformity of the SNS-PAA-PA membrane indicated that scale-up of APPIGP for TFC-PA RO membrane modification could be achieved at a uniformity level suitable for the fabrication of a spiral-wound element.

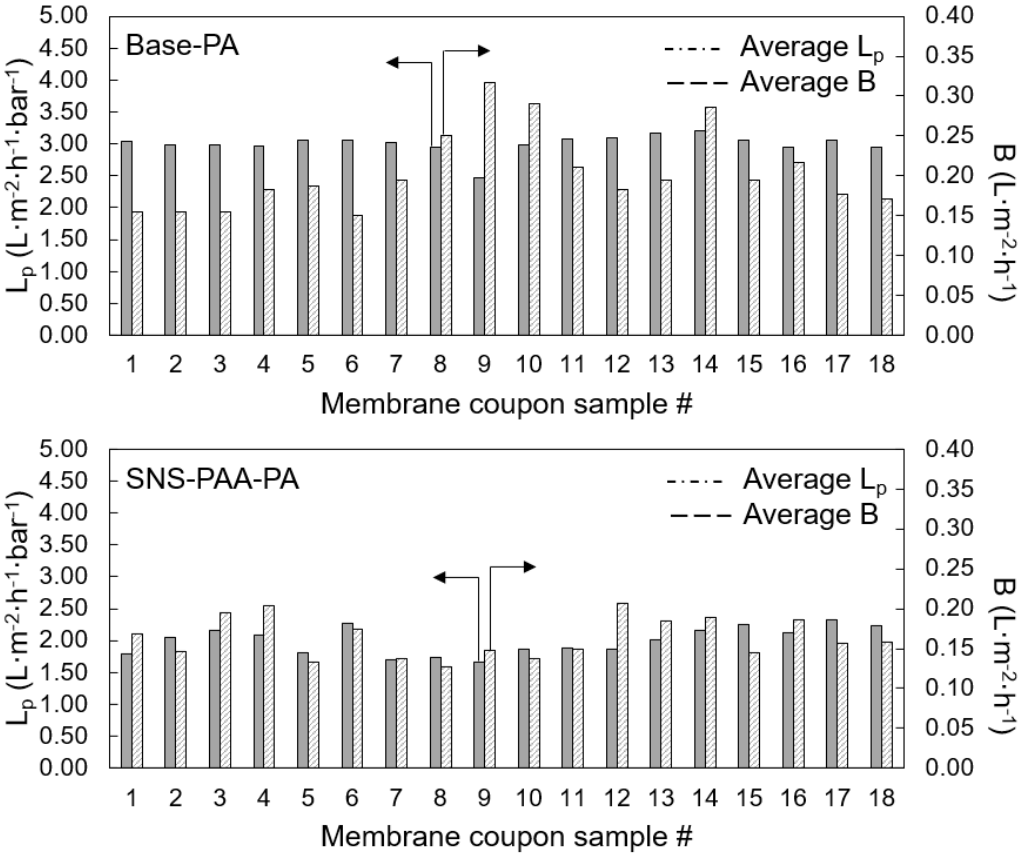

Figure 10-5. Water permeability coefficient (L_p) and salt permeability coefficient (B) for membrane coupon samples from different locations of the Base-PA (Toray 73AC) and SNS-PAA-PA 30" × 24" membrane sheets (**Fig. 10-3**). (Experimental conditions and characterization protocol are provided in **Section 10.2.6.1**).

The SNS-PAA-PA coupon membranes demonstrated, on average, separation properties suitable for seawater desalination (L_p=1.69 L·m^{-1}·h^{-1}·bar^{-1}, B=0.15 L·m^{-2}·h^{-1}, R_o=99.3%, and R_i =99.5%; **Fig. 10-5**). This was achieved based on the selection of a base membrane (Base-PA) with sufficiently high water permeability coefficient, 2.91 L·m^{-1}·h^{-1}·bar^{-1}, but of higher salt transport coefficient (B=0.24 L·m^{-2}·h^{-1}). It is noted relative to the Base-PA membrane, on average, the SNS-PAA-PA membrane displayed lower water permeability (by ~34%), reduced salt permeability coefficient (by ~20%), and increased intrinsic membrane rejection (by ~0.1%) (**Fig. 10-5**). Post-surface tethering with the PAA brush layer, membrane salt rejection increased at the expense of

water permeability reduction. As reasoned in previous studies, AA graft polymerization is likely to have led to sealing of the less selective areas ("microscopic defects") in the PA active layer (i.e., pore-filling) [170, 172, 220].

10.3.2 SNS-PAA-PA coupon membrane anti-fouling properties

Fouling performance of the SNS-PAA-PA coupon membranes was compared with the Base-PA (Toray 73AC) membrane and two commercial SWRO membranes, Dow SW30 and Toray SWRO (82V), based on filtration tests of BSA and sodium alginate model solutions (**Section 10.2.6.2**). Flux decline was observed for the different membranes, with the SNS-PAA-PA membrane demonstrating flux decline of 7.8% and 1.5%, for BSA and sodium alginate, respectively, which was 5.4-11.4% and 4.7-7.2% lower compared to the commercial Dow-SW30, Toray SWRO (82V), and Base-PA (Toray 73AC) membranes (**Table 10-3**). After each fouling test, the fouled SNS-PAA-PA membrane was cleaned with D.I. water to assess the degree of permeability restoration by removing the loosely bound/attached foulant cake layer via fluid shear [360]. Upon D.I. water cleaning, the SNS-PAA-PA membrane demonstrated 96.1% and 100% permeability recovery after the filtration of BSA and sodium alginate solutions, respectively, relative to 84.6-92.7% and 94.3-100% for the commercial membranes, Dow-SW30, Toray SWRO (82V), and Base-PA (73AC) (**Figs. 10-6a** and **10-6b**, and **Table 10-3**).

The contributions of irreversible fouling resistance to the total membrane resistance due to BSA and sodium alginate fouling of the SNS-PAA-PA membrane were lower by up to 10.9% and 5.6%, respectively, relative to the commercial membranes (**Figs. 10-6a** and **10-6b**; **Table A-2, Appendix A**). The absolute magnitude of BSA irreversible fouling for the SNS-PAA-PA membrane was lower by 52.3% and 76.7% relative to the commercial SWRO membranes, Dow SW30 and Toray SWRO

(82V) membranes, respectively (**Table A-2, Appendix A**). Irreversible fouling was not encountered for sodium alginate fouling of the SNS-PAA-PA and Dow SW30 membranes, but the Dow SW30 membrane demonstrated significantly higher total fouling resistance for BSA fouling (by a fact of 5.1) than SNS-PAA-PA membrane.

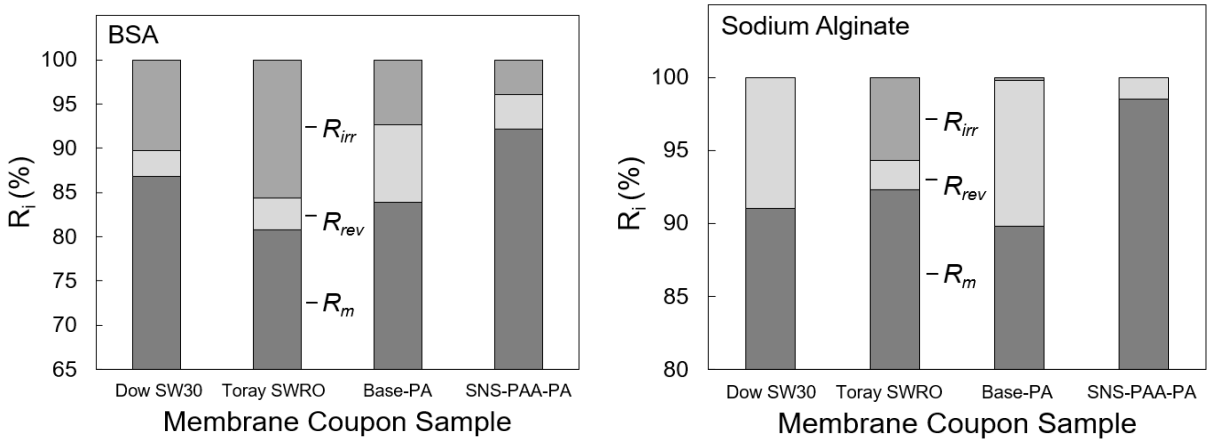

Figure 10-6. Comparison of SNS-PAA-PAA and commercial membranes (Dow SW30, Toray SWRO (82V) and Base-PA(73AC)) with respect to the contributions of membrane resistances (R_m, R_{rev}, and R_{irr}) to total membrane resistance (R_T) after 24 h fouli filtration test, followed by 30 min D.I. water flushing, for (a) aqueous saline solution (32 g/L NaCl) of 0.1 g/L BSA in and (b) aqueous saline (32 g/L NaCl) solution of 0.1 g/L sodium alginate.

Table 10-3. Data summary table of membrane BSA and Sodium Alginate fouling [a].

Membrane	Foulant	Water Permeability Coefficient (L m^{-1} h^{-1} bar^{-1})	Flux Decline	Permeability Recovery
Dow SW30	BSA	1.67	13.2%	89.7%
Toray SWRO [b]	BSA	1.28	19.2%	84.6%
Base-PA [c]	BSA	3.05	16.1%	92.7%
SNS-PAA-PA	BSA	1.26	7.8%	96.1%
Dow SW30	Sodium Alginate	1.72	9.0%	100%
Toray SWRO [b]	Sodium Alginate	1.28	7.7%	94.3%
Base-PA [c]	Sodium Alginate	2.91	10.2%	99.8%
SNS-PAA-PA	Sodium Alginate	1.33	1.5%	100%

[a] Membrane fouling tests were conducted for 24 hr filtration of the model foulant solutions composed of 0.1 g/L BSA or 0.1 g/L sodium alginate in 32 g/L NaCl.

[b] Toray SWRO is a commercial Toray 82V SWRO membrane

[c] Base-PA: commercial Toray 73AC BWRO membrane

Increased membrane cleaning efficacy of the SNS-PAA-PA membrane (as indicated by the higher permeability recovery) suggests that both the BSA and sodium alginate foulant cake layers (**Fig. A-8, Appendix A**) could be easily removed from the fouled SNS-PAA-PA membrane by mere washing with D.I. water (**Fig. A-9, Appendix A**). Such improvement in cleaning efficacy of the SNS-PAA-PA membrane may be attributed to: (i) reduced association/interaction between the foulant molecules and membrane surface due to both surface screening and partial segmental Brownian motion of the tethered hydrophilic PAA chains [46 , 47, 48], and (ii) swelling of the chains upon exposure to D.I. water which enhanced release of the deposited foulants [26, 46, 169]. Moreover, reduction in fouling propensity of the SNS-PAA-PA membrane is also associated with the increased surface hydrophilicity and thus reduced hydrophobic foulant-surface interactions [26, 28, 265-268]. Indeed, upon AA graft polymerization, the captive bubble water contact angle for the SNS-PAA-PA membrane decreased from 43.9^{o} to 20.2 ^{o}. In comparison, the contact angles for the Dow SW30 and Toray SWRO (82V) membranes (**Table 10-4**) were 35.9^{o} and 41.8^{o}, respectively. It is also noted that based on the free surface energy of hydration (**Section 10.2.5.2**), the above four membranes were classified as having hydrophilic surfaces (i.e., ΔG_{iw}<-113 mJ/m^2). However, the SNS-PAA-PA membrane exhibited a greater level of hydrophilicity as indicated by its ΔG_{iw} which was lower by 7.1-12.6% relative to the other tested membranes (**Table 10-4**).

Table 10-4. Summary of membrane surface hydrophilicity

Membrane	**CB water contact angle (°) [(a)]**		**Free energy of hydration (mJ/m^2)**
Dow SW30	35.9	± 2.3	-131.8
Toray SWRO [(b)]	41.8	± 2.9	-127.1
Base-PA [(c)]	43.9	± 3.3	-125.3
SNS-PAA-PA	20.2	± 1.4	-141.1

[(a)] water contact angle for each membrane is the average of at least 5 measurements.
[(b)] Toray SWRO is a commercial SWRO membrane (82V) obtained from Toray
[(c)] Base-PA is a commercial BWRO membrane (73AC) obtained from Toray

10.3.3 SNS-PAA-PA element fouling resistance and cleaning efficacy

Once the performance uniformity of the synthesized SNS-PAA-PA membrane sheet was confirmed as being suitable for scale up the APPIGP approach, spiral wound SNS-PAA-PA elements were fabricated (**Section 10.2.4**). The spiral-wound SNS-PAA-PA elements, and for comparison, the commercial spiral wound elements (Dow SW30) were characterized with respect to fouling resistance and cleaning efficacy using BSA and sodium alginate model solutions. Based on results of the coupon membrane fouling tests (**Section 10.3.2**), increased fouling resistance and cleaning efficacy were expected for the SNS-PAA-PA element relative to the commercial Dow SW30 element. Indeed, the SNS-PAA-PA element demonstrated flux decline of 5.2% and 10.3%, for the 24 hr BSA and sodium alginate fouling tests, respectively, relative to corresponding flux decline of 13.0% and 22.4% for the Dow SW30 element. The lower fouling propensity of the SNS-PAA-PA element relative to the Dow SW30 element was quantified by 52.4% and 14.8% lower total fouling resistance ($R_{fouling} = R_{cake}+R_{irrev}$) at the end of BSA and sodium alginate filtration tests, respectively (**Table 10-5**).

Permeability of the fouled SNS-PAA-PA elements was fully recovered (100%) via mere cleaning with D.I. water (**Fig. 10-7**), indicating that irreversible fouling did not occur with either BSA or sodium alginate. For the Dow SW30 element, at the same fouling test conditions and cleaning protocol, permeability recovery of 100% and 92.3% (R_{irr}=2.3×10^{13} m^{-1}) was achieved for the sodium alginate and BSA fouled elements, respectively. The existence of irreversible BSA fouling implied that, unlike on the surface of SNS-PAA-PA membrane, foulant molecules deposited onto the Dow SW30 membrane may form a structure tightly bound to the membrane surface [169], thus the possible need for more aggressive chemical cleaning (**Table 10-5**). The improved fouling resistance and cleaning efficacy of the fabricated SNS-PAA-PA spiral-wound element relative to

the Dow SW30 could be attributed to its higher surface hydrophilicity (**Table A-2, Appendix A**). The comparative fouling and cleaning results of the SNS-PAA-PA and Dow SW30 spiral wound elements lead to the conclusion that it is feasible to scale up the current membrane surface nano-structuring process to fabricate commercial-scale spiral wound elements with superior anti-fouling properties.

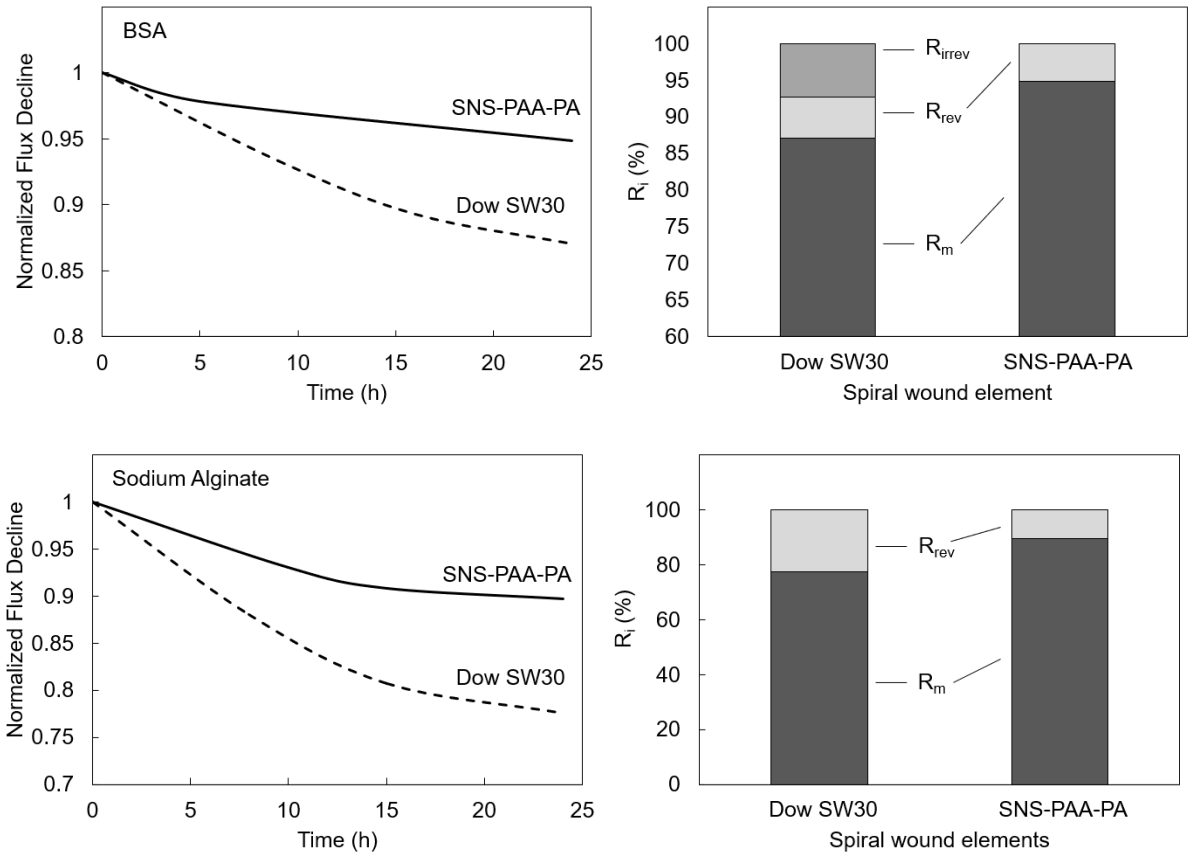

Figure 10-7. Comparison of SNS-PAA-PA and Dow SW30 spiral-wound elements in terms of flux decline (left) and relative contributions of resistances (**Table 10-5**), R_m, R_{irrev}, and R_{cake} to the total membrane permeation resistance, R_T (right) for fouling filtration tests of aqueous saline solution (32 g/L NaCl) of (a) 0.1 g/L BSA, and (b) 0.1 g/L sodium alginate. (Filtration tests at initial permeate flux of 25.5 $L \cdot m^{-2} \cdot h^{-1}$ and constant cross flow velocity of 11.4 cm/s.; Filtration period: 24 hours. Note: Intrinsic membrane resistances of the Dow SW30 #1, #2 and SNS-PAA-PA #1, #2 elements were 8.1×10^{13}, 7.8×10^{13}, 7.8×10^{13}, and 1.0×10^{14} m^{-1}, respectively.)

Table 10-5. Intrinsic membrane resistance (R_m), reversible fouling resistance (R_{rev}), and irreversible fouling resistance (R_{irrev}) for SNS-PAA-PA and Dow SW30 spiral wound elements filtration of BSA and sodium alginate [(a)].

Membrane	R_m (m^{-1})	R_{rev} (m^{-1})	R_{irrev} (m^{-1})	$R_{fouling}$ (m^{-1})
BSA Filtration				
SNS-PAA-PA #1	7.8×10^{13}	4.2×10^{12}	-	4.2×10^{12}
Dow SW30 #1	8.1×10^{13}	5.3×10^{12}	6.8×10^{12}	1.2×10^{13}
Sodium Alginate Filtration				
SNS-PAA-PA #2	1.0×10^{14}	1.2×10^{13}	-	1.2×10^{13}
Dow SW30 #2	7.8×10^{13}	2.3×10^{13}	-	2.3×10^{13}

(a) Foulant solutions were at concentrations of 0.1 g/L in aquous 32 g/L NaCl solutions. Filtration tests were for a period of 24 hr at initial permeate flux of 25.5 $L\cdot m^{-2}\cdot h^{-1}$ and cross flow velocity of 11.4 cm/s.)

10.3.4 SNS-PAA-PA element separation performance

Performance of the spiral-wound SNS-PAA-PA elements was also characterized with respect to water permeability coefficient, salt transport coefficient, and nominal and intrinsic salt rejection (**Figs. A-14** and **A-15**, and **Table A-3, Appendix A**). It is noted that the SNS-PAA-PA elements were fabricated partially manually (**Section 10.2.4**), and thus element performance can be sensitive to the various steps of the element construction process. Consequently, in order to assess the variability of element performance that may be associated with the manufacturing process, two elements (Toray SWRO #1 and #2; **Table A-3, Appendix A**) were fabricated using the same commercial flat-sheet SWRO membrane (Toray 82V; **Table 10-3**). Toray SWRO #2 element exhibited ~34% higher water permeability and ~5% increased nominal salt rejection relative to Toray SWRO #1, which was attributed to variabilities associated with the manual element fabrication process. It is also difficult to avoid the introduction of imperfection that could lead to leakage during the manual fabrication process. Such imperfections could have been introduced, for example, by variations in the positioning of the manually drawn glue line, estimation of the glue line spread width (thus, error introduced in the estimated membrane element active area),

nonuniformity of the speed and force applied in the manual membrane rolling process, and imperfection of the O-ring/gasket fitting. Here it is noted that inconsistent/imprecise position and excessively wide glue lines at the side and end seams of each membrane leaf in the manual fabrication process of RO spiral wound element can lead to inaccurately estimated membrane element active area (with an inaccuracy of >17.5%; [378]). Other imperfections that can impact element performance include, for example, O-ring failure and leakage, membrane selective layer indentation due to the feed spacer, axial dislocation of the feed spacers, and manufacturing defects or glue strips blockage in the permeate tube [378-382]. The inadvertent introduction of imperfections during the manual steps of membrane element fabrication process was evident in the present study when comparing the membrane performance based of flat sheet coupon tests and the fabricated spiral-wound elements. Performance tests of the spiral-wound SNS-PAA-PA membrane elements demonstrated water and salt permeability coefficients in the ranges of 1.26-1.60 $L \cdot m^{-1} \cdot h^{-1} \cdot bar^{-1}$, and 0.47-0.53 $L \cdot m^{-2} \cdot h^{-1}$, respectively, and nominal (observed) and intrinsic salt rejections in the ranges of 97.5-98.2%, and 98.0-98.5%, respectively (**Fig. A-15** and **Table A-3, Appendix A**). Relative performance tests of membrane coupons (extracted from the large membrane sheets), the fabricated SNS-PAA-PA elements exhibited 17.8% lower water permeability coefficient, increased salt transport coefficient (B) by a factor of 3.3, and 1.3% and 1.2% reduced nominal and intrinsic salt rejections, respectively (**Fig. A-15** and **Table A-3, Appendix A**). It is noted that similar lower performance based on testing of spiral wound membrane elements relative to flat sheet membrane was also observed for the fabricated commercial RO membranes, Base-PA and Toray SWRO. Relative to the flat sheet coupon membranes, the fabricated Base-PA and Toray SWRO elements demonstrated 55% and 22.6% reduced L_p, respectively, along with increased B by a factor of 2.3 and 4.5. By comparison, performance (i.e., L_p, B, R_o, and R_i) of the Dow SW30

elements (which are fabricated by an automated process, [378]) remained similar to the performance as characterized in the flat sheet membrane coupon (extracted from the spiral wound element) test (**Figs. A-14** and **A-15**, and **Table A-3, Appendix A**). The above evaluations suggest that the consistency (and defect-free) element fabrication process is critical to avoid leakage, blockage and ensure reproducible active membrane leaf area in the produced element. In the present study, although the performance of the produced flat sheet membranes was suitable for SWRO desalting, it was apparent that in order to improve element performance, an automated rather than manual spiral-wound element fabrication process would be essential to utilize to ensure consistent and high-performance element performance. Notwithstanding the above challenge, the current APPIGP approach was shown to be scalable to the practical size of spiral-wound elements.

10.4 Conclusions

Reverse osmosis membrane surface modification with tethered poly(acrylic acid) chains was accomplished via atmospheric pressure plasma-induced graft polymerization approach that was scaled up to a level suitable for fabrication of 2.5" x 21" spiral-wound RO elements. nano-structuring (SNS) was scaled up to synthesize ~30" × 24" SNS-PAA-PA membrane sheets suitable for the construction of commercial-scale spiral wound elements (2.5" diameter and 21" length). Laboratory testing of 18 membrane coupons (~2" × 4") extracted from the 30" × 24" SNS-PAA-PA membrane sheet in terms of water and salt permeability coefficients and intrinsic membrane rejection demonstrated the same or even higher performance uniformity level compared to Base-PA. The scaled-up SNS procedure can thus be used to surface modify the PA RO membrane at a uniformity level suitable for fabrication of commercial-scale spiral-wound elements. The fabricated SNS-PAA-PA spiral wound elements demonstrated flux decline of 5.2% and 10.3%, for the 24 hr BSA and sodium alginate fouling tests, respectively, relative to the corresponding flux

decline of 13.0% and 22.4% for the commercial Dow SW30 element. Permeability of both BSA and sodium alginate fouled SNS-PAA-PA elements was fully recovered (100%) via mere cleaning with D.I. water, relative to permeability recovery of 92.3% (R_{irr}=2.3×10^{13} m^{-1}) and 100% for the BSA and sodium alginate fouled Dow SW30 elements. The existence of irreversible BSA fouling for the Dow SW30 membrane implies the possible need for more aggressive chemical cleaning. Improved fouling resistance and cleaning efficacy of the SNS-PAA-PA membrane was demonstrated for both coupon flat sheets and spiral wound elements, attributed to the increased surface hydrophilicity, and surface screening and partial segmental Brownian motion of the surface tethered PAA chains. The above results indicate that it is feasible to scale up membrane surface nano-structuring process to fabricate commercial-scale spiral wound elements with superior anti-fouling properties. However, further efforts will be required to optimize the element fabrication process (which was achieved partially manually in the present study) to avoid the introduction of any imperfections and improve the fabricated SNS-PAA-PA spiral wound elements separation properties.

Appendix

A. Supplementary Materials

A.1. Surface characterization of PSf surfaces

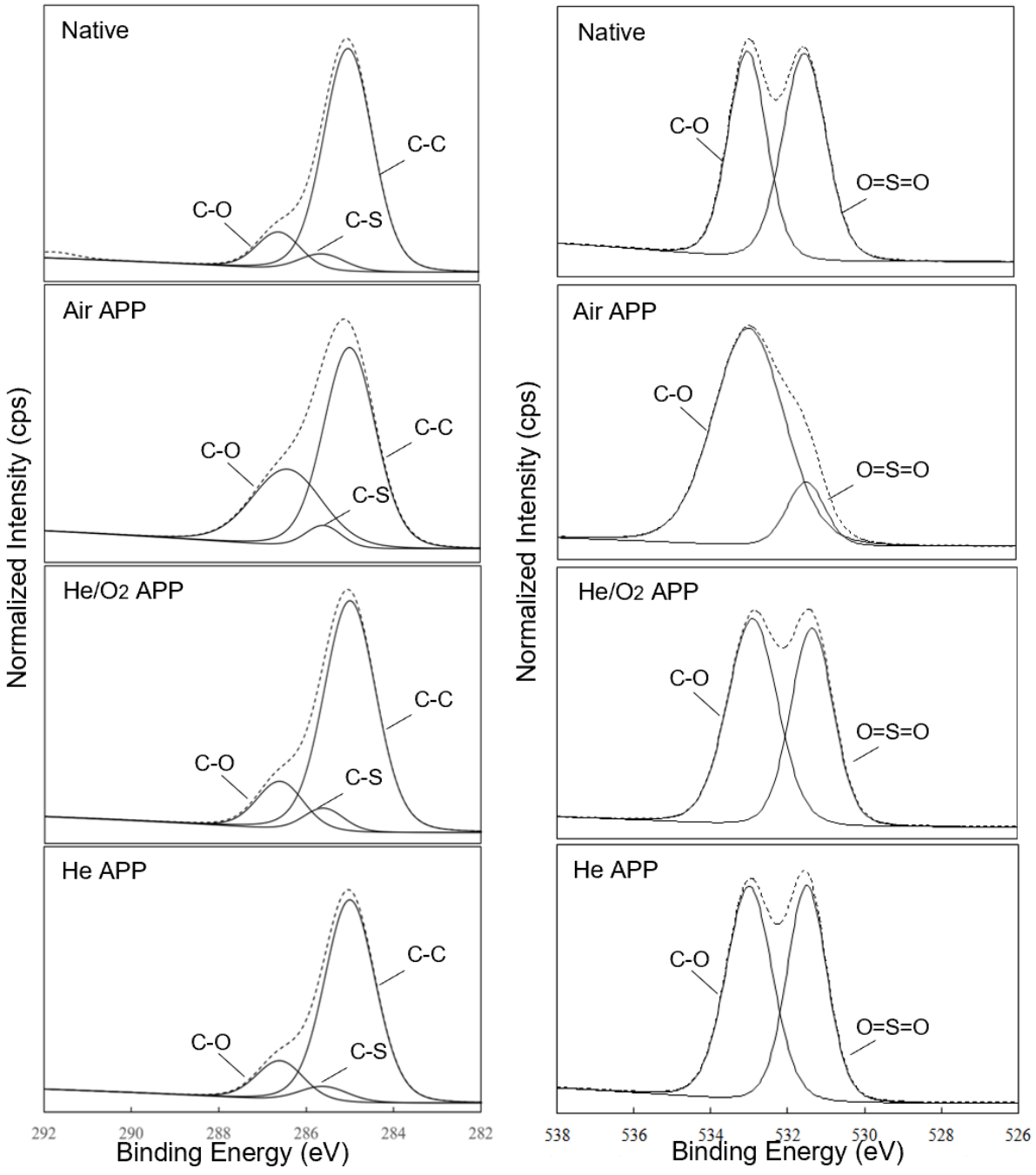

Figure A-1. XPS spectra of C 1s scan (left) and O 1s scan (right) for the native PSf-PEI-Si surface, and PSf surfaces activated with Air, He/O_2, and He plasmas (PSS = 10 mm, N = 1).

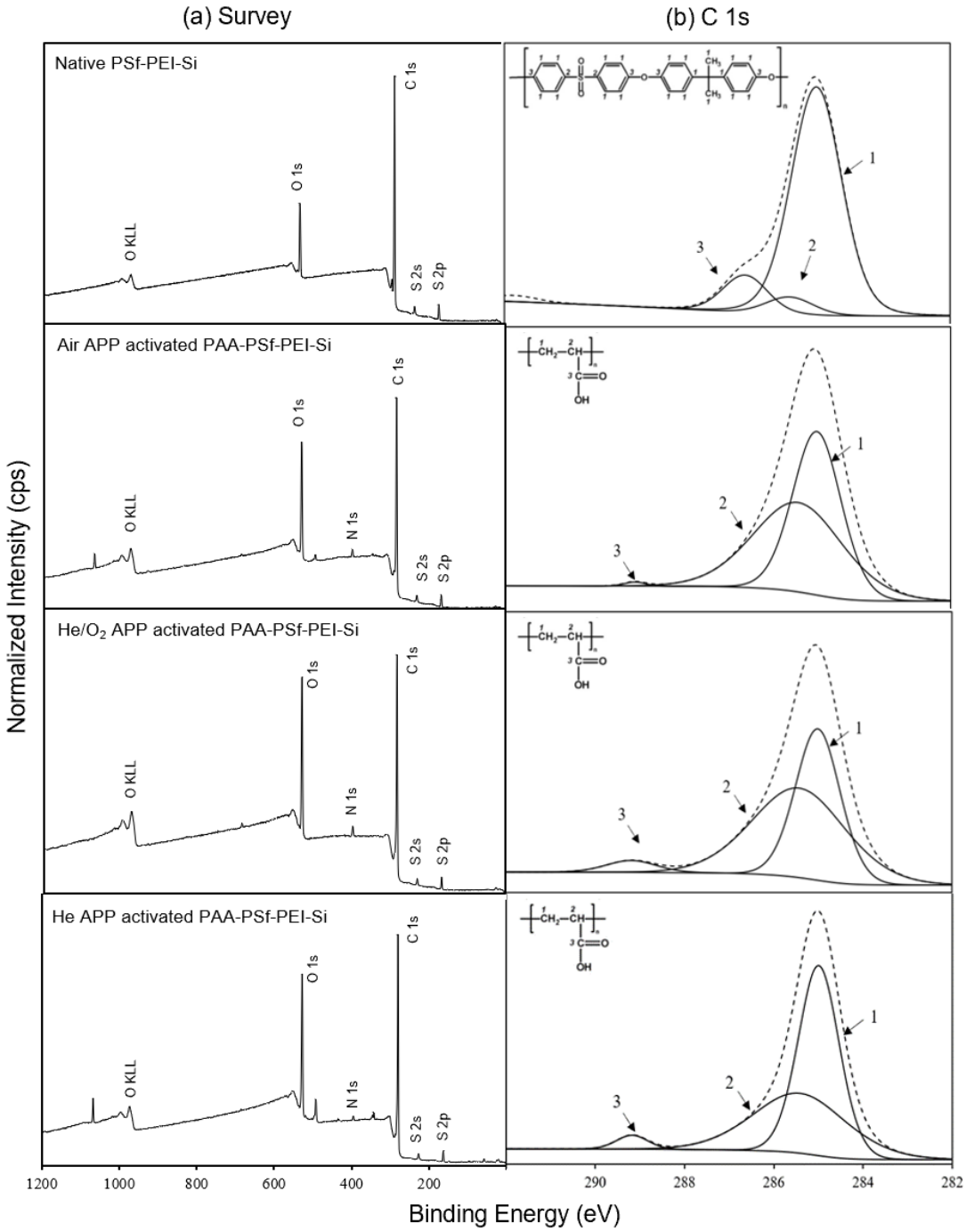

Figure A-2. XPS (a) survey spectra, and (b) C 1s scan of the native PSf-PEI-Si surface, and PAA-PSf-PEI-Si surface synthesized via AA graft polymerization post PSf surface activation via treatment with Air, He/O_2, and He plasmas.

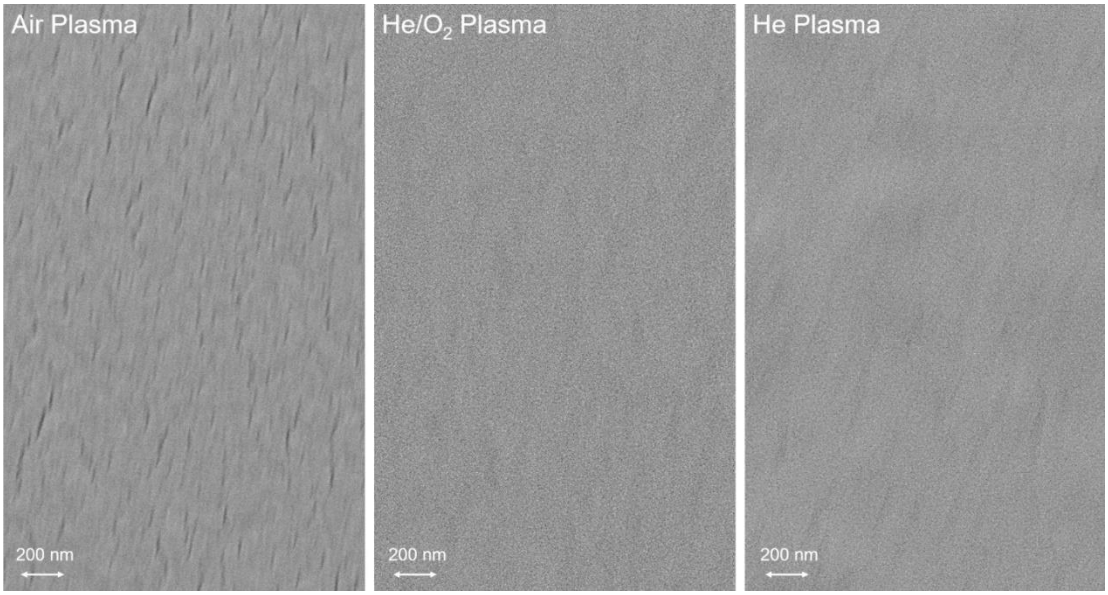

Figure A-3. Top-view SEM images of PSf-PEI-Si surfaces treated with Air, He/O_2, and He plasmas (PSS = 10 mm, N = 4).

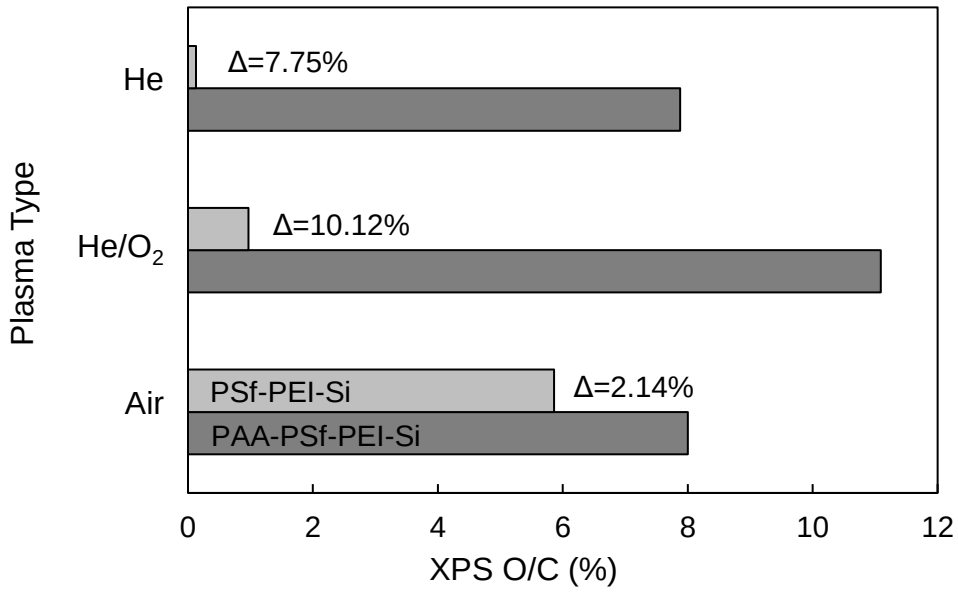

Figure A-4. Surface characterization by XPS survey showing the O/C (%) for the PSf-PEI-Si surfaces after plasma treatment with He, He/O_2, and Air plasma and post-AA graft polymerization.

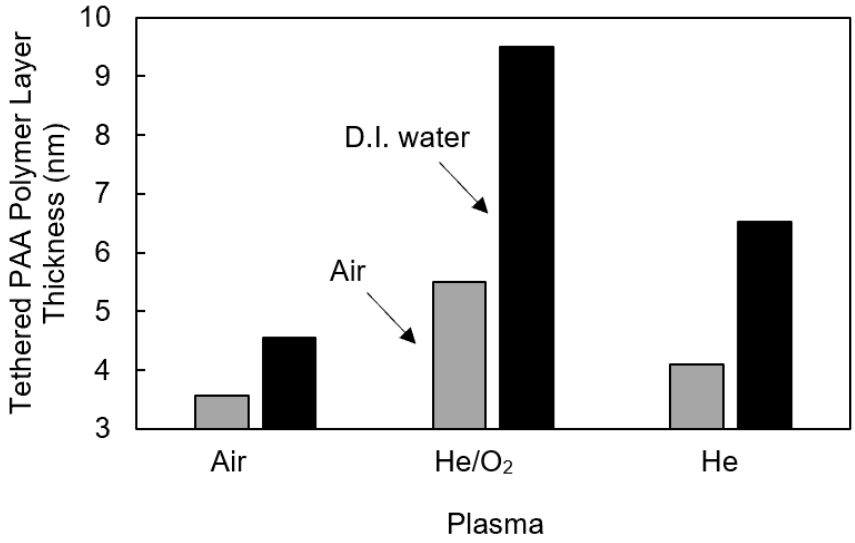

Figure A-5. Thickness of tethered PAA, synthesized onto the PSf-PEI-Si surface activated by Air, He/O_2, and He APP, determined by AFM under both air and water environments.

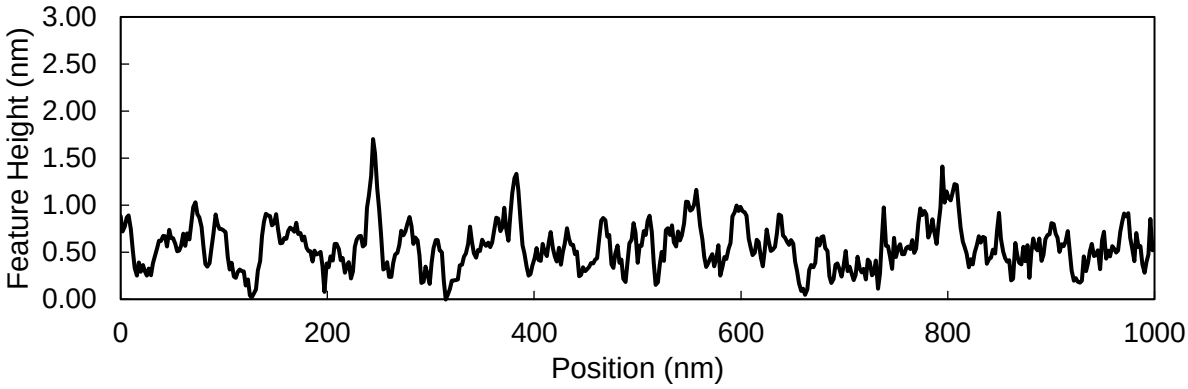

Figure A-6. Cross-sectional AFM feature height profile obtained in D.I. water for the native PSf-PEI-Si surface. The smooth Si substrate was utilized to allow characterization of surface feature changes (at the nano-scale level) due to graft polymerization.

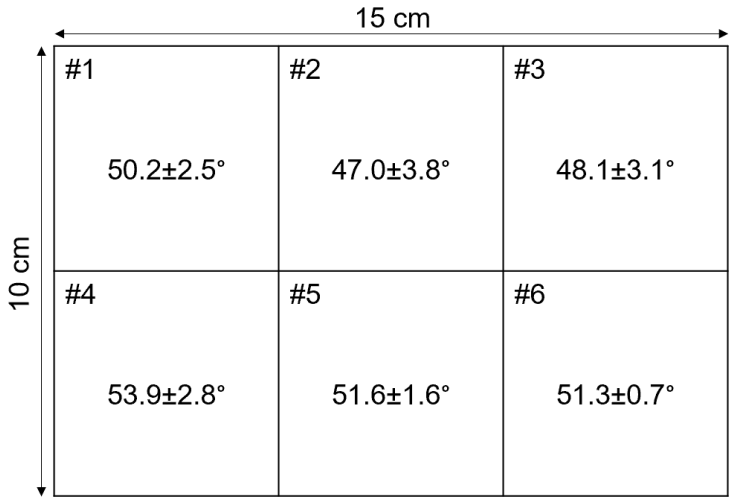

Figure A-7. Captive bubble water contact angle for six positions of the Native-PSf membrane sheet (15 cm × 10 cm) measured in D.I. water at 20°C. The uniformity measure is 92.8% calculated using as $f = (1 - sd / \overline{x}) \times 100\%$, where *sd* and $\overline{x}$ are the standard deviation and average of the surface contact angle.

A.2. Surface characterization of PA RO membranes

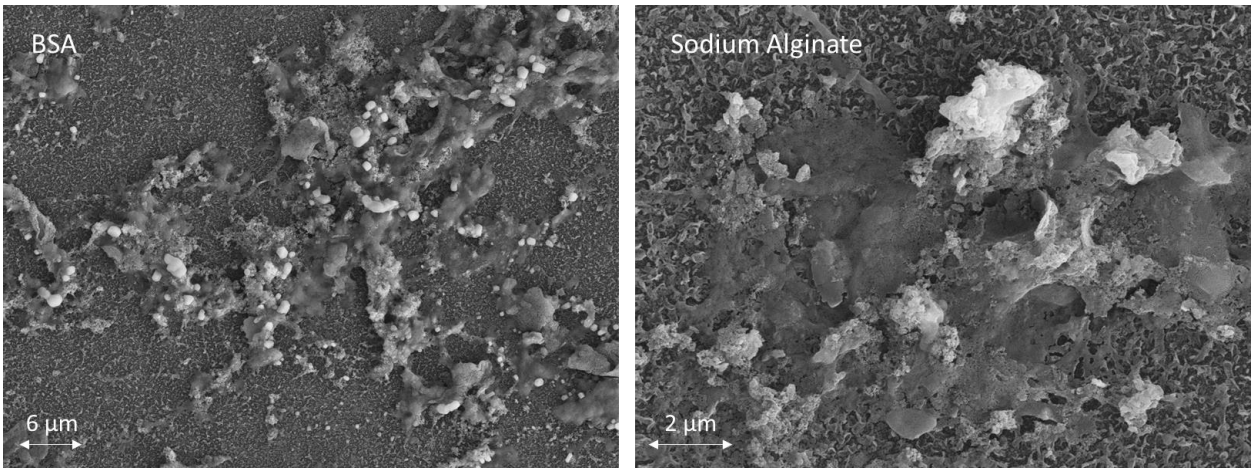

Figure A-8. SEM top-view images of the BSA (left) and sodium alginate (right) fouled SNS-PAA-PA coupon membrane surfaces post 24 hr filtration of 0.1 g/L BSA and sodium alginate in 32,000 ppm NaCl aqueous solutions, respectively. (**Figure A-9** provides SEM images of the initial clean membrane and membranes cleaned with D.I. water after the fouling test). (It is noted that due to the high salinity level (32 g/L NaCl) of the model foulant solutions, precipitated NaCl domains are observed on the BSA-fouled membrane (left SEM image) as white cubic crystals consistent with other reported images of sodium chloride crystals on RO membrane surfaces [383, 384]. It is noted that for the sodium alginate fouled membrane, the SEM images (left) show, consistent with previously published images [385], NaCl crystals that appear to be embedded/distributed within sodium alginate matrices as indicated by the white portion of the cake layer.)

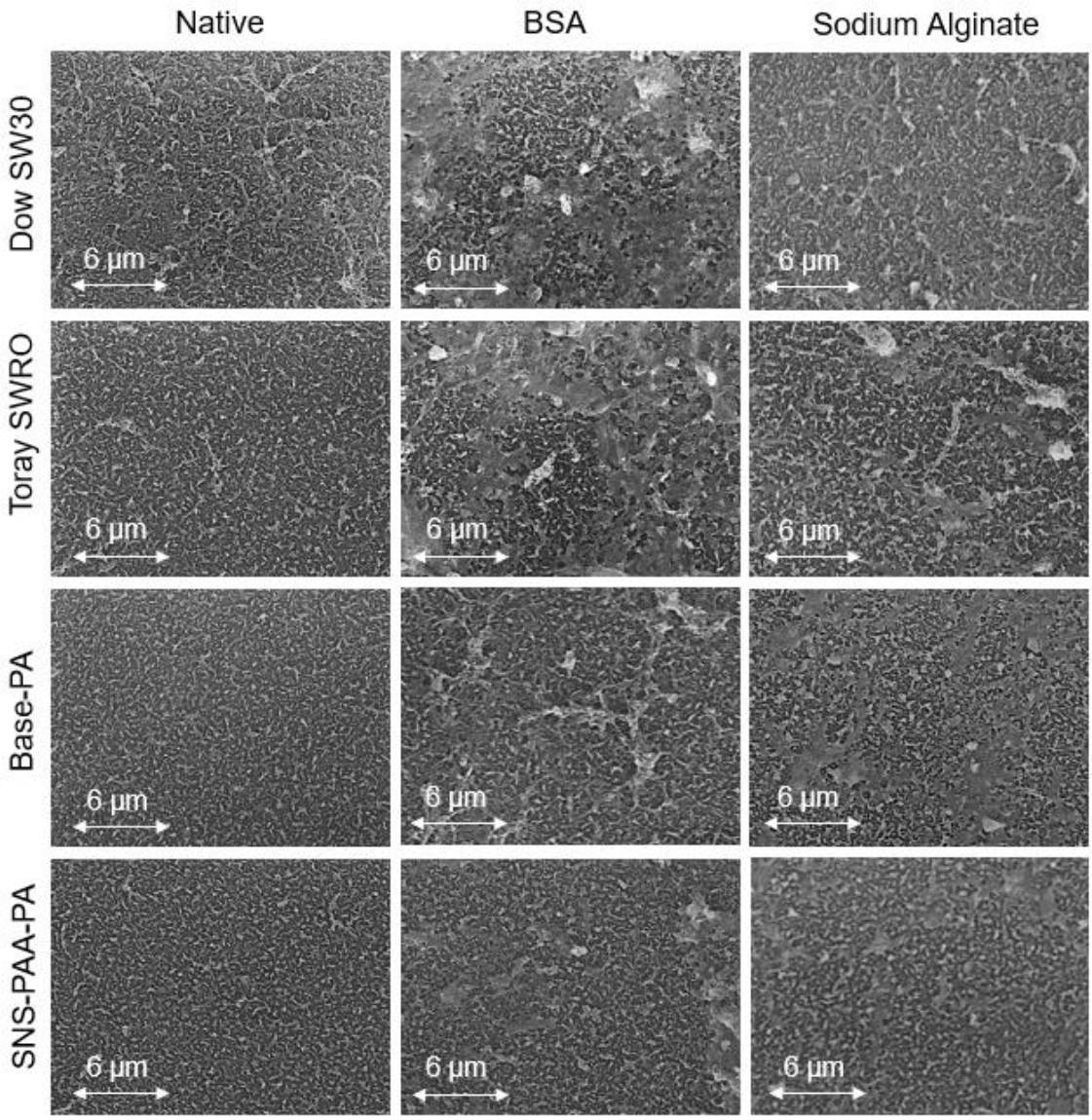

Figure A-9. SEM top-view images of native SNS-PAA-PA membrane, and SNS-PAA-PA membrane filtered with 0.1 g/L BSA in 32 g/L NaCl solution, and 0.1 g/L Sodium Alginate in 32 g/L NaCl solution, followed by 30 min D.I. water flushing, as compared to commercial membranes of Dow SW30, Toray SWRO and Base-PA.

A.3. PSf UF membrane performance characterization

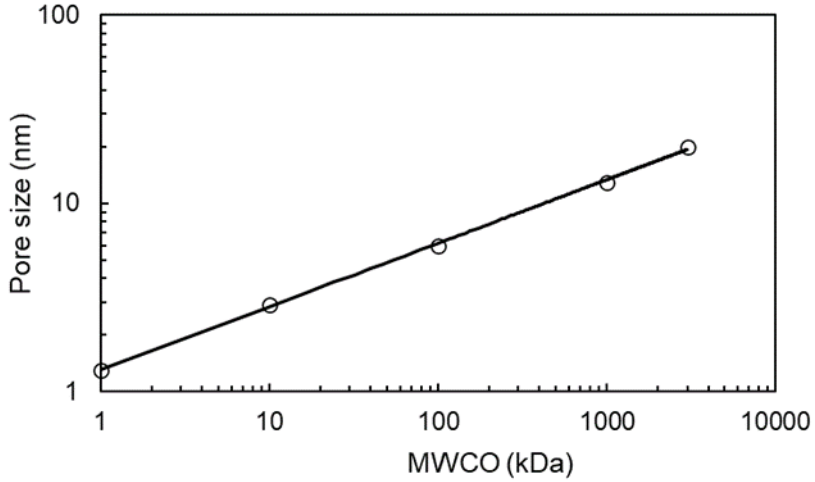

Figure A-10. Empirical relationship between membrane average pore size (diameter) and *MWCO* (data source: [87]) which is suggested for globular solutes [1]. The empirical correlation follows a simple power law model: pore size (d_p, nm) = 1.3095 × $MWCO^{0.3409}$, $R^2 > 0.999$.

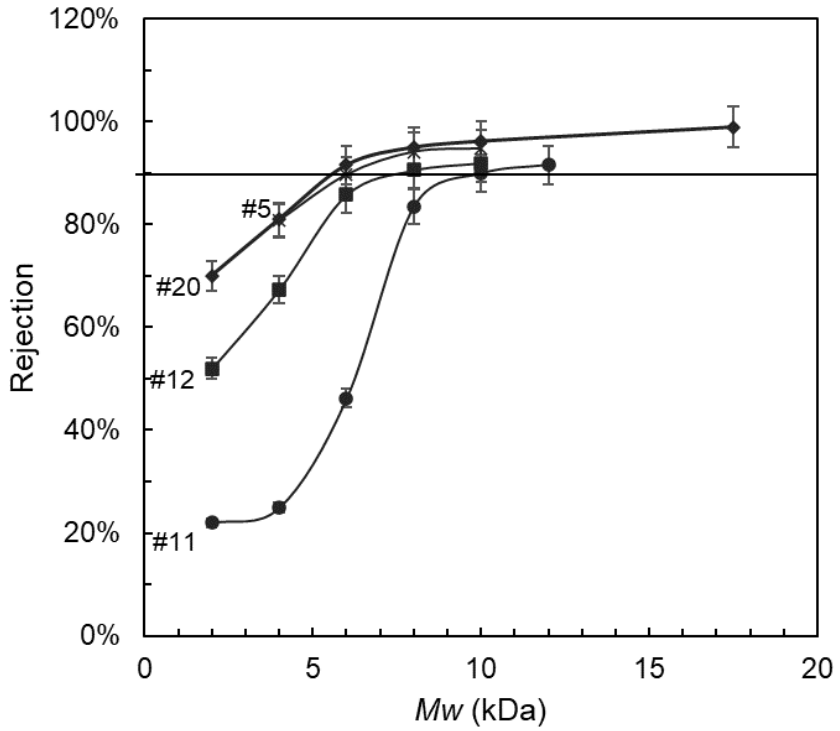

Figure A-11. SNS-PAA-PSf membranes nominal rejection with respect to solute *Mw* for a series of PEG fractions (2 - 17.5 kDa). The *MWCO*-rejection curves examples are for SNS-PAA-PSf membranes #5, 11, 12, and 20, **Table 4-2**, **Chapter 4**).

Table A-1. Surface tension of different liquids used in the present study.

Solution no.	Salt concentration[a] (g/L)	pH[b]	Surface tension (mN/m)
1	0	7	73.6
2	0	7	72.8
3	0	7	72.0
4	0	3	72.8
5	0	5	72.8
6	0	9	72.8
7	0	11	72.8
8	0.1	7	72.8
9	1	7	72.8
10	10	7	73.0
11	32	7	73.5

[a] Salt concentration (g/L) can be converted to chlorinity (Cl, g/kg), from which solution salinity (S, g/kg) can be calculated: S=1.80655·Cl [386]. The empirical correlation between the salt solution surface tension (γ_{SW}) and salinity (S) is given by:

$$\gamma_{SW} = \gamma_W[1+3.766\times10^{-4}S+2.347\times10^{-6}S\cdot t]$$

where γ_W is pure water surface tension and *t* is temperature (°C) [387].

[b] Water surface tension is independent of solution pH for the present tested range [388].

[c] Water surface tensions for different temperatures are given by [389-392].

A.4. PA RO membrane performance characterization

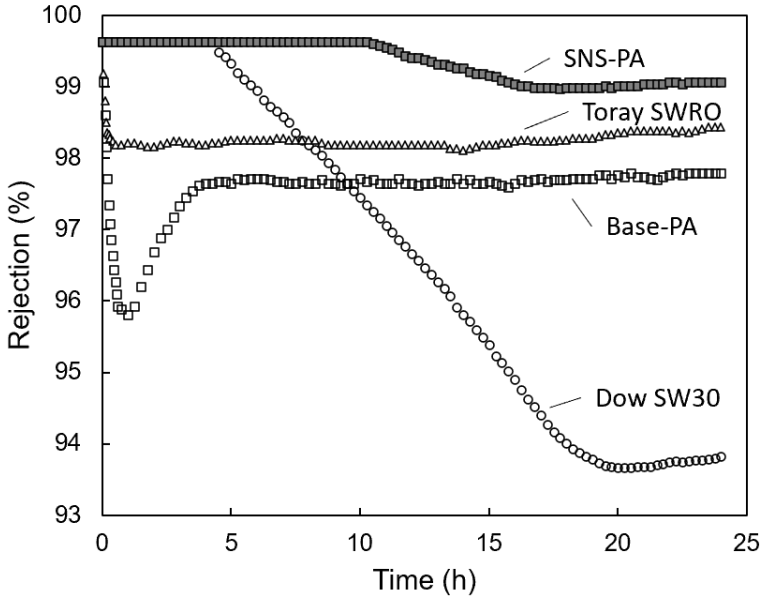

Figure A-12. Salt rejection variation for the SNS-PAA-PA and commercial membranes (Dow SW30, Toray SWRO and Base-PA) during 24 h gypsum scaling tests.

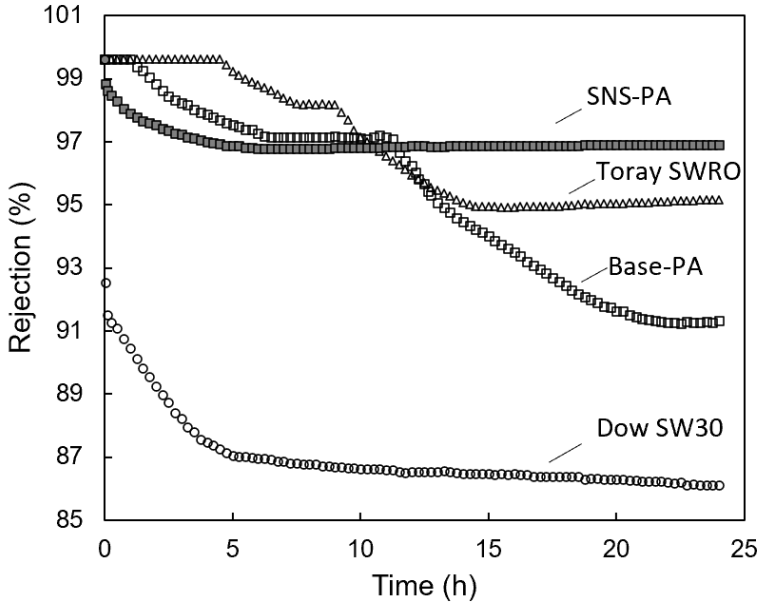

Figure A-13. Variation of solute rejection for SNS-PAA-PA membrane during 24 h calcium carbonate scaling tests compared to commercial membranes of Dow SW30, Toray SWRO and Base-PA.

Table A-2. Data summary table of membrane BSA and Sodium Alginate fouling resistances [a].

Membrane	Foulant	R_m (m^{-1})	R_{rev} (m^{-1})	R_{irr} (m^{-1})	$R_{fouling}$ (m^{-1})	R_{total} (m^{-1})
Dow SW30	BSA	7.6×10^{13}	2.9×10^{12}	8.8×10^{12}	1.2×10^{13}	8.8×10^{13}
Toray SWRO [b]	BSA	1.0×10^{14}	5.6×10^{12}	1.8×10^{13}	2.4×10^{13}	1.2×10^{14}
Base-PA [c]	BSA	4.2×10^{13}	4.8×10^{12}	3.3×10^{12}	8.1×10^{12}	5.2×10^{13}
SNS-PAA-PA	BSA	1.0×10^{14}	4.6×10^{12}	4.2×10^{12}	8.8×10^{12}	1.1×10^{14}
Dow SW30	Sodium Alginate	7.3×10^{13}	7.2×10^{12}	0.0	7.2×10^{12}	8.0×10^{13}
Toray SWRO [b]	Sodium Alginate	9.9×10^{13}	2.2×10^{12}	6.1×10^{12}	8.3×10^{12}	1.1×10^{14}
Base-PA [c]	Sodium Alginate	4.4×10^{13}	4.9×10^{12}	8.4×10^{10}	5.0×10^{12}	4.9×10^{13}
SNS-PAA-PA	Sodium Alginate	9.5×10^{13}	1.4×10^{12}	0.0	1.4×10^{12}	9.6×10^{13}

[a] Percentage of individual resistance (i.e., R_m, R_{rev}, and R_{irrev}) to the total resistance ($R_{total}=R_m+R_{rev}+R_{irrev}$).

[b] Toray SWRO is a commercial Toray 82V SWRO membrane

[c] Base-PA: commercial Toray 73AC BWRO membrane

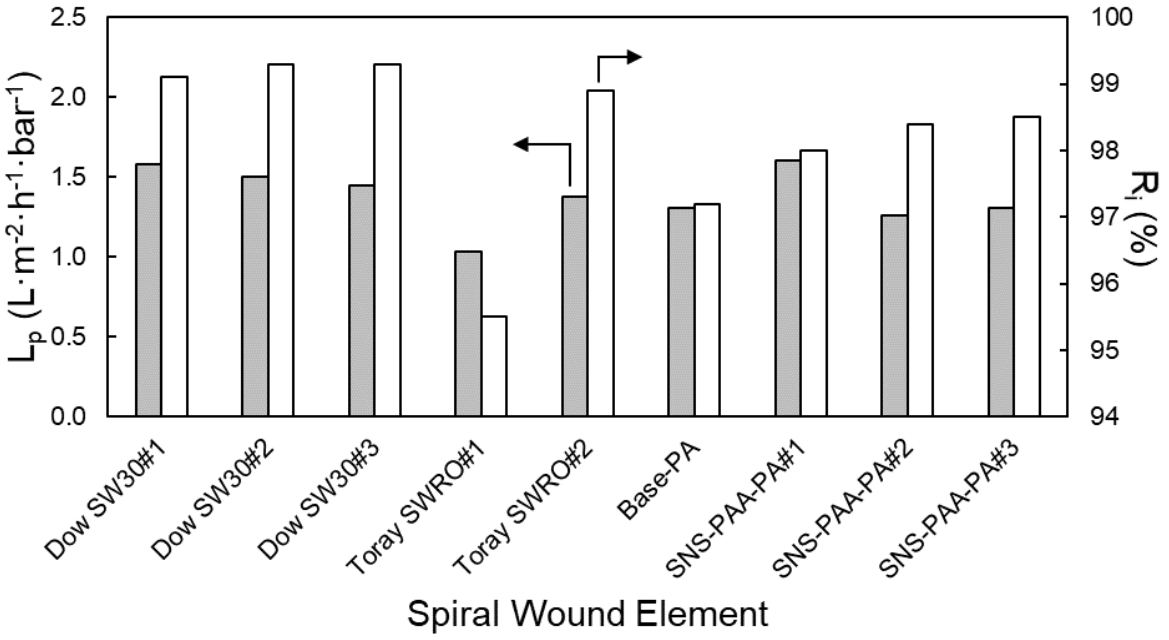

Figure A-14. Water permeability coefficient (L_p) and intrinsic salt rejection (R_i) for fabricated spiral-wound elements (i.e. SNS-PAA-PA, Base-PA, and Toray SWRO) as compared to commercial Dow SW30 elements. (Experimental conditions and characterization protocol described in **Section 10.2.6.4, Chapter 10**)

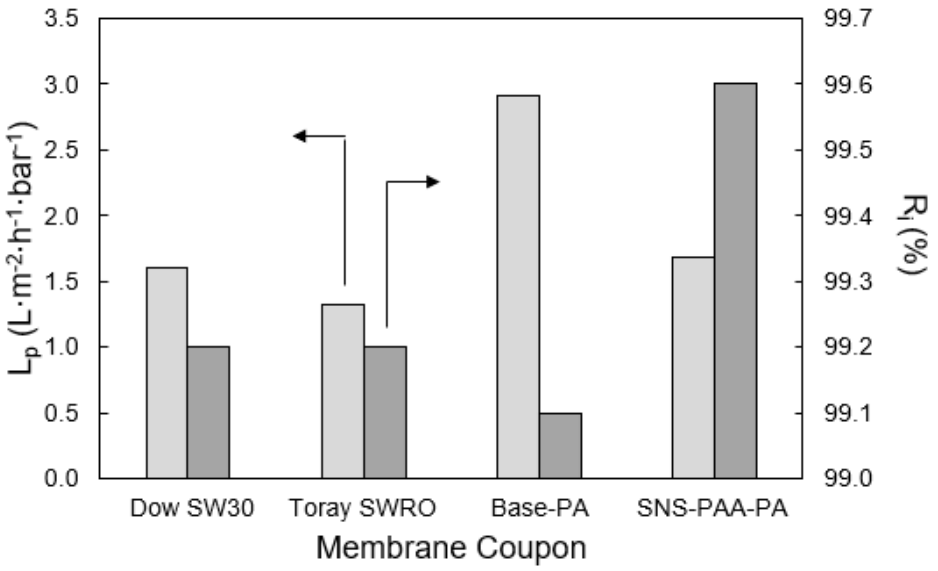

Figure A-15. Water permeability coefficient (L_p) and salt permeability coefficient (R_i) for coupon sample of SNS-PAA-PA membrane as compared to commercial membranes of Dow SW30, Toray SWRO and Base-PA (Feed concentration = 32,000 ppm NaCl).

Table A-3. Performance summary of RO coupon membranes and spiral wound elements

Coupon membranes [a]					**Spiral wound elements**				
Membrane	L_p ($L \cdot m^{-1} \cdot h^{-1} \cdot bar^{-1}$)	B ($L \cdot m^{-2} \cdot h^{-1}$)	R_o (%)	R_i (%)	Membrane	L_p ($L \cdot m^{-1} \cdot h^{-1} \cdot bar^{-1}$)	B ($L \cdot m^{-2} \cdot h^{-1}$)	R_o (%)	R_i (%)
SNS-PAA-PA	1.69	0.15	99.3	99.5	SNS-PAA-PA #1	1.60	0.53	97.5	98.0
					SNS-PAA-PA #2	1.26	0.47	98.2	98.4
					SNS-PAA-PA #3	1.31	0.49	98.2	98.5
Toray SWRO	1.33	0.24	99.0	99.2	Toray SWRO #1	1.03	1.08	94.1	95.5
					Toray SWRO #2 [b]	1.38	0.32	98.7	98.9
Base-PA	2.91	0.24	99.0	99.3	Base-PA	1.31	0.54	96.4	97.2
Dow SW30	1.60	0.25	98.9	99.2	Dow SW30 #1	1.58	0.24	99.0	99.1
					Dow SW30 #2	1.50	0.23	99.0	99.3
					Dow SW30 #3	1.45	0.20	99.2	99.3

[a] The SNS-PAA-PA, Toray SWRO, and Base-PA membrane coupon samples were obtained from the full-size flat membrane sheets used to fabricate the spiral-wound elements, while Dow SW30 membrane coupon sample was extracted from a commercial spiral wound element (Dow Filmtec SW30-2514). Each of the reported performance data represents the average performance from at least 3 samples extracted from positions (#2, 10, and 18) of the large membrane sheet (**Fig. 10-3, Chapter 10**).

[b] The Toray SWRO #2 element was fabricated on the second batch using the same Toray 82V commercial flat membrane sheet to assess the consistency of the spiral wound element fabrication process.

B. Zeta Potential Characterization Protocol

1. Open the software ‘Attract 2.1’.
2. Open the task "Calibration pH" in the Device Control (**Figure B-1**). Start the calibration using the standard solutions (pH of 4, 7, and 10) by clicking on the green ‘Calibration pH’ button. After finishing the procedure for all three buffer solutions, click on ‘OK’ to have the calibration parameters, slope and offset, calculated and stored.

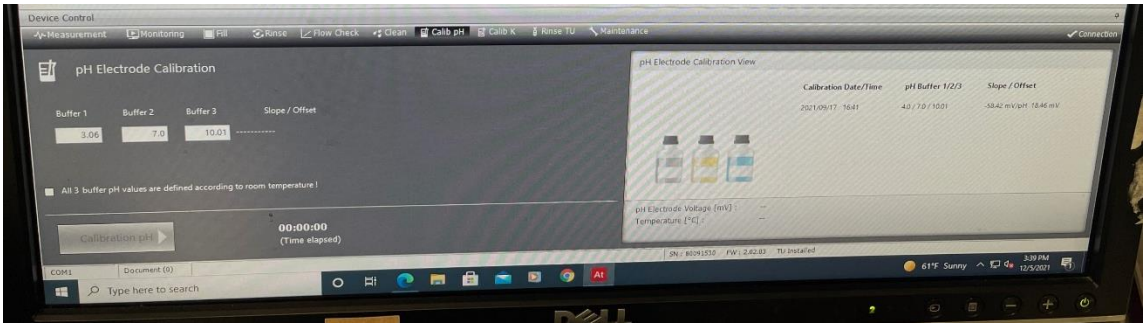

Figure B-1. Calibration pH of the SurPASS system.

3. Open the task "Calib K" in the Device Control. Select Standard Solution as calibration liquid and type in the conductivity of the standard calibration liquid. Confirm that the calibration liquid is selected correctly by clicking on the check box. Click on the green button ‘Calibration K’ to open the Conductivity Electrode Calibration dialog. Accept the calculated cell constant by clicking on the ‘OK’ button (**Figure B-2**).

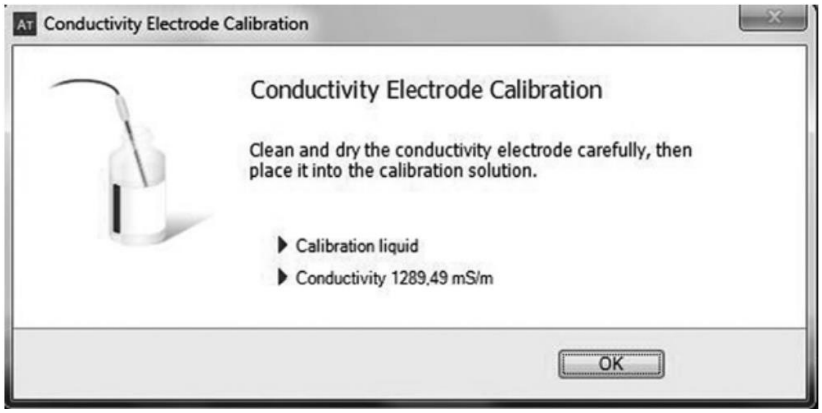

Figure B-2. Calibration conductivity of the SurPASS system.

4. Prepare a 600 mL beaker with fresh ultrapure water. Disconnect the outlet hose from the beaker cover and put it into the beaker with D.I. water (**Figure B-3**). Put the beaker cover with the inlet hose mounted on an empty 600 mL beaker. Open the task "Clean" in the Device Control and select Standard as measurement type. Select a cleaning time of 300 s, confirm that the outlet hose is dipped into the cleaning solution, and start the cleaning by clicking on the green ‘Clean’ button. Wait until the complete volume has passed through

the system and cancel the process. Reconnect the outlet hose to its original position on the beaker cover.

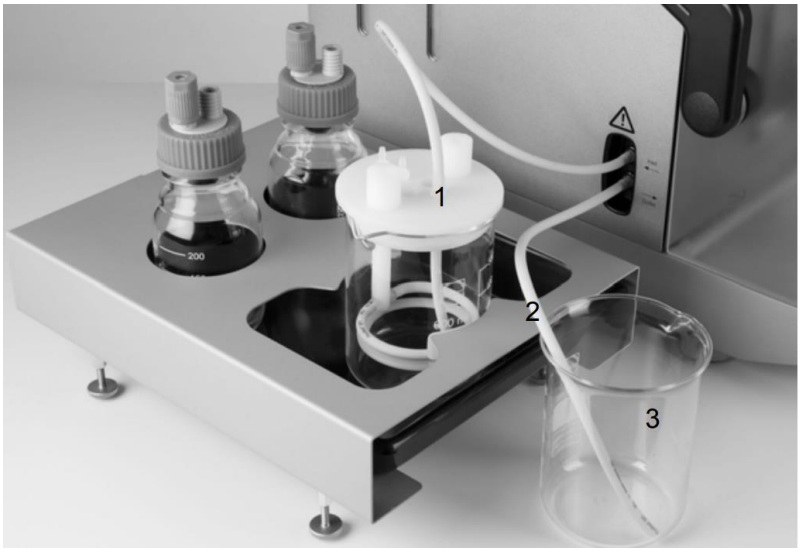

Figure B-3. Positions of the inlet and outlet hoses when cleaning the SurPASS system.

5. Open the task "Rinse TU" in the Device Control (**Figure B-4**). Select TU1 and type in 6 mL volume. Confirm that the outlet hose is connected to a waste beaker. Start the filling of the titration syringes and hoses by clicking on the green ‘Rinse TU’ button. Select TU2 and repeat the filling process.

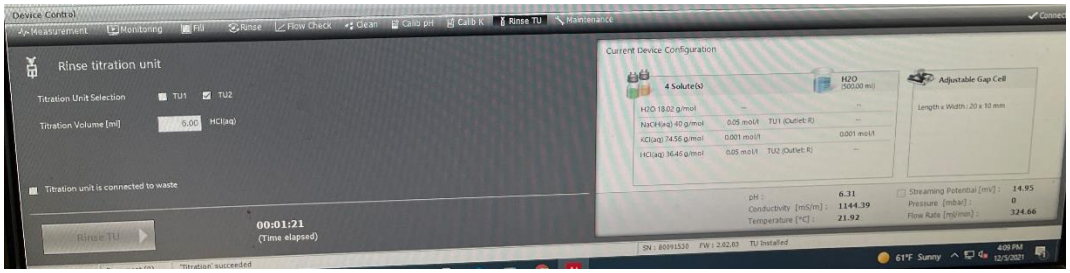

Figure B-4. Rinse TU of the SurPASS system.

6. Take out the adjustable gap cell from the SurPASS system (**Figure B-5**).

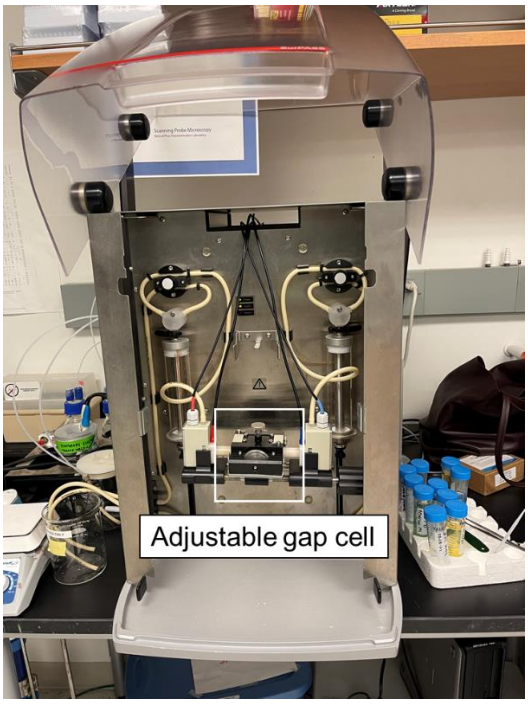

Figure B-5. The SurPASS system.

7. Disassemble the gap cell and take out the sample holder (**Figure B-6**).

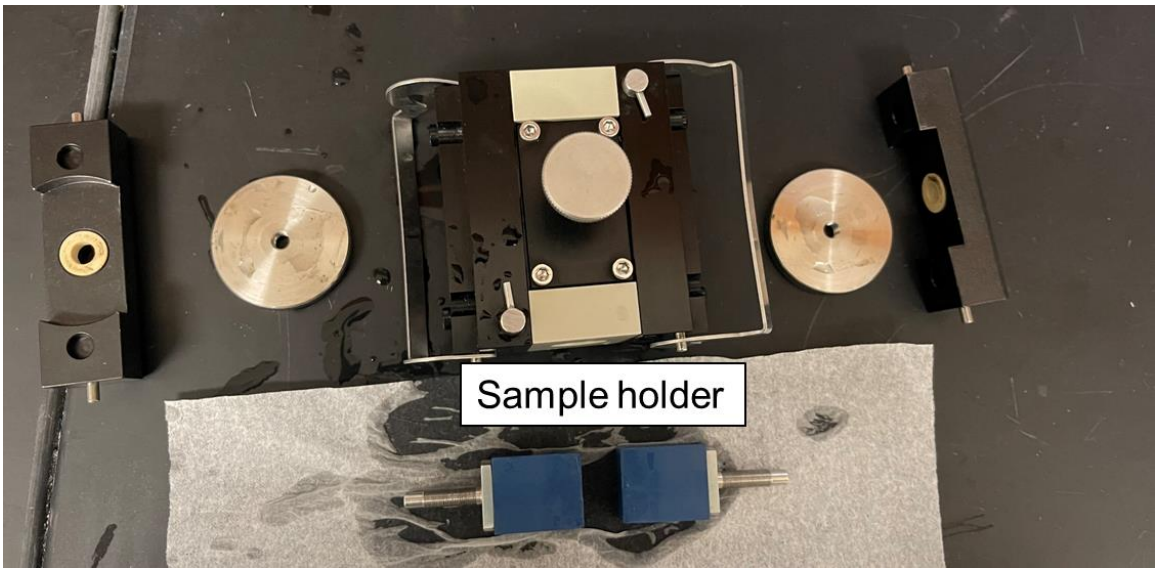

Figure B-6. Disassemble the gap cell.

8. Stick membrane on the sample holder using the double-sided adhesive tape (**Figure B-7**).

Figure B-7. Sample holders are affixed with membranes.

9. Insert the sample holders with the samples into the rectangular holes of the housing of the Adjustable Gap Cell (**Figure B-8**). Align the gap between the sample holders to the center of the flow channel.

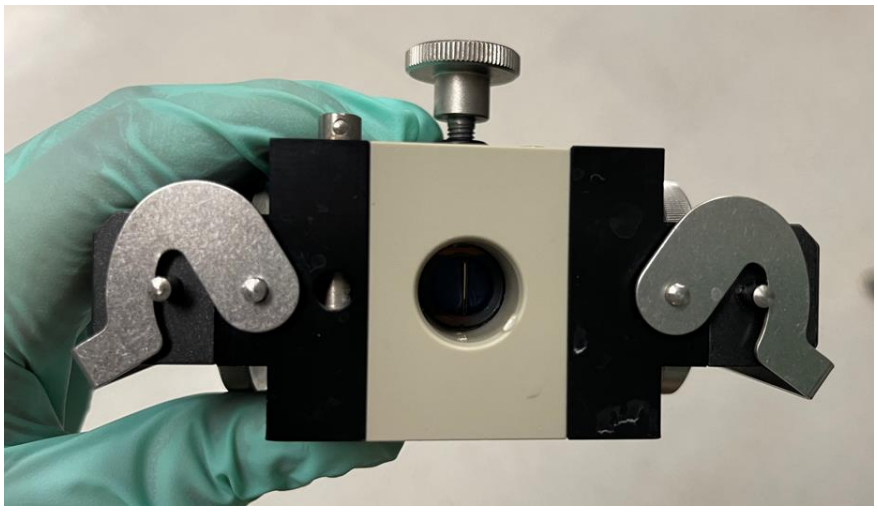

Figure B-8. Sideview of the gap cell with sample holders inserted.

10. Mount the knurled nuts with the scale on the threads of the sample holders (**Figure B-9**). Mount the counter pieces of the knurled nuts and fix the counter pieces with the clamps. Compress the silicone sealing block with the knob. Tighten the knob gently.

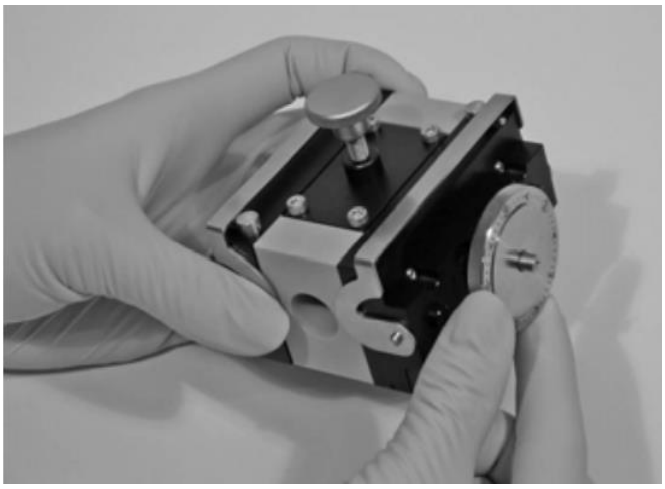

Figure B-9. Adjust the knurled nuts on both sides of the gap cell.

11. Place the adjustable gap cell back into the SurPASS system. Close the SurPASS cover and start with the preparation for the measurement.
12. Prepare an empty and dry glass beaker with a magnetic stir bar and place the beaker cover with the accessory kit for nitrogen purge mounted on it (**Figure B-10**). Weigh 45 mg KCl and place it into the dry glass beaker, with 600 mL D.I. water. Immediately purge the electrolyte solution with nitrogen.

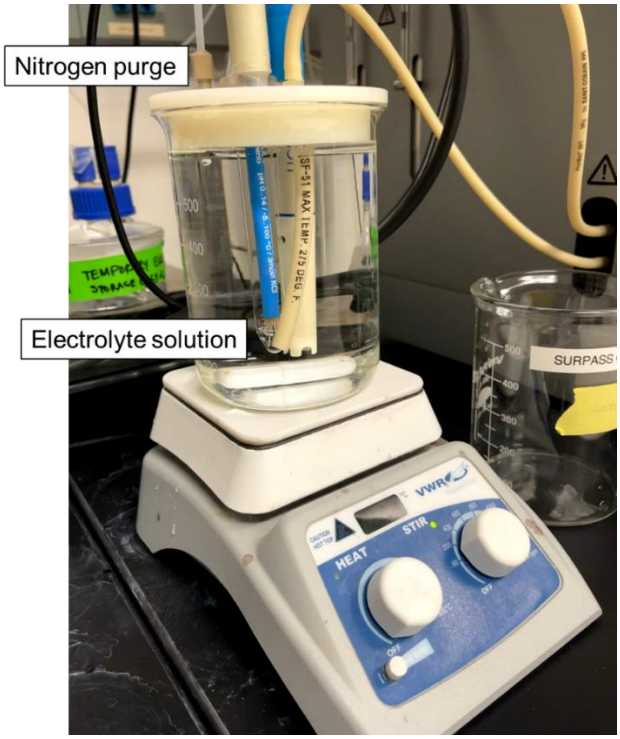

Figure B-10. Beaker setup.

13. Open the task "Fill" in the Device Control and select Standard as measurement type. Type in 150 s as fill time. Disconnect the outlet hose from the beaker cover and place the hose into a second glass beaker (“waste beaker”). Click on the green button to fill the electrolyte circuit and the measuring cell. Wait until the first cycle (i.e. a syringe movement pumping 100 mL of the electrolyte solution through the measuring cell from the left into the right syringe) has finished and monitor the actual gap height displayed in the Current Measuring View. Cancel the Fill cycle after the 100 mL were dispensed into the “waste beaker” by clicking on the red ‘Fill’ button.
14. Reconnect the outlet hose to the beaker cover and open the task "Rinse" (**Figure B-11**). Define a Rinse Time for 180 s and a Target Pressure of 400 mbar and confirm that the hoses are connected correctly on the beaker cover. Start the rinsing by clicking on the green button. Check the gap height and cancel the rinse process to adjust the gap height by rotating the knurled nuts in the appropriate direction. Restart the rinse cycle after the gap adjustment and repeat until a gap height of 100 µm is reached.

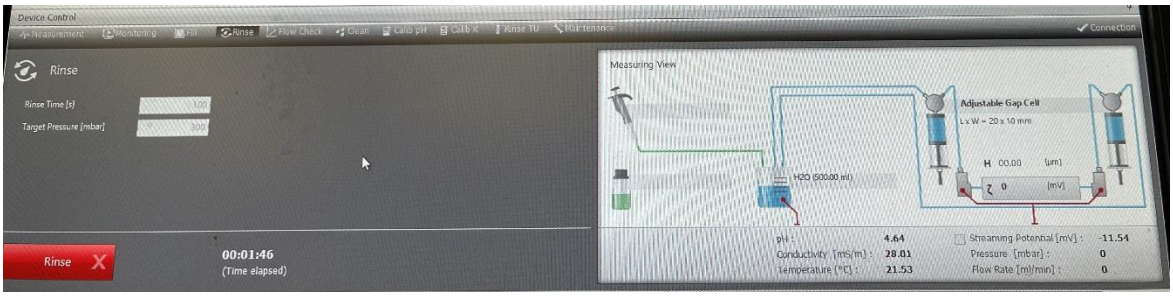

Figure B-11. Rinse the gap cell.

15. Open the task "Flow Check", define a Target Pressure of 400 mbar and confirm that the measuring cell with the sample is mounted correctly and rinsed thoroughly with the electrolyte solution. Start the flow check by clicking on the green button to make sure that the system is filled without air and to check the performance of the mounted sample.
16. Create a new measurement document in ‘application’ and then select ‘New>Standard measurement’ (**Figure B-12**).

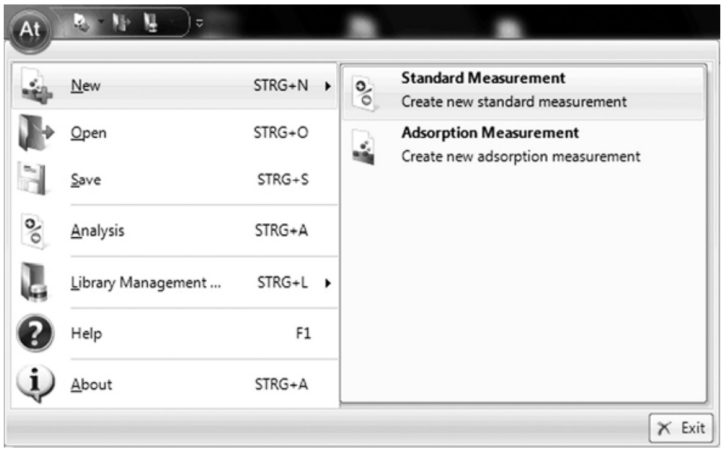

Figure B-12. Create a new measurement document.

17. Define the used solvent and its volume in the section Solvents and the solutes used for measurement in the List of Solute Settings in the tab 'Configuration 1/2: Solution Mixture' (**Figure B-13**). Open the second tab 'Configuration 2/2: Device Setting' to select the Adjustable Gap Cell as Cell Type and select Titration Unit 1 or Titration Unit 2 by clicking on the check box. Select also the used solute for titration from the drop-down menu. Select pH Titration to Limit in the Measurement Info below the configuration tabs and type in the desired target pH of the automatic pH titration.

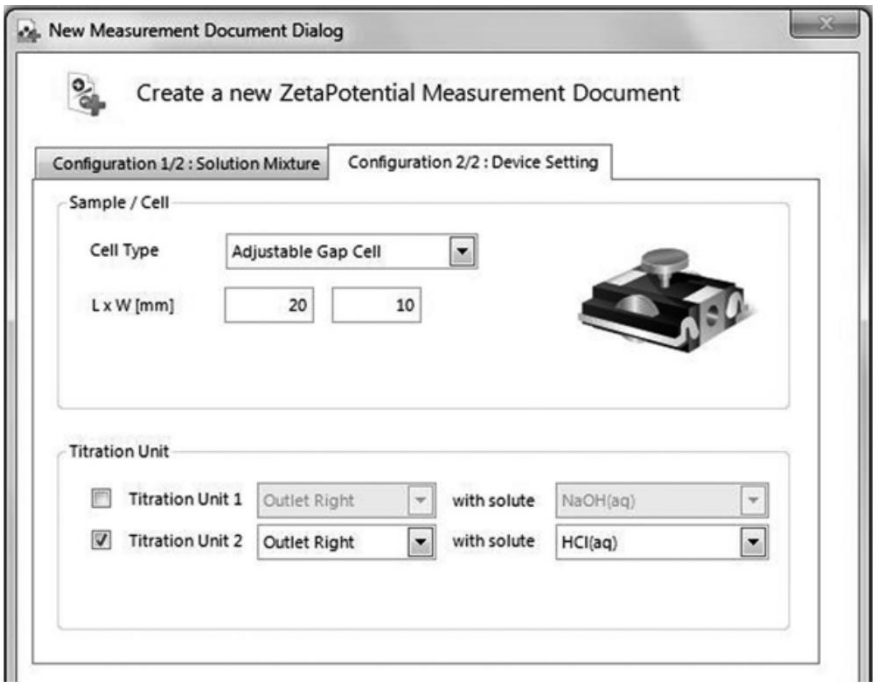

Figure B-13. Input the information of the solution and device for the measurement.

18. Type in the File Name and click on the 'OK' button to save the new measurement document.
19. Set the measuring step parameter and start the measurement (**Figure B-14**).

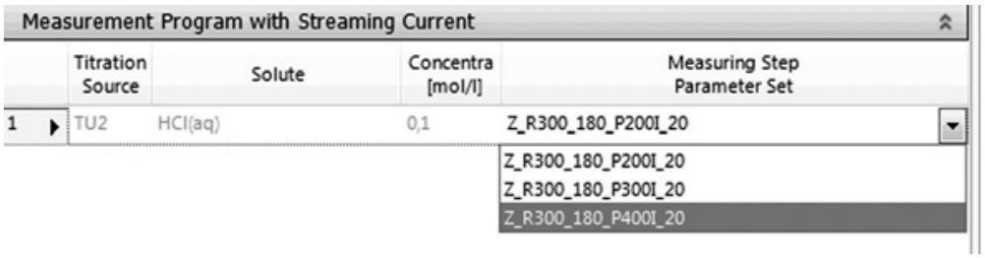

Figure B-14. Set the measuring step parameters of the measurement.

C. Membrane Surface Nano-structuring Procedures for PSf Membrane Coupons

C.1. Preparation of the base membrane

1. Base PSf UF membrane sheets were kept in D.I. water for at least 24 hr before modification or characterization (**Figure C-1)**.

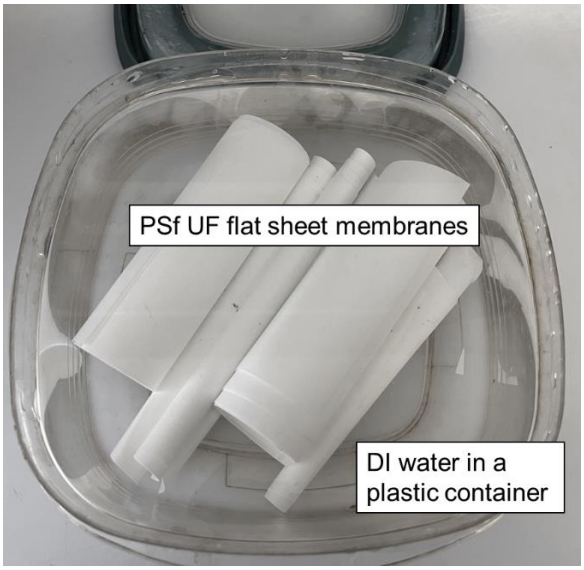

Figure C-1. Immersion of the base membrane sheets in D.I. water.

2. Extract a membrane coupon (diameter of 4.13 cm) from the base PSf UF flash sheet (**Figure C-2**).

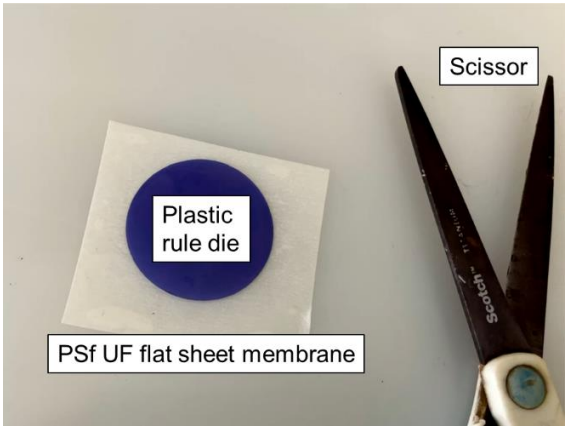

Figure C-2. Extract membrane coupon from the base membrane sheet.

3. Flush the coupon membrane with D.I. water and then blow dry with nitrogen using a PTFE nitrogen gun (**Figure C-3**).

Figure C-3. Blow-dry the coupon membrane using a nitrogen gun.

4. The dried membrane coupon was then affixed to the metal plate (using double-sided tape) of the atmospheric pressure plasma system (**Figure C-4**).

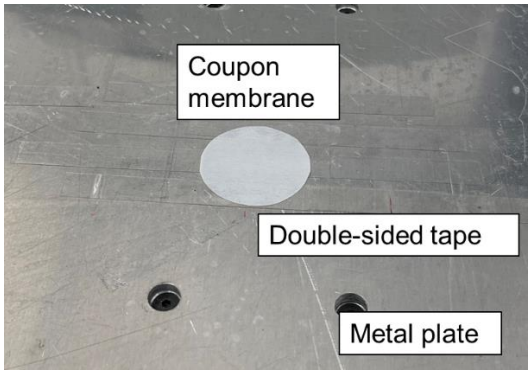

Figure C-4. Dried coupon membrane affixed to the metal plate of the plasma system.

C.2. He or He/O_2 plasmas

1. Turn on the power switch of the coolant control module (CCM) and click the 'Enter' button three times. Then turn on the power switch of the plasma controller (**Figure C-5**).

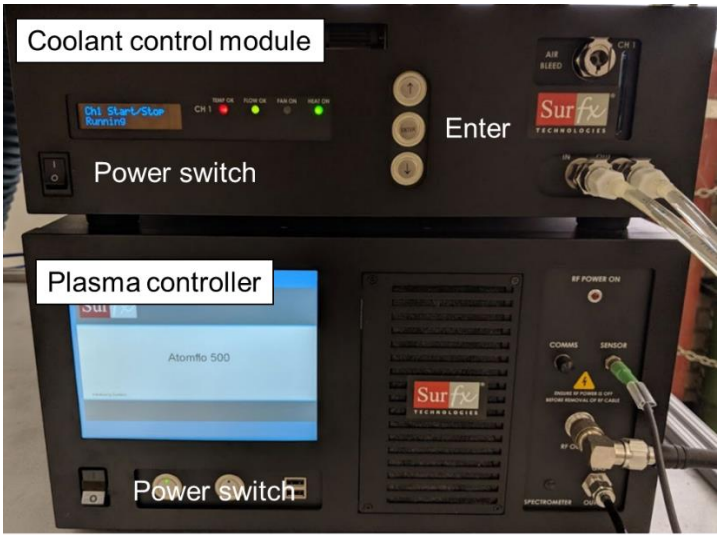

Figure C-5. Plasma system controller and coolant control module.

2. Open helium (99.99% purity) and oxygen (99.999% purity) gas cylinders (**Figure C-6**). The outlet gauges of the pressure regulators for the above gas cylinders are set to 45 psi.

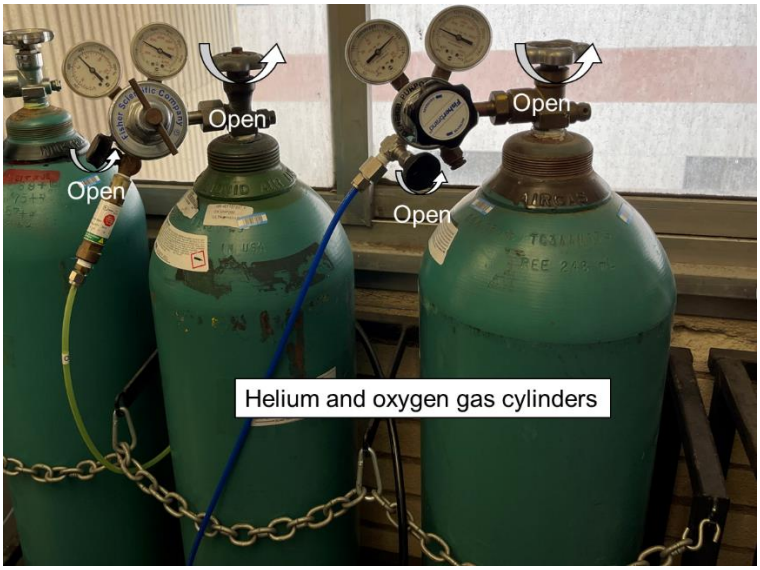

Figure C-6. Helium and oxygen gas cylinders.

3. Check if the name of the current active recipe displayed on the controller main screen is correct (**Figure C-7**). Active recipe can be changed or customized by accessing the admin mode. Change the user access type from ‘Operator’ to ‘Admin.’ Selecting ‘Admin’ will prompt a keypad to enter the PIN (i.e., 1234).

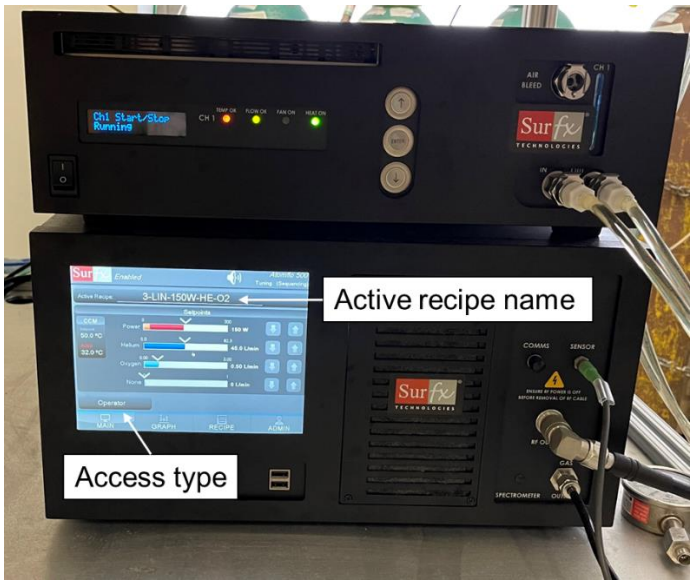

Figure C-7. Controller setup for plasma activation program.

4. Wait until the actual temperature is above 47°C, confirm the program number (i.e., plasma source separation distance, and the number of sequential plasma scans), and press the ‘START’ button on the plasma controller (**Figure C-8**). Wait until the system displays ‘Process On’ instead of ‘Tuning (Sequencing)’.

Figure C-8. Controller screen exhibitions.

5. Press ‘Home’ to return the plasma head to the initial position, then press ‘Run’ to execute the APP system for membrane surface activation (**Figure C-9**).

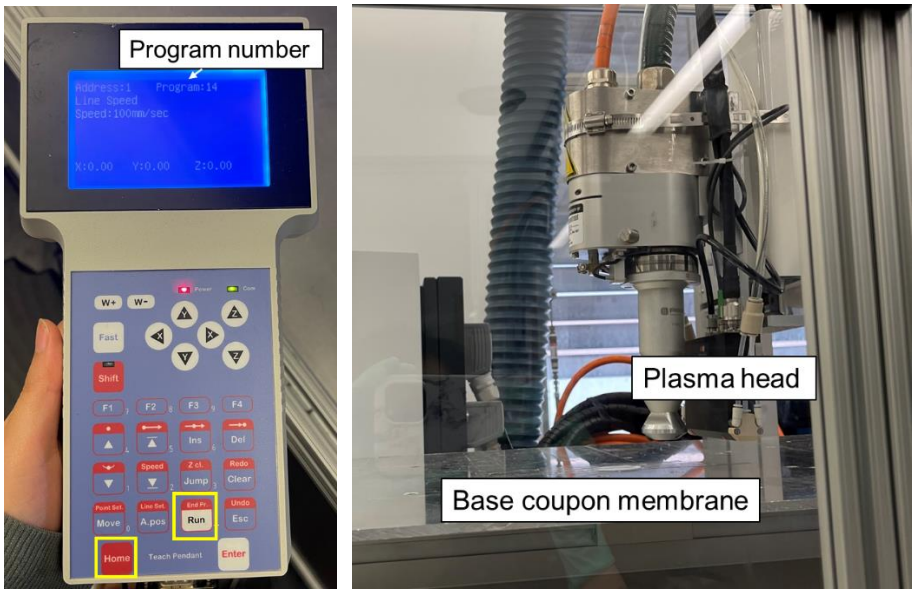

Figure C-9. Run the plasma system.

C.3. Air plasma

1. Turn on the Air plasma controller (**Figure C-10**).
2. Confirm the program number (i.e., plasma source separation distance, and the number of sequential plasma scans), and press the ‘On’ button on the plasma controller.

Figure C-10. Air plasma controller.

3. Run the APP system for membrane surface activation (**Figure C-11**).

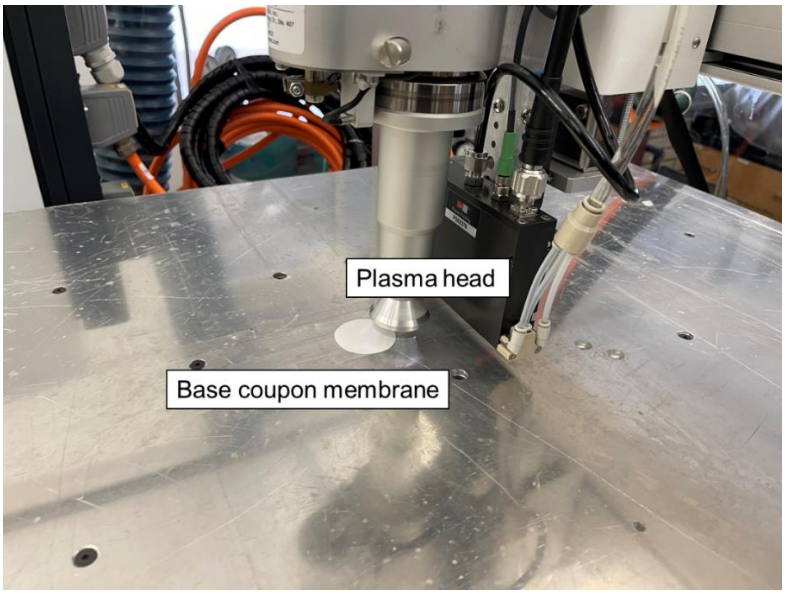

Figure C-11. Plasma membrane surface activation.

4. Press the ‘Off’ button on the plasma controller and turn off the system.

C.4. Graft polymerization

1. Prepare an aqueous acrylic acid (AA) monomer solution (of a total volume of 100 mL) in a glass jar (235 mL capacity) using acrylic acid and D.I. water (**Figure C-12**). Adjust the solution pH as needed by adding sodium hydroxide.

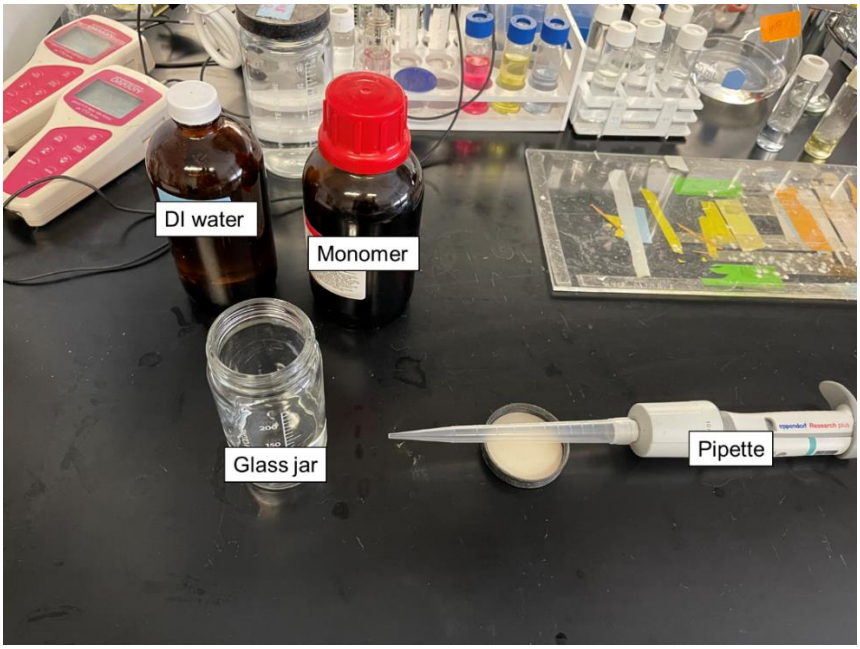

Figure C-12. Preparation of monomer solution for AA graft polymerization.

2. Place the plasma treated coupon membrane together with a Teflon PTFE rod in the monomer containing jar (**Figure C-13**). The membrane coupon is fully immersed in the monomer solution.

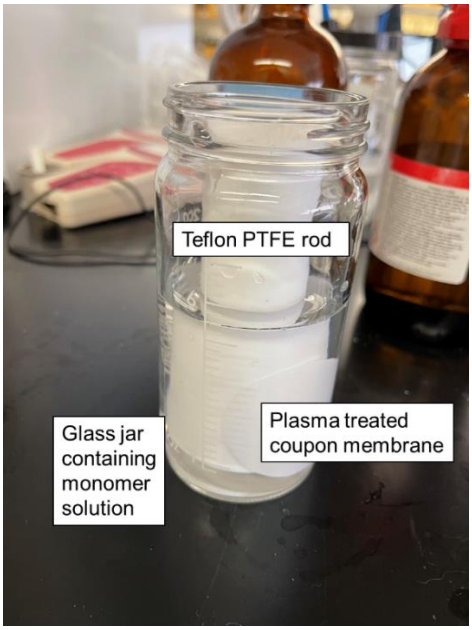

Figure C-13. Immerse the plasma treated membrane into the monomer solution.

3. Cover the glass jar with the jar lid which is connected to a nitrogen source. Immerse the jar containing the membrane-wrapped rod and nitrogen line in a temperature-controlled water bath to initiate graft polymerization (**Figure C-14**). Leave the jar in the water bath for the duration of the graft polymerization reaction.

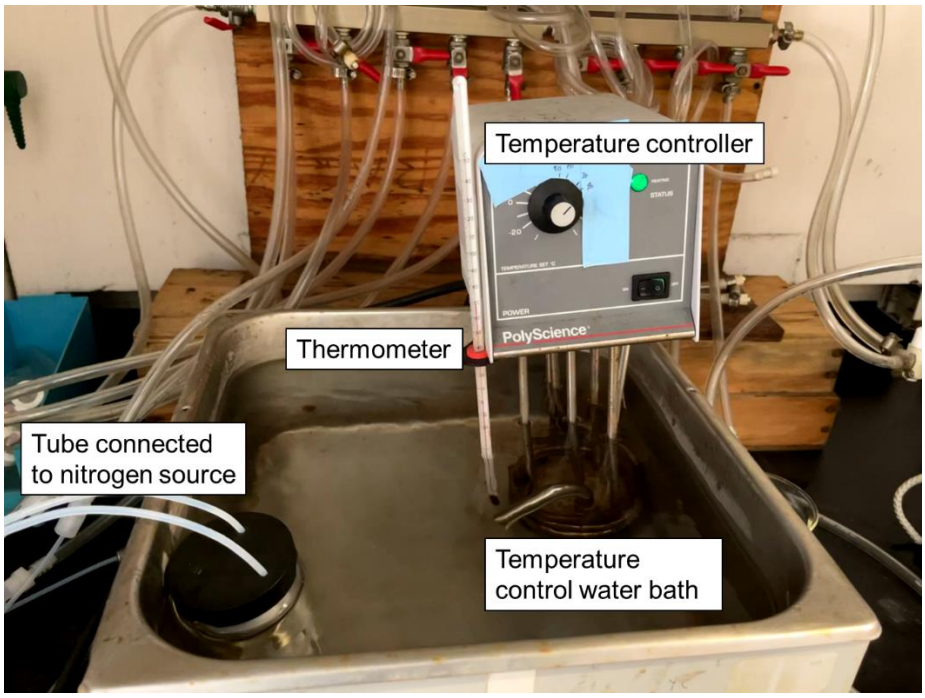

Figure C-14. Water bath for AA graft polymerization.

4. Terminate the graft polymerization by disposing of the monomer solution and rinsing the membrane coupon surface thoroughly with D.I. water.

D. Dead-end stirred-cell UF system

1. Fill the feed tank and place the coupon membrane (with the active side facing up under the O-ring) into the UF stirred cell (**Figure D-1**).

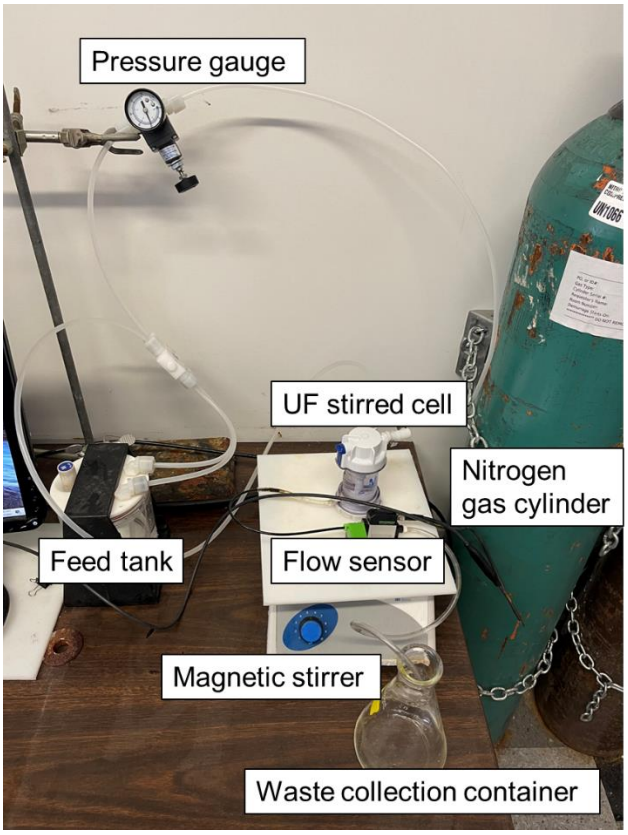

Figure D-1. The UF stirred cell system.

2. Open the nitrogen (99.5% purity) cylinder and control the feed pressure (0-50 psi) by adjusting the pressure gauge. Turn on the magnetic stirrer to rank 3.
3. Open the software 'SENSIRION', select 'Liquid Flow Sensor' for Sensor Product, 'RS485/USB Sensor Cable' for COM Hardware, and 'COM3' for the COM Port Settings. Press 'OK' (**Figure D-2**).

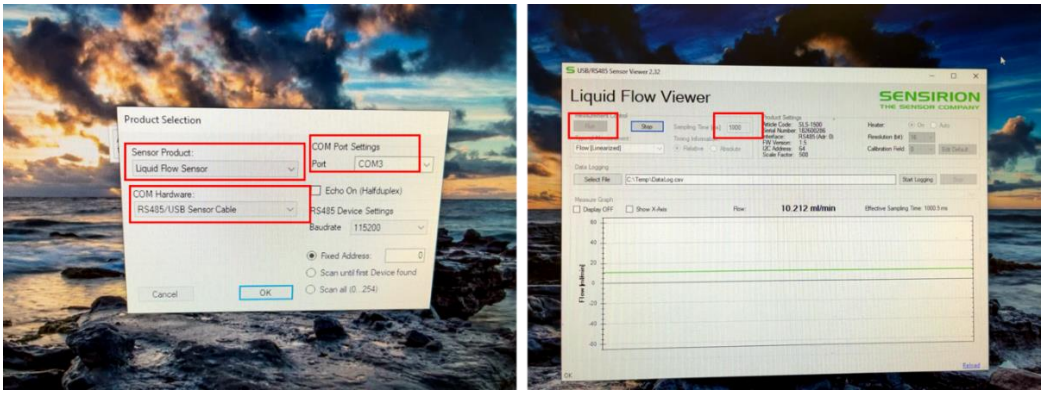

Figure D-2. Set up the SENSIRION software.

4. Input ‘1000’ for the Sampling Time [ms] and press ‘Run’ to start measuring the permeate flow rate.
5. To measure membrane rejection or *MWCO*, permeate sample was collected by replacing the waste collection container with a glass vial (**Figure D-3**).

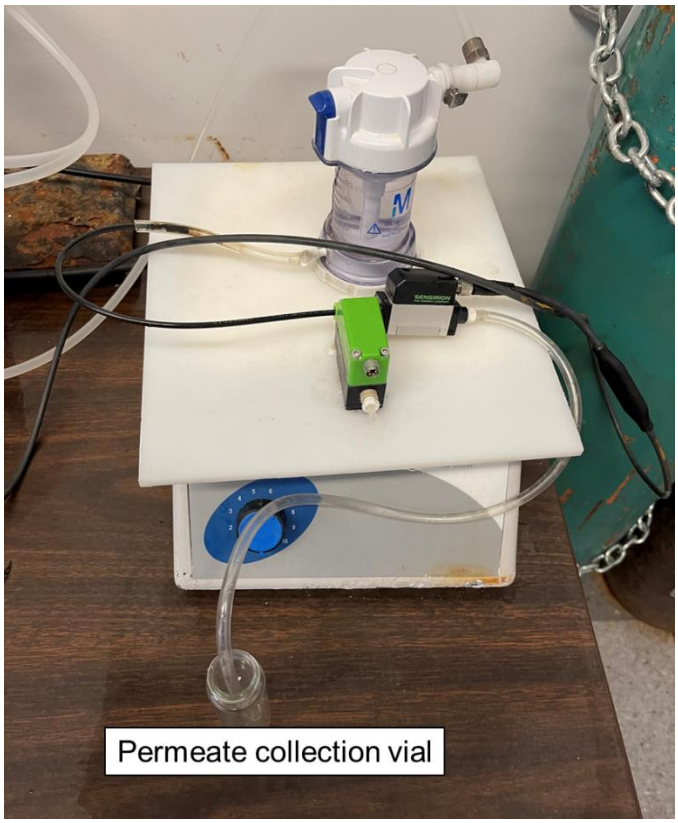

Figure D-3. System setup for collecting permeate sample.

References

[1] R.W. Baker, Membrane technology and applications, John Wiley & Sons2012.

[2] C. Fritzmann, J. Löwenberg, T. Wintgens, T. Melin, State-of-the-art of reverse osmosis desalination, Desalination 216(1-3) (2007) 1-76.

[3] N. Wang, T. Wang, Y. Hu, Tailoring membrane surface properties and ultrafiltration performances via the self-assembly of polyethylene glycol-block-polysulfone-block-polyethylene glycol block copolymer upon thermal and solvent annealing, ACS applied materials & interfaces 9(36) (2017) 31018-31030.

[4] A. Saxena, B.P. Tripathi, M. Kumar, V.K. Shahi, Membrane-based techniques for the separation and purification of proteins: An overview, Advances in colloid and interface science 145(1-2) (2009) 1-22.

[5] A.-S. Jönsson, G. Trägårdh, Ultrafiltration applications, Desalination 77 (1990) 135-179.

[6] L.J. Zeman, A.L. Zydney, Microfiltration and ultrafiltration: principles and applications, CRC Press2017.

[7] N. Prihasto, Q.-F. Liu, S.-H. Kim, Pre-treatment strategies for seawater desalination by reverse osmosis system, Desalination 249(1) (2009) 308-316.

[8] S. Li, S.G. Heijman, J. Verberk, G.L. Amy, J.C. Van Dijk, Seawater ultrafiltration fouling control: Backwashing with demineralized water/SWRO permeate, Separation and purification technology 98 (2012) 327-336.

[9] H.B. Park, J. Kamcev, L.M. Robeson, M. Elimelech, B.D. Freeman, Maximizing the right stuff: The trade-off between membrane permeability and selectivity, Science 356(6343) (2017).

[10] S. Wang, Y. Zhou, C. Gao, Novel high boron removal polyamide reverse osmosis membranes, Journal of Membrane Science 554 (2018) 244-252.

[11] A. Ghaee, M. Zerafat, P. Askari, S. Sabbaghi, B. Sadatnia, Fabrication of polyamide thin-film nanocomposite membranes with enhanced surface charge for nitrate ion removal from water resources, Environmental technology 38(6) (2017) 772-781.

[12] M.T. Uddin, M.S.I. Mozumder, A. Figoli, M.A. Islam, E. Drioli, Arsenic removal by conventional and membrane technology: an overview, (2007).

[13] H. Koseoglu, N. Kabay, M. Yüksel, S. Sarp, Ö. Arar, M. Kitis, Boron removal from seawater using high rejection SWRO membranes—impact of pH, feed concentration, pressure, and cross-flow velocity, Desalination 227(1-3) (2008) 253-263.

[14] M. Busch, W.E. Mickols, S. Jons, J. Redondo, J. De Witte, Boron removal in sea water desalination, International Desalination and Water Reuse Quarterly 13(4) (2004) 25.
[15] Y. Xu, J.-Q. Jiang, Technologies for boron removal, Industrial & Engineering Chemistry Research 47(1) (2008) 16-24.
[16] Y.J. Lim, K. Goh, M. Kurihara, R. Wang, Seawater desalination by reverse osmosis: Current development and future challenges in membrane fabrication–A review, Journal of Membrane Science (2021) 119292.
[17] L.F. Greenlee, D.F. Lawler, B.D. Freeman, B. Marrot, P. Moulin, Reverse osmosis desalination: water sources, technology, and today's challenges, Water research 43(9) (2009) 2317-2348.
[18] A. Matin, F. Rahman, H.Z. Shafi, S.M. Zubair, Scaling of reverse osmosis membranes used in water desalination: Phenomena, impact, and control; future directions, Desalination 455 (2019) 135-157.
[19] S. Zhao, L. Zou, D. Mulcahy, Brackish water desalination by a hybrid forward osmosis–nanofiltration system using divalent draw solute, Desalination 284 (2012) 175-181.
[20] H.M. Hegab, L. Zou, Graphene oxide-assisted membranes: fabrication and potential applications in desalination and water purification, Journal of Membrane Science 484 (2015) 95-106.
[21] A. Rahardianto, W.-Y. Shih, R.-W. Lee, Y. Cohen, Diagnostic characterization of gypsum scale formation and control in RO membrane desalination of brackish water, Journal of membrane Science 279(1-2) (2006) 655-668.
[22] D.L. Shaffer, M.E. Tousley, M. Elimelech, Influence of polyamide membrane surface chemistry on gypsum scaling behavior, Journal of membrane science 525 (2017) 249-256.
[23] K.G. Tay, L. Song, A more effective method for fouling characterization in a full-scale reverse osmosis process, Desalination 177(1-3) (2005) 95-107.
[24] J. Fei, W. Mai, P.S. Cheng, J. Shi, Z. Liu, Q. She, Membrane structure-dependent limiting flux behavior and membrane selectivity loss during gypsum scaling: Implications for pressure-retarded osmosis operation and membrane design, Desalination 492 (2020) 114644.
[25] H. Jaramillo, C. Boo, S.M. Hashmi, M. Elimelech, Zwitterionic coating on thin-film composite membranes to delay gypsum scaling in reverse osmosis, Journal of Membrane Science 618 (2021) 118568.

[26] M. Liu, C. Yu, Y. Wu, Z. Lü, S. Yu, C. Gao, In situ modification of polyamide reverse osmosis membrane module for improved fouling resistance, Chemical Engineering Research and Design 141 (2019) 402-412.
[27] S.S. Bucs, N. Farhat, J.C. Kruithof, C. Picioreanu, M.C. van Loosdrecht, J.S. Vrouwenvelder, Review on strategies for biofouling mitigation in spiral wound membrane systems, Desalination 434 (2018) 189-197.
[28] C. Sun, X. Feng, Enhancing the performance of PVDF membranes by hydrophilic surface modification via amine treatment, Separation and Purification Technology 185 (2017) 94-102.
[29] K. Reid, M. Dixon, C. Pelekani, K. Jarvis, M. Willis, Y. Yu, Biofouling control by hydrophilic surface modification of polypropylene feed spacers by plasma polymerisation, Desalination 335(1) (2014) 108-118.
[30] D. Ghernaout, A. El-Wakil, Requiring Reverse Osmosis Membranes Modifications—An Overview, American Journal of Chemical Engineering 5(4) (2017) 81-88.
[31] M. Jafari, M. Vanoppen, J. van Agtmaal, E. Cornelissen, J.S. Vrouwenvelder, A. Verliefde, M. van Loosdrecht, C. Picioreanu, Cost of fouling in full-scale reverse osmosis and nanofiltration installations in the Netherlands, Desalination 500 (2021) 114865.
[32] T. Tsuyuhara, Y. Hanamoto, T. Miyoshi, K. Kimura, Y. Watanabe, Influence of membrane properties on physically reversible and irreversible fouling in membrane bioreactors, Water Science and Technology 61(9) (2010) 2235-2240.
[33] G. Crozes, J. Jacangelo, C. Anselme, J. Laine, Impact of ultrafiltration operating conditions on membrane irreversible fouling, Journal of Membrane Science 124(1) (1997) 63-76.
[34] P. Blanpain-Avet, J. Migdal, T. Bénézech, The effect of multiple fouling and cleaning cycles on a tubular ceramic microfiltration membrane fouled with a whey protein concentrate: membrane performance and cleaning efficiency, Food and bioproducts processing 82(3) (2004) 231-243.
[35] W. Gao, H. Liang, J. Ma, M. Han, Z.-l. Chen, Z.-s. Han, G.-b. Li, Membrane fouling control in ultrafiltration technology for drinking water production: A review, Desalination 272(1-3) (2011) 1-8.
[36] T. Tong, A.F. Wallace, S. Zhao, Z. Wang, Mineral scaling in membrane desalination: Mechanisms, mitigation strategies, and feasibility of scaling-resistant membranes, Journal of membrane science 579 (2019) 52-69.

[37] V. Karanikola, C. Boo, J. Rolf, M. Elimelech, Engineered slippery surface to mitigate gypsum scaling in membrane distillation for treatment of hypersaline industrial wastewaters, Environmental science & technology 52(24) (2018) 14362-14370.
[38] N.W. Kang, S. Lee, D. Kim, S. Hong, J.H. Kweon, Analyses of calcium carbonate scale deposition on four RO membranes under a seawater desalination condition, Water Science and Technology 64(8) (2011) 1573-1580.
[39] R.H. Hailemariam, Y.C. Woo, M.M. Damtie, B.C. Kim, K.-D. Park, J.-S. Choi, Reverse osmosis membrane fabrication and modification technologies and future trends: a review, Advances in colloid and interface science 276 (2020) 102100.
[40] H. Adib, A. Raisi, Surface modification of a PES membrane by corona air plasma-assisted grafting of HB-PEG for separation of oil-in-water emulsions, RSC Advances 10(29) (2020) 17143-17153.
[41] Z.-M. Liu, Z.-K. Xu, L.-S. Wan, J. Wu, M. Ulbricht, Surface modification of polypropylene microfiltration membranes by the immobilization of poly (N-vinyl-2-pyrrolidone): a facile plasma approach, Journal of membrane science 249(1-2) (2005) 21-31.
[42] S. Afkham, A. Raisi, A. Aroujalian, Reducing fouling of polyethersulfone microfiltration membranes by corona air plasma, Desalination and Water Treatment 57(56) (2016) 26976-26992.
[43] D. Ankoliya, B. Mehta, H. Raval, Advances in surface modification techniques of reverse osmosis membrane over the years, Separation Science and Technology 54(3) (2019) 293-310.
[44] M. Buonomenna, Nano-enhanced reverse osmosis membranes, Desalination 314 (2013) 73-88.
[45] Y. Cohen, N. Lin, K.J. Varin, D. Chien, R.F. Hicks, Membrane surface nanostructuring with terminally anchored polymer chains, Functional nanostructured materials and membranes for water treatment (2013) 85-124.
[46] Y. Chen, M. Rovira-Bru, F. Giralt, Y. Cohen, Hydraulic Resistance and Protein Fouling Resistance of a Zirconia Membrane with a Tethered PVP Layer, Water 13(7) (2021) 951.
[47] N.H. Lin, M.-m. Kim, G.T. Lewis, Y. Cohen, Polymer surface nano-structuring of reverse osmosis membranes for fouling resistance and improved flux performance, Journal of Materials Chemistry 20(22) (2010) 4642-4652.
[48] K.J. Moses, Y. Cohen, Wettability of terminally anchored polymer brush layers on a polyamide surface, Journal of colloid and interface science 436 (2014) 286-295.

[49] S. Kim, A. Rahardianto, J.S. Walker, T. Wolfe, K. Coleman, Y. Cohen, Upgrading polyamide TFC BWRO and SWRO membranes to higher SWRO membrane performance via surface nano-structuring with tethered poly (acrylic acid), Journal of Membrane Science 597 (2020) 117736.
[50] M. Wang, Q.-F. An, L.-G. Wu, J.-X. Mo, C.-J. Gao, Preparation of pH-responsive phenolphthalein poly (ether sulfone) membrane by redox-graft pore-filling polymerization technique, Journal of membrane science 287(2) (2007) 257-263.
[51] M.A. Abbas, S. Mushtaq, W.A. Cheema, H. Qiblawey, S. Zhu, Y. Li, R. Zhang, H. Wu, Z. Jiang, R. Sadiq, Surface Modification of TFC-PA RO Membrane by Grafting Hydrophilic pH Switchable Poly (Acrylic Acid) Brushes, Advances in Polymer Technology 2020 (2020).
[52] H. Liu, S. Yang, Y. Liu, M. Miao, Y. Zhao, A. Sotto, C. Gao, J. Shen, Fabricating a pH-responsive membrane through interfacial in-situ assembly of microgels for water gating and self-cleaning, Journal of Membrane Science 579 (2019) 230-239.
[53] D. Wandera, S.R. Wickramasinghe, S.M. Husson, Stimuli-responsive membranes, Journal of Membrane Science 357(1-2) (2010) 6-35.
[54] S. Kim, Y. Cohen, K.J. Moses, S. Sharma, M. Bilal, Polysulfone surface nano-structured with tethered polyacrylic acid, Applied Surface Science 470 (2019) 411-422.
[55] Y. He, K. Xu, X. Feng, L. Chen, Z. Jiang, A nonionic polymer-brush-grafted PVDF membrane to analyse fouling during the filtration of oil/water emulsions, Journal of Membrane Science 637 (2021) 119644.
[56] Y. Cohen, G.T. Lewis, Atmospheric pressure plasma-induced graft polymerization, Google Patents, 2015.
[57] M. Gu, J.E. Kilduff, G. Belfort, High throughput atmospheric pressure plasma-induced graft polymerization for identifying protein-resistant surfaces, Biomaterials 33(5) (2012) 1261-1270.
[58] Q. Li, J. Imbrogno, G. Belfort, X.L. Wang, Making polymeric membranes antifouling via “grafting from” polymerization of zwitterions, Journal of Applied Polymer Science 132(21) (2015).
[59] J.-F. Jhong, A. Venault, C.-C. Hou, S.-H. Chen, T.-C. Wei, J. Zheng, J. Huang, Y. Chang, Surface zwitterionization of expanded poly (tetrafluoroethylene) membranes via atmospheric plasma-induced polymerization for enhanced skin wound healing, ACS applied materials & interfaces 5(14) (2013) 6732-6742.
[60] N. Hilal, M. Khayet, C.J. Wright, Membrane modification: Technology and applications, CRC press2012.

[61] S. Gassara, W. Chinpa, D. Quemener, R.B. Amar, A. Deratani, Pore size tailoring of poly (ether imide) membrane from UF to NF range by chemical post-treatment using aminated oligomers, Journal of membrane science 436 (2013) 36-46.
[62] V. Moghimifar, A. Raisi, A. Aroujalian, Surface modification of polyethersulfone ultrafiltration membranes by corona plasma-assisted coating TiO2 nanoparticles, Journal of Membrane Science 461 (2014) 69-80.
[63] A.R. Kavaiya, H.D. Raval, Highly selective and antifouling reverse osmosis membrane by crosslinkers induced surface modification, Environmental Technology (2021) 1-12.
[64] Q. Li, Q.-y. Bi, H.-H. Lin, L.-X. Bian, X.-L. Wang, A novel ultrafiltration (UF) membrane with controllable selectivity for protein separation, Journal of Membrane Science 427 (2013) 155-167.
[65] P.D. Peeva, N. Million, M. Ulbricht, Factors affecting the sieving behavior of anti-fouling thin-layer cross-linked hydrogel polyethersulfone composite ultrafiltration membranes, Journal of Membrane Science 390 (2012) 99-112.
[66] M. Reig, N. Pagès, E. Licon, C. Valderrama, O. Gibert, A. Yaroshchuk, J.L. Cortina, Evolution of electrolyte mixtures rejection behaviour using nanofiltration membranes under spiral wound and flat-sheet configurations, Desalination and Water Treatment 56(13) (2015) 3519-3529.
[67] L. Upadhyaya, X. Qian, S.R. Wickramasinghe, Chemical modification of membrane surface—overview, Current opinion in chemical engineering 20 (2018) 13-18.
[68] S. Lee, Performance Comparison of Spiral-Wound and Plate-and-Frame Forward Osmosis Membrane Module, Membranes 10(11) (2020) 318.
[69] M. Abdel-Hameed, M.M.A. ElFadl, M.E. Ali, Y.H. Kotp, H.A. Shawky, Effect of manufacture conditions on reverse osmosis desalination performance of polyamide thin film composite membrane and their spiral wound element, Presented at the EDS conference on Desalination for the Environment: Clean Water and Energy, 2016, p. 26.
[70] D.W. Solutions, Filmtec™ Reverse Osmosis Membranes, Technical Manual, Form 399(609-00071) (2010) 1-180.
[71] H. Cooley, P.H. Gleick, G. Wolff, Desalination, with a grain of salt, Pacific Institute. June (2006).

[72] G.M. Geise, H.B. Park, A.C. Sagle, B.D. Freeman, J.E. McGrath, Water permeability and water/salt selectivity tradeoff in polymers for desalination, Journal of Membrane Science 369(1-2) (2011) 130-138.
[73] Z. Yang, H. Guo, C.Y. Tang, The upper bound of thin-film composite (TFC) polyamide membranes for desalination, Journal of Membrane Science 590 (2019) 117297.
[74] D. Keeney, R.A. Olson, Sources of nitrate to ground water, Critical Reviews in Environmental Science and Technology 16(3) (1986) 257-304.
[75] M. Shrimali, K. Singh, New methods of nitrate removal from water, Environmental pollution 112(3) (2001) 351-359.
[76] J.Y. Choi, T. Lee, A.B. Aleidan, A. Rahardianto, M. Glickfeld, M.E. Kennedy, Y. Chen, P. Haase, C. Chen, Y. Cohen, On the feasibility of small communities wellhead RO treatment for nitrate removal and salinity reduction, Journal of environmental management 250 (2019) 109487.
[77] F. Edition, Guidelines for drinking-water quality, WHO chronicle 38(4) (2011) 104-108.
[78] Y.P. Tang, L. Luo, Z. Thong, T.S. Chung, Recent advances in membrane materials and technologies for boron removal, Journal of Membrane Science 541 (2017) 434-446.
[79] E. Güler, C. Kaya, N. Kabay, M. Arda, Boron removal from seawater: state-of-the-art review, Desalination 356 (2015) 85-93.
[80] A. Abejón, A. Garea, A. Irabien, Arsenic removal from drinking water by reverse osmosis: Minimization of costs and energy consumption, Separation and Purification Technology 144 (2015) 46-53.
[81] K.-S. Ng, Z. Ujang, P. Le-Clech, Arsenic removal technologies for drinking water treatment, Reviews in Environmental Science and Biotechnology 3(1) (2004) 43-53.
[82] R.N. Ratnaike, Acute and chronic arsenic toxicity, Postgraduate medical journal 79(933) (2003) 391-396.
[83] M.F. Hughes, Arsenic toxicity and potential mechanisms of action, Toxicology letters 133(1) (2002) 1-16.
[84] A.H. Smith, P.A. Lopipero, M.N. Bates, C.M. Steinmaus, Arsenic epidemiology and drinking water standards, American Association for the Advancement of Science, 2002, pp. 2145-2146.
[85] R.Y. Ning, Arsenic removal by reverse osmosis, Desalination 143(3) (2002) 237-241.
[86] J. Bohdziewicz, M. Bodzek, E. Wąsik, The application of reverse osmosis and nanofiltration to the removal of nitrates from groundwater, Desalination 121(2) (1999) 139-147.

[87] L.A. Richards, M. Vuachère, A.I. Schäfer, Impact of pH on the removal of fluoride, nitrate and boron by nanofiltration/reverse osmosis, Desalination 261(3) (2010) 331-337.
[88] K. Häyrynen, E. Pongrácz, V. Väisänen, N. Pap, M. Mänttäri, J. Langwaldt, R.L. Keiski, Concentration of ammonium and nitrate from mine water by reverse osmosis and nanofiltration, Desalination 240(1-3) (2009) 280-289.
[89] Y.-H. Kim, E.-D. Hwang, W. Shin, J.-H. Choi, T. Ha, S. Choi, Treatments of stainless steel wastewater containing a high concentration of nitrate using reverse osmosis and nanomembranes, Desalination 202(1-3) (2007) 286-292.
[90] J. Schoeman, A. Steyn, Nitrate removal with reverse osmosis in a rural area in South Africa, Desalination 155(1) (2003) 15-26.
[91] J.N. Cevaal, W.B. Suratt, J.E. Burke, Nitrate removal and water quality improvements with reverse osmosis for Brighton, Colorado, Desalination 103(1-2) (1995) 101-111.
[92] R. Rautenbach, W. Kopp, G. Van Opbergen, R. Hellekes, Nitrate reduction of well water by reverse osmosis and electrodialysis-studies on plant performance and costs, Desalination 65 (1987) 241-258.
[93] S.K. Sharma, R.C. Sobti, Nitrate removal from ground water: a review, E-Journal of Chemistry 9(4) (2012) 1667-1675.
[94] J.J. Schoeman, Nitrate-nitrogen removal with small-scale reverse osmosis, electrodialysis and ion-exchange units in rural areas, water SA 35(5) (2009).
[95] A.C.-T. Chiang, J. Chun-Te Lin, D.R. Wijayanti, D.-J. Lee, Boron removal with UTC-series reverse osmosis filtration, Journal of the Taiwan Institute of Chemical Engineers 44(2) (2013) 317-321.
[96] A. Farhat, F. Ahmad, N. Hilal, H.A. Arafat, Boron removal in new generation reverse osmosis (RO) membranes using two-pass RO without pH adjustment, Desalination 310 (2013) 50-59.
[97] E. Guler, D. Ozakdag, M. Arda, M. Yuksel, N. Kabay, Effect of temperature on seawater desalination-water quality analyses for desalinated seawater for its use as drinking and irrigation water, Environmental geochemistry and health 32(4) (2010) 335-339.
[98] E. Güler, N. Kabay, M. Yüksel, E. Yavuz, Ü. Yüksel, A comparative study for boron removal from seawater by two types of polyamide thin film composite SWRO membranes, Desalination 273(1) (2011) 81-84.

[99] C. Dominguez-Tagle, V.J. Romero-Ternero, A.M. Delgado-Torres, Boron removal efficiency in small seawater Reverse Osmosis systems, Desalination 265(1-3) (2011) 43-48.
[100] M. Taniguchi, Y. Fusaoka, T. Nishikawa, M. Kurihara, Boron removal in RO seawater desalination, Desalination 167 (2004) 419-426.
[101] B. Teychene, G. Collet, H. Gallard, J.-P. Croue, A comparative study of boron and arsenic (III) rejection from brackish water by reverse osmosis membranes, Desalination 310 (2013) 109-114.
[102] H. Elcik, S.O. Celik, M. Cakmakci, B. Özkaya, Performance of nanofiltration and reverse osmosis membranes for arsenic removal from drinking water, Desalination and Water Treatment 57(43) (2016) 20422-20429.
[103] I. Akin, G. Arslan, A. Tor, Y. Cengeloglu, M. Ersoz, Removal of arsenate [As (V)] and arsenite [As (III)] from water by SWHR and BW-30 reverse osmosis, Desalination 281 (2011) 88-92.
[104] M. Kang, M. Kawasaki, S. Tamada, T. Kamei, Y. Magara, Effect of pH on the removal of arsenic and antimony using reverse osmosis membranes, Desalination 131(1-3) (2000) 293-298.
[105] P. Brandhuber, G. Amy, Alternative methods for membrane filtration of arsenic from drinking water, Desalination 117(1-3) (1998) 1-10.
[106] L. Song, M. Elimelech, Theory of concentration polarization in crossflow filtration, Journal of the Chemical Society, Faraday Transactions 91(19) (1995) 3389-3398.
[107] J. Benecke, M. Haas, F. Baur, M. Ernst, Investigating the development and reproducibility of heterogeneous gypsum scaling on reverse osmosis membranes using real-time membrane surface imaging, Desalination 428 (2018) 161-171.
[108] M.-m. Kim, N.H. Lin, G.T. Lewis, Y. Cohen, Surface nano-structuring of reverse osmosis membranes via atmospheric pressure plasma-induced graft polymerization for reduction of mineral scaling propensity, Journal of Membrane Science 354(1-2) (2010) 142-149.
[109] Q. Liu, G.-R. Xu, R. Das, Inorganic scaling in reverse osmosis (RO) desalination: Mechanisms, monitoring, and inhibition strategies, Desalination 468 (2019) 114065.
[110] W. Guo, H.-H. Ngo, J. Li, A mini-review on membrane fouling, Bioresource technology 122 (2012) 27-34.
[111] F. Rahman, Z. Amjad, 14 Scale Formation and Control in Thermal Desalination Systems, (2010).

[112] S. Lee, C.-H. Lee, Effect of operating conditions on CaSO4 scale formation mechanism in nanofiltration for water softening, Water Research 34(15) (2000) 3854-3866.
[113] P. Zhang, J. Hu, W. Li, H. Qi, Research progress of brackish water desalination by reverse osmosis, (2013).
[114] B.L. Pangarkar, M.G. Sane, M. Guddad, Reverse osmosis and membrane distillation for desalination of groundwater: a review, International Scholarly Research Notices 2011 (2011).
[115] T. Qiu, P.A. Davies, Comparison of configurations for high-recovery inland desalination systems, Water 4(3) (2012) 690-706.
[116] S. Jiang, Y. Li, B.P. Ladewig, A review of reverse osmosis membrane fouling and control strategies, Science of the Total Environment 595 (2017) 567-583.
[117] Z. Ali, Y. Al Sunbul, F. Pacheco, W. Ogieglo, Y. Wang, G. Genduso, I. Pinnau, Defect-free highly selective polyamide thin-film composite membranes for desalination and boron removal, Journal of Membrane Science 578 (2019) 85-94.
[118] F. Peng, Z. Jiang, E.M. Hoek, Tuning the molecular structure, separation performance and interfacial properties of poly (vinyl alcohol)–polysulfone interfacial composite membranes, Journal of Membrane Science 368(1-2) (2011) 26-33.
[119] Q. Wang, X. Wang, Z. Wang, J. Huang, Y. Wang, PVDF membranes with simultaneously enhanced permeability and selectivity by breaking the tradeoff effect via atomic layer deposition of TiO2, Journal of membrane science 442 (2013) 57-64.
[120] J. Wang, J. Wang, H. Wang, S. Zhang, Preparation and characterization of positively charged composite nanofiltration membranes by coating poly (ether ether ketone) containing quaternary ammonium groups on polysulfone ultrafiltration membranes, Journal of applied polymer science 127(3) (2013) 1601-1608.
[121] K. Parashuram, S. Maurya, H. Rana, P. Singh, P. Ray, A. Reddy, Tailoring the molecular weight cut off values of polyacrylonitrile based hollow fibre ultrafiltration membranes with improved fouling resistance by chemical modification, Journal of membrane science 425 (2013) 251-261.
[122] Y. Gu, U. Wiesner, Tailoring pore size of graded mesoporous block copolymer membranes: Moving from ultrafiltration toward nanofiltration, Macromolecules 48(17) (2015) 6153-6159.

[123] Y. Sui, Z. Wang, X. Gao, C. Gao, Antifouling PVDF ultrafiltration membranes incorporating PVDF-g-PHEMA additive via atom transfer radical graft polymerizations, Journal of membrane science 413 (2012) 38-47.
[124] H. Wu, B. Tang, P. Wu, Novel ultrafiltration membranes prepared from a multi-walled carbon nanotubes/polymer composite, Journal of Membrane Science 362(1-2) (2010) 374-383.
[125] M.E. Welch, C.K. Ober, Responsive and patterned polymer brushes, Journal of Polymer Science Part B: Polymer Physics 51(20) (2013) 1457-1472.
[126] S.T. Milner, Polymer brushes, Science 251(4996) (1991) 905-914.
[127] W.J. Brittain, S. Minko, A structural definition of polymer brushes, Journal of Polymer Science Part A: Polymer Chemistry 45(16) (2007) 3505-3512.
[128] S. Edmondson, V.L. Osborne, W.T. Huck, Polymer brushes via surface-initiated polymerizations, Chemical society reviews 33(1) (2004) 14-22.
[129] B. Zhao, W.J. Brittain, Polymer brushes: surface-immobilized macromolecules, Progress in Polymer Science 25(5) (2000) 677-710.
[130] M. Ulbricht, Advanced functional polymer membranes, Polymer 47(7) (2006) 2217-2262.
[131] P.D. Peeva, T. Pieper, M. Ulbricht, Tuning the ultrafiltration properties of anti-fouling thin-layer hydrogel polyethersulfone composite membranes by suited crosslinker monomers and photo-grafting conditions, Journal of Membrane Science 362(1-2) (2010) 560-568.
[132] K. Akamatsu, W. Noto, H. Fukuzawa, A. Hara, S.-i. Nakao, Grafting of carboxybetaine polymers to polyethylene membranes via plasma graft polymerization to improve low-fouling properties and to tune the molecular weight cut-off, Separation and Purification Technology 204 (2018) 298-303.
[133] M. Ulbricht, G. Belfort, Surface modification of ultrafiltration membranes by low temperature plasma II. Graft polymerization onto polyacrylonitrile and polysulfone, Journal of Membrane Science 111(2) (1996) 193-215.
[134] A. Bhattacharya, B. Misra, Grafting: a versatile means to modify polymers: techniques, factors and applications, Progress in polymer science 29(8) (2004) 767-814.
[135] B. Gesner, P. Kelleher, Thermal and photo-oxidation of polysulfone, Journal of Applied Polymer Science 12(5) (1968) 1199-1208.

[136] S.-i. Kuroda, A. Nagura, K. Horie, I. Mita, Degradation of aromatic polymers—III. Crosslinking and chain scission during photodegradation of polysulphones, European polymer journal 25(6) (1989) 621-627.
[137] Y. Wang, J.-H. Kim, K.-H. Choo, Y.-S. Lee, C.-H. Lee, Hydrophilic modification of polypropylene microfiltration membranes by ozone-induced graft polymerization, Journal of Membrane Science 169(2) (2000) 269-276.
[138] W. Li, P. Liu, H. Zou, P. Fan, W. Xu, pH sensitive microporous polypropylene membrane prepared through ozone induced surface grafting, Polymers for Advanced Technologies 20(3) (2009) 251-257.
[139] G.T. Lewis, G.R. Nowling, R.F. Hicks, Y. Cohen, Inorganic surface nanostructuring by atmospheric pressure plasma-induced graft polymerization, Langmuir 23(21) (2007) 10756-10764.
[140] H.-Y. Yu, L.-Q. Liu, Z.-Q. Tang, M.-G. Yan, J.-S. Gu, X.-W. Wei, Surface modification of polypropylene microporous membrane to improve its antifouling characteristics in an SMBR: Air plasma treatment, Journal of Membrane Science 311(1-2) (2008) 216-224.
[141] H. Chen, G. Belfort, Surface modification of poly (ether sulfone) ultrafiltration membranes by low-temperature plasma-induced graft polymerization, Journal of Applied Polymer Science 72(13) (1999) 1699-1711.
[142] M. Bryjak, I. Gancarz, A. Krajciewicz, J. Pigłowski, Air plasma treatment of polyacrylonitrile porous membrane, Die Angewandte Makromolekulare Chemie: Applied Macromolecular Chemistry and Physics 234(1) (1996) 21-29.
[143] M. Bryjak, I. Gancarz, Plasma treatment of polyethylene ultrafiltration membranes, Die Angewandte Makromolekulare Chemie: Applied Macromolecular Chemistry and Physics 219(1) (1994) 117-124.
[144] H.-Y. Yu, Z.-K. Xu, Y.-J. Xie, Z.-M. Liu, S.-Y. Wang, Flux enhancement for polypropylene microporous membrane in a SMBR by the immobilization of poly (N-vinyl-2-pyrrolidone) on the membrane surface, Journal of membrane science 279(1-2) (2006) 148-155.
[145] H. Iwata, T. Matsuda, Preparation and properties of novel environment-sensitive membranes prepared by graft polymerization onto a porous membrane, Journal of membrane science 38(2) (1988) 185-199.

[146] I. Sadeghi, A. Aroujalian, A. Raisi, B. Dabir, M. Fathizadeh, Surface modification of polyethersulfone ultrafiltration membranes by corona air plasma for separation of oil/water emulsions, Journal of Membrane Science 430 (2013) 24-36.
[147] V. Dryakhlov, M.Y. Nikitina, I. Shaikhiev, M. Galikhanov, T. Shaikhiev, B. Bonev, Effect of parameters of the corona discharge treatment of the surface of polyacrylonitrile membranes on the separation efficiency of oil-in-water emulsions, Surface Engineering and Applied Electrochemistry 51(4) (2015) 406-411.
[148] S. Afkham, A. Aroujalian, A. Raisi, Fabrication of antimicrobial polyethersulfone microfiltration membranes by corona plasma-assisted coating of silver nanoparticles, RSC advances 6(109) (2016) 108113-108124.
[149] L.-P. Zhu, B.-K. Zhu, L. Xu, Y.-X. Feng, F. Liu, Y.-Y. Xu, Corona-induced graft polymerization for surface modification of porous polyethersulfone membranes, Applied surface science 253(14) (2007) 6052-6059.
[150] H. Guo, C. Geng, Z. Qin, C. Chen, Hydrophilic modification of HDPE microfiltration membrane by corona-induced graft polymerization, Desalination and Water Treatment 51(19-21) (2013) 3810-3813.
[151] P. Salimi, A. Aroujalian, D. Iranshahi, Graft copolymerization of zwitterionic monomer on the polyethersulfone membrane surface by corona air plasma for separation of oily wastewater, Separation and Purification Technology 258 (2021) 117939.
[152] L. Hui, E. Whiteway, M. Hilke, A. Turak, Effect of post-annealing on the plasma etching of graphene-coated-copper, Faraday discussions 173 (2014) 79-93.
[153] S. Dmitriev, L. Kravets, V. Sleptsov, Modification of track membrane structure by plasma etching, Nuclear Instruments and Methods in Physics Research Section B: Beam Interactions with Materials and Atoms 142(1-2) (1998) 43-49.
[154] C. Riccardi, R. Barni, E. Selli, G. Mazzone, M.R. Massafra, B. Marcandalli, G. Poletti, Surface modification of poly (ethylene terephthalate) fibers induced by radio frequency air plasma treatment, Applied surface science 211(1-4) (2003) 386-397.
[155] H.Y. Yu, X.C. He, L.Q. Liu, J.S. Gu, X.W. Wei, Surface modification of poly (propylene) microporous membrane to improve its antifouling characteristics in an SMBR: O2 plasma treatment, Plasma Processes and Polymers 5(1) (2008) 84-91.

[156] Y. Chen, S. Kim, Y. Cohen, Tuning the hydraulic permeability and molecular weight cutoff (MWCO) of surface nano-structured ultrafiltration membranes, Journal of Membrane Science 629 (2021) 119180.
[157] A. Schutze, J.Y. Jeong, S.E. Babayan, J. Park, G.S. Selwyn, R.F. Hicks, The atmospheric-pressure plasma jet: a review and comparison to other plasma sources, IEEE transactions on plasma science 26(6) (1998) 1685-1694.
[158] Y. Hwang, Y. Qiu, C. Zhang, B. Jarrard, R. Stedeford, J. Tsai, Y. Park, M. McCord, Effects of atmospheric pressure helium/air plasma treatment on adhesion and mechanical properties of aramid fibers, Journal of adhesion science and technology 17(6) (2003) 847-860.
[159] J. Park, I. Henins, H. Herrmann, G. Selwyn, J. Jeong, R. Hicks, D. Shim, C. Chang, An atmospheric pressure plasma source, Applied Physics Letters 76(3) (2000) 288-290.
[160] G. Wall, H. Podbielska, M. Wawrzynska, Functionalised Cardiovascular Stents, Woodhead Publishing2018.
[161] S. Ebnesajjad, C. Ebnesajjad, Surface treatment of materials for adhesive bonding, William Andrew2013.
[162] P.J. Bruggeman, F. Iza, R. Brandenburg, Foundations of atmospheric pressure non-equilibrium plasmas, Plasma Sources Science and Technology 26(12) (2017) 123002.
[163] S. Zhong, Surface modification of polypropylene microporous membrane by atmospheric-pressure plasma induced N-vinyl-2-pyrrolidone graft polymerization, Journal of Wuhan University of Technology-Mater. Sci. Ed. 27(2) (2012) 301-309.
[164] H.-L. Yang, J. Chun-Te Lin, C. Huang, Application of nanosilver surface modification to RO membrane and spacer for mitigating biofouling in seawater desalination, Water research 43(15) (2009) 3777-3786.
[165] J. Wang, Z. Wang, J. Wang, S. Wang, Improving the water flux and bio-fouling resistance of reverse osmosis (RO) membrane through surface modification by zwitterionic polymer, Journal of Membrane Science 493 (2015) 188-199.
[166] B.D. McCloskey, H.B. Park, H. Ju, B.W. Rowe, D.J. Miller, B.D. Freeman, A bioinspired fouling-resistant surface modification for water purification membranes, Journal of membrane science 413 (2012) 82-90.

[167] D.J. Miller, X. Huang, H. Li, S. Kasemset, A. Lee, D. Agnihotri, T. Hayes, D.R. Paul, B.D. Freeman, Fouling-resistant membranes for the treatment of flowback water from hydraulic shale fracturing: A pilot study, Journal of Membrane Science 437 (2013) 265-275.
[168] S. Shultz, V. Freger, In situ modification of membrane elements for improved boron rejection in RO desalination, Desalination 431 (2018) 66-72.
[169] S. Belfer, J. Gilron, Y. Purinson, R. Fainshtain, N. Daltrophe, M. Priel, B. Tenzer, A. Toma, Effect of surface modification in preventing fouling of commercial SWRO membranes at the Eilat seawater desalination pilot plant, Desalination 139(1-3) (2001) 169-176.
[170] R. Bernstein, S. Belfer, V. Freger, Improving performance of spiral wound RO elements by in situ concentration polarization-enhanced radical graft polymerization, Journal of membrane science 405 (2012) 79-84.
[171] K. Baransi-Karkaby, M. Bass, S. Levchenko, S. Eitan, V. Freger, Facile modification of reverse osmosis membranes by surfactant-assisted acrylate grafting for enhanced selectivity, Environmental science & technology 51(4) (2017) 2347-2354.
[172] K. Baransi-Karkaby, M. Bass, V. Freger, In situ modification of reverse osmosis membrane elements for enhanced removal of multiple micropollutants, Membranes 9(2) (2019) 28.
[173] S. Alexander, Polymer adsorption on small spheres. A scaling approach, Journal de physique 38(8) (1977) 977-981.
[174] P. Pincus, Excluded volume effects and stretched polymer chains, Macromolecules 9(3) (1976) 386-388.
[175] P. De Gennes, Scaling theory of polymer adsorption, Journal de physique 37(12) (1976) 1445-1452.
[176] P. De Gennes, Dynamics of entangled polymer solutions. I. The Rouse model, Macromolecules 9(4) (1976) 587-593.
[177] P.-G. De Gennes, P. Pincus, R. Velasco, F. Brochard, Remarks on polyelectrolyte conformation, Journal de physique 37(12) (1976) 1461-1473.
[178] P. Auroy, Y. Mir, L. Auvray, Local structure and density profile of polymer brushes, Physical review letters 69(1) (1992) 93.
[179] J. Rühe, W. Knoll, Functional polymer brushes, Journal of Macromolecular Science, Part C: Polymer Reviews 42(1) (2002) 91-138.

[180] R. Zhang, T. Zhou, H. Peng, M. Li, X. Zhu, Y. Yao, Nanostructured switchable pH-responsive membranes prepared via spherical polyelectrolyte brushes, Journal of Membrane Science 580 (2019) 117-124.
[181] Y.-F. Zhao, P.-B. Zhang, J. Sun, C.-J. Liu, L.-P. Zhu, Y.-Y. Xu, Electrolyte-responsive polyethersulfone membranes with zwitterionic polyethersulfone-based copolymers as additive, Journal of Membrane Science 510 (2016) 306-313.
[182] Y.-H. Chiao, S.-T. Chen, M. Sivakumar, M.B.M.Y. Ang, T. Patra, J. Almodovar, S.R. Wickramasinghe, W.-S. Hung, J.-Y. Lai, Zwitterionic polymer brush grafted on polyvinylidene difluoride membrane promoting enhanced ultrafiltration performance with augmented antifouling property, Polymers 12(6) (2020) 1303.
[183] D.M. Davenport, J. Lee, M. Elimelech, Efficacy of antifouling modification of ultrafiltration membranes by grafting zwitterionic polymer brushes, Separation and Purification Technology 189 (2017) 389-398.
[184] R. Bernstein, C.E. Singer, S.P. Singh, C. Mao, C.J. Arnusch, UV initiated surface grafting on polyethersulfone ultrafiltration membranes via ink-jet printing-assisted modification, Journal of Membrane Science 548 (2018) 73-80.
[185] T. Tripathi, M. Kamaz, S.R. Wickramasinghe, A. Sengupta, Designing Electric Field Responsive Ultrafiltration Membranes by Controlled Grafting of Poly (Ionic Liquid) Brush, International journal of environmental research and public health 17(1) (2020) 271.
[186] C. Liu, D. Song, W. Zhang, Q. He, X. Huangfu, S. Sun, Z. Sun, W. Cheng, J. Ma, Constructing zwitterionic polymer brush layer to enhance gravity-driven membrane performance by governing biofilm formation, Water research 168 (2020) 115181.
[187] C.J. Porter, J.R. Werber, C.L. Ritt, Y.-F. Guan, M. Zhong, M. Elimelech, Controlled grafting of polymer brush layers from porous cellulosic membranes, Journal of Membrane Science 596 (2020) 117719.
[188] B.M. Carter, A. Sengupta, X. Qian, M. Ulbricht, S.R. Wickramasinghe, Controlling external versus internal pore modification of ultrafiltration membranes using surface-initiated AGET-ATRP, Journal of Membrane Science 554 (2018) 109-116.
[189] S. Pourziad, M.R. Omidkhah, M. Abdollahi, Improved antifouling and self-cleaning ability of PVDF ultrafiltration membrane grafted with polymer brushes for oily water treatment, Journal of Industrial and Engineering Chemistry 83 (2020) 401-408.

[190] A. Sengupta, R. Wickramasinghe, Activator Generated Electron Transfer Combined Atom Transfer Radical Polymerization (AGET-ATRP) for Controlled Grafting Location of Glycidyl Methacrylate on Regenerated Cellulose Ultrafiltration Membranes, Journal of Membrane Science and Research 6(1) (2020) 90-98.
[191] T. Tong, S. Zhao, C. Boo, S.M. Hashmi, M. Elimelech, Relating silica scaling in reverse osmosis to membrane surface properties, Environmental science & technology 51(8) (2017) 4396-4406.
[192] R. Mushtaq, M.A. Abbas, S. Mushtaq, N.M. Ahmad, N.A. Khan, A.U. Khan, W. Hong, R. Sadiq, Z. Jiang, Antifouling and Flux Enhancement of Reverse Osmosis Membrane by Grafting Poly (3-Sulfopropyl Methacrylate) Brushes, Membranes 11(3) (2021) 213.
[193] Y. Wang, Z. Wang, J. Wang, S. Wang, Triple antifouling strategies for reverse osmosis membrane biofouling control, Journal of Membrane Science 549 (2018) 495-506.
[194] M. Liu, C. Yu, Z. Dong, P. Jiang, Z. Lü, S. Yu, C. Gao, Improved separation performance and durability of polyamide reverse osmosis membrane in tertiary treatment of textile effluent through grafting monomethoxy-poly (ethylene glycol) brushes, Separation and Purification Technology 209 (2019) 443-451.
[195] Z. Yang, D. Saeki, H. Matsuyama, Zwitterionic polymer modification of polyamide reverse-osmosis membranes via surface amination and atom transfer radical polymerization for anti-biofouling, Journal of Membrane Science 550 (2018) 332-339.
[196] U. Hirsch, M. Ruehl, N. Teuscher, A. Heilmann, Antifouling coatings via plasma polymerization and atom transfer radical polymerization on thin film composite membranes for reverse osmosis, Applied Surface Science 436 (2018) 207-216.
[197] N. Shtreimer Kandiyote, T. Avisdris, C.J. Arnusch, R. Kasher, Grafted polymer coatings enhance fouling inhibition by an antimicrobial peptide on reverse osmosis membranes, Langmuir 35(5) (2018) 1935-1943.
[198] W. Xie, A. Tiraferri, X. Ji, C. Chen, Y. Bai, J.C. Crittenden, B. Liu, Green and sustainable method of manufacturing anti-fouling zwitterionic polymers-modified poly (vinyl chloride) ultrafiltration membranes, Journal of Colloid and Interface Science 591 (2021) 343-351.
[199] Z. Liu, W. Wang, R. Xie, X.-J. Ju, L.-Y. Chu, Stimuli-responsive smart gating membranes, Chemical Society Reviews 45(3) (2016) 460-475.

[200] H. Alem, A.-S. Duwez, P. Lussis, P. Lipnik, A.M. Jonas, S. Demoustier-Champagne, Microstructure and thermo-responsive behavior of poly (N-isopropylacrylamide) brushes grafted in nanopores of track-etched membranes, Journal of Membrane Science 308(1-2) (2008) 75-86.
[201] S. Darvishmanesh, X. Qian, S.R. Wickramasinghe, Responsive membranes for advanced separations, Current Opinion in Chemical Engineering 8 (2015) 98-104.
[202] B.P. Tripathi, N.C. Dubey, F. Simon, M. Stamm, Thermo responsive ultrafiltration membranes of grafted poly (N-isopropyl acrylamide) via polydopamine, RSC advances 4(64) (2014) 34073-34083.
[203] M. Sinha, M. Purkait, Preparation and characterization of novel pegylated hydrophilic pH responsive polysulfone ultrafiltration membrane, Journal of Membrane Science 464 (2014) 20-32.
[204] B. Wu, X. Wang, J. Yang, Z. Hua, K. Tian, R. Kou, J. Zhang, S. Ye, Y. Luo, V.S. Craig, Reorganization of hydrogen bond network makes strong polyelectrolyte brushes pH-responsive, Science advances 2(8) (2016) e1600579.
[205] S. Xiao, Y. Zhang, M. Shen, F. Chen, P. Fan, M. Zhong, B. Ren, J. Yang, J. Zheng, Structural dependence of salt-responsive polyzwitterionic brushes with an anti-polyelectrolyte effect, Langmuir 34(1) (2018) 97-105.
[206] T. Chen, R. Ferris, J. Zhang, R. Ducker, S. Zauscher, Stimulus-responsive polymer brushes on surfaces: Transduction mechanisms and applications, Progress in Polymer Science 35(1-2) (2010) 94-112.
[207] M.D. Kurkuri, M.R. Nussio, A. Deslandes, N.H. Voelcker, Thermosensitive copolymer coatings with enhanced wettability switching, Langmuir 24(8) (2008) 4238-4244.
[208] Q. Shi, Y. Su, X. Ning, W. Chen, J. Peng, Z. Jiang, Graft polymerization of methacrylic acid onto polyethersulfone for potential pH-responsive membrane materials, Journal of Membrane Science 347(1-2) (2010) 62-68.
[209] Q. Ye, R. Wang, C. Chen, B. Chen, X. Zhu, High-Flux pH-Responsive Ultrafiltration Membrane for Efficient Nanoparticle Fractionation, ACS Applied Materials & Interfaces (2021).
[210] H.-Y. Yu, W. Li, J. Zhou, J.-S. Gu, L. Huang, Z.-Q. Tang, X.-W. Wei, Thermo-and pH-responsive polypropylene microporous membrane prepared by the photoinduced RAFT-mediated graft copolymerization, Journal of Membrane Science 343(1-2) (2009) 82-89.

[211] J.K. Shim, Y.B. Lee, Y.M. Lee, pH-dependent permeation through polysulfone ultrafiltration membranes prepared by ultraviolet polymerization technique, Journal of applied polymer science 74(1) (1999) 75-82.
[212] K. Fan, J. Huang, H. Yang, R. Lu, X. Sun, J. Hu, Z. Hou, pH and thermal-dependent ultrafiltration membranes prepared from poly (methacrylic acid) grafted onto polyethersulfone synthesized by simultaneous irradiation in homogenous phase, Journal of Membrane Science 543 (2017) 335-341.
[213] K. Gao, L.T. Kearney, R. Wang, J.A. Howarter, Enhanced wettability and transport control of ultrafiltration and reverse osmosis membranes with grafted polyelectrolytes, ACS applied materials & interfaces 7(44) (2015) 24839-24847.
[214] Y. Ito, Y. Ochiai, Y.S. Park, Y. Imanishi, pH-sensitive gating by conformational change of a polypeptide brush grafted onto a porous polymer membrane, Journal of the American Chemical Society 119(7) (1997) 1619-1623.
[215] M. Birkner, M. Ulbricht, Ultrafiltration membranes with markedly different pH-and ion-responsivity by photografted zwitterionic polysulfobetain or polycarbobetain, Journal of Membrane Science 494 (2015) 57-67.
[216] M. Gajda, M. Ulbricht, Capillary pore membranes with grafted diblock copolymers showing reversibly changing ultrafiltration properties with independent response to ions and temperature, Journal of Membrane Science 514 (2016) 510-517.
[217] X. Wang, D. Zhang, J. Wu, I. Protsak, S. Mao, C. Ma, M. Ma, M. Zhong, J. Tan, J. Yang, Novel Salt-Responsive SiO2@ Cellulose Membranes Promote Continuous Gradient and Adjustable Transport Efficiency, ACS Applied Materials & Interfaces 12(37) (2020) 42169-42178.
[218] Q. Yang, N. Adrus, F. Tomicki, M. Ulbricht, Composites of functional polymeric hydrogels and porous membranes, Journal of Materials Chemistry 21(9) (2011) 2783-2811.
[219] J. Meng, Z. Cao, L. Ni, Y. Zhang, X. Wang, X. Zhang, E. Liu, A novel salt-responsive TFC RO membrane having superior antifouling and easy-cleaning properties, Journal of Membrane Science 461 (2014) 123-129.
[220] M. You, P. Wang, M. Xu, T. Yuan, J. Meng, Fouling resistance and cleaning efficiency of stimuli-responsive reverse osmosis (RO) membranes, Polymer 103 (2016) 457-467.

[221] D.W. Chung, S. Higuchi, M. Maeda, S. Inoue, The pH-induced regulation of permselectivity of sugars by polymer membrane from polyvinyl-polypeptide graft copolymer, Journal of the American Chemical Society 108(19) (1986) 5823-5826.
[222] T. Hoang, G. Stevens, S. Kentish, The effect of feed pH on the performance of a reverse osmosis membrane, Desalination 261(1-2) (2010) 99-103.
[223] K.L. Tu, L.D. Nghiem, A.R. Chivas, Coupling effects of feed solution pH and ionic strength on the rejection of boron by NF/RO membranes, Chemical Engineering Journal 168(2) (2011) 700-706.
[224] G. Hagmeyer, R. Gimbel, Modelling the salt rejection of nanofiltration membranes for ternary ion mixtures and for single salts at different pH values, Desalination 117(1-3) (1998) 247-256.
[225] E.M. Van Wagner, A.C. Sagle, M.M. Sharma, B.D. Freeman, Effect of crossflow testing conditions, including feed pH and continuous feed filtration, on commercial reverse osmosis membrane performance, Journal of Membrane Science 345(1-2) (2009) 97-109.
[226] S. Bandini, J. Drei, D. Vezzani, The role of pH and concentration on the ion rejection in polyamide nanofiltration membranes, Journal of membrane science 264(1-2) (2005) 65-74.
[227] C. Bartels, R. Franks, S. Rybar, M. Schierach, M. Wilf, The effect of feed ionic strength on salt passage through reverse osmosis membranes, Desalination 184(1-3) (2005) 185-195.
[228] P. Fievet, A. Escoda, S. Bouranene, S. Déon, A. Szymczyk, Investigation of Dehydration and Pore Swelling Effects on the Transfer of PEG Through NF Membranes.
[229] S. Bouranene, A. Szymczyk, P. Fievet, A. Vidonne, Effect of salts on the retention of polyethyleneglycol by a nanofiltration ceramic membrane, Desalination 240(1-3) (2009) 94-98.
[230] J. Luo, Y. Wan, Effect of highly concentrated salt on retention of organic solutes by nanofiltration polymeric membranes, Journal of Membrane Science 372(1-2) (2011) 145-153.
[231] A. Escoda, P. Fievet, S. Lakard, A. Szymczyk, S. Déon, Influence of salts on the rejection of polyethyleneglycol by an NF organic membrane: Pore swelling and salting-out effects, Journal of Membrane Science 347(1-2) (2010) 174-182.
[232] A. Bouchoux, H. Roux-de Balmann, F. Lutin, Nanofiltration of glucose and sodium lactate solutions: variations of retention between single-and mixed-solute solutions, Journal of membrane science 258(1-2) (2005) 123-132.

[233] G. Bargeman, J. Vollenbroek, J. Straatsma, C. Schroën, R. Boom, Nanofiltration of multi-component feeds. Interactions between neutral and charged components and their effect on retention, Journal of membrane science 247(1-2) (2005) 11-20.
[234] S. Bouranene, A. Szymczyk, P. Fievet, A. Vidonne, Influence of inorganic electrolytes on the retention of polyethyleneglycol by a nanofiltration ceramic membrane, Journal of Membrane Science 290(1-2) (2007) 216-221.
[235] S. Mandale, M. Jones, Interaction of electrolytes and non-electrolytes in nanofiltration, Desalination 219(1-3) (2008) 262-271.
[236] O. Serbanescu, S. Voicu, V. Thakur, Polysulfone functionalized membranes: Properties and challenges, Materials Today Chemistry 17 (2020) 100302.
[237] Y. Huang, C. Shang, L. Li, Novel N-doped graphene enhanced ultrafiltration nano-porous polyvinylidene fluoride membrane with high permeability and stability for water treatment, Separation and Purification Technology 267 (2021) 118622.
[238] K. Cheng, N. Zhang, N. Yang, S. Hou, J. Ma, L. Zhang, Y. Sun, B. Jiang, Rapid and robust modification of PVDF ultrafiltration membranes with enhanced permselectivity, antifouling and antibacterial performance, Separation and Purification Technology 262 (2021) 118316.
[239] S. Yu, X. Zhang, F. Li, X. Zhao, Poly (vinyl pyrrolidone) modified poly (vinylidene fluoride) ultrafiltration membrane via a two-step surface grafting for radioactive wastewater treatment, Separation and purification technology 194 (2018) 404-409.
[240] D.J. Miller, D.R. Dreyer, C.W. Bielawski, D.R. Paul, B.D. Freeman, Surface modification of water purification membranes, Angewandte Chemie International Edition 56(17) (2017) 4662-4711.
[241] S. Thomas, R. Shanks, S. Chandran, Design and applications of nanostructured polymer blends and nanocomposite systems, William Andrew2015.
[242] Y. Cohen, M.-M. Kim, G.T. Lewis, N.H.-Y. Lin, Fouling and scaling resistant nano-structured reverse osmosis membranes, Google Patents, 2013.
[243] Q. Zeng, Z. Wan, Y. Jiang, J. Fortner, Enhanced Polysulfone Ultrafiltration Membrane Performance through Fullerol Addition: A Study Towards Optimization, Chemical Engineering Journal (2021) 134071.
[244] R. Levy, M. Maaloum, Measuring the spring constant of atomic force microscope cantilevers: thermal fluctuations and other methods, Nanotechnology 13(1) (2001) 33.

[245] V. Freger, Swelling and morphology of the skin layer of polyamide composite membranes: an atomic force microscopy study, Environmental science & technology 38(11) (2004) 3168-3175.
[246] R.S. Faibish, W. Yoshida, Y. Cohen, Contact angle study on polymer-grafted silicon wafers, Journal of colloid and interface science 256(2) (2002) 341-350.
[247] S. Salgin, U. Salgin, N. Soyer, Streaming potential measurements of polyethersulfone ultrafiltration membranes to determine salt effects on membrane zeta potential, Int. J. Electrochem. Sci 8(3) (2013) 4073-4084.
[248] H.-S. Choi, Y.-S. Kim, Y. Zhang, S. Tang, S.-W. Myung, B.-C. Shin, Plasma-induced graft co-polymerization of acrylic acid onto the polyurethane surface, Surface and Coatings Technology 182(1) (2004) 55-64.
[249] N. Inagaki, Plasma surface modification and plasma polymerization, CRC press1996.
[250] C. Wang, J.-R. Chen, Studies on surface graft polymerization of acrylic acid onto PTFE film by remote argon plasma initiation, Applied Surface Science 253(10) (2007) 4599-4606.
[251] M.L. Steen, L. Hymas, E.D. Havey, N.E. Capps, D.G. Castner, E.R. Fisher, Low temperature plasma treatment of asymmetric polysulfone membranes for permanent hydrophilic surface modification, Journal of Membrane Science 188(1) (2001) 97-114.
[252] J. Hopkins, J. Badyal, XPS and atomic force microscopy of plasma-treated polysulfone, Journal of Polymer Science Part A: Polymer Chemistry 34(8) (1996) 1385-1393.
[253] E. Gonzalez, M. Barankin, P. Guschl, R. Hicks, Remote atmospheric-pressure plasma activation of the surfaces of polyethylene terephthalate and polyethylene naphthalate, Langmuir 24(21) (2008) 12636-12643.
[254] J. Wang, X. Chen, R. Reis, Z. Chen, N. Milne, B. Winther-Jensen, L. Kong, L.F. Dumée, Plasma modification and synthesis of membrane materials—a mechanistic review, Membranes 8(3) (2018) 56.
[255] Y.Q. Song, J. Sheng, M. Wei, X.B. Yuan, Surface modification of polysulfone membranes by low-temperature plasma–graft poly (ethylene glycol) onto polysulfone membranes, Journal of applied polymer science 78(5) (2000) 979-985.
[256] I. Gancarz, G. Poźniak, M. Bryjak, Modification of polysulfone membranes 1. CO2 plasma treatment, European Polymer Journal 35(8) (1999) 1419-1428.

[257] E. Gonzalez, M.D. Barankin, P.C. Guschl, R.F. Hicks, Ring opening of aromatic polymers by remote atmospheric-pressure plasma, IEEE transactions on plasma science 37(6) (2009) 823-831.
[258] M. Bryjak, I. Gancarz, G. Poźniak, W. Tylus, Modification of polysulfone membranes 4. Ammonia plasma treatment, European polymer journal 38(4) (2002) 717-726.
[259] I. Gancarz, G. Poźniak, M. Bryjak, Modification of polysulfone membranes: 3. Effect of nitrogen plasma, European Polymer Journal 36(8) (2000) 1563-1569.
[260] D.S. Wavhal, E.R. Fisher, Modification of porous poly (ether sulfone) membranes by low-temperature CO2-plasma treatment, Journal of Polymer Science Part B: Polymer Physics 40(21) (2002) 2473-2488.
[261] V. Nguyen, W. Yoshida, J.D. Jou, Y. Cohen, Kinetics of free-radical graft polymerization of 1-vinyl-2-pyrrolidone onto silica, Journal of Polymer Science Part A: Polymer Chemistry 40(1) (2002) 26-42.
[262] P. De Gennes, Polymers at an interface; a simplified view, Advances in colloid and interface science 27(3-4) (1987) 189-209.
[263] N. Dumitrascu, G. Borcia, G. Popa, Corona discharge treatments of plastified PVC samples used in biological environment, Journal of applied polymer science 81(10) (2001) 2419-2425.
[264] B. Chen, H. Jiang, X. Liu, X. Hu, Observation and analysis of water transport through graphene oxide interlamination, The Journal of Physical Chemistry C 121(2) (2017) 1321-1328.
[265] J.N. Israelachvili, Intermolecular and surface forces, Academic press2015.
[266] W.J. Feast, H.S. Munro, Polymer surfaces and interfaces, Wiley1987.
[267] A. Marshall, P. Munro, G. Trägårdh, The effect of protein fouling in microfiltration and ultrafiltration on permeate flux, protein retention and selectivity: a literature review, Desalination 91(1) (1993) 65-108.
[268] A. Fane, C. Fell, A. Suki, The effect of pH and ionic environment on the ultrafiltration of protein solutions with retentive membranes, Journal of membrane science 16 (1983) 195-210.
[269] T. Chittrakarn, Y. Tirawanichakul, S. Sirijarukul, C. Yuenyao, Plasma induced graft polymerization of hydrophilic monomers on polysulfone gas separation membrane surfaces, Surface and Coatings Technology 296 (2016) 157-163.
[270] D. Breite, M. Went, A. Prager, A. Schulze, The critical zeta potential of polymer membranes: how electrolytes impact membrane fouling, RSC advances 6(100) (2016) 98180-98189.

[271] M. Mullet, P. Fievet, A. Szymczyk, A. Foissy, J.-C. Reggiani, J. Pagetti, A simple and accurate determination of the point of zero charge of ceramic membranes, Desalination 121(1) (1999) 41-48.
[272] P. Van der Meeren, H. Saveyn, S.B. Kassa, W. Doyen, R. Leysen, Colloid–membrane interaction effects on flux decline during cross-flow ultrafiltration of colloidal silica on semi-ceramic membranes, Physical Chemistry Chemical Physics 6(7) (2004) 1408-1412.
[273] E. Arkhangelsky, A. Duek, V. Gitis, Maximal pore size in UF membranes, Journal of Membrane Science 394 (2012) 89-97.
[274] R. Van Reis, A. Zydney, Membrane separations in biotechnology, Current Opinion in Biotechnology 12(2) (2001) 208-211.
[275] D.S. Wavhal, E.R. Fisher, Hydrophilic modification of polyethersulfone membranes by low temperature plasma-induced graft polymerization, Journal of Membrane Science 209(1) (2002) 255-269.
[276] X. Wang, D. Huang, B. Cheng, L. Wang, New insight into the adsorption behaviour of effluent organic matter on organic–inorganic ultrafiltration membranes: a combined QCM-D and AFM study, Royal Society open science 5(8) (2018) 180586.
[277] Z. Liu, Z. Mi, C. Chen, H. Zhou, X. Zhao, D. Wang, Preparation of hydrophilic and antifouling polysulfone ultrafiltration membrane derived from phenolphthalin by copolymerization method, Applied Surface Science 401 (2017) 69-78.
[278] Y. Chen, J. Zhang, Y. Cohen, Fouling Resistant and Performance Tunable Ultrafiltration Membranes via Surface Graft Polymerization induced by Atmospheric Pressure Air Plasma, Separation and Purification Technology (2022) 120490.
[279] T.S. Williams, H. Yu, R.F. Hicks, Atmospheric pressure plasma activation of polymers and composites for adhesive bonding, Reviews of Adhesion and Adhesives 1(1) (2013) 46-87.
[280] A. Pourjavadi, M.J. Zohuriaan-Mehr, Modification of carbohydrate polymers via grafting in air. 1. ceric-induced synthesis of starch-g-polyacrylonitrile in presence and absence of oxygen, Starch-Stärke 54(3-4) (2002) 140-147.
[281] N. Pezeshk, D. Rana, R. Narbaitz, T. Matsuura, Novel modified PVDF ultrafiltration flat-sheet membranes, Journal of membrane science 389 (2012) 280-286.
[282] Z. Wang, H. Yu, J. Xia, F. Zhang, F. Li, Y. Xia, Y. Li, Novel GO-blended PVDF ultrafiltration membranes, Desalination 299 (2012) 50-54.

[283] E. Eren, A. Sarihan, B. Eren, H. Gumus, F.O. Kocak, Preparation, characterization and performance enhancement of polysulfone ultrafiltration membrane using PBI as hydrophilic modifier, Journal of Membrane Science 475 (2015) 1-8.
[284] V. Vatanpour, A. Ghadimi, A. Karimi, A. Khataee, M.E. Yekavalangi, Antifouling polyvinylidene fluoride ultrafiltration membrane fabricated from embedding polypyrrole coated multiwalled carbon nanotubes, Materials Science and Engineering: C 89 (2018) 41-51.
[285] E. Kang, Y. Lee, K. Chon, J. Cho, Effects of hydrodynamic conditions (diffusion vs. convection) and solution chemistry on effective molecular weight cut-off of negatively charged nanofiltration membranes, Desalination 352 (2014) 136-141.
[286] A. Hassan, A. Ismail, Characterization of nanofiltration membranes by the solute transport method: Some practical aspects in determining of mean pore size and pore size distributions, Regional Symposium on Membrane Science and Technology, Johor, Malaysia, Citeseer, 2004.
[287] N. Tsubokawa, Y. Shirai, K. Hashimoto, Effect of polymerization conditions on the molecular weight of polystyrene grafted onto silica in the radical graft polymerization initiated by azo or peroxyester groups introduced onto the surface, Colloid and Polymer Science 273(11) (1995) 1049-1054.
[288] P.C. Hiemenz, T.P. Lodge, Polymer chemistry, CRC press2007.
[289] Z.M. TAGHI, M.A. Darvishi, Kinetics and mechanism of heterogeneous graft polymerization of acrylonitrile onto polyvinyl alcohol initiated with ceric ammonium nitrate, Iranian Polymer Journal 10 (2001) 283-292.
[290] T. Swift, L. Swanson, M. Geoghegan, S. Rimmer, The pH-responsive behaviour of poly (acrylic acid) in aqueous solution is dependent on molar mass, Soft Matter 12(9) (2016) 2542-2549.
[291] G. Blauer, Polymerization of methacrylic acid at pH 4 to 11, Transactions of the Faraday Society 56 (1960) 606-612.
[292] M. Riahinezhad, N. McManus, A. Penlidis, Effect of monomer concentration and pH on reaction kinetics and copolymer microstructure of acrylamide/acrylic acid copolymer, Macromolecular Reaction Engineering 9(2) (2015) 100-113.
[293] E. Currie, A. Sieval, G. Fleer, M.C. Stuart, Polyacrylic acid brushes: surface pressure and salt-induced swelling, Langmuir 16(22) (2000) 8324-8333.

[294] E. Currie, A. Sieval, M. Avena, H. Zuilhof, E. Sudhölter, M. Cohen Stuart, Weak polyacid brushes: preparation by LB deposition and optically detected titrations, Langmuir 15(21) (1999) 7116-7118.
[295] K. Kim, K. Lee, K. Cho, C. Park, Surface modification of polysulfone ultrafiltration membrane by oxygen plasma treatment, Journal of membrane science 199(1-2) (2002) 135-145.
[296] E.M. Hoek, A.K. Ghosh, X. Huang, M. Liong, J.I. Zink, Physical–chemical properties, separation performance, and fouling resistance of mixed-matrix ultrafiltration membranes, Desalination 283 (2011) 89-99.
[297] X. Zhao, A. Qin, D. Liu, C. He, Tuning the antifouling property of PVDF ultrafiltration membrane with surface anchored polyelectrolyte complexes for sewage treatment, RSC Advances 5(78) (2015) 63580-63587.
[298] H.T. Dang, R.M. Narbaitz, T. Matsuura, Double-pass casting: A novel technique for developing high performance ultrafiltration membranes, Journal of Membrane Science 323(1) (2008) 45-52.
[299] A. Lazea, L. Kravets, B. Albu, C. Ghica, G. Dinescu, Modification of polyester track membranes by plasma treatments, Surface and Coatings Technology 200(1-4) (2005) 529-533.
[300] C. Riccardi, R. Barni, M. Fontanesi, Experimental study and simulations of electronegative discharges at low pressure, Journal of Applied Physics 90(8) (2001) 3735-3742.
[301] J.F. Kolb, A.-A.H. Mohamed, R.O. Price, R.J. Swanson, A. Bowman, R. Chiavarini, M. Stacey, K. Schoenbach, Cold atmospheric pressure air plasma jet for medical applications, Applied Physics Letters 92(24) (2008) 241501.
[302] L. Guo, P.H. Santschi, Ultrafiltration and its applications to sampling and characterisation of aquatic colloids, IUPAC Series on Analytical and Physical Chemistry of Environmental Systems 10 (2007) 159.
[303] M. Cheryan, Ultrafiltration and microfiltration handbook, CRC press1998.
[304] E. Bittrich, M. Kuntzsch, K.J. Eichhorn, P. Uhlmann, Complex pH-and temperature-sensitive swelling behavior of mixed polymer brushes, Journal of Polymer Science Part B: Polymer Physics 48(14) (2010) 1606-1615.
[305] J. Wang, P. Somasundaran, Reversible conformational behavior of poly (acrylic acid) LB film with changes in pH, ionic strength and time, Colloids and Surfaces A: Physicochemical and Engineering Aspects 273(1-3) (2006) 63-69.

[306] R. Good, E. Kotsidas, Contact angles on swollen polymers: the surface energy of crosslinked polystyrene, (1979).
[307] C. Kostaras, D. Kati, A. Christoulaki, N. Spiliopoulos, D. Anastassopoulos, A. Vradis, C. Toprakcioglu, G. Priftis, STIMULI-RESPONSIVE POLYMER BRUSHES IN NANOCONFINED GEOMETRY.
[308] S. Nicolas, B. Balannec, F. Beline, B. Bariou, Ultrafiltration and reverse osmosis of small non-charged molecules: a comparison study of rejection in a stirred and an unstirred batch cell, Journal of Membrane Science 164(1-2) (2000) 141-155.
[309] X. Jin, Y.-L. Hsieh, pH-responsive swelling behavior of poly (vinyl alcohol)/poly (acrylic acid) bi-component fibrous hydrogel membranes, Polymer 46(14) (2005) 5149-5160.
[310] M.T. Bernards, G. Cheng, Z. Zhang, S. Chen, S. Jiang, Nonfouling polymer brushes via surface-initiated, two-component atom transfer radical polymerization, Macromolecules 41(12) (2008) 4216-4219.
[311] G. Kang, Y. Cao, H. Zhao, Q. Yuan, Preparation and characterization of crosslinked poly (ethylene glycol) diacrylate membranes with excellent antifouling and solvent-resistant properties, Journal of Membrane Science 318(1-2) (2008) 227-232.
[312] F. Zamani, A. Ullah, E. Akhondi, H.J. Tanudjaja, E.R. Cornelissen, A. Honciuc, A.G. Fane, J.W. Chew, Impact of the surface energy of particulate foulants on membrane fouling, Journal of Membrane Science 510 (2016) 101-111.
[313] Y. Tan, M. Guo, Using surface free energy method to study the cohesion and adhesion of asphalt mastic, Construction and Building Materials 47 (2013) 254-260.
[314] D.K. Owens, R. Wendt, Estimation of the surface free energy of polymers, Journal of applied polymer science 13(8) (1969) 1741-1747.
[315] P.M. López-Pérez, A.P. Marques, R.M. da Silva, I. Pashkuleva, R.L. Reis, Effect of chitosan membrane surface modification via plasma induced polymerization on the adhesion of osteoblast-like cells, Journal of Materials Chemistry 17(38) (2007) 4064-4071.
[316] B. Jańczuk, T. Białopiotrowicz, W. Wójcik, The components of surface tension of liquids and their usefulness in determinations of surface free energy of solids, Journal of colloid and interface science 127(1) (1989) 59-66.
[317] S. Wu, Polymer interface and adhesion, Routledge2017.

[318] Q. Wang, Y. Guo, Z. Wang, J. Zhang, J. Yao, L. Jiang, Z. Wu, Effects of graphene derivatives on PVDF membrane modification evaluated with XDLVO theory and quartz crystal microbalance with dissipation, Water Environment Research: a Research Publication of the Water Environment Federation (2020).
[319] A. Masse, O. Arab, V. Séchet, P. Jaouen, M. Pontié, N.-E. Sabiri, S. Plantier, Performances of dead-end ultrafiltration of seawater: From the filtration and backwash efficiencies to the membrane fouling mechanisms, Separation and Purification Technology 156 (2015) 512-521.
[320] L.H.T. Lyly, B.S. Ooi, J.K. Lim, C. Derek, S. Low, Correlating the membrane surface energy to the organic fouling and wetting of membrane distillation at elevated temperature, Journal of Environmental Chemical Engineering 9(1) (2021) 104627.
[321] S. Zhao, Z. Liao, A. Fane, J. Li, C. Tang, C. Zheng, J. Lin, L. Kong, Engineering antifouling reverse osmosis membranes: A review, Desalination 499 (2021) 114857.
[322] Y. He, J. Liu, G. Han, T.-S. Chung, Novel thin-film composite nanofiltration membranes consisting of a zwitterionic co-polymer for selenium and arsenic removal, Journal of Membrane Science 555 (2018) 299-306.
[323] P. Xu, M. Capito, T.Y. Cath, Selective removal of arsenic and monovalent ions from brackish water reverse osmosis concentrate, Journal of hazardous materials 260 (2013) 885-891.
[324] N.R. Council, Arsenic in drinking water, (1999).
[325] J.J. Camacho-Cristóbal, J. Rexach, A. González-Fontes, Boron in plants: deficiency and toxicity, Journal of Integrative Plant Biology 50(10) (2008) 1247-1255.
[326] S. Madaeni, S. Koocheki, Influence of di-hydrogen phosphate ion on performance of polyamide reverse osmosis membrane for nitrate and nitrite removal, Journal of Porous Materials 17(2) (2010) 163-168.
[327] A.M. Comerton, R.C. Andrews, D.M. Bagley, Evaluation of an MBR–RO system to produce high quality reuse water: Microbial control, DBP formation and nitrate, Water research 39(16) (2005) 3982-3990.
[328] B. Tepuš, M. Simonič, I. Petrinić, Comparison between nitrate and pesticide removal from ground water using adsorbents and NF and RO membranes, Journal of hazardous materials 170(2-3) (2009) 1210-1217.

[329] S. Shultz, M. Bass, R. Semiat, V. Freger, Modification of polyamide membranes by hydrophobic molecular plugs for improved boron rejection, Journal of Membrane Science 546 (2018) 165-172.
[330] O. Coronell, B. Mi, B.J. Mariñas, D.G. Cahill, Modeling the effect of charge density in the active layers of reverse osmosis and nanofiltration membranes on the rejection of arsenic (III) and potassium iodide, Environmental science & technology 47(1) (2013) 420-428.
[331] J.J. Waypa, M. Elimelech, J.G. Hering, Arsenic removal by RO and NF membranes, Journal-American Water Works Association 89(10) (1997) 102-114.
[332] Y. Li, S. Wang, X. Song, Y. Zhou, H. Shen, X. Cao, P. Zhang, C. Gao, High boron removal polyamide reverse osmosis membranes by swelling induced embedding of a sulfonyl molecular plug, Journal of Membrane Science 597 (2020) 117716.
[333] R. Bernstein, S. Belfer, V. Freger, Toward improved boron removal in RO by membrane modification: feasibility and challenges, Environmental science & technology 45(8) (2011) 3613-3620.
[334] V. Vatanpour, A. Sanadgol, Surface modification of reverse osmosis membranes by grafting of polyamidoamine dendrimer containing graphene oxide nanosheets for desalination improvement, Desalination 491 (2020) 114442.
[335] X. Zhai, J. Meng, R. Li, L. Ni, Y. Zhang, Hypochlorite treatment on thin film composite RO membrane to improve boron removal performance, Desalination 274(1-3) (2011) 136-143.
[336] Y. Chen, S. Kim, Y. Kim, J.S. Walker, T. Wolfe, K. Coleman, Y. Cohen, Scale up of polyamide reverse osmosis membranes surface modification with tethered poly (acrylic acid) for fabrication of low fouling spiral-wound elements, Desalination 536 (2022) 115762.
[337] A.L. Zydney, Stagnant film model for concentration polarization in membrane systems, Journal of Membrane Science 130(1-2) (1997) 275-281.
[338] I. Sutzkover, D. Hasson, R. Semiat, Simple technique for measuring the concentration polarization level in a reverse osmosis system, Desalination 131(1-3) (2000) 117-127.
[339] Y. Fernández-Nava, E. Marañón, J. Soons, L. Castrillón, Denitrification of high nitrate concentration wastewater using alternative carbon sources, Journal of Hazardous Materials 173(1-3) (2010) 682-688.

[340] M.M. Nasef, M. Nallappan, Z. Ujang, Polymer-based chelating adsorbents for the selective removal of boron from water and wastewater: a review, Reactive and Functional Polymers 85 (2014) 54-68.
[341] D. Mohan, C.U. Pittman Jr, Arsenic removal from water/wastewater using adsorbents—a critical review, Journal of hazardous materials 142(1-2) (2007) 1-53.
[342] P. Cheng, M.M. Kelly, N.K. Moehring, W. Ko, A.-P. Li, J.C. Idrobo, M.S. Boutilier, P.R. Kidambi, Facile size-selective defect sealing in large-area atomically thin graphene membranes for sub-nanometer scale separations, Nano Letters 20(8) (2020) 5951-5959.
[343] W.E. Mickols, Composite membrane with polyalkylene oxide modified polyamide surface, Google Patents, 2001.
[344] A.C. Sagle, E.M. Van Wagner, H. Ju, B.D. McCloskey, B.D. Freeman, M.M. Sharma, PEG-coated reverse osmosis membranes: desalination properties and fouling resistance, Journal of Membrane Science 340(1-2) (2009) 92-108.
[345] M. Zheng, X. Zhao, S. Xu, D. Lu, Ultrathin support-free membrane with high water flux for forward osmosis desalination, Water, Air, & Soil Pollution 230(6) (2019) 1-8.
[346] Y.D. Ahdab, J.H. Lienhard, Desalination of brackish groundwater to improve water quality and water supply, Global Groundwater, Elsevier2021, pp. 559-575.
[347] D.M. Warsinger, J. Swaminathan, E. Guillen-Burrieza, H.A. Arafat, Scaling and fouling in membrane distillation for desalination applications: a review, Desalination 356 (2015) 294-313.
[348] B. Mi, M. Elimelech, Silica scaling and scaling reversibility in forward osmosis, Desalination 312 (2013) 75-81.
[349] B. Cao, A. Ansari, X. Yi, D.F. Rodrigues, Y. Hu, Gypsum scale formation on graphene oxide modified reverse osmosis membrane, Journal of Membrane Science 552 (2018) 132-143.
[350] Z. Amjad, K. Demadis, Mineral scales and deposits, Scientific and Technological Approaches, Elsevier2015.
[351] P. Dydo, M. Turek, J. Ciba, Scaling analysis of nanofiltration systems fed with saturated calcium sulfate solutions in the presence of carbonate ions, Desalination 159(3) (2003) 245-251.
[352] J. Ochando-Pulido, M. Victor-Ortega, A. Martinez-Ferez, On the cleaning procedure of a hydrophilic reverse osmosis membrane fouled by secondary-treated olive mill wastewater, Chemical Engineering Journal 260 (2015) 142-151.

[353] A. Rahardianto, B.C. McCool, Y. Cohen, Reverse osmosis desalting of inland brackish water of high gypsum scaling propensity: kinetics and mitigation of membrane mineral scaling, Environmental science & technology 42(12) (2008) 4292-4297.
[354] F. Kiefer, A. Präbst, T. Sattelmayer, Membrane scaling in Vacuum Membrane Distillation-Part 2: Crystallization kinetics and process performance, Journal of Membrane Science 590 (2019) 117293.
[355] M. Gryta, Calcium sulphate scaling in membrane distillation process, Chemical Papers 63(2) (2009) 146-151.
[356] W.-Y. Shih, A. Rahardianto, R.-W. Lee, Y. Cohen, Morphometric characterization of calcium sulfate dihydrate (gypsum) scale on reverse osmosis membranes, Journal of membrane science 252(1-2) (2005) 253-263.
[357] O.D. Supekar, D.J. Park, A.R. Greenberg, J.T. Gopinath, V.M. Bright, Real-time detection of early-stage calcium sulfate and calcium carbonate scaling using Raman spectroscopy, Journal of Membrane Science 596 (2020) 117603.
[358] F. He, K.K. Sirkar, J. Gilron, Studies on scaling of membranes in desalination by direct contact membrane distillation: CaCO3 and mixed CaCO3/CaSO4 systems, Chemical Engineering Science 64(8) (2009) 1844-1859.
[359] C. Tzotzi, T. Pahiadaki, S. Yiantsios, A. Karabelas, N. Andritsos, A study of CaCO3 scale formation and inhibition in RO and NF membrane processes, Journal of membrane science 296(1-2) (2007) 171-184.
[360] K.J. Varin, N.H. Lin, Y. Cohen, Biofouling and cleaning effectiveness of surface nanostructured reverse osmosis membranes, Journal of membrane science 446 (2013) 472-481.
[361] A. Klimchouk, The dissolution and conversion of gypsum and anhydrite, International Journal of Speleology 25(3) (1996) 2.
[362] T.E. Larson, A.M. Buswell, H.F. Ludwig, W. Langelier, Calcium carbonate saturation index and alkalinity interpretations [with discussion], Journal (American Water Works Association) (1942) 1667-1684.
[363] X. Zhang, J. Tian, S. Gao, W. Shi, Z. Zhang, F. Cui, S. Zhang, S. Guo, X. Yang, H. Xie, Surface functionalization of TFC FO membranes with zwitterionic polymers: Improvement of antifouling and salt-responsive cleaning properties, Journal of Membrane Science 544 (2017) 368-377.

[364] A. Drechsler, M.M. Elmahdy, P. Uhlmann, M. Stamm, PH and salt response of mixed brushes made of oppositely charged polyelectrolytes studied by in situ AFM force measurements and imaging, Langmuir 34(16) (2018) 4739-4749.
[365] M. Shmulevsky, X. Li, H. Shemer, D. Hasson, R. Semiat, Analysis of the onset of calcium sulfate scaling on RO membranes, Journal of membrane science 524 (2017) 299-304.
[366] F. Banat, N. Jwaied, M. Rommel, J. Koschikowski, M. Wieghaus, Desalination by a "compact SMADES" autonomous solarpowered membrane distillation unit, Desalination 217(1-3) (2007) 29-37.
[367] F. Banat, N. Jwaied, M. Rommel, J. Koschikowski, M. Wieghaus, Performance evaluation of the "large SMADES" autonomous desalination solar-driven membrane distillation plant in Aqaba, Jordan, Desalination 217(1-3) (2007) 17-28.
[368] M. Gryta, Long-term performance of membrane distillation process, Journal of Membrane Science 265(1-2) (2005) 153-159.
[369] M. Gryta, Effectiveness of water desalination by membrane distillation process, Membranes 2(3) (2012) 415-429.
[370] E. Guillén-Burrieza, J. Blanco, G. Zaragoza, D.-C. Alarcón, P. Palenzuela, M. Ibarra, W. Gernjak, Experimental analysis of an air gap membrane distillation solar desalination pilot system, Journal of Membrane Science 379(1-2) (2011) 386-396.
[371] Ş.G. Öner, N. Kabay, E. Güler, M. Kitiş, M. Yüksel, A comparative study for the removal of boron and silica from geothermal water by cross-flow flat sheet reverse osmosis method, Desalination 283 (2011) 10-15.
[372] M.S. Gaikwad, C. Balomajumder, Simultaneous rejection of fluoride and Cr (VI) from synthetic fluoride-Cr (VI) binary water system by polyamide flat sheet reverse osmosis membrane and prediction of membrane performance by CFSK and CFSD models, Journal of Molecular Liquids 234 (2017) 194-200.
[373] Y. Cengeloglu, G. Arslan, A. Tor, I. Kocak, N. Dursun, Removal of boron from water by using reverse osmosis, Separation and Purification Technology 64(2) (2008) 141-146.
[374] L. McKeen, 4-markets and applications for films, containers, and membranes, Permeability Properties of Plastics and Elastomers (2012) 59-75.
[375] H. Gu, A.R. Bartman, M. Uchymiak, P.D. Christofides, Y. Cohen, Self-adaptive feed flow reversal operation of reverse osmosis desalination, Desalination 308 (2013) 63-72.

[376] L. Gao, A. Rahardianto, H. Gu, P.D. Christofides, Y. Cohen, Energy-optimal control of RO desalination, Industrial & Engineering Chemistry Research 53(18) (2014) 7409-7420.
[377] L. Gao, Self-Adaptive Control of Integrated Ultrafiltration and Reverse Osmosis Desalination Systems, University of California, Los Angeles2017.
[378] I. Lomax, Experiences of Dow in the field of seawater reverse osmosis, Desalination 224(1-3) (2008) 111-118.
[379] W. Salim, V. Vakharia, Y. Chen, D. Wu, Y. Han, W.W. Ho, Fabrication and field testing of spiral-wound membrane modules for CO2 capture from flue gas, Journal of Membrane Science 556 (2018) 126-137.
[380] K.K. Chen, W. Salim, Y. Han, D. Wu, W.W. Ho, Fabrication and scale-up of multi-leaf spiral-wound membrane modules for CO2 capture from flue gas, Journal of Membrane Science 595 (2020) 117504.
[381] M. Kumar, S. Adham, J. DeCarolis, Reverse osmosis integrity monitoring, Desalination 214(1-3) (2007) 138-149.
[382] Y. Ohkouchi, T. Ase, Determination of log removal values of bacteria by spiral-wound reverse osmosis modules and a hollow fiber ultrafiltration module using Escherichia coli and indigenous heterotrophic bacteria as indicators, Journal of Water and Health 18(6) (2020) 956-967.
[383] X. Ji, E. Curcio, S. Al Obaidani, G. Di Profio, E. Fontananova, E. Drioli, Membrane distillation-crystallization of seawater reverse osmosis brines, Separation and Purification Technology 71(1) (2010) 76-82.
[384] M. Gryta, M. Tomaszewska, K. Karakulski, Wastewater treatment by membrane distillation, Desalination 198(1-3) (2006) 67-73.
[385] X. Wei, Y. Luo, P. Huang, 3D bioprinting of alginate scaffolds with controlled micropores by leaching of recrystallized salts, Polymer Bulletin 76(12) (2019) 6077-6088.
[386] N.A. Qasem, M.M. Generous, B.A. Qureshi, S.M. Zubair, A Comprehensive Review of Saline Water Correlations and Data: Part II—Thermophysical Properties, Arabian Journal for Science and Engineering (2021) 1-39.
[387] K. Nayar, D. Panchanathan, G. McKinley, J. Lienhard, Surface tension of seawater, Journal of Physical and Chemical Reference Data 43(4) (2014) 043103.

[388] J.K. Beattie, A.M. Djerdjev, A. Gray-Weale, N. Kallay, J. Lützenkirchen, T. Preočanin, A. Selmani, pH and the surface tension of water, Journal of colloid and interface science 422 (2014) 54-57.
[389] Y. Lü, B. Wei, Second inflection point of water surface tension, Applied physics letters 89(16) (2006) 164106.
[390] D. Fu, J.-F. Lu, T.-Z. Bao, Y.-G. Li, Investigation of surface tension and interfacial tension in surfactant solutions by SAFT, Industrial & engineering chemistry research 39(2) (2000) 320-327.
[391] F. Goncalves, J. Kestin, J. Sengers, Surface-tension effects in suspended-level capillary viscometers, International journal of thermophysics 12(6) (1991) 1013-1028.
[392] P. Nikitas, A. Pappa-Louisi, Thermodynamic and modelistic study of surface solutions: aqueous solutions containing 2-butanol, Journal of Physical Chemistry 94(1) (1990) 361-370.